LANDSLIDE DISTRIBUTIONS AROUND GLACIERS IN HIGH MOUNTAINS

M S ALLAN

PhD

2018

LANDSLIDE DISTRIBUTIONS AROUND GLACIERS IN HIGH MOUNTAINS

MARK STUART ALLAN

A thesis submitted in partial fulfilment of the requirements of the University of Northumbria at Newcastle for the degree of Doctor of Philosophy

Research undertaken in the
Faculty of Engineering and Environment

August 2018

Abstract

Landslides, hereafter referred to as slope failures, are key geomorphic processes in mountain basins. The slope failure response to de-glaciation represents an important but poorly understood feedback to climate change. This PhD study uses a high-resolution state-of-the-art photogrammetric approach to detect and quantify failures across slopes above and around five glaciers in the Mont Blanc massif; Glacier d'Argentière, Mer de Glace, Glacier de Bossons, Ghiacciaio del Miage and Pre de Bard, over a monitoring period of one year. The statistical distributions are examined by means of a probabilistic magnitude-frequency analysis, and spatial distributions are analysed using GIS. The 3D data are also used to examine the structural properties and stability of a recently de-glaciated rock-slope by means of an innovative approach to assigning a rock mass strength classification. The analysis yielded an extensive inventory of 900 failures ranging over several orders of magnitude in volume, of which 43 are primary (i.e. rock-slope failure) and 857 are secondary (i.e. sediment remobilisation). The majority of failure activity within the observation period have happened along the steep-sided sediment-mantled lateral moraines at both glaciated and de-glaciated sites, representing a significant volume of sediment input into the glacial/ fluvial system of $3.7 \times 10^5 m^3$ over one year. The results highlight the high frequency of small-magnitude failures and both primary and secondary slope failures form a characteristic magnitude-frequency distribution with an inverse tail and a rollover. A power-law can be fitted above a lower bound of 59.40 and 167.00 m^3 for primary and secondary failures respectively with scaling exponents of 3.02 and 1.75 indicating a predominance of small-magnitude events, though a log-normal model is found to be a more suitable fit than a power-law across a wider range of magnitudes at the majority of sites. The log-normal can be fitted to the data above lower bounds of 60.20 and 13.80 for primary and secondary failures respectively with scaling exponents of 4.02, 0.79 and 1.32, 2.99. The fitted models fail to correctly characterise the likelihood of large-magnitude failures which has significant implications for resolving the probabilistic nature of slope failure distributions in the future. Slope failures from rock-slopes are shown to occur in areas of highly fractured rock, whilst maximal frequencies of secondary events are shown to occur on over-steepened slopes with a SW-aspect which suggests a link with meteorological conditions though further work would be required to understand driving processes. The data shows a significant input of sediment from failures is achieved well in-advance of the complete de-glaciation of mountain valleys and delivery to glacier surface. Highest rates of moraine erosion are observed at glaciers that a characterised by continuous debris-cover. The early onset of the paraglacial slope response has been presented as a conceptual model of sediment yield. The yield is driven by sediment availability, connectivity and slope stability and remains higher than the geological norm through the period of de-glaciation whilst un-worked sediments are continually exposed through ongoing glacier shrinkage, before declining to background 'norm' following the complete removal of ice. This work is the first attempt to examine the distribution of slope failures at such a high-resolution and across such a scale, considering slopes above actively wasting glaciers and those in the recently de-glaciated pro-glacial zone, providing a unique insight into range-scale slope failure distributions.

List of Contents

List of Figures

List of Tables

List of Equations

List of Acronyms and Abbreviations

CDF	Cumulative Density Function
HARW	High Alpine Rockwall
LIA	Little Ice Age
L-N	Log-Normal
LOD	Level of Detection
MF	Magnitude-Frequency
MVS	Multi-View Stereo
PDF	Probability Density Function
P-L	Power-Law
SfM	Structure-from-Motion
TLS	Terrestrial Laser Scanning
UAS	Unmanned Aerial System
UAV	Unmanned Aerial Vehicle

List of Terminology and Definitions

Slope Failure	Refers to all types of slope collapses (as outlined in section 2.2.1) due to weakened self-retainability. No process-based assumptions are made.
Primary Slope Failure	Slope failures that occur from a rockslope.
Secondary Slope Failure	Slope failures that occur from sediment-mantled slopes (i.e. reworked sediments).
Mass Movement	Movement of surface material caused by gravity.
Size Distribution	Analysis of the distribution of slope failures by means of their respective magnitude (e.g. area and volume).
Spatial Distribution	Analysis of the distribution of slope failures by means of their respective characteristics (e.g. altitude, aspect and slope angle).

Acknowledgements

This thesis has proven to be a significant challenge over the last few years and one that I cannot be prouder to have overcome and completed. It would not have been possible without the support and encouragement of a great many people, to whom I extend my utmost gratitude. They have all played a part in making sure I stuck with it and helped make the doctoral journey an exciting and enjoyable one. In particular I'd like to acknowledge:

The help and guidance of my supervisory team; Dr Stuart Dunning, Dr Michael Lim and Prof John Woodward. Thank you for the opportunity to work with you and your patience and encouragement throughout the course of this PhD. I am also grateful to Dr M Kirkbride and Dr F Pellicciotti for their encouraging feedback during the VIVA examination process. Dr Kirkbride's comments contributed to improving this thesis.

The continuous support and guidance from Dan Holdsworth, without whom this PhD would not have existed. You've presented countless opportunities for which I am eternally grateful and have made this PhD journey completely unique and very enjoyable.

I would like to acknowledge and thank the staff and friends of the Royal Geographical Society and Jaguar Land Rover for awarding the bursary in the first year of my PhD which greatly supported the first season of fieldwork.

Those who assisted me in the field; carrying equipment, cooking meals and placing themselves in not-at-all dangerous situations to GPS the perfect ground control target, or collect a drone from impromptu water submergence tests. In particular, the support and encouragement of Pippa Summers, Ingeborg Pay, Andrew Newton and Dorota Medrzycka throughout my PhD has often brought a smile to my face at the end of a tough day. Also, to Thomas Shaw, with whom I have been fortunate enough to share the journey from the Masters at Sheffield. Rupert Bainbridge and Kate Winter, we started together, and it was a privilege to have worked alongside you both. My officemates and fellow postgraduate colleagues who I haven't mentioned already, for the laughter and interesting conversations that made our office a particularly positive working environment; Bradley Sparkes, Michael Cullum, Sina Panitz, Clare Webster, Flavia Burger, Jack Longman, Scott Taylor, Tom Watts, Stephanie Strother, Peter Gilbert and Otaigbe Inegbedion (Phil). To my good friends outside of academia; Jonathan Kellagher and Thomas Raine.

Coming back to this thesis after a year of intensive teacher training was a profoundly difficult task and I could not have done it without the support of my loving partner, Bridget Gardner, for which I am eternally grateful.

Finally, the support, encouragement and love of my family; my mum (Patricia), dad (David) and sister (Rachel).

Thank you!

Declaration

I, Mark Stuart Allan, declare that the work contained in this thesis entitled “Landslide distributions around glaciers in high mountains” has not been submitted for any other award and that the work is my own.

I confirm that this work was done wholly while in candidature for the research degree of Doctor of Philosophy at Northumbria University at Newcastle upon Tyne, and that it fully acknowledges opinions, ideas and contributions from the work of others.

Any ethical clearance for the research presented in this thesis has been approved. Approval has been sought and granted by the University Ethics Committee on 19/12/2013.

I declare that the Word Count of this Thesis is 58,136 words.

Name: Mark Stuart Allan

Signature:

Date: 31/08/18

1 Introduction and Aims

1.1 Introduction

Mountain systems account for approximately one-fifth of the Earth's continental land mass, are a key element in the global hydrological cycle and provide indirect life support to over 50 % of the World's population (Haeberli and Beniston, 1998). Slope failures are complex phenomena that play a significant role in the evolution of such environments and connectivity of sediment systems. The interactions between glacial and slope processes shape these landscapes and reflect an important but poorly understood response to climatic change. Throughout most mountain environments, warming climates have resulted in the substantial retreat of glaciers, for example; the volume of glacier ice in the European Alps has halved in the last 150 years (Haeberli and Beniston, 1998), exposing vast quantities of unstable and metastable sediment stores (Curry, Cleasby and Zukowskyj, 2006). An environment and its geomorphological adjustment in response to the removal of glacier ice can be considered a transient system (Lane *et al.*, 2016), where the recently exposed sediment stores are eroded through the means of *paraglacial* processes (Carrivick and Heckmann, 2017). The slopes above glaciers can deliver vast quantities of sediment to the ice surface and valley floor through a diverse range of mass movement processes, such as avalanches, slides and flows which may significantly affect glacier behaviour and the dynamics of the fluvial system.

In recently deglaciated, and actively deglaciating valleys, three main sources of sediment can be identified: (i) that which is derived from glacial erosion and subglacial sediment storage, (ii) that which is produced by weathering and instability of deglaciated bedrock, and (iii) that of glacigenic origin that covers hillslopes or accumulates in depositional landforms such as lateral and terminal moraines (Carrivick and Heckmann, 2017). With these three main sources, the links between different paraglacial landsystems can be represented as an interrupted sediment cascade (Ballantyne, 2002b), where ongoing ice retreat has been shown to continuously reveal previously-stored supplies of sediment (Cossart and Fort, 2008). Perhaps the clearest manifestation of responsive slope adjustment is the erosion of steep-sided sediment-mantled slopes comprising unconsolidated and unvegetated glacigenic sediment (e.g. fig. 1.1) (Curry, Cleasby and Zukowskyj, 2006). The sedimentological characteristics of these landforms have been shown to be poorly sorted and predominantly angular clasts mixed with sub-rounded and rounded clasts representing ice-contact and glacio-fluvial sediment respectively, forming unstable slopes (Hambrey and Ehrmann, 2004). Their dynamics and development following deglaciation have been described in conceptual models, such as the exhaustion model of Ballantyne (2002a) where all failures are assumed to be from the same finite number of slopes, and following a trajectory towards stabilisation and exhaustion of the unstable sediment store. *Sediment Exhaustion*, discussed more

thoroughly in chapter 2, describes the relationship between *time since deglaciation* and the proportion of 'available' sediment remaining in the system (i.e. sediment that is available for release as a consequence of glacial conditioning). The sediment exhaustion model presented by Ballantyne (2002a) implies that the rate of release activity (e.g. through slope failures etc.) is dependent on the proportion of sediment available for release or reworking and thus, in the early stages of deglaciation, such as the state of sites presented in this thesis, sediment availability and rate of sediment release will be at its greatest.

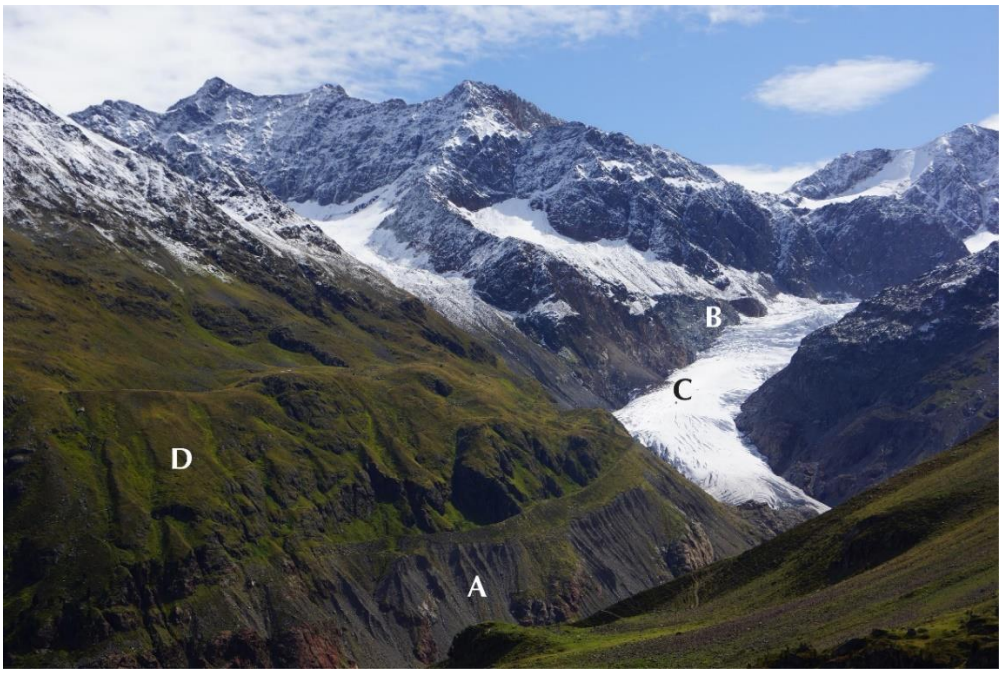

Figure 1.1: An example of an Alpine glacier, the Weißseespitze glacier (Kaunertal, Austria) and its proglacial zone. Steep-sided, sediment-mantled, gullied slopes that make up the lateral moraines of the glacier can clearly be seen in the foreground (A), whilst high-altitude rockwalls can be seen flanking the glacier in the ablation zone (B). Debris deposited on the glacier surface from a recent slope failure can be seen on the right-side of the glacier, close to the terminus (C), whilst stabilised, vegetated slopes are visible above the LIA trimline, with evidence of historic slope failure activity (D).

The observation, detection and quantification of geomorphological activity over the short-term is no trivial matter, as covering spatial scales can prove logistically challenging and small-sized events have low preservation potential and are often censored by other processes (Carrivick and Heckmann, 2017). The increasing availability of high-resolution topographic data and associated technology presents an opportunity for quantitative analysis of change across greater scales than previously shown. This thesis is concerned with the high-resolution detection and analysis of slope failures that occur above and around actively retreating glaciers in high-mountain environments over an observation period of one year; principally their spatial and size distributions, and their role in the sediment budget. It presents a number of sites in the Mont Blanc massif, European Alps, that have been selected for analysis using photogrammetric modelling of slope topography and 3D

change analysis to construct an inventory of slope failures. The methodological development of an emergent photogrammetric technique is shown before detailed observations and analyses for each site are given.

This introductory chapter seeks to provide a brief introduction to the main topic of the thesis, an overview of the rationale and existing gap in the literature and subject knowledge as well as outlining the principal aim and objectives of the research presented herein. An overview of each thesis chapter is also given as an indication of thesis structure.

1.2. Research Gap and Rationale

Glaciated environments are strongly influenced by fluctuations in the global climate system, providing the most visible evidence of warming and cooling through reduction and growth of ice mass over a variety of timescales. Continuous glaciations and deglaciations have shaped the mountain environments around the World, eroding and revealing landscapes that are particularly susceptible to rapid geomorphological change. The erosion and redistribution of sediment supplies in active mountain ranges results in cascades which can vary dramatically in time and space (Davies and Korup, 2010) and whilst a large body of research has examined the long-term failure distributions, reported the effects of specific failure events or observed the rate of site-specific failure activity, research on failure distributions along actively deglaciating and recently deglaciated slopes remains largely limited. Thus, such environments are still poorly understood, partly owing to the difficulties associated with obtaining observational data across large-enough scales which are often limited by logistical and financial constraints. Some researchers have found that paraglacial slope adjustment can occur with extreme rapidity (Curry, 1999) which highlights the necessity for observational data across these recently deglaciated landscapes for accurately quantifying the volume of failure material entering the system which in turn, has significant implications for fluvial dynamics and downstream activity. Where failures fall onto glaciers, they may affect the behaviour of the ice and have been shown to both protect against and exacerbate surface melting depending on thickness (Reznichenko *et al.*, 2010).

Development and understanding of mountain sediment budgets requires a thorough understanding of all slope processes and storage elements (Laute and Beylich, 2014). Despite the potential for serious implications of changes in sediment yield, there have been few considerations for the resulting geomorphic processes from a rapid transition from glacial to non-glacial conditions (Lane *et al.*, 2016). Additionally, analysis of a landsystem's sediment connectivity requires sound knowledge of three key elements (fig. 1.2); (i) frequency-magnitude distributions, (ii) spatial and temporal feedbacks, and (iii) mechanisms of mobility (Bracken *et al.*, 2015). Furthermore, the statistical analyses of failure distributions resolve their probabilistic nature and are a useful tool for

understanding slope evolution. A number of studies have addressed the magnitude-frequency of failures in various mountain ranges around the World (Bennett *et al.*, 2012), and quantities are often shown to follow an inverse power-law distribution with a rollover (i.e. a 'flattening' or 'rolling' off' of the distribution away from the negative correlation between landslide volume and probability) below a threshold magnitude (x_{min}). Some attribute this rollover to data bias, and a systematic under-sampling of failures below a certain magnitude, owing to a lack of substantial monitoring data at a high-enough resolution, poor preservation of small failures, whilst others suggest a physical basis (Stark and Hovius, 2001; Barlow *et al.*, 2012). This research presents a unique opportunity to; a) capture data at a resolution high-enough to detect failures that would usually fall below the threshold magnitude; b) compile an inventory that can be used to examine their statistical distributions; c) highlight whether a power-law is the most suitable fit and; d) explore whether the rollover is caused by geomorphological processes or a manifestation of data bias. The results presented in this thesis will have significant implications for understanding range-scale slope failure distributions and highlight a number of key characteristics of spatial and size distribution which can then be used to explore potential drivers and controls.

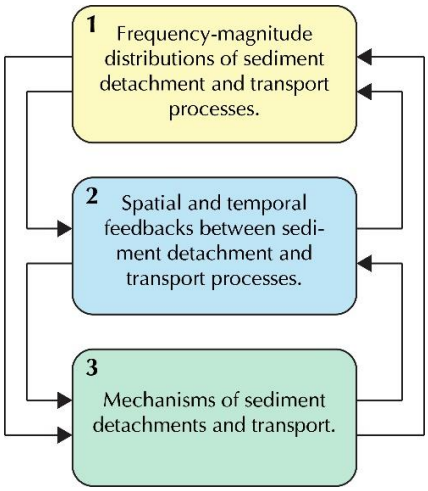

Figure 1.2: Sediment connectivity framework highlighting important linkages between three key elements. Adapted from Bracken et al. (2015).

1.3. Thesis Aims and Objectives

The aim of this research is to:

Understand the spatial and size distributions of slope failures above and around wasting glaciers.

This aim will be addressed by the following primary objectives:

1) Exploring the potential drivers and controls of short-term slope failures using their spatial distributions and through structural analysis of a recently deglaciated rockslope.

2) Analysing the effect of observed failure activity on the modification of slope form and mobilisation of sediment within the landsystem. Developing a conceptual model of a sediment yield and a deglaciating landsystem that considers the implications of these findings alongside existing knowledge.

These will be achieved by:

a) using an emergent photogrammetric technique to reconstruct the complex topography of mountain slopes. Building upon an existing body of recent literature and developing an optimal and appropriate workflow for minimising and dealing with known sources of error consistently;
b) detecting and quantifying failures at a number of glacial sites in the Mont Blanc massif using high-resolution topographic data created using the workflow developed in the previous step. Resolving their probabilistic nature by means of magnitude-frequency distributions and analysing their spatial distribution using GIS, and;
c) utilising a statistical goodness-of-fit test to determine the best model fitted to the magnitude-frequency distributions of detected slope failures and resolve whether the rollover in small-magnitude failures observed in other inventories are likely to be caused by geomorphological processes or a manifestation of data bias.

1.4. Thesis Structure

To address the aim and objectives of this research, the thesis is structured into four parts (introduction, methods, results and discussion/ conclusions) and seven chapters. It's important to note that the development of the SfM-MVS technique required a significant amount of testing; the results of which are found in chapter 4. An overview of each chapter is given here:

Chapter 2 introduces the literature surrounding slope failures, with a particular focus on mountain landscapes and the paraglacial response of the environment. The classification of failures, significant mechanisms of failure and the geomorphological consequences are also discussed. Insights into the paraglacial concept and landscape evolution models are given as the chapter builds a general picture of the hillslope response to deglaciation. The literature review also provides an overview of rock-slope stability and the current state of knowledge for classifying rock mass strength using topographic data. Finally, the chapter provides a background and overview of techniques for creating high-resolution topographical models for the purpose of quantifying change, with particular focus on the background, development and existing applications of SfM-MVS photogrammetry.

Chapter 3 presents the physical settings and descriptions of the Mont Blanc massif and Rhône glacier (used for methodological development) study sites, as well as the selected valleys within the range. It provides a general description of their history, current conditions and geology.

Chapter 4 is the methods chapter and presents the route taken to develop a suitable workflow alongside the results of a number of tests that were performed to assess the accuracy, usability and repeatability of the SfM-MVS technique. The development of a fully 3D workflow for the computation of change and calculation of volumetric differences with SfM-MVS data is also presented, as well as the workflow for analysis of failure distributions and the approach for verifying the significance of those results. The technique and algorithms used for the analysis of rock mass strength using 3D data are also outlined.

Chapter 5 is the results chapters, applying the methods outlined in chapter 4. The results from change analysis across all of the slopes studied in the project are presented on a site-by-site basis, before distributions are presented as a combined inventory. The method for assessing rock mass strength outlined in chapter 4 is applied at one site and presented here. The extracted discontinuity information and calculated strength rating are given, and any correlations between rock mass strength and detected failures are highlighted.

Chapter 6 discusses in detail the major trends and findings from the results. The wider implications and relevance of the results and its relation to the academic literature are then compiled and the conceptual models which address objective 5 are presented.

Chapter 7 presents the summary conclusions of this thesis in respect to each of the research objectives, highlighting key limitations and suggesting suitable directions for future work.

Two appendices accompany these chapters. These contain relevant supplementary information and additional data for the thesis that are briefly outline below:

Appendix A: Comprehensive list of all detected failures and their properties: *ID, location, type* and *size*.

Appendix B: An overview of the collaborations and outreach projects which have shaped this unique PhD project. The work produced with UK artist, Dan Holdsworth, is discussed and a list of exhibitions where this work has been presented is given. The Royal Geographical Society Land Rover bursary is also outlined, with a number of outreach events and publications also presented.

2 Literature Review

2.1 Introduction

The development of the World's mountain chains are governed by a complex interplay of tectonically-driven uplift and down-wasting by a variety of weathering, erosion and mass movement processes (Hovius, Stark and Allen, 1997; Mitchell and Montgomery, 2006; Barr and Spagnolo, 2014). Slope failures are complex phenomena and play a fundamental role in this development (Korup, Densmore and Schlunegger, 2010) and research of slope failures in high mountains, above and around glaciers in particular, has increased significantly over recent years. However, the distribution of such events and contribution to land system sediment budgets - important for understanding the landscape response to global climate change - are still poorly understood.

This chapter intends to combine insights from existing literature to present a background to the research described herein. Section 2.2 will introduce slope failures, their characterisation and factors that influence their occurrence. Following on from this, section 2.3 will give an overview of how rock mass strength can dictate the likelihood of rockslope failure, as well as introducing the Slope Mass Rating (SMR) and how it has been shown to correlate with rockwall erosion rates in previous studies. After this, section 2.4 looks at the effect of Climate Change on the distribution of slope failures with a focus on the degradation of permafrost and its effect on slope failure distributions. Section 2.5 presents the framework for paraglacial geomorphology within which this thesis is concerned. Particular focus in this section is given to the theory of glacial debuttressing, work on sediment-mantled slopes in the glacier foreland and theoretical models of sediment exhaustion. Next, section 2.6 focussed on the movement of sediment through the system with a focus on sediment connectivity and its changing dynamics through time. The glacial and fluvial consequences of slopes failures are discussed in section 2.7 as well as their role as hazards and the impact they have on communities and the tourism industry.

Sections 2.8 to 2.10 present the theoretical framework for the methodological approaches adopted in this thesis. Section 2.8 looks at the use of slope failure inventories to generate probability distributions, as well as the importance of the statistical analysis of these. Section 2.9 introduces Structure-from-Motion Multi-View Stereo photogrammetry; its background, development and applications within the geosciences, highlighting key points and areas for development. Finally, an overview of using topographical datasets for the purpose of detecting change is given in section 2.10 before a summarisation of key ideas in section 2.11.

2.2 Slope Failures

"Landslide: the failure and movement of a mass of rock, sediment, soil, or artificial fill under the influence of gravity." (Clague, 2013)

Slope failures are commonly associated with environments dominated by steep topography, though they can also occur in areas of lower relief (Clague, 2013). They constitute significant natural hazards, and play a major role in landscape evolution (Malamud *et al.*, 2004a). The classification and hazard-assessment of slope failures is made upon the basis of their size, velocity and material. The cause and trigger of a slope failure is not necessarily the same thing; causes can be understood as the prolonged processes fundamentally altering the nature of the slope and the trigger can be considered as a single event that results in the failure of a slope. Different triggers are often associated with different slope failure types (section 2.3); although in some cases it is difficult to pin-point a triggering mechanism. In most cases, water content and temperature conditions play an important role in the stability of a slope, which has led to a number of studies examining the consequence of climate change on the frequency and distribution of slope failures globally (section 2.4). At higher altitudes and latitudes, where temperatures fluctuate above and below 0° C, cyclic freeze-thaw mechanisms have been shown to weaken rock-walls (section 2.4.1).

Slope failures hold the potential to deliver vast quantities of sediment to the valley-floor (into the fluvial or glacial system) which in itself poses a new set of potential hazards and changes to the dynamics of the system (section 2.7). The monitoring and characterisation of slope failures, both historic and current, is hampered by a number of issues (section 2.9), which has resulted in a poor understanding of the frequency-likelihood of slope failures in prone areas. The role of glaciation on the frequency and spatial distribution of slope failures in high-mountains has long been discussed (section 2.5), with glacial erosion rapidly steepening slopes and enhancing failure likelihood.

2.2.1 Types of Slope Failure

There are a number of different types of slope failure, categorised based on their movement-type and material (fig. 2.1). One of the most widely used systems of slope failure classification is that of Varnes (1978). It is divided into 6 types of movement; fall, topple, sliding, lateral spreading, flow and complex. Sliding is further divided into rotational- and translational-type movements. For each type of movement, a classification of the process based upon source type is given for rock, debris and Earth material (Varnes, 1978; Cruden and Varnes, 1993). Furthermore,

slope failure velocities (mm/s) are scaled as; extremely slow, very slow ($0.5x10^{-6}$), slow ($50x10^{-6}$), moderate ($5x10^{-3}$), rapid ($5x10^{-1}$), very rapid ($5x10^{1}$) and extremely rapid ($5x10^{3}$) (Cruden and Varnes, 1993; Hungr, Leroueil and Picarelli, 2013). Hungr, Leroueil and Picarelli (2013), propose an updated version of the classification to account for mechanical properties of the source material (table 2.1). The material types and their respective descriptions, based upon a simplification of existing soil and rock description systems, are outlined in detail in Hungr, Leroueil and Picarelli (2013) (table 3). The types include: rock, clay, mud, silt, sand, gravel, boulders, debris, peat and ice.

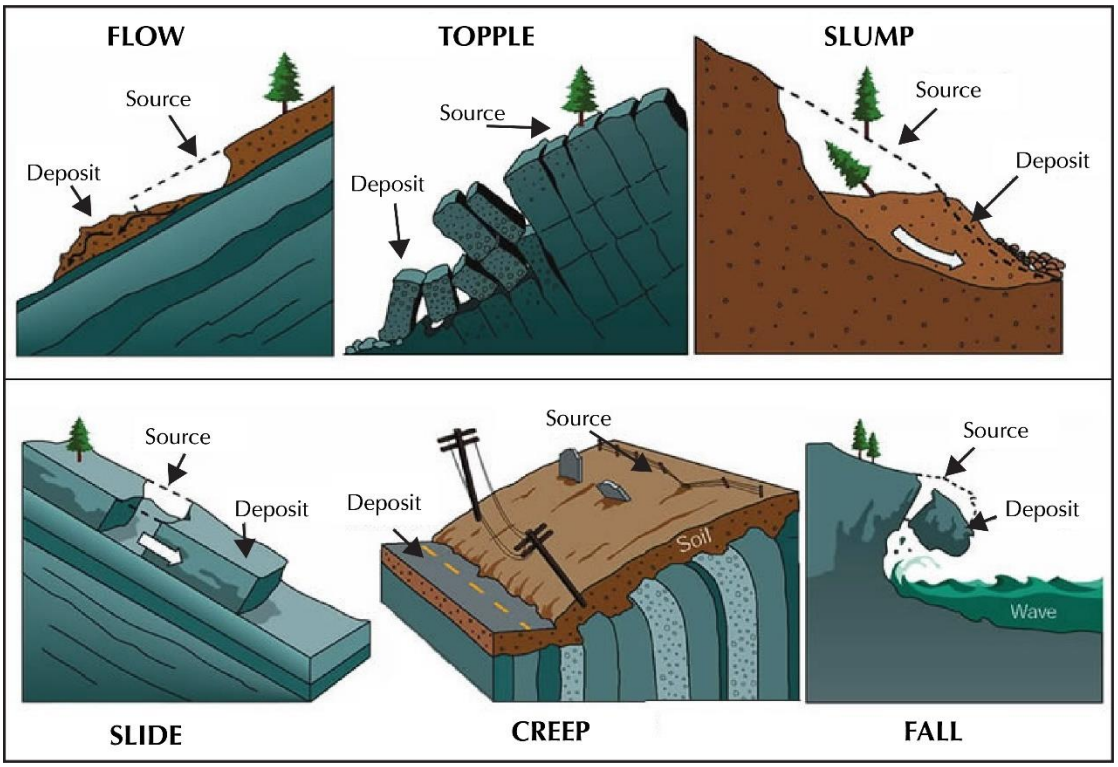

Figure 2.1: Schematic representation of the different types of slope failures. From the British Columbia Geological Survey.

In the updated classification system, there are six principle forms of slope failure movement/type, as defined by Hungr, Leroueil and Picarelli (2013), based on the Varnes (1978), classification system and others (Hutchinson, 1988; Hungr et al., 2001): falls, topples, slides, spreads, flows and slope deformations (table 2.1). A fall describes the detachment, fall, rolling and bouncing of the source material which is usually of limited volume, whilst a topple involves the forward movement or flexing/bending of a material column or cohesive mass (Hungr, Leroueil and Picarelli, 2013). Sliding refers to the down-slope movement of a weakened material and can be further sub-categorised into; rotational-, planar-, wedge-, compound- and irregular-type movements depending on the form of the rupture surface; cylindrical, planar, the surface of a downward-facing intersection between two planes, several planes or uneven curvature and a

surface of randomly orientated joints respectively (Hungr, Leroueil and Picarelli, 2013). A spread describes an elongation and lateral spreading of the failed mass which is usually slow in rock but rapid in soil (Varnes, 1978; Hungr, Leroueil and Picarelli, 2013). The flow category encompasses the fastest types of slope failures which can occur across a number of scales. The rapid flow-like movement has been shown to fracture, crush and grind the source material producing 'signature' sedimentology that some have used to identify historic rock avalanche events (Reznichenko, 2012; Reznichenko *et al.*, 2012). Finally, slope deformations are slow, and can range from small-scale movement of surficial soil layers to large-scale movements of entire mountain slopes under gravitational forces (Hungr, Leroueil and Picarelli, 2013).

There are a number of considerations when discussing the initiation of a slope failure, namely the preconditioning, preparatory and triggering factors (sections 2.3.1 to 2.3.3). It is important to understand the differences between these as despite the concepts all defining end points on a continuum, preconditioning and preparatory factors are often a combination of external and internal conditions whilst a slope failure is triggered by a single event (Clague, 2013).

Table 2.1: Summary of the 'new' version of the Varnes classification system (Varnes, 1978). The words in italics are placeholders (use only one). From Hungr, Leroueil and Picarelli (2013).

Type of Movement	Rock	Soil
Fall	1. Rock/ ice fall [a]	2. Boulder/ debris/ silt fall [a]
Topple	3. Rock block topple [a]	5. Gravel/ sand/ silt topple [a]
	4. Rock flexural topple	
Slide	6. Rock rotational slide	11. Clay/ silt rotational slide
	7. Rock planar slide [a]	12. Clay/ silt planar slide
	8. Rock wedge slide [a]	13. Gravel/ sand/ debris slide [a]
	9. Rock compound slide	14. Clay/ silt compound slide
	10. Rock irregular slide [a]	
Spread	15. Rock slope spread	16. Sand/silt liquefaction spread [a]
		17. Sensitive clay spread [a]
Flow	18. Rock/ ice avalanche [a]	19. Sand/ silt/ debris dry flow
		20. Sand/ silt/ debris flowslide [a]
		21. Sensitive clay flowslide [a]
		22. Debris flow [a]
		23. Mud flow [a]
		24. Debris flood
		25. Debris avalanche [a]
		26. Earthflow
		27. Peat flow
Slope Deformation	28. Mountain slope deformation	30. Soil slope deformation
	29. Rock slope deformation	31. Soil creep
		32. Solifluction

[a] Movement types that usually reach extremely rapid velocities as defined by Cruden and Varnes (1993). The other slope failure types are most often (but not always) extremely slow to very rapid (Hungr, Leroueil and Picarelli, 2013). For full definitions of the slope failure types, see Hungr, Leroueil and Picarelli (2013).

2.2.2 Preconditioning Factors

Preconditioning factors are static and inherent properties of the failing mass (McColl, 2012). In terms of rock-slopes, many authors have suggested that the principle controls on stability and preconditioning for failure are the rock-mass properties, such as the orientation and characteristics of discontinuities and hydrological conditions (Augustinus, 1995; Moore *et al.*, 2009; McColl, 2012). Some have commented on the fact that despite all valleys previously being glaciated, not all have failed and thus, the lithology and structure of the rock mass ultimately control the likelihood of failure (Bovis, 1982; McColl, 2012). So, preconditioning can be observed as the 'fixed' inherent properties of the slope that must be understood through extensive analysis of the rock mass strength and its ability to resist stresses (see section 2.8). However, the precondition of a slope can change through time due to a combination of preparatory and triggering mechanisms (McColl, 2012) (sections 2.3.2 and 2.3.3).

2.2.3 Preparatory Factors

Preparatory factors are dynamic and gradually reduce the stability of the failing mass over time, without initialising movement (McColl, 2012). An example of preconditioning would be the erosional power of glaciation, producing steep-sided valleys which increase the stresses within slopes. Glacial over-steepening is sometimes used to describe such preconditioning (e.g. Kellerer-Pirklbauer, Proske and Strasser (2010)) though McColl (2012), explains that this should be avoided unless unequivocally proven, as it is seldom the case that glacial erosion increases the stress above critical values, rather that it simply exposes unfavourable pre-existing rock-mass defects that reduce the slope stability. Climatic changes are also observed by many to directly influence slope failures through increases in precipitation and atmospheric temperatures. This is discussed in more detail in section 2.4.

2.2.4 Triggering Factors

Triggering factors are those which initiate movement of the failing mass through a transition from marginally stable to actively unstable state (McColl, 2012). They're often single events that capitalise on the preconditioning and preparatory mechanisms to trigger failure and include; rain-storms (e.g. Glade (1998); Guthrie and Evans (2004)), Earthquakes, magmatic or phreatic surface activity (e.g. the lateral collapse of the Ritter Island volcano in 1888 (Ward and Day, 2003)), loading stresses, pore pressures and anthropogenic landscape interaction (e.g. the Vaiont Dam disaster of 1963 (Kilburn and Petley, 2003)). In some cases, the interplay between two or more

triggering mechanisms may have initiated failure. For example, Dortch *et al.* (2009), used cosmogenic dating and structural mapping to determine the likely triggers of four large slope failures in the Himalayas, finding that increases in pore water pressure from monsoon rains and seismic shaking are the most likely mechanisms. Particular triggering mechanisms tend to dominate in various environments depending on the climatological and geological characteristics of the landscape. For example, the principle triggering mechanism in the United Kingdom is rainfall (fig. 2.2), where slope failures often result from water loading of the slope and a reduction in soil strength. In the Southern Alps of New Zealand, slope failures are mostly triggered by seismic activity (e.g. Korup (2005)) and across the high altitude rock-walls of the European Alps, where it is rare for seismic activity to produce significant Earthquakes, increases in pore water pressure through extraordinary precipitation (e.g. Fischer *et al.* (2010)) and thawing ice (i.e. permafrost degradation) is a major triggering mechanism (e.g. Ravanel and Deline (2011)).

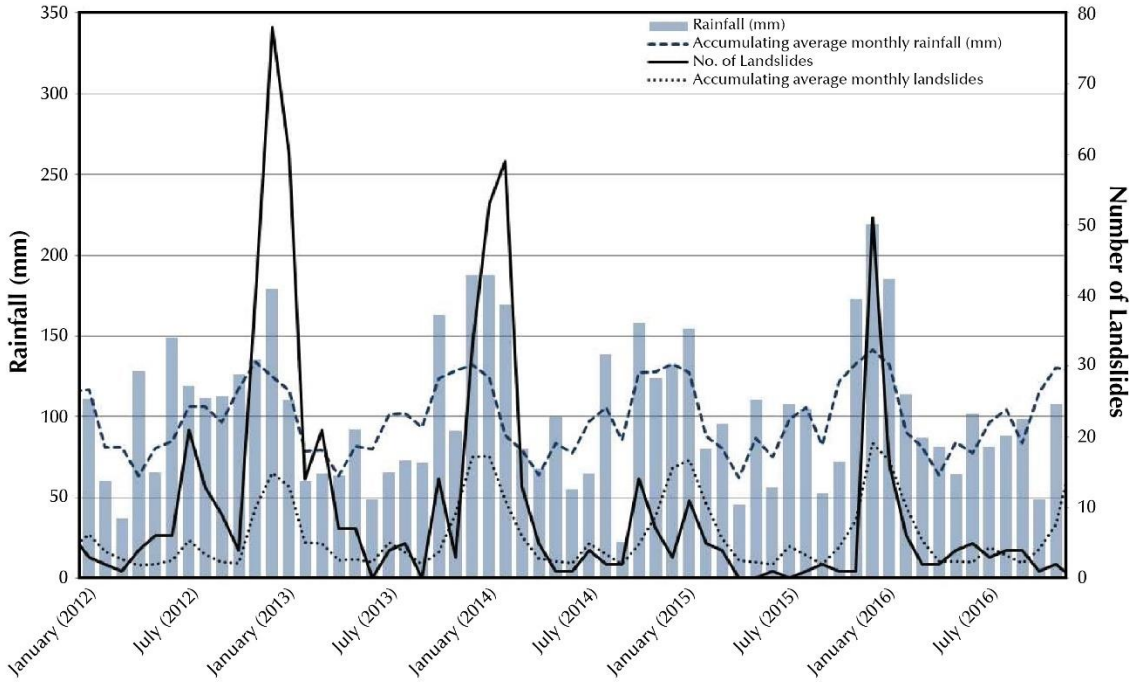

Figure 2.2: Graph showing the amount of rainfall and number of slope failures in the UK. Rainfall data: Met Office. Slope failure data: British Geological Survey. Graph modified from http://www.bgs.ac.uk/slope failures/slope failuresAndRainfall.html.

2.3 Rock Mass Strength and Slope Failures

Rock mass strength defines the stability, strength and weakness of a rock mass. All rock masses contain discontinuities (Hoek, 2000) (joints and faults) that are structures across and within the rock-wall mass and result from brittle behaviour in which blocks of rock are displaced relative to one another across narrow and approximately planar distances (Hobbs, Means and Williams,

1976), in most cases reducing the strength and increasing the likelihood of failure. The level of stability varies with the inclination and characteristics of discontinuity surfaces, with vertical and horizontal examples being significantly more stable than those that dip towards the slope face at angle of between 30° and 70° (Hoek and Bray, 1981). Most joints form by fracturing, and usually occur as families (joint sets) of fractures with a relatively regular spacing and they're often parallel to one another (Hobbs, Means and Williams, 1976). When several joint sets occur together, as is commonly the case, rock-wall exposures are given a blocky or fragmented appearance (Hobbs, Means and Williams, 1976) (e.g. Bossons, fig. 3.3 d).

Rock-mass strength is controlled by a number of factors, principally the geometrical characteristics of in-situ discontinuities (Hoek and Bray, 1981; Selby, 1982) which determine the strength and failure-likelihood through reducing the cohesive strength and friction properties of the rock mass. At hill-slope-scale, the geometric properties of joints are more influential in the determination of slope failure size than the intact rock strength of the slope (Korup *et al.*, 2007a). A rock-slope is typically formed of rock blocks separated by various joints (Riquelme *et al.*, 2015) along which, the strength has been described by a Mohr envelope in a straight line form (Hoskins, Jaeger and Rosengren, 1968). The spacing between joints determines the susceptibility of the rock mass to weathering processes and water pressures (Selby, 1993) and thus, the weaker rock masses are characterised by closely spaced joints. Orientation of principle joints with respect to the slope also play a dominant role in the overall stability of a slope (Terzaghi, 1962), though the theoretical critical hill-slope angle for stability seldom applies in its exact form due to variable factors which are difficult to constrain, such as roughness (Barton, 1978) and water-content. Extrinsic climatological factors can influence the rate of mechanical behaviour, and are exaggerated in high mountainous environments, such as the destabilisation of ice-filled discontinuities as a consequence of permafrost degradation (Davies, Hamza and Harris, 2001; Gruber, Hoelzle and Haeberli, 2004).

Rock mass strength classifications are a means of slope stability characterisation by a simple arithmetic algorithm for engineering geologists and geomorphologists and provide a straightforward method of summarising rock mass properties. A number of systems have been developed as means for the assessment of slope stability based upon structural parameters including; Rock Mass Strength (RMS) (Selby, 1980), Geologic Strength Index (GSI) (Marinos, Marinos and Hoek, 2007), Rock Mass Rating (RMR) (table 2.2) (Bieniawski, 1976), and Slope Mass Rating (SMR) (Romana, 1993). Each system has often been developed for a specific engineering application and account for a number of structural variables including joints, discontinuity spacings, rock mass conditions and fill.

The RMR originally included eight rock parameters, one of which was the strike and dip orientations of joints, and emphasis was placed on using RMR whilst surveying tunnels (Romana, 1993). In the second version (Bieniawski, 1976), a number of major changes were introduced, and after calculating an RMR value based on five rock mass parameters, a corrective adjustment was made to account for the orientation of discontinuities in the rock mass. These ranged from 'very favourable' to 'very unfavourable', though no guidelines were published for the definition of each class and thus is a particularly subjective approach to factoring discontinuities into the assessment of slope stability. Romana (1993) explains that the heavy adjustments made with these subjective classes can supersede by far any other careful evaluation of the rock mass. RMR however, remains one of the most versatile classification systems that is capable of evaluating a wide range of rock types and cliff morphologies, that requires relatively straightforward and efficient field measurements (Moore *et al.*, 2009). Without the discontinuity orientation correction factors, the index takes the form of table 2.2. Others have built upon the RMR, providing quantitative approaches of evaluating discontinuity orientation and reducing the potential for subjective error in slope analysis. The most prominent of these is the SMR (section 2.8.1.1).

Table 2.2: Bieniawski (1976) System for Rock Mass Rating (RMR) index without correction for discontinuity orientation. A = Strength of intact rock material; B = Drill Core Quality; C & D = Discontinuities; E = Groundwater in Joints.

	Parameters	Ranges of Values			
A	Point Load Index (MPa)	> 10	4 - 10	2 - 4	1 - 2
	Uniaxial Compressive Strength (MPa)	> 250	100 - 250	50 - 100	25 - 50
	Rating	**15**	**12**	**7**	**4**
B	RQD (%)	90 - 100	75 - 90	50 - 75	25 - 50
	Rating	**20**	**17**	**13**	**8**
C	Spacing (m/ *mm*)	> 2	0.6 - 2	*200 - 600*	*60 - 200*
	Rating	**20**	**15**	**10**	**8**
D	Condition	Very Rough Surfaces Not Discontinuous No Separation Unweathered Wall Rock	Slightly Rough Surfaces Separation < 1 mm Slightly Weathered Walls	Slightly Rough Surfaces Separation < 1 mm Highly Weathered Walls	Slickenside Surfaces or Gouge < 5 mm Thick or Separation 1 - 5 mm Continuous
	Rating	**30**	**25**	**20**	**10**
E	Description	Completely Dry	Damp	Wet	Dripping
	Rating	**15**	**10**	**7**	**4**
A	Point Load Index (MPa)	At this range, Uniaxial Compressive Strength is preferred			
	Uniaxial Compressive Strength (MPa)	5 - 25	1 - 5	< 1	
	Rating	**2**	**1**	**0**	
B	RQD (%)		< 25		
	Rating		**3**		
C	Spacing (m/ *mm*)		*< 60*		
	Rating		**5**		
D	Condition		Soft Gouge > 5 mm or Separation > 5 mm Continuous		
	Rating		**0**		
E	Description		Flowing		
	Rating		**0**		

Mapping discontinuities across a slope in support of stability analysis is an important but traditionally a time-consuming, laborious process which is sometimes in challenging environments (Haneberg, 2008). A number of approaches to using remote sensing technologies for characterising slope discontinuities have been proposed (Slob *et al.*, 2005; Haneberg, 2008; Abellán *et al.*, 2014; Assali *et al.*, 2016) which all set out with common aims for using 3D data to overcome the inherent disadvantages of manual field surveys such as; bias introduced through user knowledge, sampling method and instrument error; safety risks when operating in proximity to unstable slopes or along busy highways and; difficulty associated with accessing steep, tall rock faces with obscure ridges and overhangs (Slob et al., 2005). Advances in the capabilities of laser- and photogrammetry-based techniques in recent years have allowed un-paralleled levels of detail which lends itself well to deployment in remote, unsafe and difficult-to-access areas.

Dunning, Massey and Rosser (2009) explore the use of Terrestrial Laser Scanning (TLS) for characterising geometry and structural geology of unstable slopes in the Himalayas. Using commercially-available packages, they extracted structural information and noted the considerable benefits over traditional engineering approaches such as the logistical operation with portable equipment in difficult terrain (Dunning, Massey and Rosser, 2009). A number of innovative packages and algorithms have been developed that make use of (solid) images and survey data for analysing the characteristics of slope discontinuities, which as already discussed, are the principal source of instability in slopes. Bornaz and Dequal (2004) introduced the notion of "solid image" as the enrichment of a classical 2D digital image with the corresponding 3D geometrical information (e.g. a photogrammetric point cloud, TLS reflectivity data etc.). Some examples of this are presented by Assali *et al.* (2016), who create a product that uses solid images to model discontinuities; Slob *et al.* (2005), and Lato and Vöge (2012), who both present a method for using 3D survey data to determine the orientation of discontinuity sets and; Riquelme *et al.* (2015) and Riquelme, Abellán and Tomás (2015), who present a Matlab-based approach to the automatic characterisation of discontinuities based on their orientation and a method for calculating their spacing.

2.3.1 Slope Mass Rating (SMR)

The SMR (Romana, 1993) was also originally developed for tunnelling applications, and the system derives from the RMR (Bieniawski, 1976) with the addition of four slope correction factors which account for the geometrical characteristics of discontinuities relative to the slope and the slope excavation method (if any). The classifications of SMR and their respective descriptions are summarised in table 2.3 (Romana, 1993), though support mechanisms have been removed from the original table as they are not applicable in this study of natural (unsupported) slopes. As in the case of RMR, SMR is a discrete classification system which can lead to major changes in the final

quality rating assigned to a slope due to a relatively minor adjustment in one of the input variables (Tomás, Delgado and Serón, 2007). SMR can be obtained using the following expression:

$$SMR = RMR_b + (F_1 F_2 F_3) + F_4$$

Equation 2.1

where RMR_b is the basic RMR index (table 2.2) (Bieniawski, 1976) without any correction; F_1, F_2 and F_3 are slope correction factors where F_1 depends on the parallelism between discontinuities and the slope face; F_2 depends on the discontinuity dip and; F_3 depends on the relationship between the slope face and the discontinuity dip. F_4 is a descriptive value that identifies the excavation method (if any) (Romana, 1993). RMR_b is the equivalent to the corrected RMR after subtracting the term which correctively adjusts for discontinuity orientation (r_c), so that:

$$\mathrm{RMR_b} = \mathrm{RMR} - \mathrm{r_c} = \mathrm{r_\sigma} + \mathrm{r_X} + \mathrm{r_J} + \mathrm{r_G} + \mathrm{r_{RQD}}$$

Equation 2.2

where r_σ is the point load strength of the rock, r_X and r_J are the spacing and condition of discontinuities respectively, r_G accounts for the hydraulic conditions and r_{RQD} is the rock quality designation (RQD).

Table 2.3: Slope Mass Rating (SMR) class descriptions (Romana, 1993).

Class	SMR	Description	Stability	Failures
I	81-100	Very good	Completely stable	None
II	61-80	Good	Stable	Some blocks
III	41-60	Normal	Partially stable	Some joints or many wedges
IV	21-40	Bad	Unstable	Planar or big wedges
V	0-20	Very bad	Completely unstable	Big planar or soil-like

Tomás, Delgado and Serón (2007) proposed a modification of the SMR in order to remove any potential subjective interpretations using continuous functions for F_1, F_2 and F_3. The use of continuous formulation reduces any doubt surrounding values assigned near the border of Romana's (1993) discrete classification system (Romana, 1993; Tomás, Delgado and Serón, 2007). Moore *et al.* (2009) apply the SMR in the Sierra Nevada of California and demonstrate the influence of rock-mass strength on alpine cliff erosion. They explore the correlation between rock-wall recession rates and a number of topographical characteristics as well as examine the influence of

rock mass strength and propose the following relationship for predictions of rock-wall erosion where SMR is known:

$$\mathrm{E} = 10.25\mathrm{e}^{-0.065\mathrm{SMR}}$$

Equation 2.3

where the rock-wall recession rate E is in mm/yr. No significant correlation of alpine rock-wall retreat rates with topographical characteristics such as elevation or slope angle was found, and their results demonstrated rates were principally controlled by rock mass properties (**Error! Reference source not found.**3) (Moore et al., 2009).

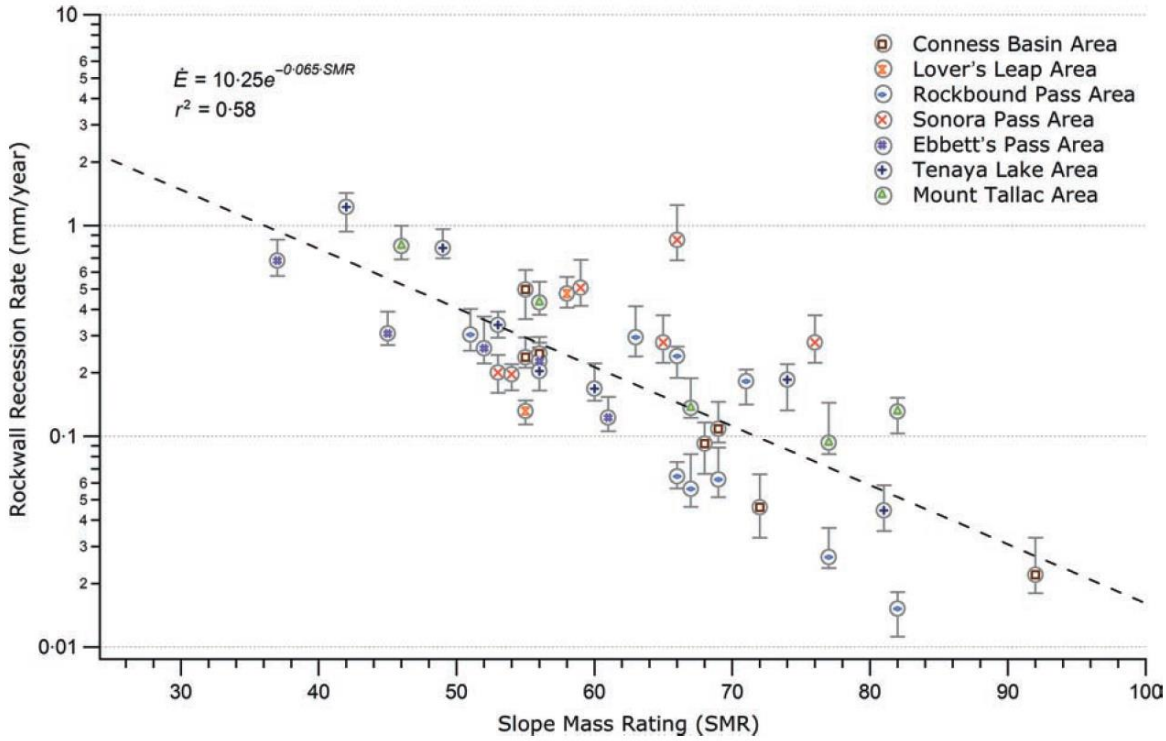

Figure 2.3: Variation of rock-wall recession rate with cliff SMR. Dashed line shows the exponential best fit trend to all data, and the numerical expression is given (Moore et al., 2009).

2.4 Climate Change and Slope Failures

Climate change and its effect on the rate and nature of geomorphic activity in high mountainous environments has been widely discussed to date. It is accepted amongst the majority of scientists that the global climate is changing at accelerated rates in response to anthropogenic activity. The fifth assessment report of the Intergovernmental Panel on Climate Change (IPCC) (Stocker *et al.*, 2013) predict an increase in global mean air temperature and more extreme hot days in the future as a result of the Greenhouse Effect. Therefore, it is important to understand

how these climate scenarios are likely to affect the frequency and magnitude of slope failure hazards globally. Changes in the climate have had a major impact on Earth`s surface systems, especially in high-latitude and high-altitude cold environments through feedback associated with high-elevation subsurface temperatures and heat budgets (Haeberli *et al.*, 2007; Keiler, Knight and Harrison, 2010; Beylich and Lamoureux, 2016). Temperature changes in the European Alps for example, have increased twice as much as the global average since the late nineteenth century with precipitation and other phenomena also increasing non-linearly (Haeberli *et al.*, 2007; Brunetti, Guzzetti and Rossi, 2009; Keiler, Knight and Harrison, 2010). In these environments, climate change shapes land system processes not just by altering vegetation patterns and anthropogenic activities but also through its impact on frost coverage and duration within the ground surface layers (Beylich and Lamoureux, 2016). Changes in global temperatures also exerts a strong control on cryospheric systems, influencing the form and mass balance of glaciers and ice sheets, as well as the extent and severity of glacial, periglacial and paraglacial processes (section 2.5) (Beylich and Lamoureux, 2016). Such changes have had a major impact on sediment transfer processes, affecting patterns of erosion, transport and deposition of sediments (section 2.7) (Beylich and Lamoureux, 2016).

Crozier (2010), states that a warming trend is predicted to result in a greater frequency of heavy precipitation, the most common triggering mechanism for slope failures (e.g. Krautblatter and Moser (2009)) (section 2.3.3). Krautblatter and Moser (2009), use a net system to measure rock-fall activity under different meteorological conditions (**Error! Reference source not found.**4) and find an intensity threshold of 9-13 mm of precipitation over 30 minutes is required for coupling with rock-fall intensity and that the response above this threshold is highly non-linear. Some authors have exploited the complex relationship between climate variability and slope failure frequency, and used it as a proxy measurement for climate change (e.g. Schmidt and Dikau, 2004; Borgatti and Soldati, 2010; Deline *et al.*, 2014). Borgatti and Soldati (2010), found a match between the global paleoclimatic framework and clusters of slope failures though they suggested taking a cautious approach using slope failure inventories as accurate proxies of climate, as they are susceptible to several biases. For example, they tend to be dominated by younger slope failures, as older slope failures are harder to find and measure (Borgatti and Soldati, 2010). The 'TEmporal Stability and activity of Landslides in the Europe with respect to Climate change' (*TESLEC*) project (Dikau and Schrott, 1999) aimed to examine the temporal stability of slopes to assess future behaviour. They found that the relationship between climate controls and slope failure mechanisms are too complex to apply a universal law across all of Europe however, a precipitation-duration threshold was identified in some areas for activating slope failures (Dikau and Schrott, 1999).

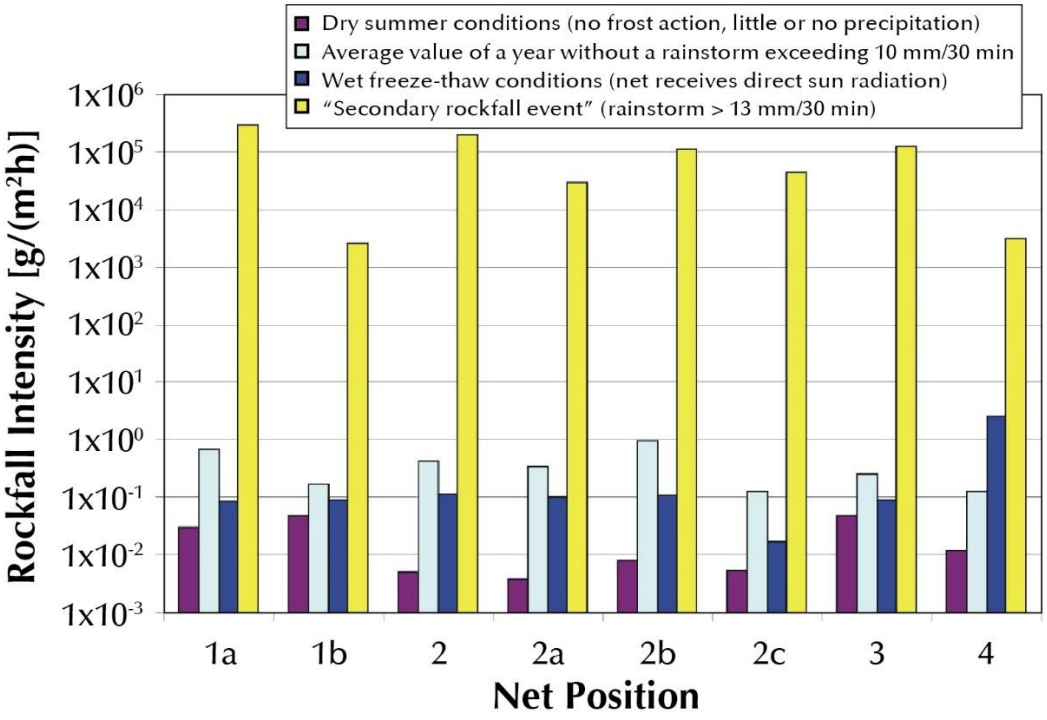

Figure 2.4: Rockfall intensity in response to meteorological conditions (from Krautblatter and Moser (2009)). Secondary rock-fall events are defined as: "a short-term mass deposition of fine-grained rock-fall material that originates from intermediate storage in the rock wall and is released by fluvial processes and debris-saturated flows active in the rock face" (Krautblatter and Moser, 2009).

Crozier (2010) also explains that results to date give sufficient indications of a slope failure response to climate change to provoke precautionary management decisions, but explains that there is still a high level of uncertainty surrounding global predictions. Huggel, Clague and Korup (2012) argue that the evidence for linking slope stability with climate variability is ambiguous and speculative. They conduct a comprehensive analysis of recent slope failures in mountain ranges around the world (the European Alps, Americas and Caucasus), to determine whether a link exists. They state that research of slope failure frequency through a warming phase is still limited and that "there is still no unambiguous evidence that the frequency or the magnitude of slope failures has changed over this period" (Huggel, Clague and Korup, 2012). However, they identify three principal mechanisms through which climate change may affect the nature of slope failure activity in high-mountainous environments (Huggel, Clague and Korup, 2012):

1) "positive feedbacks acting on mass movement processes that can be reinforced after a climatic stimulus independently of climate change;
2) threshold behaviour and tipping points in geomorphic systems;
3) storage of sediment and ice involving important lag-time effects."

In regards to mechanism number 2, they suggest that warming above certain thresholds may trigger a tipping point where a sudden shift to a contrasting dynamical regime could occur (Huggel, Clague and Korup, 2012).

2.4.1 Permafrost

Areas of high altitudes and latitudes such as the steep rock-walls found in many parts of the European Alps are influenced by permafrost (Hasler, Gruber and Beutel, 2012) and ice-filled discontinuities (Davies, Hamza and Harris, 2001) which are particularly vulnerable to thawing as a consequence of climatic warming. Permafrost is a term used to refer to subsurface material that exists at a constant temperature of 0° C or below for a minimum of two years (Muller, 1947), whilst the active layer defines a subsurface layer that is subject to annual thawing and freezing. Elevation and topographic aspect are the most important factors governing permafrost distribution with the influence of the latter increasing with continentality (Etzelmüller and Frauenfelder, 2009). In high-relief regions, such as the Alps study sites in this thesis, topographic aspect is a key parameter when assessing the permafrost distribution pattern (Gruber and Hoelzle, 2001; Etzelmüller and Frauenfelder, 2009). The thawing of permafrost across North-facing slopes in the Alps is controlled through the influence of air temperature (long-wave radiation) whilst South-facing slopes additionally receive solar insolation (short-wave radiation) and therefore exhibit greater inter-annual variability of thaw depth (Gruber, Hoelzle and Haeberli, 2004). The degradation of permafrost and deepening of the active layer is considered to be an increasing hazard in alpine environments and its effect is thought to increase the likelihood of rock-fall activity (Krautblatter, Funk and Günzel, 2013). In response to changes in atmospheric temperatures across high-altitude rock-walls in the European Alps, surface and subsurface ice loss has resulted in the destabilisation of large parts of mountain faces, initiating a cascade of slope failures which have received considerable attention in the literature (Huggel, Clague and Korup, 2012).

Ravanel *et al.* (2010), identified a number of pieces of evidence to support the hypothesis of increased rock falls in line with increasing atmospheric temperatures;

1) physical processes linking climate and collapses exist;
2) many collapses originate from permafrost areas;
3) cracks filled with ice are common in high mountain rock walls and, frequently, ice is exposed in fresh detachment scars, or seeping water can be observed, even in very dry conditions;
4) the intense rock fall activity of the 2003 summer heat wave points to permafrost degradation as the only plausible explanation (Gruber, Hoelzle and Haeberli, 2004) and;

5) permafrost degradation has been measured and is consistent with atmospheric warming.

The stabilising influence of ice within rock-wall discontinuities is lost when this ice melts because of increasing temperature, resulting in the loss of joint 'bonding'. An increase in pore water pressures is also observed when this meltwater cannot drain away leading to a reduction in the shear strength of the joint (Davies, Hamza and Harris, 2001). Ravanel and Deline (2011), used historical photographs of the Aiguilles above Chamonix to investigate the frequency of rock-fall activity, observing maximal frequencies of rock-fall activity during periods of increased temperature. They explain that all 42 observed rock-falls (since 1862) were within areas of permafrost, and the maximal frequency of rock-falls occurred during a heatwave in 2003 (Ravanel and Deline, 2011). The hot summer of 2003 was also discussed by Gruber, Hoelzle and Haeberli (2004), who use climate models to argue that the coming decades will see reduced rock-wall stability in response to hotter summers. In Norway in 2008, a slope failure detached from the NE-facing slope of Mount Polvartinden, causing considerable damage to livestock pastures (Frauenfelder *et al.*, 2016). The slope failure was observed to have detached from an area of in-situ ice which led scientists to believe that degrading permafrost could have played a role in its initiation (Frauenfelder *et al.*, 2016). Magnin *et al.* (2016) modelled the long-term evolution of permafrost across the Mont Blanc massif, stating that by the end of the 21st century, permafrost will disappear from altitudes below 3300 m a.s.l. This work emphasises the importance in understanding rock-wall response to the thawing and removal of subsurface ice as it is projected rock-fall hazards will increase in the future as a response to global climate change.

2.5 Paraglacial Geomorphology

"Paraglacial land systems and their constituent landforms represent not only the legacy of glaciation and de-glaciation, but of complex and incompletely understood environmental changes that have shaped the rate and nature of sediment flux since the retreat and disappearance of glacier ice." (Ballantyne, 2002b)

Paraglacial geomorphology is defined by Ballantyne (2002b) as the study of "earth-surface processes, sediments, landforms, landsystems and landscapes that are directly conditioned by former glaciation and deglaciation". The paraglacial concept is controversial in that its definition has prompted significant debate (Slaymaker, 2009). The reduction and retreat of glacial mass in Alpine environments reveals an environment that is particularly susceptible to rapid geomorphological change (Ballantyne, 2002b). Originally used by Church and Ryder (1972), to

define the glacial perturbation of fluvial systems, paraglacial research has seen much development and elaboration beyond this in the years since their work (Ballantyne, 2002b). Etymologically the term paraglacial literally means *next to the ice* (Mercier, 2008) and thus, geomorphic activity, slope stability and the trajectory of hill-slopes toward stabilisation through failures during a period of de-glaciation can be considered within the framework of paraglacial geomorphology (Curry, 1999; Ballantyne, 2002b; McColl, 2012). This concept refers to non-glacial processes that are triggered or prepared (whereby deglaciation is the preparatory factor as defined in section 2.3.2) by the transition of an environment from glacial to non-glacial conditions. It does not introduce any new phenomena as all processes can be seen elsewhere in environments where no glaciation has occurred but specifically considers events where the effect of ice removal has in some way affected their occurrence (Ballantyne, 2002a). Paraglacial land systems are complex and their behaviour span a range of time-scales from immediacy to millennia, limited by sediment supply and natural and anthropogenic secondary perturbations (Ballantyne, 2002a; Curry, Cleasby and Zukowskyj, 2006). These land systems are also typically staggered by intermediate sediment storage (Ballantyne, 2002b; Mercier, 2008).

Research has typically focussed on the following contexts: (i) adjustment of rock-slopes, (ii) adjustment of sediment-mantled slopes, (iii) modification of glacier forelands, (iv) fans, debris cones and valley fills, (v) sedimentation and fluvial redistribution, (vi) lacustrine sedimentation and (vii) coasts and glaciated shelves (Ballantyne, 2002b). Ballantyne (2002b) provides an extensive review within each context, whilst McColl (2012), provides a detailed review of paraglacial rock-slope stability and Curry (1999), looks specifically at the modification of sediment-mantled slopes. **Error! Reference source not found.**10 is an interrupted sediment cascade presented by Ballantyne (2002b) to demonstrate the links between each of the paraglacial land systems from source to sink. At the initial stages, terrestrial inputs of sediment form a number of depositional landforms which are susceptible to reworking and form secondary landforms. As the supply of sediment to these stores slows, successive erosion will carry the sediment to its sink, resulting in a net erosion across the land system (Ballantyne, 2002b). Mercier (2008) presented the land system schematic in **Error! Reference source not found.**5 to demonstrate the spatial distribution of various paraglacial landforms in the pro-glacial zone. Much of the existing literature has focussed on the pro-glacial zone, or within valleys that are no longer occupied by ice. The paraglacial zone defines the extent of the area in which paraglacial activity occurs and is known to be transient and hard to define (Lane *et al.*, 2016), yet there is relatively little existing work that focusses on the adjustment of slopes in actively deglaciating mountain valleys like that presented herein. The sediment cascade presented by Ballantyne (2002b) does not account for glacial reworking of deposited sediments, or changes in glacial behaviour as a consequence of failures (section 2.7.1).

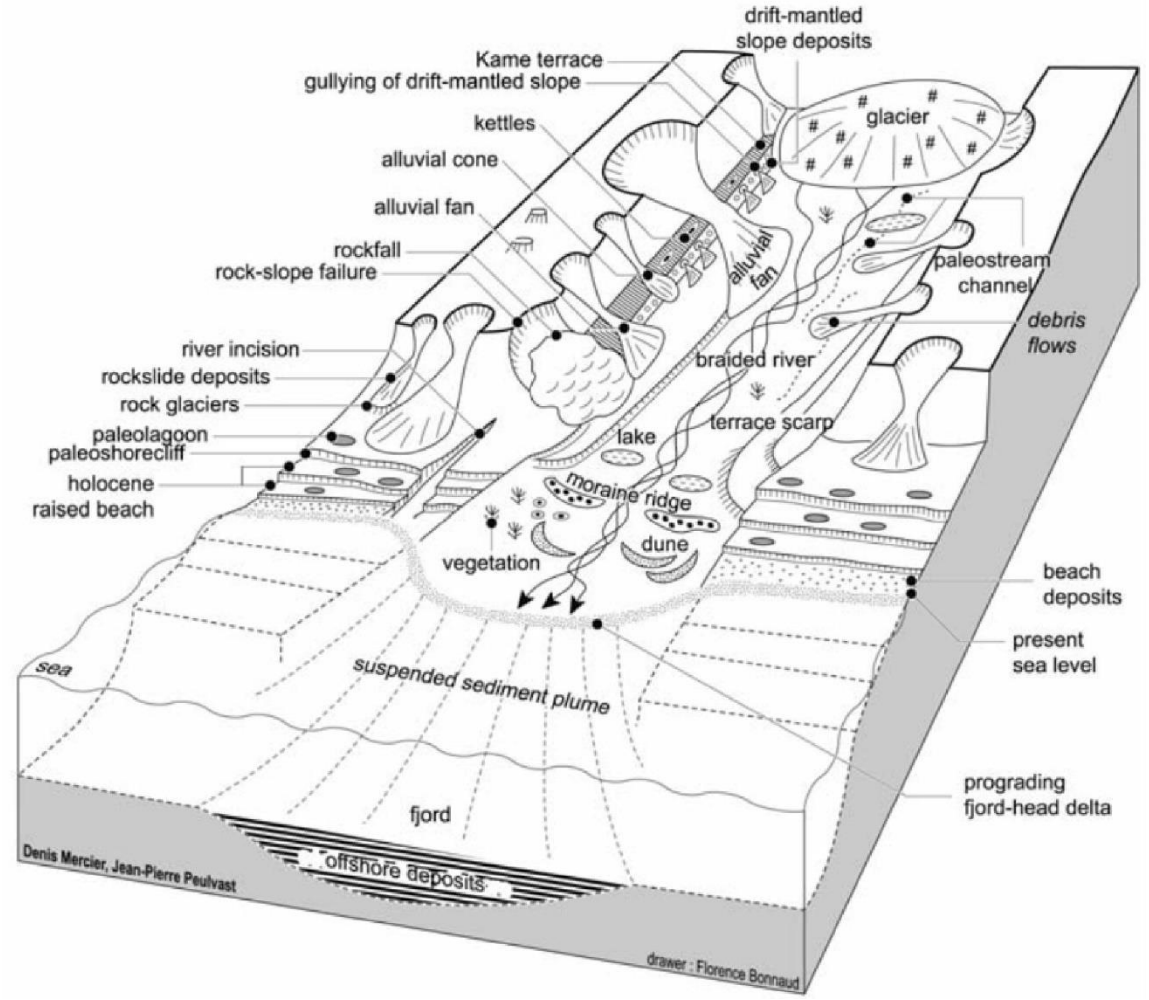

Figure 2.5: Schematic of a paraglacial land system (from Mercier, 2008).

2.5.1 Glacial Debuttressing

Following the removal of a load from a rock-wall, the slope undergoes *rebound*, defined by Nichols (1980), as "the expansive recovery of surficial crustal material, either instantaneously, time-dependently or both, initiated by the removal or relaxation of super-incumbent loads." Whilst tectonic stresses are the most common cause of joints in rock masses, rebound can result in a number of non-tectonic joints which some have suggested can be created through glacial processes (Augustinus, 1995; Ballantyne, 2002b). Others have argued that the loading and subsequent unloading of a glacier may not be enough to produce stress-release joints (McColl and Davies, 2013). Discontinuities (used here as an encompassing term for joints, fractures and other features where continuous rock mass is interrupted) penetrate all rocks to some extent, and are typically part of well-defined sets which differ in persistence, spacing, curvature and parallelism (Harland, 1957). They weaken the rock mass, providing failure surfaces and pathways for water flow and weathering processes (McColl, 2012) (see section 2.8).

Non-tectonic joints are easily distinguishable from those of tectonic origin as they are dominantly extensional fractures, usually sub-parallel to the local topography, increase in density towards the surface, are very local in extent, normally have little or no filling material and sometimes cross-cut or terminate at tectonic joints (Nichols, 1980; McColl, 2012). Often referred to as *sheeting joints* (also as exfoliation, stress-relief or -release joints), they have been a topic of discussion for many years (e.g. Nile (1872)) and are renowned for their role in landscape development (Martel, 2006). They have been observed to exist in environments that have previously undergone high compressive stresses parallel to the surface (Nile, 1872; Martel, 2006). Often they occur where stresses are measured to be higher in the horizontal than vertical orientation (i.e. slope-parallel rather than slope-perpendicular) (Hencher *et al.*, 2011), which indicates that the failure may have been induced by compressive stresses (McColl, 2012). Collins and Stock (2016) demonstrated the instability of sheeting joints and highlighted their importance of cyclic heating and cooling on the rate of deformation of sheeting joints in the Yosemite National Park. They monitored a sheet of rock (weighing 20 tonnes) that fluctuated towards and away from the intact rock by up to 1 cm each day under the effect of thermal expansion and contraction, which they state will ultimately lead to the propagation of failure (Collins and Stock, 2016).

Ballantyne (2002b) explains that in areas previously glaciated, the loading of rock by the weight of the overlain ice induces internal stresses that are far greater than can be expected from self-weight loading alone. The removal or downwastage of the ice releases strain energy, which may result in the redistribution of the principle stress field and development of a region of tensile stress behind the slope (Ballantyne, 2002b). These phenomena have been widely discussed in the paraglacial literature (section 2.5) and often referred to as *glacial de-buttressing*. The underlying principle of this theory is that the removal of a load pressure as a glacier retreats and thins is enough to reduce stability (in the case of a preparatory mechanism) or even trigger failure if the slope is already unstable. However, McColl (2010) argues that this is most likely not the case as rock has a much higher density than ice. Therefore, the ice buttress would simply 'flow' under the applied stress of a failed slope, allowing said slope to fail into the ice whilst the glacier is still in place (McColl, 2010; McColl and Davies, 2013). In this case, the glacier will potentially not prevent failure, though the retreat of ice and exposure of the rock-wall may hasten collapse (McColl, 2012).

2.5.2 Sediment-Mantled Slopes

The rate of glacial thinning significantly influences the processes of sediment reworking (Cossart *et al.*, 2008). Steep-sided, gullied lateral moraines are a common feature of actively deglaciating and deglaciated landscapes and are inherently unstable, conditioned by their gradient and morphology (Curry, Sands and Porter, 2009). It has been found that paraglacial modification of

slope form has led to a localised reduction in overall slope gradients, whilst the development of the slope-foot and debris cone accumulation results in an overall reduction in slope concavity (Ballantyne and Benn, 1994; Curry, 1999; Curry, Cleasby and Zukowskyj, 2006). The development of gully systems is observed to be the primary mechanism of paraglacial slope adjustment by Curry (1999), and explains that glacigenic sediment is stripped from the upper parts of the slope and deposited downslope in debris cones. Curry, Sands and Porter (2009) find that the steep-sided sediment-mantled slopes are able to survive decadal time-scales in a quasi-stable state, dependent on the lithology and fabric of the sediment though within 50 years of de-glaciation, the gully systems are considered to have reached their maximum dimensions (approximately 26 m deep and 46 m wide) (Curry, Cleasby and Zukowskyj, 2006).

Ballantyne (2002b) provides a comprehensive review of the paraglacial modification of sediment-mantled slopes, explaining that debris flows (see section 2.2.1) are the most dominant agent of erosion. A number of authors have noted that debris flows and debris slides commonly occur across recently-exposed lateral moraines (Dortch *et al.*, 2009). The deposition of parallel levees at the base of the slope is characteristic of individual flows (Ballantyne, 2002b) and Ballantyne and Benn (1994) find that some were initiated by rainstorms whilst others occurred during rapid spring melting of late-lying snowbeds at gully heads. Others have found that in valleys where glacier downwastage has recently exposed steep-sided lateral moraines, the slopes can be rapidly and extensively modified by translational sliding, debris falls and debris avalanches (see section 2.2.1) (e.g. Blair, 1994). At higher altitudes, ice-cored sediment slopes are susceptible to modification as the underlying ice melts (Ballantyne, 2002b). Curry (2000) and Curry, Cleasby and Zukowskyj (2006) suggest that initial slope gradients of >30˚ are required for slope modification by debris flows (fig. 2.6), and that a higher density of gullies is associated with a sediment layer thickness of >10 m. Gullying was also shown to be positively linked with mean annual precipitation (Curry, 2000; Ballantyne, 2002b). The prevalence of debris flows across sediment-mantled slopes has interesting implications that must be considered during the analysis of slope failure distributions in this study. Quantified events are most likely not discrete rockfalls and rather a mass movement of in the form of a rapid downslope flow of poorly sorted sediment and water.

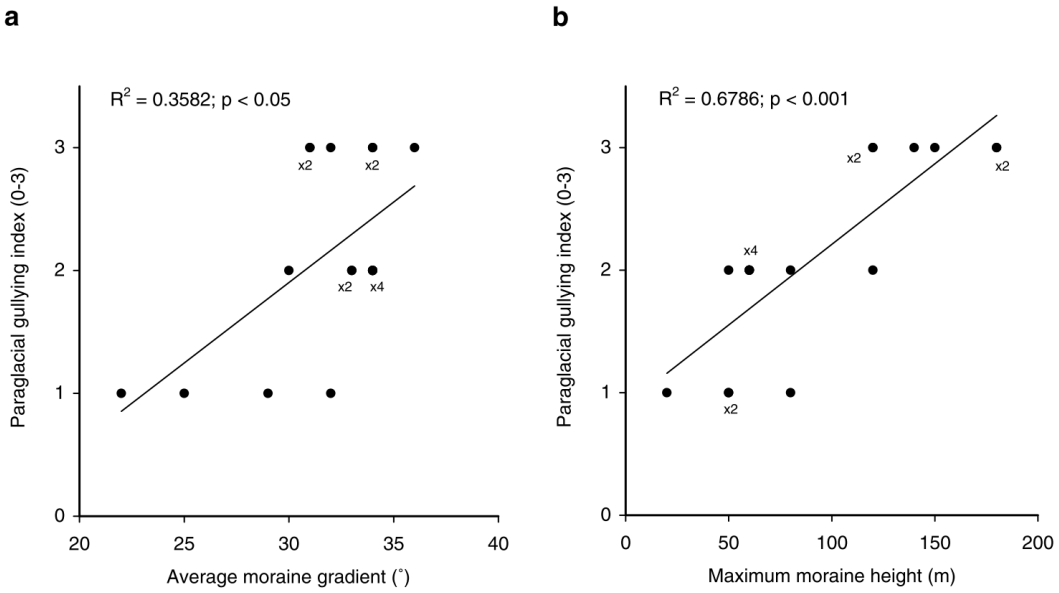

Figure 2.6: Gully erosion relations with moraine (a) gradient and (b) height at sites around the Val d'Herens, Mattertal, and Saastal, Valais. The gullying index describes the extent of paraglacial gully erosion on moraines investigated: (0) none; (1) <10 gullies per kilometre; (2) 10–40 gullies per kilometre; (3) >40 gullies per kilometre (from Curry, Cleasby and Zukowskyj, 2006).

2.5.3 Paraglacial Models

Following the removal of ice and the exposure of over-steepened slopes, slope failure frequency is thought to increase rapidly before returning to background norm, principally linked to the availability of sediment. Church and Ryder (1972) originally represented the progress of sediment movement through the paraglacial period with a curve (**Error! Reference source not found.**7 a), where the maximum amount of movement occurred very soon after the onset of de-glaciation (the pro-glacial period in **Error! Reference source not found.**7 a) with rates continuing to decline thereafter, towards the normal rate of denudation (Church and Ryder, 1972; Ballantyne, 2002a). The curve of Church and Ryder (1972) is sometimes referred to as the 'sediment wave' (**Error! Reference source not found.**7 a) and was invoked to provide a simple characterisation of the exponential decrease in sediment yield since the late Pleistocene (Church and Ryder, 1972; Kovanen and Slaymaker, 2015). However, by virtue of its simplicity it does not consider the true variability of the sediment cascade with respect to changing sources and sinks over time (Kovanen and Slaymaker, 2015).

Cruden and Hu (1993) and Ballantyne (2002a, 2002b) proposed a negative exponential exhaustion model for summarising paraglacial slope behaviour (**Error! Reference source not found.**7 b), which suggests that the number of slope failures following de-glaciation exponentially decreases with time with an immediate enhancement of rock-wall retreat rates (Cossart and Fort, 2008; Fischer *et al.*, 2012; Laute and Beylich, 2013). The exhaustion model assumes that all slope

failures are from the same finite number of slopes and following a trajectory towards stabilisation. Following the continuous erosion of over-steepened slopes (where deglaciation has acted as a preparatory factor in over-steepening and subsequently reducing slope stability) through failures, assuming no further disturbance occurs (in this case, disturbance is de-glaciation), the hazard potential becomes zero (Cruden and Hu, 1993). Ballantyne (2008) proposes that the rate of sediment yield is related to the remaining sediment available by the function:

$$S_t = S_0\, e^{-\lambda t}$$

Equation 2.4

where t is time elapsed since de-glaciation, S_t is sediment available for reworking at time t, S_0 is the sediment available for reworking at t = 0 and λ is the rate of sediment loss by release and/or stabilisation (Ballantyne, 2008). If $S_0 = 1.0$ at $t = 0$, then the rate of loss of available sediment is:

$$\lambda = \mathrm{In}(S_t)/-t$$

Equation 2.5

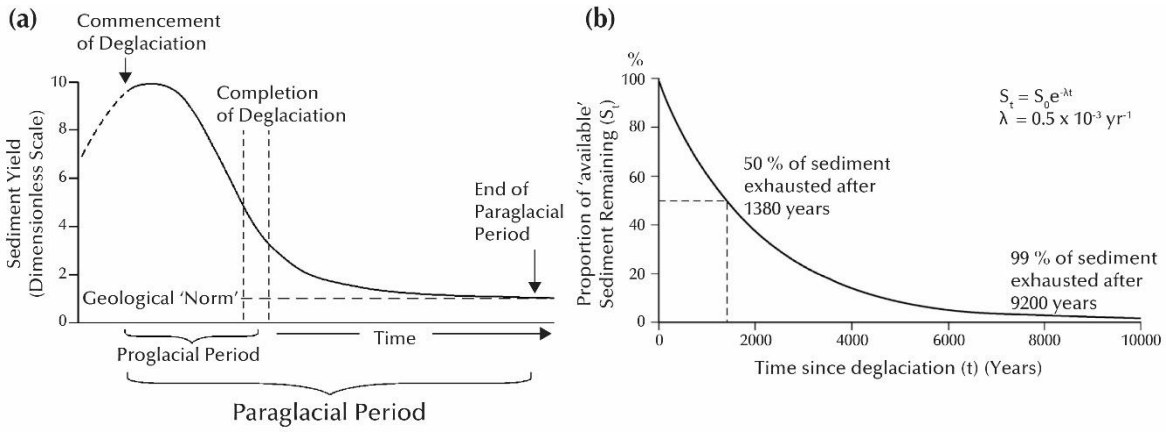

Figure 2.7: (a) The temporal pattern of paraglacial sediment reworking as envisaged by Church and Ryder (1972); (b) Exhaustion model of paraglacial sediment release, in which rate of decline in sediment release (λ) is related to the proportion of 'available' sediment. In this example λ = 0.002 yr^{-1} (i.e., 0.002% of remaining 'available' sediment is released per year), 50 % of initial 'available' sediment is removed in the first 345 years and 99 % of 'available' sediment has been removed after 2,300 years, defining the approximate length of the paraglacial period (from Ballantyne (2002a)).

One crucial assumption is that the system is in steady-state where there are no changes in the processes driving slope failures or other extrinsic factors, which is rarely the case (Ballantyne, 2008). Cossart and Fort (2008) explain that sediment transfer cannot necessarily always be

summarised by a function of time elapsed since deglaciation such as that in the sediment exhaustion model (Ballantyne, 2002a, 2002b). Influences from climatological, tectonic and anthropogenic factors may vary through time, and prolong sediment reworking, reinitiate slope adjustment or renew sediment supply; all of which are likely to cause secondary perturbations in the model of landscape adjustment (Ballantyne, 2008) (e.g. **Error! Reference source not found.**8). Reworked material found in lateral moraines, talus cones, debris cones and alluvial fans are subject to erosional losses at the same time as accumulation.

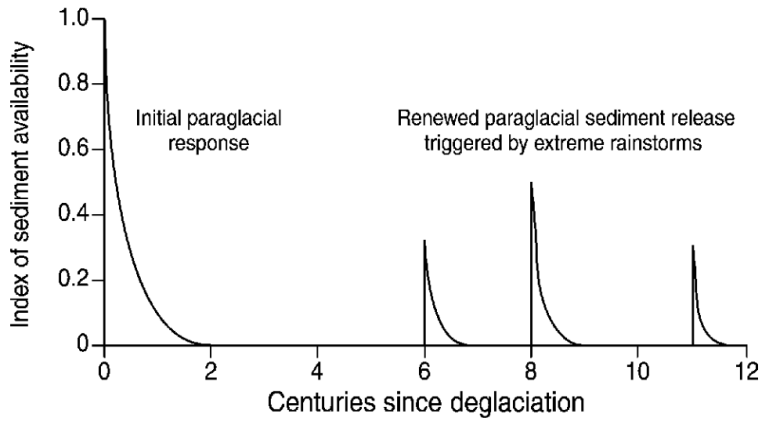

Figure 2.8: Influence of external perturbation on the temporal pattern of paraglacial sediment release. In this example, pulses of renewed paraglacial sediment reworking on drift-mantled slopes are resulting from slope failure triggered by extreme rainstorm events (Ballantyne, 2002a).

Ballantyne (2008) proposes an approximation of the volume of sediment in storage S at time t by assuming rates of loss are conditioned by the volume of sediment in storage:

$$S = \left(S_0 - S_0\, e^{-\lambda t}\right) e^{-kt}$$

Equation 2.6

where k is the rate of sediment loss from the store. Kovanen and Slaymaker (2015) demonstrate the compatibility of the sediment wave (Church and Ryder, 1972) and sediment exhaustion (Ballantyne, 2002a, 2002b) models in the Fraser Lowland, British Columbia, explaining that the former accurately describes the large delivery of late Pleistocene sediments into the marine embayment, whilst the latter has become progressively more appropriate to describe the secondary release of sediments from a variety of reworked paraglacial sediment stores. Curry, Cleasby and Zukowskyj (2006) apply the sediment exhaustion model to their studies of sediment-mantled slopes in glacier forelands of the central Swiss Alps (fig. 2.9). They find that 50 % of the available sediment is exhausted within ca. 10 – 50 years and that primary sediment transfer (from

sediment-mantled slopes through gullying) is effectively complete within a couple of centuries (Curry, Cleasby and Zukowskyj, 2006).

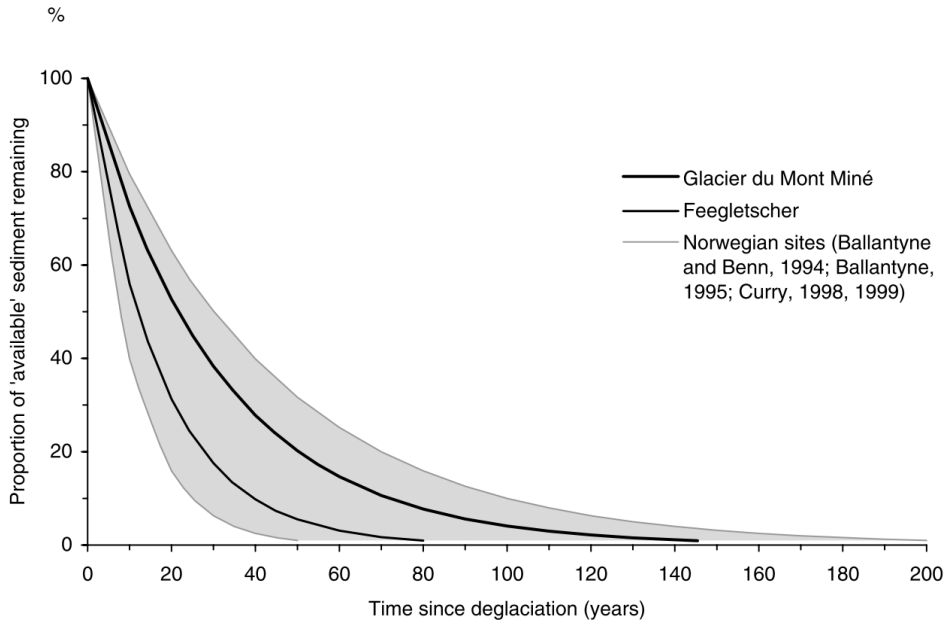

Figure 2.9: Exhaustion curves and envelope for paraglacial gully development and accumulation of small debris cones, based on Ballantyne's (2002b) model and data in this and Norwegian studies (from Curry, Cleasby and Zukowskyj (2006)).

2.6 Sediment in the Land System

As discussed in section 2.5, de-glaciation in mountain environments exposes vast stores of sediment that are particularly vulnerable to processes of release, reworking and re-deposition at rates that greatly exceed the background norm (Curry, Cleasby and Zukowskyj, 2006). The generation of this sediment, its sources, sinks and stores are a complex interplay of geomorphological processes that mobilise sediment through erosion, mobilisation, deposition and subsequent remobilisation and re-deposition. Difficulties in predicting sediment discharge from mountain basins arise from its inherent non-linear nature, where storage effects, geomorphic thresholds and sediment connectivity all play a crucial part in the overall flux (Bennett *et al.*, 2014). There remains a number of questions concerning the precise timing and delivery of sediments to the mountain basins during de-glaciation; a critical factor in predicting the future sedimentological response of valleys to further climatic changes (de Winter, Storms and Overeem, 2012).

2.6.1 Sources

In the pro-glacial system, three main sources of sediment can be identified: (i) that which is derived from glacial erosion and sub-glacial sediment storage, linked to the erosional power of

the glacier and rates of sediment evacuation have been shown to be variable; (ii) that which is produced by weathering and instability of de-glaciated bedrock, where over-steepened rock-slopes are prone to failures through processes such as those discussed in section 2.5 and; (iii) that of glacigenic origin that covers hill-slopes or accumulates in depositional landforms such as lateral and terminal moraines, and is subject to significant reworking following de-glaciation through a wide range of geomorphological processes (Carrivick and Heckmann, 2017). Ballantyne (2002b) also suggests a fourth; coastal glacigenic deposits, though the focus of this thesis is mountain environments, so this will not be discussed further.

2.6.2 Stores

Depositional landforms often create neighbouring, overlapping or underlying land surface patterns where sediment is stored demonstrating coupling and decoupling relationships (section 2.6.4) (Otto *et al.*, 2009). The capacity of these storages is considered a critical parameter in determining the paraglacial sediment budget (Ballantyne, 2002a; Otto *et al.*, 2009). Primary depositional landforms such as talus accumulations, debris cones, alluvial fans and valley fills and secondary stores such as valley fills and lake deposits all act to interrupt the transfer of sediments from source to sink.

2.6.3 Connectivity

Sediment connectivity is defined by Bracken *et al.* (2015) as the "connected transfer of sediment from source to a sink in a system, controlled by how the sediment moves between all geomorphic zones in a landscape." In a well-connected catchment, eroded sediment (or that which has been remobilised) is effectively transferred along sediment cascades, whereby it flows from hill-slopes, through a network of transportation channels down to a catchment outlet. In this system, there are no long-term stores where sediments may be deposited. In reality, most land systems are complicated with temporary storages such as those discussed in section 2.6.2 and Ballantyne (2002b) considers this in terms of an interrupted sediment cascade (**Error! Reference source not found.**10). At the initial stages, sediment input from terrestrial sources produce a range of primary depositional landforms (see section 2.6.2), and eventually as sediment influx to these primary stores slows, it is succeeded by net erosion (Ballantyne, 2002b). Some of this material may work its way through the entire system to its depositional destination, whilst other quantities may undergo successive cycles of re-deposition and remobilisation through secondary sediment stores, the speed of which is influenced by a whole host of extrinsic factors such as uplift rates, climate change, extreme climatic events (e.g. Kociuba (2015)) and where present; anthropogenic activity (Ballantyne, 2002b).

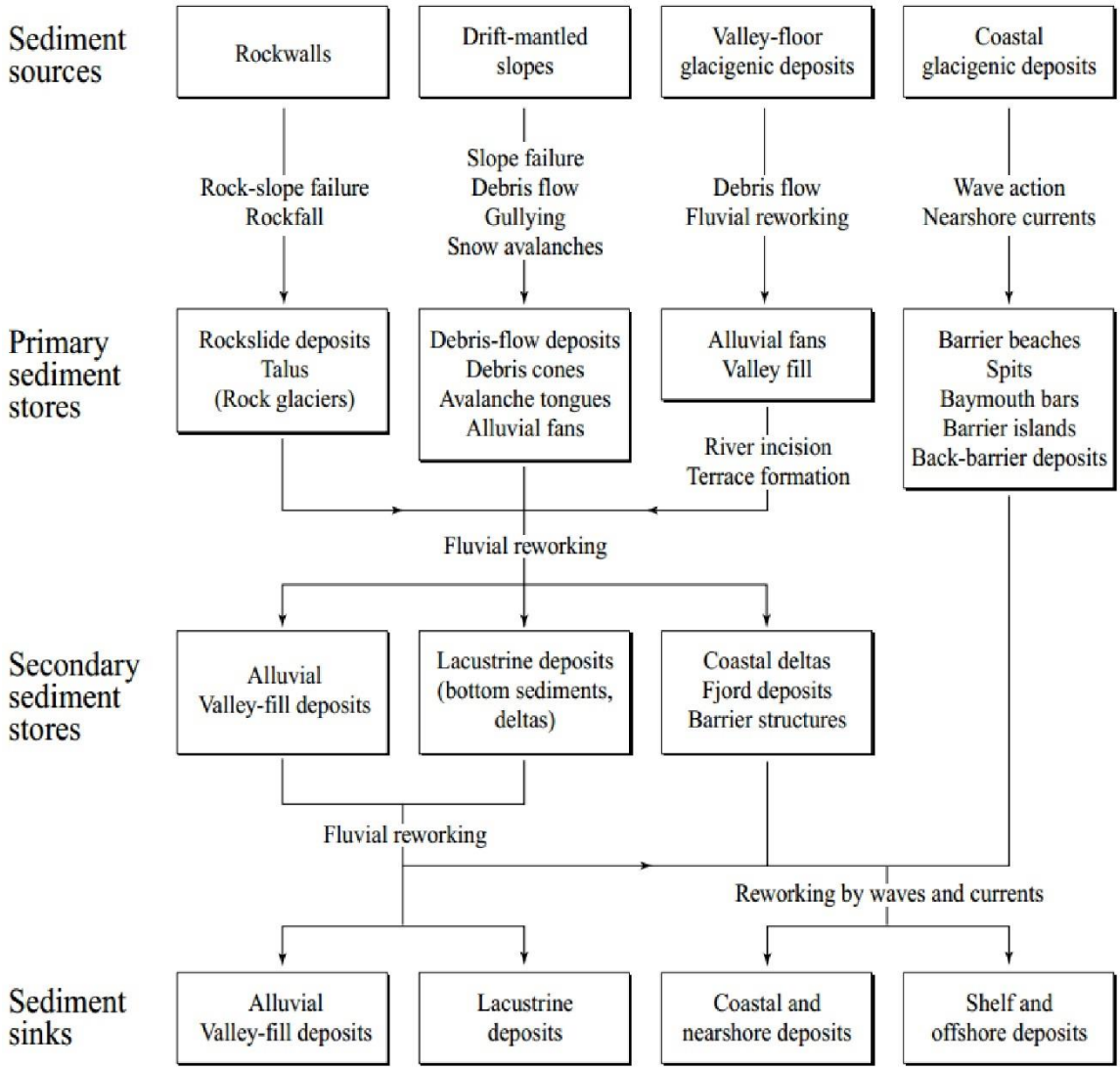

Figure 2.10: Simplified paraglacial sediment cascade, showing the principal primary and secondary sediment stores and main sediment transfer processes (from Ballantyne, 2002).

Sediment connectivity is determined by the spatial configuration of landforms and the activity of geomorphological processes (Carrivick and Heckmann, 2017). The sediment cascade and quantity of sediment exported from the glacial valley depends on (a) the rate of sediment production, and (b) the degree to which the subsystems of transport networks are decoupled from one another or interrupted (Geilhausen *et al.*, 2013). Geilhausen *et al.* (2013), examined the sediment discharge from the pro-glacial zone of the Obersulzbachkees, Austria. They found that a pro-glacial lake significantly reduced the connectivity between sediment production and downstream fluxes, hypothesising that a gradual build-up of sediment in the lake will drastically alter its future role within the cascade from a sink to a throughput, which will in turn affect the stream power and downstream sediment yield (Geilhausen *et al.*, 2013). Kociuba (2015) also finds that a lake that periodically forms in the upper part of the Scott River valley serves as an outflow

regulator, buffering the supply of sediment from the glacier. The existence or non-existence of lateral moraines has also been found to have significant impacts on the rate of sediment transfer and available space for storage landforms (Laute and Beylich, 2014; Carrivick and Heckmann, 2017). For example, Heckmann *et al.* (2016) observe that the space between the crests of LIA lateral moraines and the adjacent hill-slope can intercept slope failure material from falling to the valley floor.

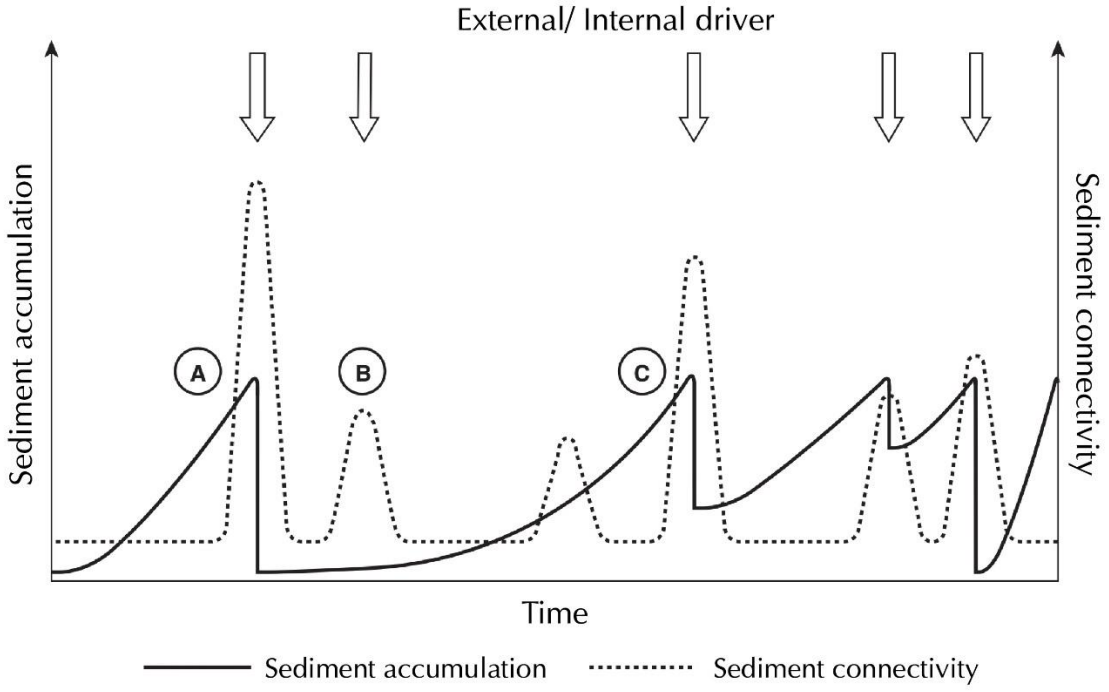

Figure 2.11: Conceptual figure demonstrating the link between sediment accumulation and sediment connectivity, and the dependence of the latter on the sequence of previous events. Event (A) produces a significant amount of sediment connectivity because of the extensive sediment accumulation before its occurrence, but event (B), shortly afterwards is limited by the sediment supply. Sediment connectivity is subsequently stronger when accumulation has again reached a suitable level, as in event (C). From Bracken et al. (2015), after Wolman and Miller (1960).

Bracken *et al.* (2015) provides a comprehensive overview of sediment connectivity, explaining that broader-scale connectivity can often be facilitated over the short-term by the redistribution, accumulation and storage of sediments. They go on to explain that as a consequence of sediment availability, the degree of connectivity within a land system is largely dependent upon the time elapsed since previous events (Bracken *et al.*, 2015) (**Error! Reference source not found.**11). Furthermore, they describe how high-frequency small-magnitude events will continue to supply sediment from slope failures in the time between lower-frequency high-magnitude events, and that a suitable approach for addressing issues arising from this spatial and temporal variability is the use of frequency-magnitude distributions that account for cross-scale dependencies (Bracken *et al.*, 2015). Kirkbride and Deline (2018) explain that whilst glacial retreat

exposes vast stores of sediment, the level of connectivity is likely to reduce during the post-glacial phase as sediment delivery from lateral moraines through slope failure does not reach the proglacial channels. This is discussed further in section 2.7.2. Ultimately, sediment dynamics remain highly location specific with various factors controlling the connectivity of a landsystem. Geilhausen *et al.* (2013) look at how the presence of a proglacial lake can also serve to decouple the system explaining that if glacial retreat, accelerated by climate change, exposes natural basins being capable of forming proglacial lakes, then the downstream hydrological and geomorphological systems in such catchments will be significantly altered by the associated discharge modifications, suspended sediment trapping, decoupling effects and long-term sediment storage.

2.7 Consequences of Slope Failures

Slope failures are a principle source of sediment into mountain land systems and have a number of geomorphological consequences that can vastly alter land system processes and sediment connectivity. Developing a better understanding of how slope failures and de-glaciation affect sedimentary transfer processes and sediment budgets in Alpine environments is a difficult task.

2.7.1 Glacial Consequences

Slope failures that fall onto glaciers can drastically alter their behaviour. Continuous debris cover across a glacier surface has the potential to both increase and decrease rates of ablation, dependent principally on cover thickness, albedo feedbacks and insulation (Reznichenko *et al.*, 2010). This was observed by Agassiz (1840), in some of the earliest glacial studies, who noted that there was a reduction of ice melting under medial moraines and supra-glacial debris. For example, the Miage glacier in the Italian Alps, continues to flow right down into Val Veny at lower altitudes than other glaciers at similar latitudes due to the thick protective covering of successive slope failure deposits (Mihalcea *et al.*, 2008). Following a rock avalanche onto the neighbouring Brenva glacier, the ice advanced 100 m over the following two years, continuing to do so well beyond 1925 when other glaciers in the area ceased to advance, until 1941 where it almost reached its LIA maximum extent (Porter and Orombelli, 1980; Deline, 2009; Reznichenko, 2012). In areas where rock avalanches have fallen onto the surfaces of warm-based glaciers, the mass added has been shown to accelerate the ice-flow velocity (Shulmeister *et al.*, 2009). In the Himalayas, superficial debris cover has been shown to prevent glacial retreat in a similar fashion to the Miage however, the glaciers continue to thin beneath the cover, losing mass at similar rates to debris-free glaciers leaving some in a critical state (Brun *et al.*, 2016). This has been referred to as the *debris-covered glacier anomaly* (Pellicciotti *et al.*, 2015) and has been shown in part to be a result of mass lost at

supra-glacial water bodies and ice cliffs (Brun *et al.*, 2016; Miles *et al.*, 2016). As a hazard, the glaciers of the Himalayas provide water resources for tens of millions of people so understanding their dynamics and the effects that slope failures may have on them is of fundamental importance to predicting the future of this resource.

2.7.2 Fluvial Consequences

Delivery of any quantity of sediment into the fluvial system holds the potential to change the behaviour of the entire catchment. However, different scales of slope failures will result in different scales of behaviour. One particular disturbance is through the formation of slope failure dams, a common consequence in active mountain belts with the potential to generate catastrophic outburst flows if they fail (Korup, Strom and Weidinger, 2006). Lin *et al.* (2008) report on the effect of failures following the Chi-Chi Earthquake (Taiwan, 1999) on fluvial sediment transfer and explain that the suspended sediment load in the primary outlet river increased by a factor of 3.8. Lane *et al.* (2016) measured the quantity of sediment filtered before passing through a hydroelectric power generator in an Alpine drainage basin, observing an increased level of sediment connectivity to pro-glacial areas following glacial recession and an apparent link between sediment export and temperature. They suggest that the latter may have been a result of increased permafrost degradation at higher altitudes (section 2.4.1) maintaining a supply of sediment into the system or that a general increase in connectivity led to an increase in the ability to identify temperature relationships (Lane *et al.*, 2016). In contrast to the paraglacial expectation of maximal sediment delivery following deglaciation, several studies show that proglacial terraces aggrade during periods of glacier advance/ maxima and that reduced sedimentation leading to incision is typical during retreat (Maizels, 1983; Roussel *et al.*, 2008; Wilkie and Clague, 2009).

Kirkbride and Deline (2018) examine the spatial heterogeneity of the paraglacial response in four headwater cirques, testing the extent to which post-LIA maximum system response follows the rapid paraglacial trajectory envisaged by the time-dependent response outlined in section 2.5. They find a contrast between till-floored and rock-floored proglacial cirques whereby the latter is characterised by postglacial stream networks that are remnant subglacial networks with little or no channel mobility (Kirkbride and Deline, 2018). Messenzehl, Hoffmann and Dikau (2014) also find that the dominance of bedrock in the upper hanging valleys of Val Müschauns obstructs sediment output from a significant proportion of the slopes stating that bedrock is a relatively static buffer when compared to debris cones. Till-floored cirques are shown to 'reorganise' from an inefficient 'glacial' mode to a more integrated 'postglacial' mode. However, the effect of such increases in channel efficiency does not necessarily facilitate increased coupling with proximal moraine slopes (main source of sediment) as the cirque floors are wide and channel migration is limited to narrow

corridors. As well as this, over the longer term drainage is organised into a single dominant channel that is poorly coupled with sediment stores. (Kirkbride and Deline, 2018). They conclude that increases in aggradation during the deglaciation phase occur stochastically, mainly where the outwash channel is permitted by local topography to come into contact with lateral moraines or where exceptional lateral moraine failure has occurred but otherwise state that catchment connectivity is maximised during glacial maxima (Kirkbride and Deline, 2018).

2.7.3 Slope Failures as Hazards

“The conditions have been so extreme… and the retreat of the Alps’ eternal snows and glaciers so pronounced, that the range – and its multi-billion-pound tourist industry – may never fully recover.” (Rose, 2003)

"Geomorphological hazards such as slope failures are part of a larger group of natural hazards, including for instance floods, soil or water quality risks due to agricultural technologies, desertification, sudden weather changes and wildfires" (Kalvoda and Rosenfeld, 1998). The nature of hazardous phenomena is described by Davies, 2014 (Davies and Shroder, 2014), to be one with the potential to detrimentally affect society. Climate change has been shown to have much less of an influence on the number of slope failure fatalities than population growth (Petley, 2012) and thus, it is with good reason that we seek to examine the nature and frequency of slope failures as a threat to society and ways whereby this can be reduced in the future (Davies and Shroder, 2014). The risk that a slope failure poses to a society can be expressed as the probability of the hazard and the potential consequences it may have (Clague, 2013). The decision on whether measures are required to counter a risk are often based upon probabilistic analysis of the hazard (Davies and Shroder, 2014), including the likelihood analysis of an occurrence, based on the geology, slope characteristics, geotechnical properties, vegetation cover, weathering and drainage patterns (Clague, 2013). This in itself is a difficult task as within a planning timeframe, it is unlikely that you will observe the true distribution of events and thus the precision derived in this manner would be spurious at best (Davies and Shroder, 2014).

Nöthiger and Elsasser (2004) explains that there are direct and indirect effects of natural hazards within the context of tourism and society. Direct effects of natural hazards are summarised by Nöthiger and Elsasser (2004) as 'the costs associated as a direct impact from the event, such as damage to buildings, infrastructure, forests and farmland'. Whilst indirect effects of the costs associated with a change in conditions as a result of the event and typically take much longer to subside than the direct effects, such as loss of earning, evacuations and closure of roads (Nöthiger

and Elsasser, 2004). Tourism in the European Alps is under increasing risk from the effects of climate change. Besides the loss of glaciers as attractive landscape features, there are also changes in the environmental systems that increase slope instability and the threat this poses (Pröbstl-Haider, Dabrowska and Haider, 2016). Tourism and alpinism in the Alps have considerable weight within the economy. Chamonix in particular, with a resident population of approximately 10,000 people is boosted to 100,000 during the summer and 60,000 during the winter. Given the likely increase of natural hazards in response to a changing climate, relatively little research has been conducted on the threat to societies within the mountains and the impact this may have on the tourism industry.

As discussed earlier, there are a number of potential links between a warming climate, and the frequency of slope failures at higher altitudes (section 2.4). In the exceptionally warm summer of 2003, many routes across the Mont Blanc range were closed as a result of an increased risk in rockfall activity (Noetzli, Hoelzle and Haeberli, 2003; Rose, 2003; Gruber, Hoelzle and Haeberli, 2004; Ravanel and Deline, 2011). Ravanel and Deline (2011) use historic imagery to precisely date rockfalls that have occurred in the Mont Blanc range since the LIA. They explain that during the past two decades, 16 of the 22 rockfalls occurred during three of the seven hottest years and 12 during the 2003 summer heatwave (Ravanel and Deline, 2011). As the climate continues to warm in-line with predictions in by Stocker *et al.* (2013), rockfalls are expected to occur more frequently in response to a deepening of the active layer and thus, pose an ever-more significant hazard in Alpine resorts. Purdie, Gomez and Espiner (2015) demonstrated an indirect effect of warming on the potential risk from slope failures; that the thinning of Fox glacier in New Zealand resulted in a 'flattening' of the surface profile of the glacier, removing troughs in which slope failures were previously trapped. The consequence of this is a marked increase in the distance slope failure deposits from over-steepened slopes can travel across the ice surface (Purdie, Gomez and Espiner, 2015). High-altitude near-vertical rock-walls are popular with climbers and extreme-sport pursuits, which are at significant risk from rock-fall, and rock avalanche activity (Magnin *et al.*, 2015). Pröbstl-Haider, Dabrowska and Haider (2016) examines the perception of risk in the European Alps, predicting that the risk for mountain tourists and the tourism industry will increase in the future. Following a survey amongst 300 participants, they found that respective perception of risk did not influence their choice to travel to the destination (Pröbstl-Haider, Dabrowska and Haider, 2016).

2.8 Inventories and Distributions

A number of inventories have already been created that aim to look at the size distribution of slope failures over a variety of time-scales as understanding this, is crucial for quantitative hazard analysis. Historical inventories include the sum of many slope failures that have occurred over time (Malamud *et al.*, 2004b) and are typically categorised by slope failure area, which includes failure and runnout area (Malamud *et al.*, 2004a), as these are more straightforward to quantify from

aerial maps than slope failure area, excluding runnout, and volume (section 2.9.2). Malamud *et al.* (2004a), explains that inventories created soon after an event are substantially more complete than those which span tens to thousands of years which suffer from *censoring* of deposits and failure areas through secondary Earth system processes. As a result, historical inventories are characteristically associated with underestimating the existence of small-magnitude slope failures (Malamud *et al.*, 2004a). However, where larger-magnitude slope failures fail into glacial or fluvial systems, they too have been shown to rapidly be reworked and censored within the land system (e.g. Dunning *et al.*, 2015). Malamud *et al.* (2004a) also outlines a number of factors that can affect the reliability of historic slope failure inventories:

i) the age of the slope failure and its "freshness" (i.e. how visible it is in the landscape);
ii) the quality, scale and resolution of aerial imagery and base maps used for identifying slope failures;
iii) the morphological and geological complexity, and whether this obscures the aerial imagery or the ability to identify slope failures;
iv) how the land is used, and how it may have been modified since the slope failure;
v) the degree of experience and level of knowledge of the researcher(s) involved.

Slope failure inventories can also be tailored for focussing on the effect of particular magnitudes, for example, Korup *et al.* (2007b) compiled an inventory of slope failures above a threshold magnitude of 10^8 m^3 to specifically examine whether larger slope failures govern mean local relief in mountain ranges around the world. They find that hill-slope adjustment is significantly accommodated by large slope failures and that landscape evolution models which rely on critical relief thresholds for failures may significantly underestimate the role of large-magnitude events in landscape erosion (Korup *et al.*, 2007b). Guzzetti *et al.* (2008) use an inventory prepared by Cardinali *et al.* (2001), of over 18.5 thousand slope failures in central Italy to examine their distribution. They found the principal control to be the surface geological conditions, noting that the slope failures had altered the topography considerably (Guzzetti *et al.*, 2008).

2.8.1 Measuring Slope Failures

Historical inventories are typically created using maps and aerial imagery and the number of slope failures in an area is relatively easy to obtain where complete and accurate inventory maps exist. So too, is the calculation of area and density of slope failures from maps in digital form using GIS software, as well as the frequency of slope failures when these resources are available in multi-temporal series. However, the calculation of volume is a more difficult task as it requires

information about the surface and subsurface geometry of the slope failure that simply isn't available on most inventory maps (Guzzetti *et al.*, 2009). As such, researchers rely on empirical relationships between the measured volumes of slope failures and their 2D geometrical characteristics (e.g. area, width and height) to infer volumes in their distributions. Volume and erosion estimates are therefore reliant on scaling relationships created using relatively few field measurements:

$$\mathrm{V_L} = \alpha \mathrm{A_L^{\gamma}}$$

Equation 2.7

where the predicted slope failure volume (V_L) of a slope failure with a given area (A_L) depends on a scaling exponent (γ) and intercept (α) such that (Larsen, Montgomery and Korup, 2010).

In-situ measurements of volumes using high-resolution topographical modelling (section 2.11) techniques such as LiDAR and photogrammetry are also widely used for monitoring slope failures through time-series analysis. Such work provides a quantitative basis for the empirical relationships used to estimate historical events and successive models throughout an observation period can build a picture of the frequency and nature of failures across a wide range of temporal and spatial scales. Abellán *et al.* (2014) provide a comprehensive review of the use of TLS for monitoring rock slopes, explaining that the technology allows an enhanced understanding of the failure mechanisms. Rosser *et al.* (2007) applied a TLS approach to monitoring slope failures along a coastal cliff in North Yorkshire, creating an inventory of rock-fall activity that was shown to be scale-invariant over a limited range of magnitudes.

2.8.2 Magnitude-Frequency

There is a large body of literature that use slope failure inventories to examine the statistical likelihood of slope failure magnitudes, as a means of resolving the probabilistic frequency of their distribution. The distribution and probability density of slope failures expressed as a magnitude-frequency curve is important for the characterisation of hazards and knowledge of hill-slope denudation in mountainous regions (Guthrie *et al.*, 2007). The probability density of slope failures has to some degree, been shown to exhibit behaviour that agrees with the concept of self-organised criticality (i.e. a series of events resulting from additive or cascade processes being generated from equivalent initial conditions) (Bak, Tang and Wiesenfeld, 1987b; Guzzetti *et al.*, 2002; Frigg, 2003; Casas *et al.*, 2016). Generally, it is found that the frequency-area/volume distributions follow an inverse power-law above a lower bound, below which the probability 'tails'

off (**Error! Reference source not found.**12) (e.g. Guzzetti *et al.*, 2002, 2008, 2009; Brardinoni and Church, 2004; Guthrie and Evans, 2004; Malamud *et al.*, 2004a, 2004b; Hungr *et al.*, 2008; Bennett *et al.*, 2012; Li, Lan and Wu, 2016). This tailing is often referred to as the rollover and is discussed further in section 2.9.1. The power-law and its significance are discussed in more detail in section 2.9.3. Table 2.4 from Bennett *et al.* (2012), summarises the distributions of slope failure magnitudes found in a number of studies, including the range of magnitudes across which the power-law is applicable and the scaling exponents.

Below the lower bound (x_{min}), a rollover in the frequency is typically observed (e.g. fig. 2.12), and its origin has remained a topic of discussion and debate for some time. Some attribute the rollover to a systematic undersampling of slope failures below the threshold magnitude (Hovius and Stark, 2006) whilst others explain the threshold is too large to be subject to data biasing and the parting from the trend could be driven by physical processes (Guthrie *et al.*, 2007).

Table 2.4: Comparison of values of the exponents of the power-law tails obtained for slope failure and rock-fall inventories, ordered from low to high. Table includes the slope failure type (R = Rockfall, L = Landslide), geological setting, time window, attribute (V=Volume, A= Area) and the power-law scaling exponent (α). Modified from Bennett et al. (2012).

Study	Slope Failure Type	Geological Setting	Time Window	Attribute*	α
Malamud et al., 2004	R	Mixed	Mixed	V	0.07
Guzzetti al., 2003	R	Granitic cliffs	145 years	V	0.1
Dussauge-Peisser et al., 2002	R	Calcareous cliffs	60 years	V	0.41 ± 0.11
Hungr et al., 1999	R	Massive felsic rock	30 years	V	0.43
Dussauge-Peisser et al., 2002	R	Metamorphic and sedimentary rock	22 years	V	0.45 ± 0.15
Dussauge-Peisser et al., 2002	R	Granitic cliffs	78 years	V	0.46 ± 0.11
Dussauge-Peisser et al., 2003	R	Undifferentiated rock cliffs	10,000 years	V	0.52
Hungr et al., 1999	R	Jointed metamorphic rock	22 years	V	0.65
Gardner, 1970	R	Calcareous and quarzitic rock	2 summers	V	0.72
Lim et al., 2010	R	Sandstone + mudstone capped in glacial till	20 months	V	0.8
Malamud et al., 2004	L	Various	Mixed	V (from A)	0.93
Stark and Guzzetti, 2009	L	Sandstones, marls, limestones	17 / 28 years	V (from A)	1
Rousseau, 1999	R	Basaltic cliff	2 months	A (eroded)	1
Stark and Hovius, 2001	L	Vegetated slopes with thin regolith cover	2 years	A (disturbed)	1.11
Stark and Guzzetti, 2009	L	Clay and silt and clastic sediments	17 / 28 years	A (disturbed)	1.19
Malamud et al., 2004	L	Weakly cemented clastic sediment	Few hours	A (disturbed)	1.4
Malamud et al., 2004	L	Clay and silt and clastic sediments	Weeks	A (disturbed)	1.4
Malamud et al., 2004	L	Soil, siltstone, volcanic rocks, phyllite and schist	2 months	A (disturbed)	1.4
Stark and Hovius, 2001	L	Schists and gneisses with thin regolith cover	8 years	A (eroded)	1.48

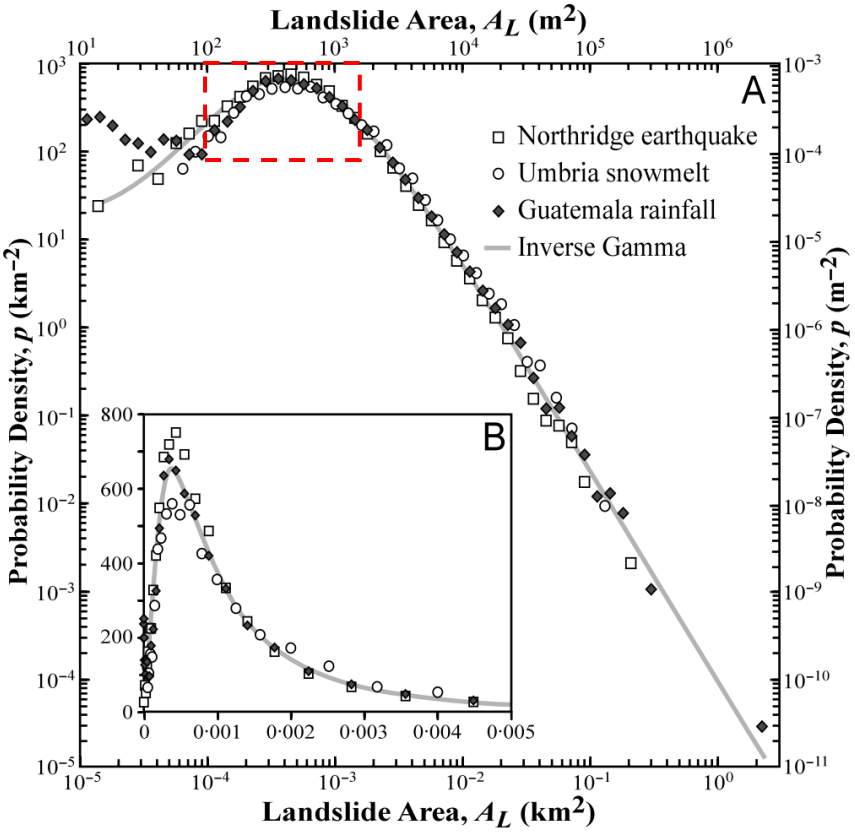

Figure 2.12: Dependence of landslide probability densities (p) on landslide area (A_L) for three landslide inventories (from Malamud et al. (2004a)). The 'rollover' in probability density of small-magnitude landslides is highlighted with the red dashed box.

Guthrie *et al.* (2007) explores the magnitude-frequency relationship to determine whether the rollover is attributable to bias or physical conditions, concluding that both the rollover and exponents of the power-law distribution are results of the physiographic limitations of the slope and its characteristics. However, Stark and Hovius (2001) used data sets of differing resolutions to demonstrate that the scale of the aerial imagery affected the lower bound, showing that the rollover value for the higher resolution dataset was lower. Root cohesion and anchorage acting to limit the occurrence of low-magnitude events has been proposed as a physical factor (Stark and Hovius, 2001; Barlow *et al.*, 2012) however, Malamud *et al.* (2004b) demonstrate a power-law scaling across an entire size range using three inventories of rock-fall data, noting that this is not a physical process that occurs across cliff-faces. This demonstrates the importance of considering background mechanics when examining the statistical distributions of natural phenomena. Rock-fall data should be considered separately to other types of slope failure data as the applicable physics are different, where rock-falls are controlled by fragmentation processes and other types are controlled by processes of slope stability Malamud *et al.* (2004b).

The identification, classification and characterisation of small-magnitude slope failures over time become increasingly difficult as they are gradually censored by extrinsic factors within the

glacial and fluvial zones they are deposited within. As such, historic inventories quite often only account for and misrepresent the frequency and probability of medium- to large-scale slope failures (contributing to a rollover in their calculated probability density) (Malamud *et al.*, 2004b; Hovius and Stark, 2006). However, the importance of small-magnitude slope failures must not be underestimated as they often cause the highest number of rock-fall casualties in Alpine environments and are significant agents of geomorphic change with great importance in mountain sediment budgets (Krautblatter and Moser, 2009). Hovius and Stark (2006) explain that over the long term, the area disturbed by slope failures is dominated by small- to medium-magnitude events yet the representation of these scales in datasets assembled over the years are unreliable.

2.8.3 Statistical Distributions

As discussed in section 2.8.2, magnitude-frequency probability distributions (i.e. the likelihood of a slope failure of size *x* occurring) are often shown to follow an inverse power-law across medium- to large-magnitude failures. A statistical distribution, such as a power-law or log-normal, is a method of summarising complex phenomena by means of a relatively straightforward relationship. Power-laws have been shown to occur across a diverse range of disciplines though very few follow the distribution across the entire range, often removing the lower values of the variable (Newman, 2005).

A good statistical distribution within an empirical dataset can present interesting perspectives on driving mechanisms. Deviations from that distribution can suggest scale-dependent processes in the natural environment. Datasets that satisfy a power-law distribution are sometimes said to be 'scale-invariant' which suggests that the common small events at the lower end of the distribution display no qualitative difference from the rarer, large events (Virkar and Clauset, 2014). Deciphering the best fit to the magnitude-frequency distribution of slope failure volumes has important implications for; (i) understanding the physical processes that drive their generative models (e.g. test whether small-magnitude failures driven by different physical processes to larger magnitudes that limit their likelihood); (ii) assessing the land system response to changes in the cryosphere (e.g. assess the extent to which the probability of slope failures increases in response to deglaciation), and; (iii) facilitating statistical extrapolations about the probable likelihood of future events (e.g. understand the risks posed by slope failures and the likely timescales of a landscape response based on quantitative observation data). These factors, and the degree to which inventories adhere to power-laws, remain under considerable debate (Guzzetti *et al.*, 2002; Perline, 2005; Bennett *et al.*, 2012), though for distributions that are shown to follow power-law scaling, the concept of self-organised criticality (see definition in section 2.8.3) is commonly discussed (Frigg, 2003). In cases where the probability distribution of slope failures satisfy a power-

law (eqn. 4.6), they are considered scale invariant, whereby there is a commonality in form and process across a wide range of scales (Bak, Tang and Wiesenfeld, 1987a; Wood, Harrison and Reinhardt, 2015). However, gaining quantitative evidence of scale invariance of slope failures is no trivial matter and would require survey scales of at least the temporal and spatial scale over which the distribution is implied. Perhaps the most renowned example of this behaviour in geomorphology is that of the Sand Pile model, where sand particles are steadily added one by one to a pile and their behaviour is driven by gravity and friction. When a critical slope is established, simply adding one more grain of sand could generate a 'failure' until eventually, the slope will stabilise around the angle of repose (van den Eeckhaut *et al.*, 2007).

It is commonly seen in Earth Science literature, that natural phenomena are interpreted as following a power-law based on the approximation of a straight-line on a doubly logarithmic plot, however, this has been shown by several authors to not be a sufficient method of satisfying such a distribution (Newman, 2005; Stumpf and Porter, 2012; Virkar and Clauset, 2014; Gillespie, 2015). Chapter 4 (section 4.7) details the methodological approach (from Clauset, Shalizi and Newman (2009)) used in this thesis to statistically validate power-law and log-normal distributions drawn from the data. Whilst a power-law is the most commonly used statistical distribution to describe the probability of slope failures (e.g. Guzzetti *et al.*, 2002; Barlow *et al.*, 2012; Bennett *et al.*, 2012), some authors have found that a log-normal statistical distribution is a better fit (e.g. Kelsey *et al.*, 1995; Dunning *et al.*, 2007; Chaytor *et al.*, 2009). In this thesis, the validity of both distributions are tested. To understand the implications of whether a dataset is better fit to a power-law or log-normal, it is necessary to highlight the difference between them. They often connect naturally through similar generative models and thus, it is not uncommon for datasets to apparently follow both. However, distinguishing between the two is no trivial matter and in this study, a statistical likelihood test initially proposed by Clauset, Shalizi and Newman (2009) is performed to generate a goodness of fit value for both power-law and log-normal distributions (see section 4.7).

A log-log distribution over several orders of magnitude is strictly required for a power-law. Such a distribution also typically generates orders of magnitude more events of larger magnitude than would be expected under a normal distribution (Virkar and Clauset, 2014). A dataset is said to be log-normal when the probability distribution of the logarithm of x is normally distributed (i.e. magnitude (V_L) is log-normally distributed if $log(V_L)$ has a normal distribution). A log-normal distribution, much in the same way as a power-law distribution, is a skew distribution with many small values of magnitude and fewer large values and therefore the mean is usually found to be greater than the mode. A log-normal distribution suggests a lower likelihood of smaller magnitude failures than a power-law and could go some way to explaining the rollover in their probability in existing inventories (e.g. fig. 2.12). The argument over whether a log-normal or power-law distribution is a better fit to empirically observed data is a matter that has been widely discussed

and debated across a large variety of disciplines from biology to astronomy, chemistry to computer sciences (Mitzenmacher, 2004). Mitzenmacher (2004) states that "given the close relationship between the two models [P-L and L-N], it is not clear that a definitive answer is possible [as to which is better]; it may be that in seemingly similar situations slightly different assumptions prevail." However, Mitzenmacher (2004) stresses that if a distribution such as a power-law or log-normal are to be used to predict the future behaviour based on current data (i.e. extrapolating the likelihood of a specific magnitude of slope failure to occur based on empirical data) then misrepresenting the tail of the distribution could have severe consequences.

2.9 SfM-MVS Photogrammetry

Topographic gradients are a principle factor in the movement of mass and energy in natural systems, where attributes such as slope and roughness play fundamental roles in the transfer of material and sediment budgets (Passalacqua *et al.*, 2015). The rapid increase in the capture and availability of high-resolution topography (HRT) from satellite, aerial and terrestrial remote sensing techniques over the recent decades has heralded new opportunities for understanding Earth surface processes. Survey techniques which yield three-dimensional data such as LiDAR and photogrammetry are "completely changing our perception of the surrounding environment" (Abellan, Derron and Jaboyedoff, 2016). The application of HRT modelling using TLS, an active laser range-finding method, has been successfully demonstrated in a number of geomorphic process studies (e.g. Rosser *et al.*, 2005; Abellán, Vilaplana and Martínez, 2006; Carrivick *et al.*, 2013; Crepaldi *et al.*, 2015; Strunden *et al.*, 2015). The same is true for the application of photogrammetry, the use of matching features in overlapping imagery for 3D point generation (e.g. Barker, Dixon and Hooke, 1997; Lim *et al.*, 2005; Stumpf *et al.*, 2014). As technology has progressed, so too has the accessibility of HRT technologies and the ability to capture data at even higher resolutions.

Recent advances in the fields of HRT modelling and computer vision technologies have led to the development of new innovative approaches for reconstructing 3D geometry using consumer-grade camera equipment, following a mostly-automated workflow (Westoby *et al.*, 2012; Fonstad *et al.*, 2013; Smith, Carrivick and Quincey, 2015). 'Structure-from-Motion Multi-View Stereo' (SfM-MVS) was first developed within the field of computer vision technologies, introduced for the purpose of modelling-built structures using a vast database of imagery acquired online from a variety of sensors, capturing the object-of-interest from a number of perspectives. It operates under a similar principle to that of traditional stereoscopic photogrammetry in that 3D structure can be resolved from a series of offset overlapping images. However, it requires significantly less involvement from the end user as much of the alignment and model construction is performed automatically (Westoby *et al.*, 2012; Fonstad *et al.*, 2013). As a result of its relative ease-of-use, low

costs and simple approach, SfM is increasingly being used (**Error! Reference source not found.**13) across a variety of geoscience applications including monitoring glacial dynamics (Ryan *et al.*, 2015), mapping slope failure displacements (Lucieer, Jong and Turner, 2013) and deformation (Stumpf *et al.*, 2014), recording the morphology of gully erosion (Frankl *et al.*, 2015), analysis of agricultural watersheds (Ouédraogo *et al.*, 2014a) and modelling the topography of shallow braided rivers (Javernick, Brasington and Caruso, 2014). When combined with Multi-View Stereo (MVS) algorithms, SfM provides a workflow that has been shown to produce results of comparable quality to more established high-resolution survey techniques such as Terrestrial Laser Scanning (TLS) (Remondino *et al.*, 2014).

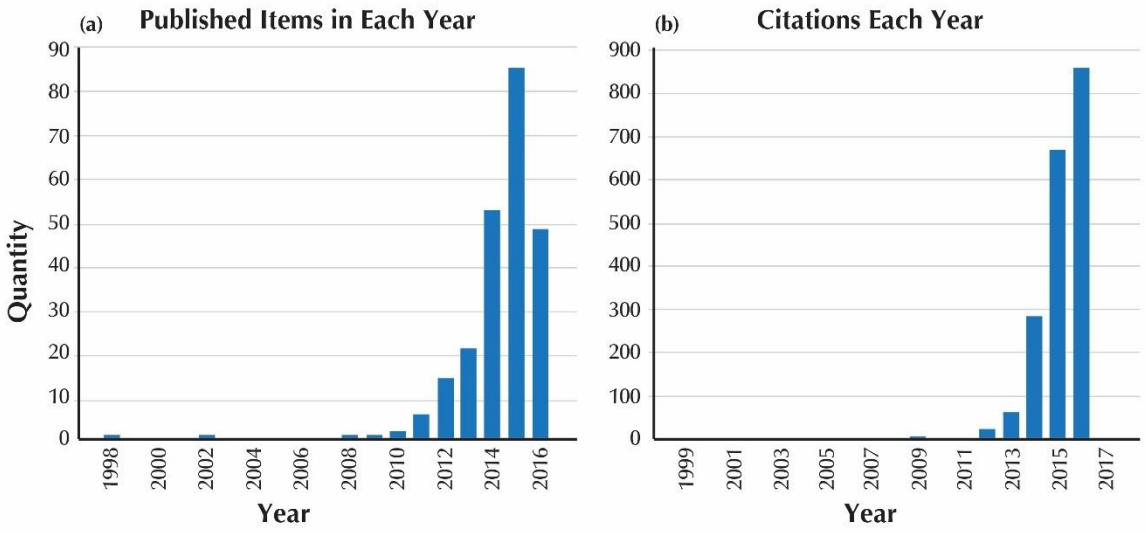

Figure 2.13: (a) Number of publications, and (b) number of citations in the Web of Science database containing the terms "structure from motion" in the field TOPICS between 1970 and 2014. Analysis made in November 2016 and restricted to the 'Geosciences-multidisciplinary', 'Geography Physical', 'Geology', 'Environmental Sciences' and 'Soil Sciences' segments.

The technique is well-suited for many geoscience applications, particularly those that involve fieldwork in landscapes that present significant logistical challenges such as mountains. In terms of equipment, the technique requires no more than a small consumer-grade camera, though for quantitative measurements it is recommended that accurate ground control data is collected which requires additional equipment (such as DGPS, total station etc.) however, some authors have worked on the development of a workflow that does not require this, further improving the logistical capabilities of the method (e.g. Rizaldy and Firdaus, 2012; Carbonneau and Dietrich, 2016). SfM-MVS is quickly becoming a 'go-to' method for rapid topographic analysis within the geosciences and is particularly well-suited to this study.

2.9.1 Background and Development

Much of the SfM technique in its current form is down to the work of Snavely (2008), whose PhD thesis focussed on the reconstruction and digital visualisation of scenes from mass-downloaded internet photo collections. His work focussed on solving the problem of calculating the camera position, without any priori GPS information, along with producing two pieces of visualisation software which together, create a "3D experience for famous sites" (Snavely, 2008). The principle was that areas of particular interest to tourists are photographed millions of times each year from a number of similar perspectives, though slightly different positions (**Error! Reference source not found.**14), the overlapping, matching pixels of which can be used to reconstruct the 3D geometry of the scene. There are a number of problems that are encountered when trying to do so, namely the large variations in viewpoint, illumination, weather conditions and image resolutions amongst others (Snavely, Seitz and Szeliski, 2008). The workflow adopted by Snavely et al. (2008) is given in section 4.3.1, and a detailed review of the full SfM-MVS workflow can also be found in Smith, Carrivick and Quincey (2015).

Figure 2.14: Large collections of internet photo-sets, used to automatically reconstruct 3D geometry at three popular tourist destinations (Snavely, 2008).

Westoby *et al.* (2012) presented the first introduction to SfM-MVS and its potential application in the geosciences, with examples from a number of contrasting locations (glacial landforms) and an assessment of model quality compared to TLS across a cliff section in Wales. They highlight the computational intensity of SfM-MVS data processing and storage demands owing to the sheer size of output datasets partly off-setting its logistical advantages (Westoby *et al.*, 2012). Fonstad *et al.* (2013) followed this, finding that the results of an SfM-MVS workflow were of

comparable accuracy and precision to LiDAR data, noting the obvious benefits of such an accessible technique within geomorphological studies.

2.9.2 Accuracy and Repeatability

Using a SfM-MVS workflow, James and Robson (2012) report a relative precision of approximately 1:1000 with a Root Mean Square Error (RMSE) of ~1 m at a viewing distance of ~1000 m using open source algorithms. Stumpf *et al.* (2014) suggest that relative precision of 1:500 and better is possible. In the case of the latter, images taken from a distance of 500 m from the subject (e.g. slope, cliff face, ground surface etc.) could yield topographical data from SfM-MVS processing that is precise to within ± 1 m. Both studies explain that although the SfM technique cannot yield the precision of the very latest high-end laser-based technology, it does offer a suitable alternative at a fraction of the cost, bulk and time (James and Robson, 2012). Lucieer, Jong and Turner (2013) achieved a precision similar to that suggested by Stumpf *et al.* (2014) of 1:500 with an RMSE of ~8 cm at a distance of ~40 m, identifying a number of key sources of uncertainty. Mancini *et al.* (2013) found that the topographic quality and vertical accuracy of SfM-MVS models created using UAS imagery were directly comparable with GNSS survey data, whilst Nouwakpo, Weltz and McGwire (2015) found that flat surfaces showed the best level of agreement when benchmarking SfM-MVS data against TLS. They found that vegetation was a significant problem for HRT modelling using both technologies, and also observed a smoothing of fine-scale details in the SfM-MVS model, which they state highlights the importance of assessing model quality (Nouwakpo, Weltz and McGwire, 2015). Smith, Carrivick and Quincey (2015) explain that a general relationship between model quality and survey range is found across a synthesis of studies that have applied an SfM-MVS workflow.

2.9.3 Applications in Geoscience

SfM-MVS provides a unique opportunity for small- to medium-scale surveys to help further our understanding of complex fluvial systems. Such landscapes present a number of challenges to researchers, owing to the varied topography, partial inundation and high sediment mobility (Javernick, Brasington and Caruso, 2014). Woodget et al. (2014) used a UAS and SfM-MVS workflow for quantifying submerged fluvial topography, testing the techniques reproducibility and accuracy. After collecting imagery from two contrasting river locations, they found that their outputs were of 'hyperspatial' resolution, with accuracy values approaching those typically obtained using costlier approaches such as TLS (Woodget *et al.*, 2014). Tamminga, Eaton and Hugenholtz (2015) exploited the flexibility and ability to rapidly conduct an SfM-MVS survey by collecting pre- and post-flood topographic data along the Elbow River, Canada. It is unusual to obtain pre- and post-flood data

such as this as these events are rare and largely unpredictable, but doing so offers a unique insight into the morphodynamics of a river system under flooding conditions (Tamminga, Eaton and Hugenholtz, 2015). Smith *et al.* (2014) also aimed to examine flooding, by quantifying flash-flood magnitudes using a coupling of SfM-MVS with 2D hydraulic modelling. They explain that compared to other approaches to discharge measurements, such as a 1D cross-sectional approach, their method with a UAS and SfM-MVS yielded higher estimates and avoided the subjectivity associated with choosing a cross-section location (Smith *et al.*, 2014). The topography of shallow braided rivers was modelled using SfM-MVS by Javernick, Brasington and Caruso (2014), who surveyed a 3.3 km river reach. They explain that dense vegetation poses a significant problem, though this is common across a number of topographical modelling techniques (Brodu and Lague, 2012), but highlighted the potential for the workflow to produce detailed DEMs enabling a number of new research opportunities (Javernick, Brasington and Caruso, 2014).

The nature of glaciers often means they're located in areas that present significant logistical problems, requiring high capital investment and time-consuming data collection. SfM-MVS presents a desirable cost-effective technique for deployment in such remote, hazardous environments and has seen its use for such work increase rapidly over the last few years. For example, Ryan et al. (2015) used a UAS and SfM-MVS to assess calving dynamics at the terminus of Store Glacier on the Greenland ice sheet. The models they produced allowed an insight into the complex interactions of crevasse systems at the terminus of a marine-terminating glacier that would only be otherwise possible with 'prohibitively expensive' techniques such as airborne LiDAR (Ryan *et al.*, 2015). Their work highlighted a number of caveats, most notably the lack of ability to construct duller (poorly lit) areas of the crevasse network at deeper sections which resulted in a conservative estimate of crevasse depth in some places (Ryan *et al.*, 2015). Brun et al. (2016) produced a 3D model of a section of the Lirung glacier, a debris-covered glacier in the Nepalese Himalayas, for analysing the loss of ice volume from ice cliff backwasting. They collected imagery with a fixed-wing UAS at a ground resolution of approximately 4 to 7 cm, and used an innovative TIN-based approach for quantifying volume-loss; the first-such attempt and important for confirming results from other modelling studies (Brun *et al.*, 2016). The same glacier was used by Immerzeel *et al.* (2014)to research glacial dynamics using high-resolution data from an SfM-MVS workflow. Ice-flow velocity was measured with orthomosaics and feature-tracking, whilst DEM-differencing was used for quantifying mass loss (Immerzeel *et al.*, 2014). An off-glacier area of rock mass was used to assess the error, and they found an average deviation of 0.02 m $\pm$ 0.33 m based on an area of 1.6 km^2 (Immerzeel *et al.*, 2014).

The mass balance of the Montasio Occidentale glacier, Italy, was examined by Piermattei *et al.* (2015) using SfM-MVS and TLS. The researchers used natural features (i.e. bedrock) as GCPs for georeferencing, extracting their respective coordinates from the TLS dataset (Piermattei,

Carturan and Guarnieri, 2015), obtaining 'almost identical volumetric changes and mass balance estimates' from the two techniques. They highlight that camera network geometry and image baselines are important to consider, suggesting that a larger number or images with shorter baselines are preferable to a lower number of images with larger baselines (Piermattei, Carturan and Guarnieri, 2015). Rippin, Pomfret and King (2015) deployed a fixed-wing UAV above the Midtre Lovénbreen glacier in Svalbard, using SfM-MVS to create a Digital Elevation Model (DEM) and Orthomosaic (OM) with spatial resolutions of 10 cm and 5 cm respectively. They explain that one of the advantages of a technique that can yield such resolutions is the unique insight into the supraglacial hydrology of Midtre Lovénbreen, an often-overlooked area of glaciology (Rippin, Pomfret and King, 2015). The knowledge of supraglacial channelling afforded by SfM-MVS photogrammetry is crucially important in assessing ice surface roughness and thus, the energy balance. They go on to suggest that the effect of supraglacial drainage networks is most pronounced on glaciers where a lack of crevasses result in little water being directed internally (i.e. polythermal glaciers) and stress the importance of SfM-MVS (combined with UASs) of achieving similar insights across other areas of glaciology (Rippin, Pomfret and King, 2015).

Coastal geomorphology requires high-resolution topographic data for a range of purposes to further our understanding of coastal sediment budgets. A number of researchers have utilised SfM-MVS as a way of achieving this, for example Mancini et al. (2013) assessed the use of the technique by comparing the data with TLS across an area of dunes on the North Adriatic coast, Italy. They demonstrate that both techniques show good agreement with GNSS ground truth data, adding that the point density of the SfM-MVS data appeared to correlate with the images textural properties (Mancini *et al.*, 2013). Gienko and Terry (2014) utilised an SfM-MVS technique for modelling the shape of coastal boulders and calculating their respective volumes. They highlight the necessity to ensure homogeneous illumination across the survey area, and present a number of over-exposed examples where feature extraction failed and the SfM-MVS workflow fails (Gienko and Terry, 2014).

Gonçalves and Henriques (2015) state that over the last century, rising sea, winds and storms have severely degraded sectors of the European coastal zone, and that frequent surveys are essential for monitoring geomorphic changes. They explain that the most problematic areas are frequently rather small (< 1 km extension) and that costly large-scale aerial surveys are unnecessary (Gonçalves and Henriques, 2015). In these instances, small UAS and the SfM-MVS workflow present a desirable alternative to more established techniques. Finally, Brunier et al. (2016) tested the application of SfM-MVS on Montjoly beach, French Guiana, to assess the mass budget changes associated with a unique type of beach rotation mechanism. They explain that the technique is a good 'compromise between accuracy, data density and measurement reproducibility for morphometric surveys of geomorphologically dynamic landforms', achieving an accuracy of less

than 10 cm and commenting on the negative impact of the 'bowl effect' (Brunier *et al.*, 2016). The 'bowl effect' is a concave distortion that appears across a number of studies (Kaiser *et al.*, 2014; Ouédraogo *et al.*, 2014b; Brunier *et al.*, 2016; Haas *et al.*, 2016), and is an artefact of inherent lens distortions in un-calibrated cameras. It can mostly be removed by combining nadir imagery with oblique images and appropriate ground control distribution as demonstrated in the methodological development of this research (section 4.3.2).

Regularly monitoring hill-slopes using high spatial and temporal resolution provide significant insights into their behaviour and hazard potential however, by their very nature, hill-slope studies are often performed in environments where access, equipment and movement all present significant logistical challenges. Often terrestrial studies are restricted in scale because of this, whilst aerial studies are restricted by the requirement for high capital investment. These problems are largely overcome by using an SfM-MVS workflow, where the equipment is small and robust enough to be carried into the most challenging environments, cheap enough to be accessible for even the most modest of budgets, and rapid enough to cover large areas in a relatively small amount of time. Lucieer, Jong and Turner (2013) used SfM-MVS to map an active rotational slump in southern Tasmania, using 39 DGPS GCPs which resulted in a vertical and horizontal RMSE of 6.2 and 7.4 cm respectively. They explain that illumination of the scene presents a major source of uncertainty, alongside changes in vegetation height between consecutive time-series analysis (Lucieer, Jong and Turner, 2013). In order to quantify horizontal ground displacements, an image correlation algorithm (COSI-Corr) was used and the results matched well with visual interpretations (Lucieer, Jong and Turner, 2013).

The Super-Sauze slope failure, a clay-rich slow-moving slope movement in the French Alps, was monitored by Stumpf et al. (2014). They used the 3D cloud-to-cloud differencing algorithm, M3C2 (Lague, Brodu and Leroux, 2013) to quantify change between consecutive surveys, stating that it was a 'versatile and accurate tool for reliable detection of changes' (Stumpf *et al.*, 2014). The work utilised open-source solutions for implementing SfM-MVS and thus, further reduced the required capital to produce topographical datasets that are of comparable quality (albeit slightly lower in this case) to TLS or GPS (Stumpf *et al.*, 2014). Al-Rawabdeh et al. (2016) conducted research in an area of Jordan prone to rainfall-induced creep slope failures. Using a 3D point cloud created using SfM-MVS with a consumer-grade UAS and surface roughness, they present a novel workflow for automatically detecting slope failure scarps in 3D datasets hence reducing the need for hazardous ground data collection (Al-Rawabdeh *et al.*, 2016). They explain that future work would benefit from multi-temporal SfM-MVS analysis as well as the development of filtering techniques to remove point cloud features that are typically associated with erroneous measurements such as vegetation and shadowing (Al-Rawabdeh *et al.*, 2016).

A review of the geoscientific literature where SfM-MVS photogrammetry has been deployed has highlighted a number of key points; i) SfM-MVS is capable of producing topographical datasets of comparable quality to more established techniques such as TLS/ALS; ii) poor illumination and surface features such as vegetation decrease the quality of SfM-MVS-derived models; iii) the cost and logistical advantages of the SfM-MVS technique make it particularly well-suited to deployment in areas that would otherwise prove quite challenging; iv) model distortion as a result of inherent camera lens properties - common across all disciplines of photogrammetry – can be largely overcome by combining nadir and oblique imagery. The work reviewed here will be used to inform the development of an SfM-MVS workflow to be deployed across slopes in the European Alps for the purpose of 3D slope failure detection and characterisation.

2.9.4 Unmanned Aerial Systems

Unmanned Aerial Systems (UAS) (sometimes referred to as Unmanned Aerial Vehicles (UAV), Remotely Piloted Aircraft Systems (RPAS) and Drones) are remotely operated aerial vehicles that allow a range of sensors to be mounted. The use of UASs in recent years has increased massively in response to greater accessibility, lower costs and higher-grade sensors attached to off-the-shelf ready-to-fly (RTF) UAS packages. Most RTF UASs are accompanied by ground station software for pre-planning flights and semi-autonomous data collection which allows the user to program flying height, distance, overlap and speed amongst other parameters. In combination with a high-grade sensor, the ability to adjust flying parameters allows an unparalleled level of control over survey quality at a temporal resolution far superior to that of satellites and other more conventional aerial platforms (Turner, Lucieer and Wallace, 2014) and a spatial resolution of comparable quality to more established survey technologies such as TLS and ALS.

Successful application of UASs in geosciences are demonstrated by Lucieer, Jong and Turner (2013), who mapped slope failure displacements in South East Tasmania, Vasuki *et al.* (2014), who used photogrammetric data for analysing geological structures in rock-walls, Westoby *et al.* (2015a), in Antarctica for recovering grain-size information from UAS imagery, and Immerzeel *et al.* (2014), who used high-resolution UAS imagery from a fixed-wing setup for monitoring high-altitude glacial dynamics in the Himalayas. Other applications of UASs in the geosciences span several sub-disciplines including glaciology, geomorphology, geology, ecology and hydrology. A comprehensive review of the development and evolution of UASs for remote sensing studies is provided by Colomina and Molina (2014).

2.10 Change Detection

Measuring topographic change is of fundamental importance for the study of geomorphic processes, and is a powerful tool for discovering links within connected land systems and understanding rates, patterns and spatial behaviours of erosional processes (Cook, 2016). Time-series analysis of HRT datasets for understanding the magnitude, frequency and spatial distribution of change has been demonstrated by a huge number of studies (e.g. Otto *et al.* (2009), Schürch *et al.* (2011), Strunden *et al.* (2015b) and Westoby *et al.* (2015b) amongst others). The use of HRT data for change detection involves calculating the difference (i.e. the topographical change) between successive surveys and usually takes the form of a *DEM of Difference* (e.g. Javernick, Brasington and Caruso, 2014), *Cloud to Mesh* (e.g. Barnhart and Crosby, 2013) or *Cloud to Cloud* (e.g. Benjamin, Rosser and Brain, 2016) differencing approach, implemented in GIS or specialist 3D manipulation software and each with their advantages and disadvantages.

2.10.1 2D, 2.5D and 3D

2D representations of a 3D surface are often in a two-axis vector or raster grid format (*x* and *y*). 2.5D is the reduction of a 3D surface to a *quasi-3D* state whereby the surface elevation isn't an independent variable and there can only be a single elevation value (*z*) for any surface at any location. 3D surfaces are a true representation of 3D data where three completely independent dimensions (*x*, *y* and *z*) fully describe 3D geometry of objects.

Topographical datasets are traditionally stored and analysed as 2/2.5D grids of elevation (raster datasets) such as Digital Elevation Models (DEMs) and triangulated irregular networks (TINs) and as such, a large library of algorithms and programs that are dedicated to analysing these formats currently exist (Lague, 2014). The same is true for the quantification of change and volumetric calculations (Benjamin, Rosser and Brain, 2016). A number of studies have used 2D and 2.5D approaches to successfully estimate differences in time-series data such as; for monitoring coastal cliff erosion (e.g. Lim *et al.*, 2005) and surface elevation differences of alpine glaciers (e.g. Piermattei, Carturan and Guarnieri, 2015). However, all instruments that generate high-resolution topographical datasets natively (i.e. the raw data format from the instrument) create them in 3D point cloud format (e.g. ALS, TLS, SfM) and an interpolation of these datasets for 2/2.5D analysis will inevitably result in a loss of detail, limiting the accuracy of change detection on complex surfaces (Lague, 2014; Benjamin, Rosser and Brain, 2016). A gridded representation of 3D topographical data necessarily introduces bias on vertical and overhanging areas, and differencing successive datasets in this manner provides a single dimension of change, usually in the direction of the sensor position leading to issues with occlusion (Lague, Brodu and Leroux, 2013; Benjamin, Rosser and Brain, 2016).

Lague, Brodu and Leroux (2013) presented a multi-scale model to model cloud comparison algorithm, M3C2, that operates directly on point clouds without the need for 2/2.5D interpolation. The advantages of using such an approach is the preservation of the original geometry of the surface and true 3D displacement variables, as well as the use of surface roughness and point density to estimate the confidence of detected change (Lague, Brodu and Leroux, 2013). This technique has been widely adopted across many applications, including; rock-fall detection along cliffs in North Yorkshire, UK (Benjamin, Rosser and Brain, 2016), surface evolution of moraines in Antarctica (Westoby *et al.*, 2015b)and ice-cliff degradation in the Himalayas (Brun *et al.*, 2016). More information about the M3C2 algorithm is given in the methods section 4.5.1).

2.11 Summary

This chapter has sought to provide a general background to failures, approaches to its classification, consequences and the principle mechanisms that act as preconditioning, preparatory and triggering factors. It also provides an overview of the current state of knowledge in the effect of climate change on slope failure activity and the paraglacial response of landscapes to de-glaciation. Much research has already been conducted into the distribution of slope failures and the paraglacial response of mountain slopes however, our understanding remains poor in some areas. Such as; (i) the representation of small-magnitude slope failures in current inventories and distributions, and (ii) the 'immediate' paraglacial response of slopes above actively retreating/ thinning glaciers. A review of the current approaches to determining slope failure distributions from historical inventories demonstrates their reliance on empirical scaling relationships for determining V_L from A_L and highlights the importance of field data for calibrating such relationships.

It's also clear that recent developments in the acquisition and handling of high-resolution topographical data have heralded a new era in accessibility of good quality data. SfM-MVS photogrammetry combined with the latest technologies, such as multi-rotor and fixed-wing UASs, provides a unique opportunity to capture data in remote and difficult-to-access environments across spatial scales where previous research would have been limited. However, a number of issues are identified by several authors including; (i) erroneous surface reconstruction in areas of heavy shadowing, and (ii) non-linear model distortions resulting from inherent lens properties. Clearly, these must be addressed in any work that makes use of this technique. Innovative algorithms and the development of new software also allows this good-quality data to be utilised across a much broader spectrum of applications. It could be argued that the technology is far out-pacing the power available to process data, with processing times of multiple days for large datasets. As the power of computers continues to increase, so too will the ability to handle ever-larger topographical datasets at a fraction of the time traditionally associated with doing so.

This literature review establishes the research goals of this thesis outlined in section 1.3 and highlights key areas of focus for research in the future.

3 Study Areas

Far, far above, piercing the infinite sky,
Mont Blanc appears - still, snowy, and serene -
Its subject mountains their unearthly forms
Pile around it, ice and rock; broad vales between
Of frozen floods, unfathomable deeps,
Blue, as the overhanging heaven, that spread
And wind among the accumulated steeps.

Mont Blanc, Percy Bysshe Shelley, 1816

3.1 Introduction

This chapter will discuss relevant background information each of the field sites, as well as a general background to the Mont Blanc massif in general.

3.1.1 Site Selection

The data for this research were collected across slopes of the Mont Blanc Massif (MBM). An additional dataset was collected in the first season from the Rhône glacier, Switzerland, for the purpose of testing the methodological approach. In this chapter an introduction to the MBM and the Rhône glacier, their settings and general conditions are given. The principle study site, the MBM, was selected for a number of reasons;

1) The range is characterised by a variety of glacier types offering a unique opportunity to capture data above clean-ice and debris-covered glaciers, as well as extensive areas of de-glaciated terrain with contrasting properties.
2) It holds a central place in the history of alpinism and as such, is well documented through history. Past glacial extents are well constrained at a number of sites which is useful for determining whether slope failure distributions are driven by past glacial conditions.
3) The range attracts over six million visitors per annum with approximately one in five accessing the mountains. Such popularity has resulted in a well-established mountain infrastructure which permits access to areas of the range that would otherwise take a considerable amount of time and logistics to achieve.

3.2 Mont Blanc Massif (background)

The MBM (fig. 3.1) straddles the borders of France, Italy and Switzerland with an area of approximately 440 km^2 and roughly 40 % glacier coverage. To the NW, the range is bordered by the steep valley of Chamonix and is characterised by a combination of steep arêtes and jagged ridges. The slopes on the SW side of the range are more gentle with the majority of glaciers terminating at higher altitudes than those on the NW side. A combination of past and present glaciations, along with its topographical characteristics has resulted in a high rate of geomorphological activity within the range (Nussbaumer, Zumbühl and Steiner, 2007; Deline *et al.*, 2012; Bodin *et al.*, 2015). Between 1990 and 2011, the French mountain police register reported 291 rescue operations in the Goûter Couloir, along the standard route to the summit of Mont Blanc, which resulted in 74 deaths and 180 injuries. 30 % of the recorded accidents were caused by slope failure activities (Petzl, 2014).

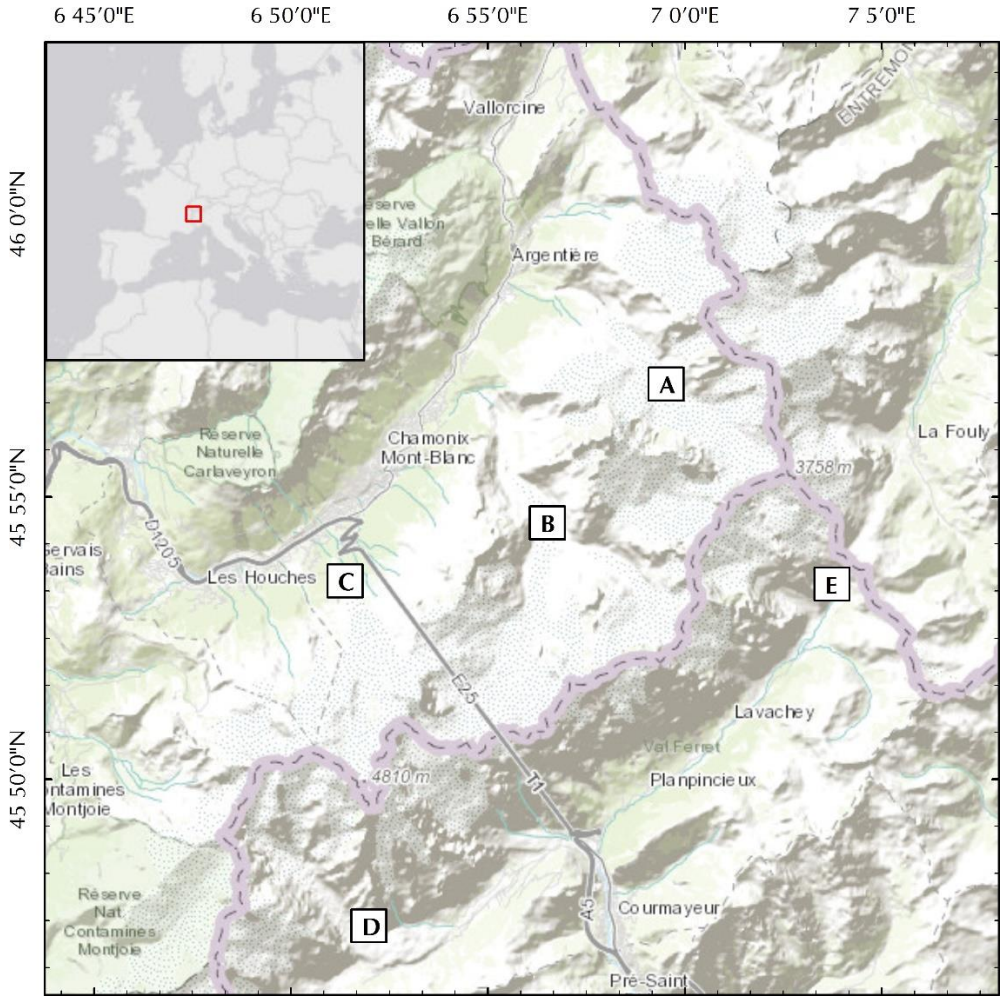

Figure 3.1: Study sites within the Mont Blanc massif; (A) Argentière; (B) Mer de Glace; (C) Bossons; (D) Miage; (E) Pre de Bard. Inset Top Left for location. (Credit: ESRI)

Home to the tallest mountain in Europe and some of the most spectacular peaks in the Alps, a widespread mountain-access infrastructure and a major international transport corridor; the MBM has rich history of alpinism and research. In 1741 two Englishmen, William Windham and Richard Pococke, discovered the Chamonix valley and explored the Mer de Glace. The publication of their discovery in European journals sparked an interest in many and in 1770, the first guest-house was opened (ChamonixNet, 2016). Its popularity as a tourist destination continued to grow exponentially throughout the 19th century and has resulted in a rich archive of tourist imagery, capturing the fluctuations of glaciers and evolving mountain slopes since the dawn of photography. Some researchers (e.g. Nussbaumer, Zumbühl and Steiner, 2007; Zumbühl, Steiner and Nussbaumer, 2008; Nussbaumer and Zumbühl, 2012) have made use of this archive of change to analyse fluctuations of the range's glaciers.

High mountain environments like the MBM are more sensitive to fluctuations in the climate than other environments (Haeberli and Beniston, 1998; Fischer *et al.*, 2013). Since the termination of the Little Ice Age (LIA), the mass balance of the MBM glaciers (principally controlled by the interplay of winter precipitation and summer melt) has resulted in an overall retreat, with a 43 % loss in glacier area on the Italian side between 1852 and 2010, and 24 % loss on the Swiss side between 1850-2000 (Deline *et al.*, 2012). This retreat was interrupted by a number of short advances as a result of an increase in winter precipitation compared with the twentieth century average however, over the last four decades the rate of retreat has accelerated (Deline *et al.*, 2012). Although low in frequency compared to other mountain ranges such as the Andes and Himalayas, there are a number of debris-covered glaciers in the MBM with debris supplied from slope failure activity (e.g. Miage and Brenva on the Italian side) and erosion of lateral moraines (e.g. Mer de Glace on the French side) (Deline *et al.*, 2012). The presence of debris on a glacier greatly affects its dynamic response to extrinsic factors and termini of debris-covered glaciers are observed to retreat much slower than those that are clean-ice. There have been no recorded large slope failure events in the MBM which have been triggered by retreating glaciers however, Vivian (1975, in French) reports a number of small rockfalls in the proglacial margins of the Mer de Glace and Argentière following their recent retreat (Deline *et al.*, 2012).

Variations in subsurface ice through degradation of permafrost can have a strong impact on the stability of steep rockwalls (Haeberli and Beniston, 1998; Fischer *et al.*, 2013). The European Alps are south of the Northern hemisphere continuous permafrost zone, but permafrost persists within high-altitude rockwalls where an increase in rockfall activity has been attributed to increases in global mean temperatures (Ravanel and Deline, 2011). An ongoing project, PERMAdataROC, has collected annual and seasonal time-series TLS data, along with in-situ observations from mountain guides, hut keepers and researchers across several rockwalls within the MBM since 2005 (Deline *et*

al., 2008). Throughout 2007 and 2008, the majority of observed rockfalls initiated in zones of warm permafrost (0 to -5˚C).

3.2.1 Geological Setting

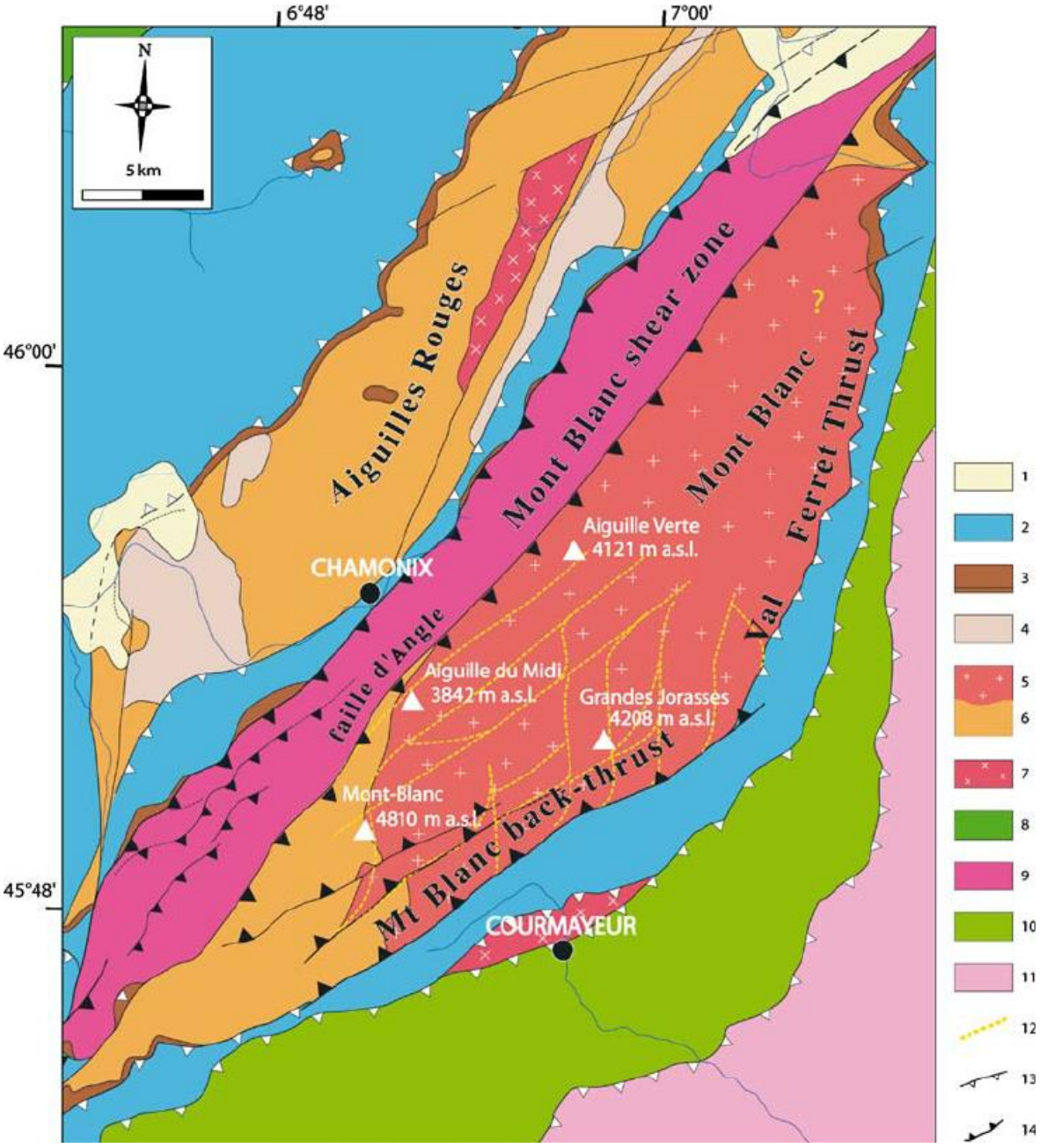

Figure 3.2: Geological map of the Mont Blanc area (after Leloup et al. 2005 and Rolland et al. 2003, modified by Ravanel et al., 2010). 1 Quaternary, 2 Dauphinois and Helvetic Mesozoic sediments, 3 Triassic, 4 carboniferous, 5 Mont Blanc granite, 6 Variscan metamorphic rocks (gneiss), 7 undifferentiated granites, 8 Penninic klippe, 9 Mont Blanc shear zone (gneiss), 10 Versoyen + Valais, 11 internal zones, 12 mapped shear zone network, 13 thrust, 14 late reverse fault.

The MBM is made up of paragneisses, orthogneisses, migmatites and granites (Rolland *et al.*, 2003). The range forms part of a series of basement windows exposing poly-metamorphic Late Proterozoic to Early Palaeozoic gneisses intruded by Late Variscan granitic plutons (von Raumer and Bussy, 2004; Egli and Mancktelow, 2013) (fig. 3.2). In the Western Alps, following the Alpine arc and referred to as external crystalline massifs (ECM), these windows expose European crustal rocks covered by Late Palaeozoic to Palaeogene sediments with present day uplift rates of approximately 1 mm/year (Glotzbach *et al.*, 2008; Egli and Mancktelow, 2013). The MBM is comprised of crystalline rocks (granite, gneiss and schists) which are of Variscan age and part of the Hercynian system (Imhof, 2010). It is mainly a granitic batholith (fig. 3.2) and the summit (Mont Blanc) is on the contact of micaschists and gneiss units. Ravanel *et al.* (2010) explains that the MBM granite has a very coarse-grained texture. Matasci *et al.* (2014) uses Terrestrial Laser Scanning and high-resolution imagery to characterise the scars of rockfalls across the West face of the Dru (a prominent peak above the Mer de Glace in the MBM) and identifies that rockfall activity is strongly linked to the presence of sub-horizontal discontinuities across the rockface that leads to the propagation of steep wedges (section 2.8). The combination of past and present glaciations, steep, fractured rock walls, and a strong relative relief results in a high magnitude of geomorphological activity (Ravanel *et al.*, 2010).

3.3 Field Sites

At the MBM, five field sites were selected whilst a further test site for methodological development was established at the Rhône glacier, Switzerland (fig. 3.3). These are each introduced with a brief description below.

3.3.1 Glacier d'Argentière, France

The Glacier d'Argentière (fig. 3.3 a) is roughly 9 km long, and flows from an altitude of 3400 m a.s.l. to its tongue at an altitude of 1600 m a.s.l. (Helmstetter *et al.*, 2015). Apart from the tongue, the glacier is free from debris and has an ice-fall in it lower section between 2,000 and 2,400 m a.s.l. (Vincent *et al.*, 2009). Glaciological observations have occurred at the glacier since the beginning of the twentieth century, with interest from a hydroelectric power company facilitating continuous measurements of glacier fluctuations since the 1970s (Vincent *et al.*, 2009). This long-term analysis highlighted that the glacier reacts very quickly to changes in the surface mass-balance (SMB), with a maximum of 3 years between changes in the SMB and consequent ice flux (Vincent *et al.*, 2009). Its terminus sits atop a steep bedrock ridge with a separated body of ice at the base. This ice is stagnant and supplied through collapsing seracs from the main body of the glacier.

Figure 3.3: Photographs of each of the field sites; (a) Argentière; (b) Mer de Glace; (c) Aiguille du Midi; (d) Bossons; (e) Bionnassay; (f) Miage; (g) Pre de Bard and; (h) Rhone.

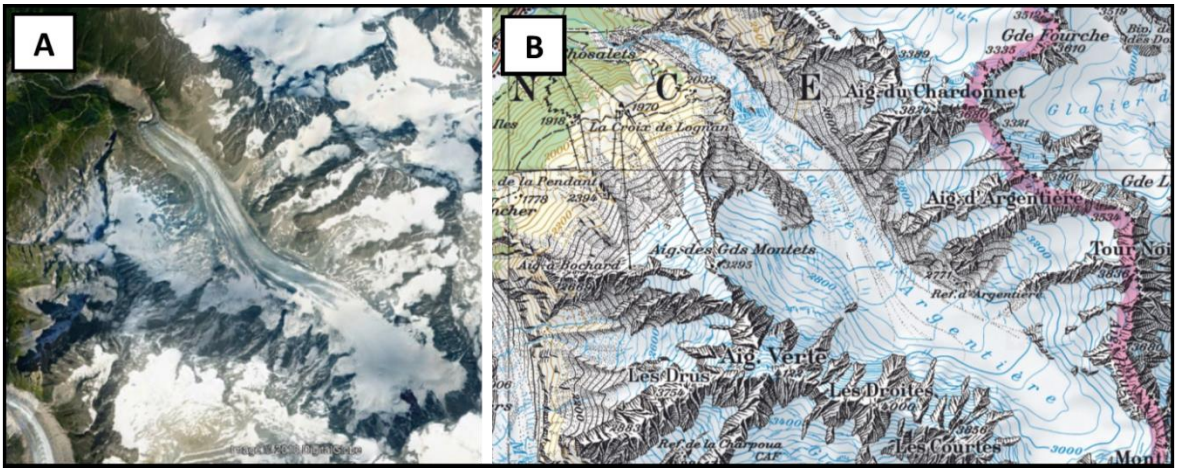

Figure 3.4: Overview imagery of the Glacier d'Argentière (France) field site; (A) satellite imagery and; (B) topographic map. (Credit: *A – © 2018 DigitalGlobe; B - © SwissTopo*)

3.3.2 Mer de Glace, France

The Mer de Glace (fig. 3.3 b) is the largest glacier in the French Alps with an area of approximately 30 km^2 (Zumbühl, Steiner and Nussbaumer, 2008) and a maximum elevation of roughly 4,300 m a.s.l. (Berthier and Vincent, 2012). In the MBM, the glacier is one of the most popular tourist attractions, with access made possible via a railway station at Montenvers and cable-car access down to the ice-surface for an ice-cave attraction during the summer. Access to the glacier for alpinism is made possible via a series of ladders attached to the NE-facing slope a little way along from the train station. As a result of this popularity, the Mer de Glace is one of the most photographed glaciers in the World, providing a rich and unique archive of imagery which has been used by researcher to examine 19th century glacial fluctuations (Zumbühl, Steiner and Nussbaumer, 2008). Records extending to 1878 indicate an overall retreat of 1.27 km (Le Roy *et al.*, 2015).

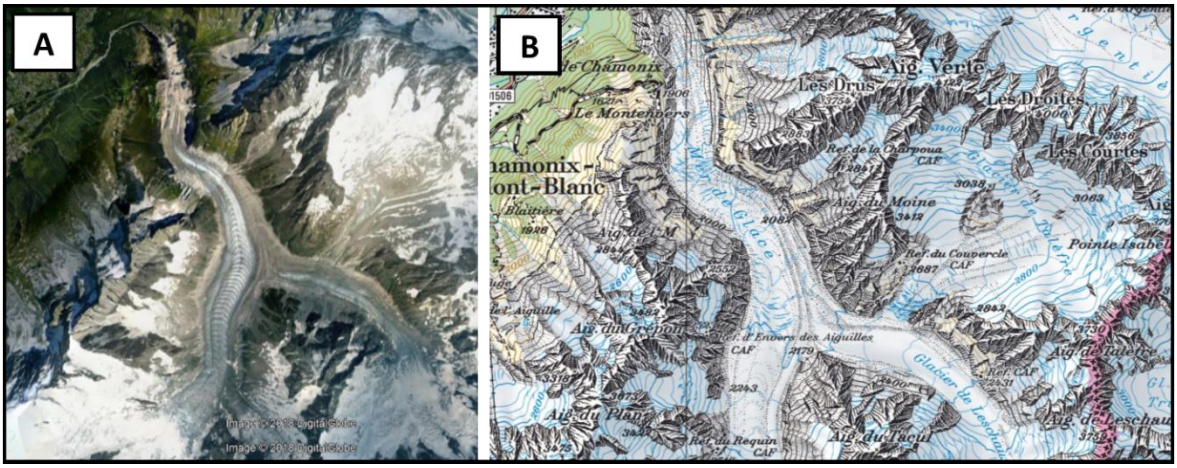

Figure 3.5: Overview imagery of the Mer de Glace (France) field site; (A) satellite imagery and; (B) topographic map. (Credit: A – © 2018 DigitalGlobe; B - © SwissTopo)

3.3.3 Glacier de Bossons, France

The Glacier de Bossons (fig. 3.3 d) lies on the N side of Mont Blanc and covers the peak before extending down to an altitude of approximately 1,450 m a.s.l. The glacier is characterised by a series of crevasses and seracs and flows down an exceptionally steep slope (~28˚) at a rate of more than 1 m/day in the Summer (Godon *et al.*, 2013). It has retreated more than 600 m since 1981 (Nussbaumer and Zumbühl, 2012), and its pro-glacial zone is characterised by an alluvial plain approximately 1 km from the terminus. This is flanked by large LIA moraines preceding a steep bedrock slope leading to the terminus, which is bordered by bedrock slopes with loose debris at the base. Between 1968 and 1975, the Bossons advanced over a distance of approximately 110 m and this advance was accompanied by extensive net aggradation (c. 1300 m3 yr-1) and a steepening of the whole valley train as maximum amounts of coarse debris accumulated on the proximal slope (Maizels, 1979, 1983). The surveyed slope falls within the Bossons (and Mont Blanc) watershed which is made up of several lithologies, but dominantly the homogeneous ~303 Ma Mont Blanc calc-alkaline granite and the older poly-metamorphic basement (von Raumer and Bussy, 2004; Godon *et al.*, 2013). The slope is highly jointed with a dominant near-vertical structure amongst several other discreet planes.

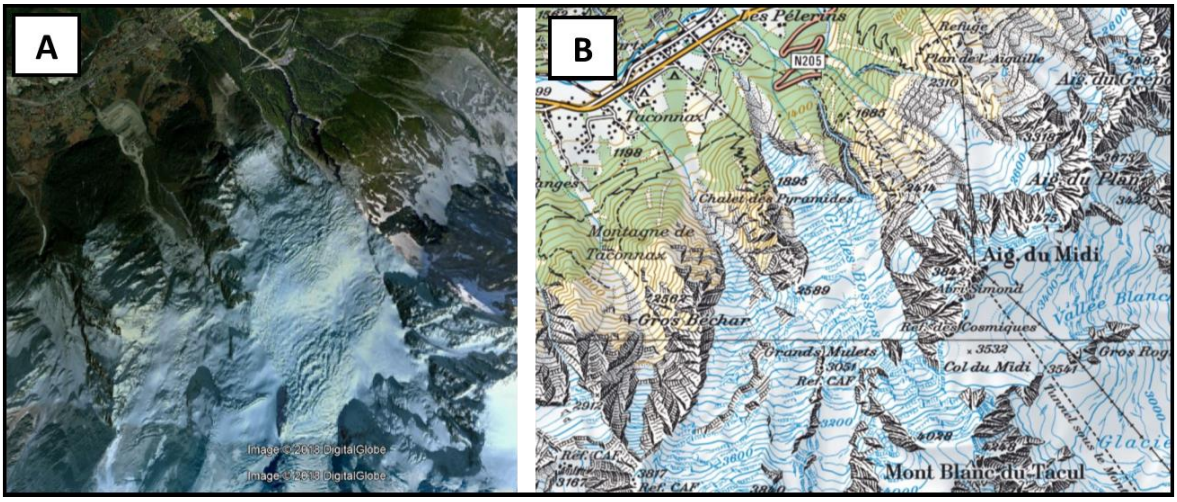

Figure 3.6: Overview imagery of the Glacier de Bossons (France) field site; (A) satellite imagery and; (B) topographic map. (Credit: A – © 2018 DigitalGlobe; B - © SwissTopo)

3.3.4 Ghiacciaio del Miage, Italy

The Ghiacciaio del Miage (fig. 3.3 f) is the third largest Italian glacier and flows from 3,900 m a.s.l. on the SE side of the MBM (Deline, 2005b). It has a surface area of approximately 11 km^2, with roughly 4 km^2 of supra-glacial debris cover (Pelfini *et al.*, 2007), which formed at the end of the 19th century through continuous rockfall activity from the adjacent slopes (Deline, 2005a; Leonelli and Pelfini, 2013). Its terminus is one of the lowest in the Alps at 1,730 m a.s.l. (Conforti and Deline, 2005) with the ice-contact Miage lake to the right of the glacier near its terminus. The lake has received considerable attention from a number of studies and in 1996, a large block of ice detached from the glacier and fell into the lake causing a wave which resulted in a number of serious injuries to tourists (Tinti, Maramai and Cerutti, 1999). The glacier is flanked by large lateral moraines and steep rock slopes for its entire length.

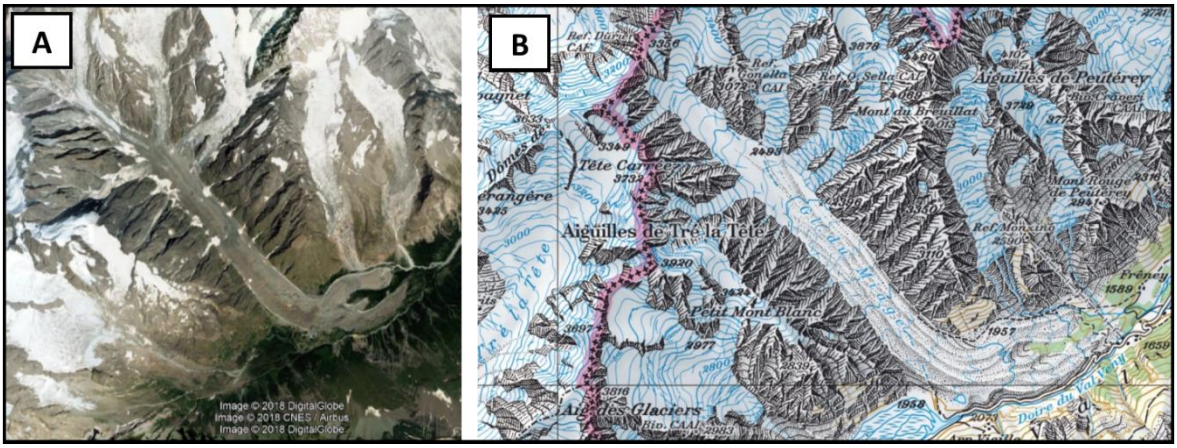

Figure 3.7: Overview imagery of the Ghiacciaio del Miage (Italy) field site; (A) satellite imagery and; (B) topographic map. (Credit: A – © 2018 DigitalGlobe, © 2018 CNES/Airbus; B - © SwissTopo)

3.3.5 Pre de Bard, Italy

The Pre de Bard glacier (fig. 3.3 g) has received relatively little research attention when compared with other areas in the MBM. It lies at the head of Val Ferret on the Italian side of the range with a surface area of roughly 3.1 km^2 and length of 3.4 km. The glacier currently terminates at an elevation of approximately 2,120 m a.s.l. The right side of the glacier has a level of debris from rockfall activity across the adjacent slopes of the Aiguilles Rouges de Triolet (Imhof, 2010). In the proglacial zone, a melt-water channel is flanked by large LIA moraines which clearly indicate the previous extent of the glacier. The survey was performed across a NE-facing sediment-mantled slope in the proglacial zone that has been ice-free for several decades, as shown in figure 3.9.

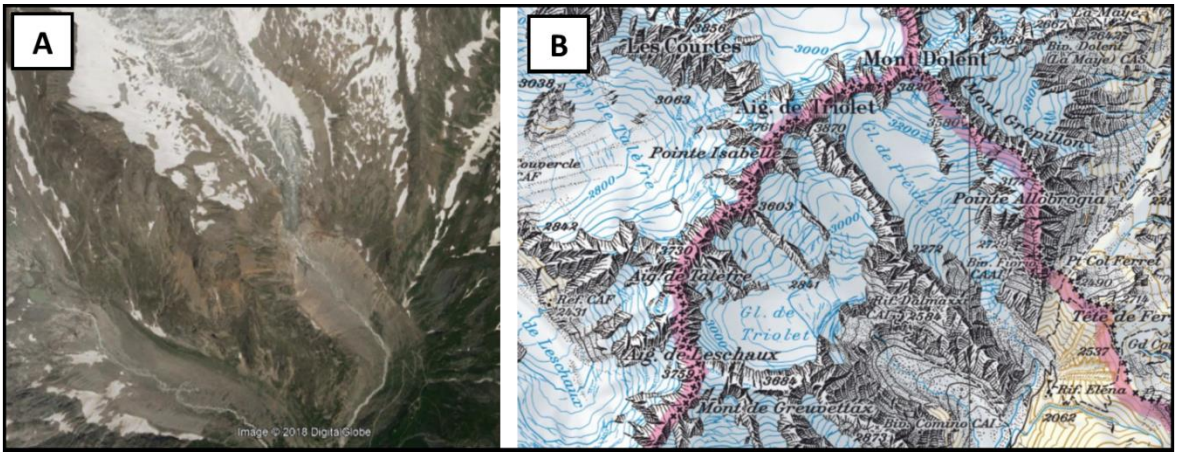

Figure 3.8: Overview imagery of the Ghiacciaio del Pre de Bard (Italy) field site; (A) satellite imagery and; (B) topographic map. (Credit: A – © 2018 DigitalGlobe; B - © SwissTopo)

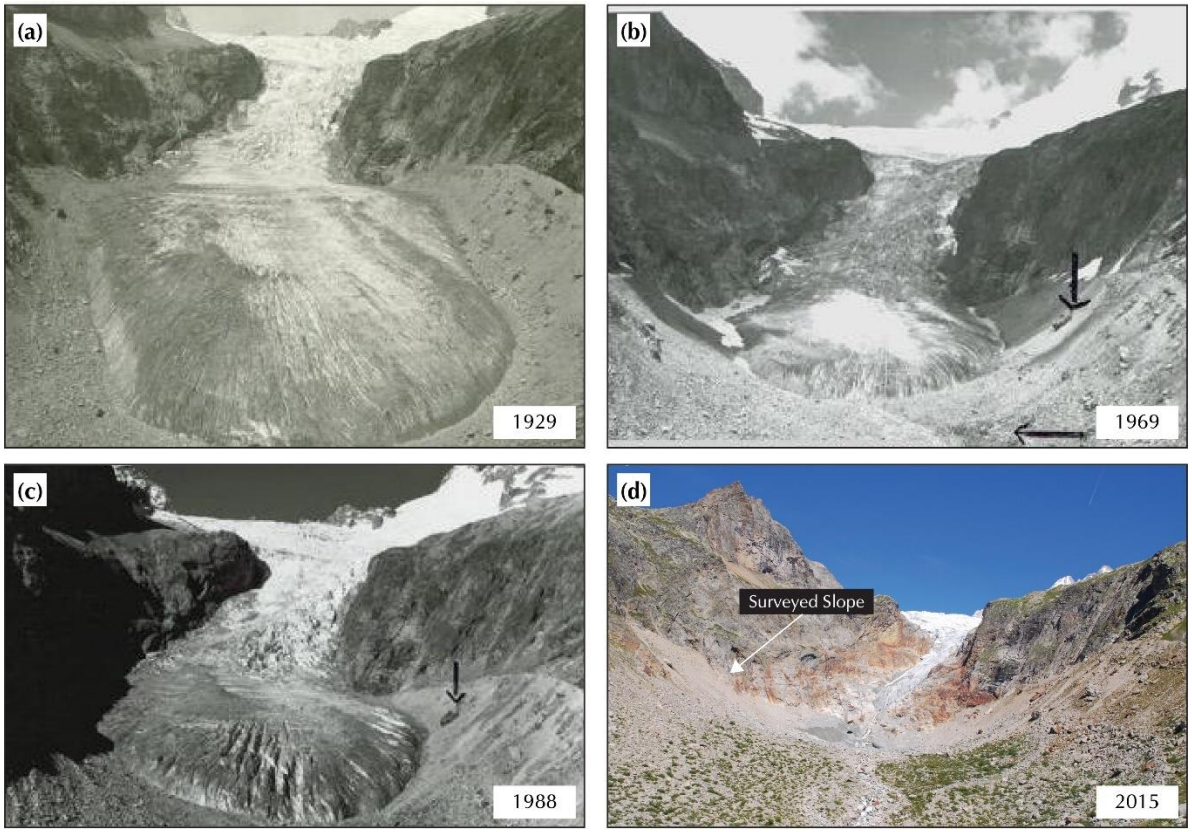

Figure 3.9: Photographs documenting the extent and retreat of the Pre de Bard glacier in 1929 (a), 1969 (b), 1988 (c) and 2015 (d). Surveyed slope indicated in (d). (Historic imagery credit: http://foto.ilsole24ore.com).

3.3.6 Rhônegletscher, Switzerland (Test Site)

The Rhône glacier (fig. 3.3 h) lies in the Alps of south-central Switzerland, flowing southwards from the slopes of the Dammastock Peak (fig. 3.10}) (Allen, 2006). It was the largest glacier in the Swiss Alps during the last glacial maximum (LGM) and remains one of the largest today at approximately 9 km in length with a surface area of roughly 17 km^2. During the LIA, the terminus was about 600 m lower and 3 km further down-valley than its current position (Goehring *et al.*, 2012), where it sits behind a terminus lake at the head of a bedrock riegel (transverse pro-glacial bedrock ridge). This site was chosen to conduct a number of methodological tests in the first field season as it is easily accessible via a tourist path which leads to the front of the glacier and an ice-cave attraction, from which the glacier can also be accessed.

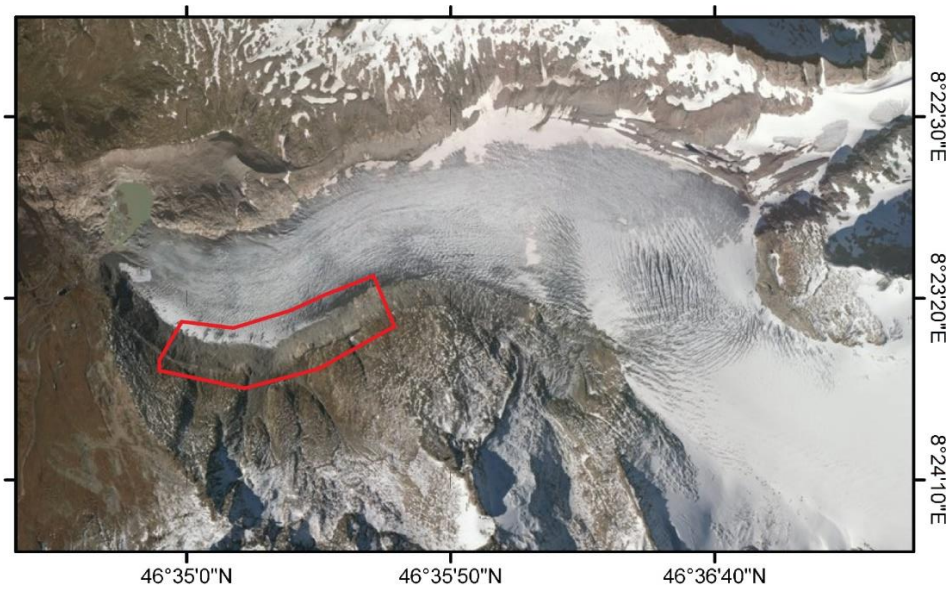

Figure 3.10 Rhône Glacier, Switzerland. The survey was conducted along the lateral moraine which can be seen on the left of the glacier (flow-direction) at the lower meander. For context, the white sheeting used by Swiss authorities to reduce summer melting above the ice cave can be seen on the left-side of the terminus. The lake in front of the glacier is bound by a steep bedrock riegel. Red box denotes area of surveyed slope. (Credit: ESRI)

3.4 Summary

Data from the six sites introduced here will be presented in this thesis. Each site was surveyed on a different scale; for example, the Mer de Glace and Argentière surveys were conducted across the whole valley, encompassing reworked material of the lateral moraines and the rock-walls above them, whereas the Miage and Pre de Bard surveys were conducted on smaller scales across lateral moraines above the glacier and in the pro-glacial zone respectively. This variation in scale and type is the first of its kind and allows a much better understanding of range-scale failure distributions; with smaller-scale surveys complimenting the larger-scales and vice versa.

4 Methods

4.1 Introduction

This chapter will introduce the methods and outline the workflow created as a result of methodological development.

4.1.1 Objectives

The objectives of this chapter are to;

1) Present the workflow for taking photographs on Alpine slopes and using the Structure from Motion – Multi-View Stereo (SfM-MVS) photogrammetric technique to create accurate 3D models;
2) Outline the steps taken to understand sources of error during the creation of 3D models using SfM-MVS and the approach taken to ensure these do not propagate through to the final results through the effective use of thresholding;
3) Explain how the multi-scale point cloud comparison algorithm, M3C2, was used to detect areas of significant change between consecutive surveys and calculate volume using the 3D data output;
4) Outline the statistical approach for examining the size distribution of detected slope failures and determining its significance;
5) Describe how GIS is used to analyse the spatial distribution of slope failures in order to identify any patterns across the study area.
6) Outline the algorithms used to identify and characterise the structure of the Bossons rock-slope for the analysis of rock mass strength.
7) Present example of each of the models created at the Mont Blanc massif, and outline the Level Of Detection (LOD) thresholds at each in preparation for the presentation of results in the following chapter.

4.2 Field Methodology

4.2.1 Image Collection

There are a number of considerations when acquiring images for SfM-MVS but it is most important to capture a static area of interest from as many viewpoints as possible, with each point on the surface appearing in at least two images, though ideally more. The quantity of images is proportional to the size of the area being surveyed and can range from tens to hundreds though a large number of high-quality images may result in larger processing times. Sharp changes in the

levels of illumination and heavy shadowing should be avoided, though this isn't necessarily possible when operating in challenging environments within time constraints and as such ensuring a consistent level of lighting and minimising the interval between image capture is most ideal. Patches of featureless cover such as areas of clean snow and ice should be avoided as key point identification will struggle and result in lower point densities with poorer localisation accuracies.

In this study, a combination of terrestrial, UAV and helicopter platforms were used for acquiring imagery, following the considerations above. The spatial coverage of imagery and the time taken to collect enough imagery with sufficient overlap to satisfy the desired spatial extent differed greatly depending on a number of factors. As well as this, the quality of imagery in terms of pixel ground coverage was also considerably different depending on the distance from the slope and the angle of incidence for each image. In the context of a mountain landscape, images captured from a terrestrial perspective (i.e. from the valley floor or glacier surface) were at a steeper angle with each pixel in the upper area of the image covering a significantly greater area than those at the lower part of the image. Increasing the height of the camera for capturing images enabled a more consistent level of pixel ground resolution across the whole image and this was achieved using an UAV and in the case of two sites, a helicopter. Model quality is also determined by the quality of the sensor and data collection, in that a higher resolution camera or images captured in closer proximity to the slope can achieve a better ground sampling distance (GSD) (see fig. 4.1), from which it is possible to extract a greater level of detail. The time taken to complete a survey from a terrestrial perspective was significantly greater than the UAV and exponentially greater than the helicopter but allowed a much greater level of overlap/side-lap between consecutive images and in some cases, a shorter distance between the camera and the surveyed slope. Spatially, the helicopter platform permitted the greatest distance to be covered in the shortest period of time but cannot be flown too close to the slope and flies at much greater speeds than can be achieved on-foot and with a UAV. The helicopter was used for the full-valley surveys of the Mer de Glace and Argentière glaciers. Consequently, the amount of side-lap between consecutive images is significantly less and the pixel ground coverage is significantly greater. However, the ability to survey an entire valley within a matter of minutes at a resolution suitable enough to detect and quantify medium- to large-scale slope failures offers several advantages, including a greater understanding of their spatial distribution and magnitude-frequencies at valley-scale. The UAV was used for smaller-scale surveys where the elevated sensor position was preferable to a ground-based approach and weather permitted, whilst terrestrial imagery was used at small sites where moraines or rock-walls were not tall enough to pose a significant issue with pixel ground coverage and when weather conditions prevented the deployment of a UAV.

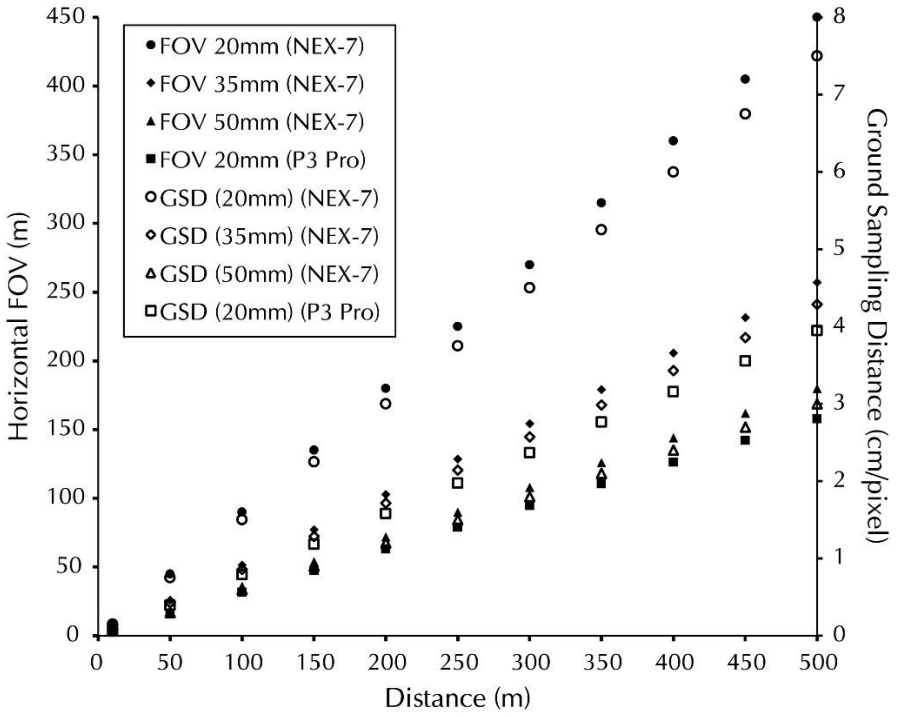

Figure 4.1: Graph showing how distance away from a surface influences the horizontal field-of-view and ground sampling distance from the two sensors used in this study; the Sony NEX-7 and the DJI Phantom 3 Professional UAV. Variable focal lengths are shown for the NEX-7 sensor.

Two UAVs were used; in the first season a DJI S800 Evo with a Sony NEX-7 camera attached (fig. 4.2 (b)), and in the second season a DJI Phantom 3 Professional (P3P) (fig. 4.3 (C)) which has an integrated stabilised camera system with a Sony sensor. The Sony NEX-7 was also the camera used for terrestrial surveys. The S800 is a six-rotor heavy-lifting aerial platform designed for professional aerial imaging, capable of lifting a variety of sensors. A 3-axis stabilised Zenmuse gimbal was used to carry the NEX-7 which is a 24 mega-pixel compact SLR, combined with a fixed 20 mm lens. The P3P is a consumer-grade quadcopter with an integrated 3-axis stabilised 12 mega-pixel camera with a Sony CCD sensor. The image quality from the NEX-7 is superior to that of the P3P however, in terms of practicality, the smaller quad-rotor P3P is much better suited to operating in mountain environments than the six-rotor S800 which is more of a logistical challenge to carry great distances to study sites. No significant difference in the quality of models generated from different sensors was observed, other than point density following the densification of point clouds however for change detection, point clouds were sub-sampled to standard distances to ensure comparability between consecutive datasets.

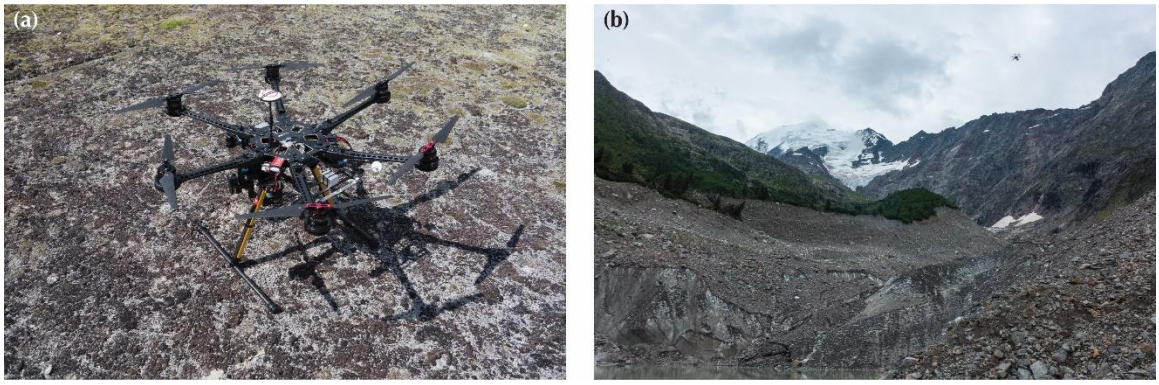

Figure 4.2: Field photos showing the DJI S800 Evo UAS on the ground (a) and whilst in operation (b) at the Bionnassay field site where access to glacier was restricted by near-vertical slopes and loose debris.

4.2.2 Ground Control

A network comprising of a number of Ground Control Points (GCPs) across the surveyed area is required to scale and georeference the models. Clearly visible GCPs with an obvious centre-point, that can be easily identified in the acquired images are most ideal and should be well distributed across the slope. The methodological approach for establishing a ground control network changed after the first field season for a number of reasons. In the first field season a series of scaled targets were placed across the scene and the centre-point of each was registered using a DGPS (fig. 4.3 (B)). This approach encountered two main issues; (1) DGPS signal is quite weak when operating within confined glacial valleys resulting in poor accuracy, and (2) deploying targets across steep, unstable mountain slopes is difficult and often restricted to the more accessible lower areas of the slope. This meant that the network was poorly distributed across the surveyed area, which resulted in a poorer alignment quality at higher (inaccessible) elevations once returning from the field. To correct for this in the second field season, ground control was re-collected using a reflectorless total station (fig. 4.3 (A)) and distinctive bedrock features as targets. This allowed a much greater distribution of ground control across inaccessible sections of the slope, and all models were re-georeferenced with this new ground control data following the second field season. Others have explored the use of 'direct-referencing'; georeferencing in the absence of GCPs, relying on known camera positions from RTK-GPS measurements and an inertial measurement unit (IMU) (Rizaldy and Firdaus, 2012; Turner, Lucieer and Wallace, 2014; Carbonneau and Dietrich, 2016). This presents significant advantages over using GCPs in areas where ground-access may be difficult for GCP placement and measurement, reduces costs associated with high-end survey equipment such as total station and DGPS and points to the direction of future developments of the SfM-MVS technique.

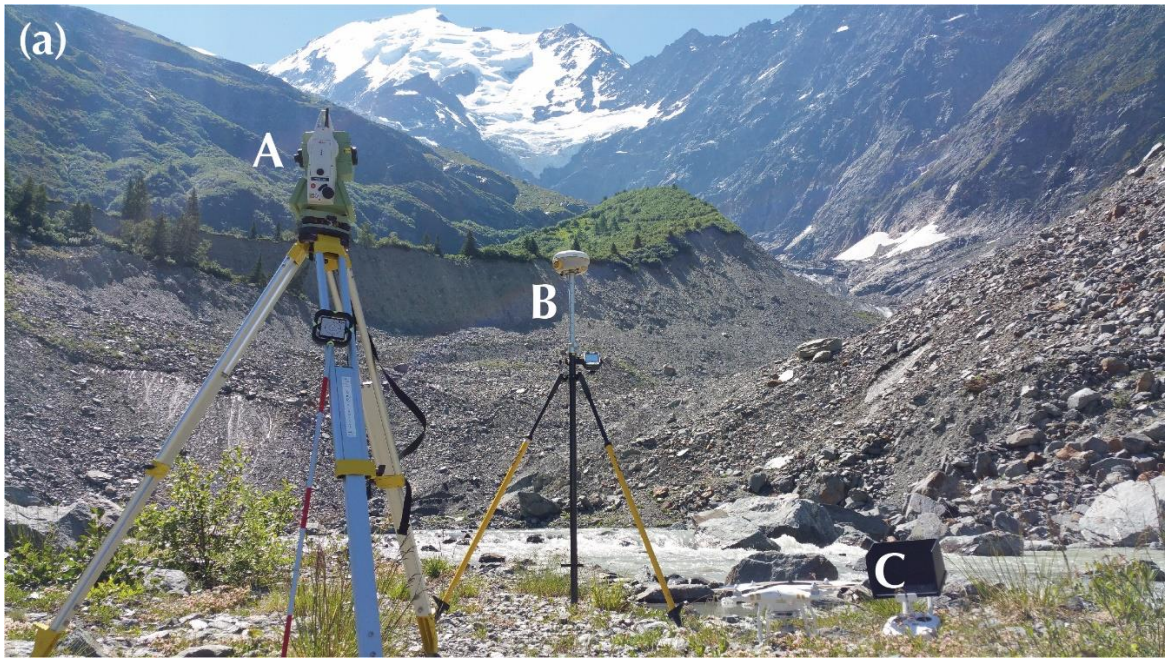

Figure 4.3: Field photograph of the Leica reflectorless total station (A), Trimble DGPS rover unit (B) and DJI Phantom 3 Professional (C) in front of the terminus of Bionnassay glacier, Mont Blanc massif. Mont Blanc can be seen in the background.

4.3 Structure-from-Motion Multi-View Stereo (SfM-MVS)

Thorough descriptions and reviews of the SfM-MVS workflow and its application in geosciences are given by Westoby *et al.* (2012), Smith, Carrivick and Quincey, (2015) and Eltner *et al.* (2016), whilst a detailed overview is given in this section, and the processing workflow is summarised in the next section. This workflow is typical of all software packages and open-source code that implement SfM-MVS, and though the terminology and operating algorithms may differ slightly at each stage, there exists a clear commonality (Smith, Carrivick and Quincey, 2015). In this research the commercial software, Agisoft Photoscan Professional (v. 1.2.6) is used for the production of models. The workflow is also implemented in a number of freely-available packages such as VisualSfM (Wu, 2015) and SFMToolkit (Astre, 2015). Other commercial packages are also available, such as Pix4D (Pix4D, 2015) and 123D Catch (Autodesk, 2015). These generally offer a more user-friendly (often black-box) interface, implementing similar approaches. (Remondino *et al.*, 2014), conduct a comprehensive analysis of the quality of SfM models derived from four different packages (two open-source and two commercial) identifying a number of advantages and disadvantages of each package. However, in most cases these are simply a function of user-input parameter selections (Remondino *et al.*, 2014) highlighting the necessity for due care and consideration throughout.

At the first stage, a number of features (or 'keypoints') are identified across each of the images in the set. These keypoints are required to be invariant to changes in scale and orientation.

The *Scale Invariant Feature Transform* (SIFT) object recognition system (Lowe, 1999, 2004) is commonly used within most SfM-MVS workflows at this stage. For each keypoint, SIFT uses 128 vectors as a descriptor and the next stage is the identification of corresponding keypoints across multiple images. A threshold to identify matches is applied and to reduce computational intensity, modified *k*-dimensional trees are used to partition the data and eliminate large search spaces (Smith, Carrivick and Quincey, 2015). One example is the *Approximate Nearest Neighbour* (ANN) solution, which increases the efficiency of the workflow by searching only the top-ranked match candidates (Arya *et al.*, 1998; Smith, Carrivick and Quincey, 2015). At this point, a filter is applied across the corresponding keypoints to identify and remove erroneous matches before the SfM procedure. SfM uses a bundle adjustment approach to estimate the 3D geometry of the scene and the extrinsic and intrinsic camera conditions resulting in a jointly optimal 3D structure and camera parameters (Smith, Carrivick and Quincey, 2015). One such open-source example is the *Bundler* bundle adjustment system (Snavely, 2008; Snavely, Seitz and Szeliski, 2008). Following SfM, a sparse, arbitrarily-scaled 3D point cloud is generated, as well as the camera positions and pose information.

At this stage, the model can be scaled and georeferenced using a minimum of three GCPs and a seven-parameter linear similarity transformation (i.e. three global translation parameters, three rotational parameters and one scaling parameter). Previous work has shown that much larger number than three is ideal, and they should be evenly distributed across the whole extent of scene (James and Robson, 2012; Smith, Carrivick and Quincey, 2015). Having established the camera positions and parameters, the next stage is to recover a denser point cloud which is achieved using an MVS algorithm. Following optimisation, and with the SfM points as a sparse proxy for dense MVS reconstruction, the algorithm recovers 3D geometric information by estimating a depth value at pixel level in each image and merges the resulting 3D points into a single model (Agarwal *et al.*, 2011). The *Patch-based Multi-view Stereo* (PMVS2) algorithm (Furukawa and Ponce, 2007) is one example of an MVS technique, though is memory-intensive and limited by RAM availability as all the images to be matched are processed simultaneously (James and Robson, 2012). A pre-processing step, the *Clustering View for Multi-view Stereo* (CMVS) algorithm (Furukawa *et al.*, 2010) is used to group images based on their respective camera orientations and surface points (identified during the SfM bundle adjustment), which are then sequentially processed by PMVS2 (James and Robson, 2012).

4.3.1 SfM-MVS Processing Workflow

Data processing was performed in the commercially available software package, Agisoft Photoscan (AP) v1.2 (AgiSoft LLC, 2016), on processing computers with 64 GB of RAM and dedicated

GPUs. Figure 4.4 is provided as an example of the AP interface at each stage and a general introduction to the operating procedures. Given its commercial nature, little information is available about the algorithms operating at each stage though it follows a standard workflow for SfM-MVS and as such, it can be assumed that the background algorithms are of a similar nature. In response to a request for further information, AP state that the algorithms are based in part on published work however, they are implemented into the software from scratch and are "thoroughly optimised" for faster processing capabilities however, favouring approaches with higher accuracy over faster approaches (Semyonov, 2014). Processing speeds were proportional to the size of the image set being processed and ranged from hours to days for small to large surveys respectively using high quality settings which are summarised in table 4.1.

Table 4.1: Settings applied to AP during the SfM and MVS processing stages for all datasets.

Structure from Motion		Multi-View Stereo	
Accuracy:	High	Quality:	High
Key Point Limit:	250,000	Depth Filtering:	Aggressive
Tie Point Limit:	25,000		

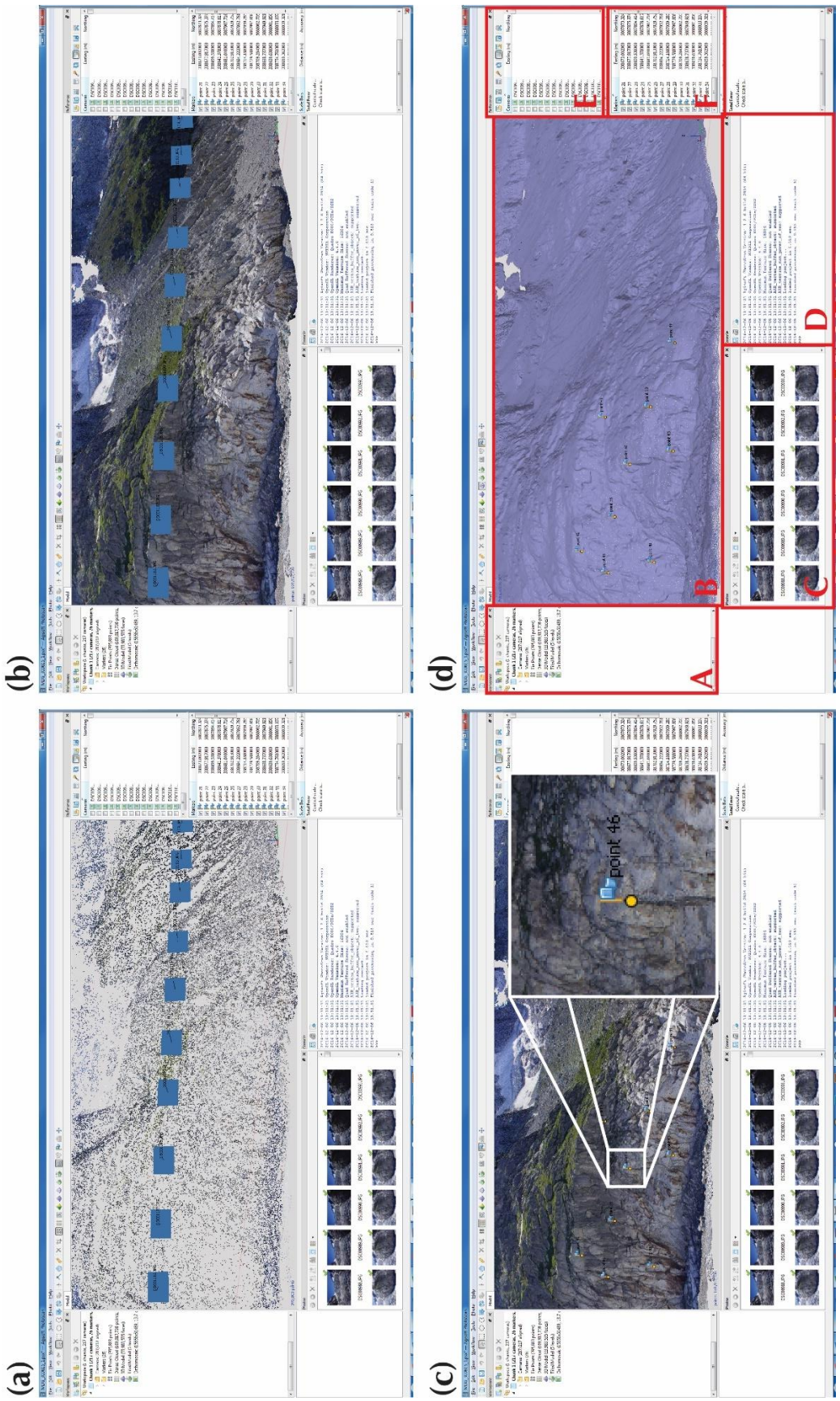

Figure 4.4: Screenshots of the Agisoft Photoscan Professional interface at each stage of the workflow; (a) initial camera alignment and sparse alignment point cloud, (b) generation of the dense point cloud and (c) georeferencing using ground control points. (d) Overview of the interface; (A) the workspace, an area where the current models are listed, (B) model view, interactive 3D model view with full user control, (C) list of input photographs and their associated calibration information, (D) console showing progress of processing at each stage, (E) reference pane for images that have GPS coordinates associated with them (e.g. images from the P3P) and (F) list of ground control points and their measured coordinates for georeferencing the model.

The workflow that was used for the generation, georeferencing and alignment of 3D models using SfM-MVS photogrammetry in this study is shown in a flow-chart in figure 4.5. Further information about the processes and algorithms operating at each stage is given in the previous section. The purple boxes are typical of an SfM-MVS workflow, though the terminology and specifics do vary from one software package to another. In this study, Agisoft Photoscan Professional was used.

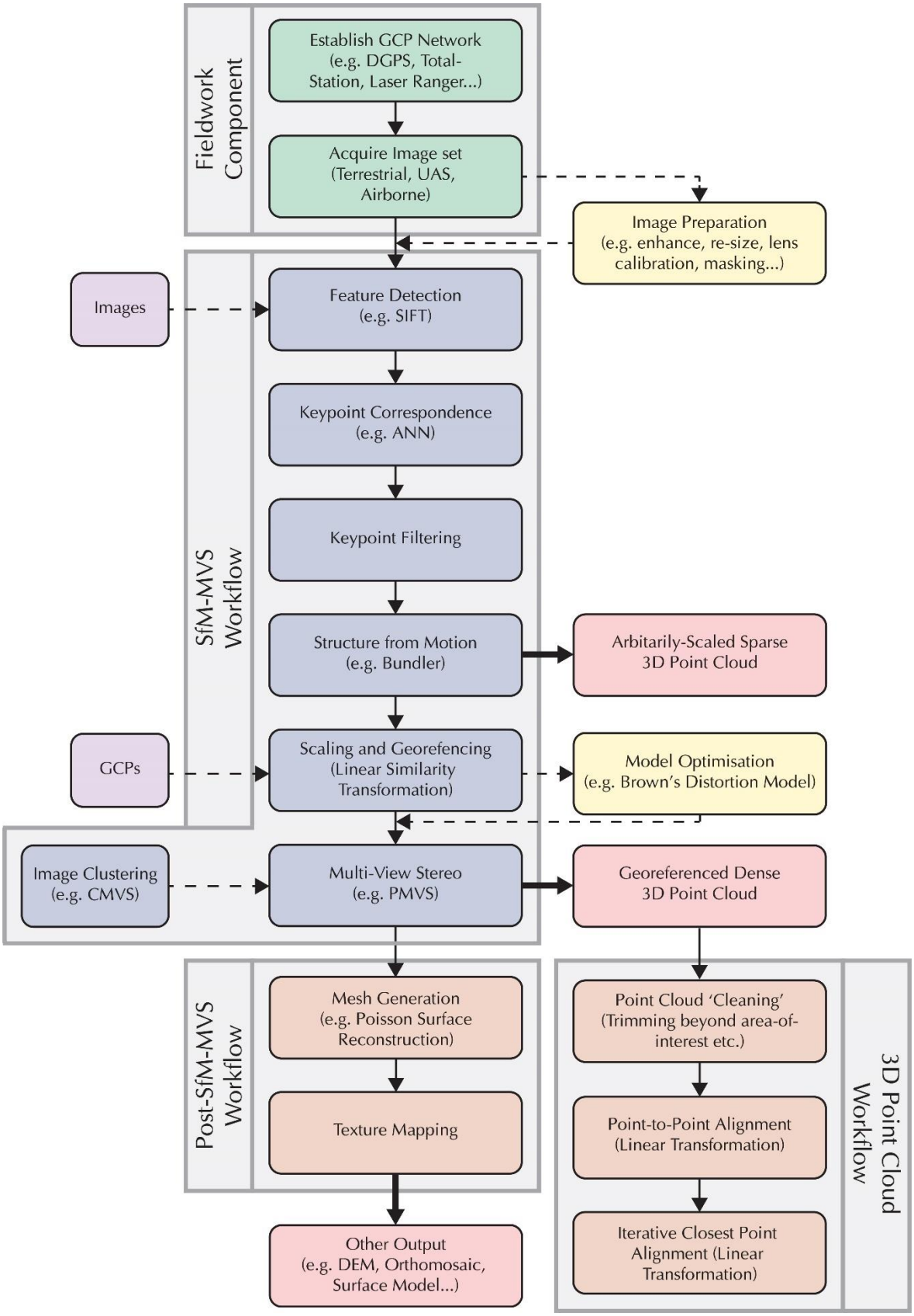

Figure 4.5: Workflow to produce georeferenced point clouds from image sets using an SfM-MVS pipeline. Fieldwork, SfM-MVS and post-processing workflows are separated with inputs in smaller purple boxes, outputs in red boxes and optional side-flows in yellow boxes. (Modified from Westoby et al., 2012 and Smith, Carrivick and Quincey, 2015).

4.3.2 Optimisation, Alignment and Registration

To ensure any non-linear distortions of the model do not propagate through to the final dataset, the model is optimised following the initial alignment using the GCPs to minimise the sum of re-projection error. Non-linear distortions are commonly observed following the image-alignment and bundle-adjustment phase of the workflow; the most common of which is a bowling/doming of the model caused by optical lens distortion (Ouédraogo *et al.*, 2014b; Leon *et al.*, 2015; Carbonneau and Dietrich, 2016). Ideally, a digital photograph would be a perfect representation of the scene however, lens designs in non-calibrated cameras result in barrel or pin-cushion distortion patterns (Hugemann, 2010; Carbonneau and Dietrich, 2016), and standard photogrammetric practice is to correct this distortion using the Brown-Conrady (Conrady, 1919; Brown, 1965) lens distortion model, rather than allowing such distortions to propagate through to the final topographical model. To correct for this radial and tangential distortion caused by alignment imperfections of the physical camera body, Photoscan offers an optimisation workflow employing the Brown-Conrady distortion model (Conrady, 1919; Brown, 1965) where the user-identified GCPs are used to refine the camera calibration parameters and minimise non-linear distortions. Correction for model distortion is the only stage of the SfM-MVS workflow where the model is non-linearly transformed.

Once the models had been produced, they were extracted in ASCII point cloud format and registered using a 7-parameter rigid transformation and tie-points across common features. Following this, areas of unchanged bedrock were extracted and the Iterative Closest Point (ICP) algorithm (Besl and McKay, 1992) was used to finely align the point clouds and establish and RMSE between successive surveys, with all points considered and an overlap typically in the region of 95 to 100 %. The resulting transformation matrix from the fine alignment of bedrock features was then applied to the remaining area of the point cloud. Alignment and change detection were performed in the open-source point cloud software; CloudCompare (Danielgm.net, 2016).

4.4 SfM-MVS Methodological Development

SfM-MVS is increasingly being used across a number of disciplines for the development of high-resolution 3D datasets and as such, a number of publications have specifically dealt with the assessment of the technique and its accuracy. To ensure the impact of a number of factors was fully understood prior to data acquisition, a number of tests were performed to asses their impact on model quality and devise a suitable workflow for removing erroneous points through effective thresholding and ensure suitable data for best model-quality results were acquired in the field.

4.4.1 Pre-Fieldwork Testing

In order to familiarise with the workflow and ensure a thorough understanding of the processes at each stage, a survey above a local site (City Stadium, Newcastle upon Tyne) was conducted to test the workflow and ensure the equipment was functional. Using the DJI Phantom 3 Professional, a Trimble R4 dGPS rover unit and 5 large fabric targets with a clearly-visible centre point, a single campaign was flown using a pre-defined flightpath. The weather was slightly overcast and bright which meant lighting across the survey area remained relatively homogeneous for the entire campaign. An altitude of approximately 40 m above ground level resulted in a ground resolution of 1.81 cm/pixel with 315 images captured across an area of 0.06 km^2. 159 nadir images were collected on the first flight and complimented with 153 oblique images captured on a second flight following the same pre-defined flight path. 5 GCPs were laid out and registered prior to flying; one at each corner of the cinder track and one in the centre of the field. Approximately 208,000 tie points were used for initial alignment, and densification resulted in a point cloud of roughly 54 million points in size. Key point identification and image matching took 5 hours, and densification took 12.5 hours on a processing machine with 32 GB of RAM and a dedicated GPU. The limit for key point identification was set to 40,000 per image with a maximum of 4,000 tie points per image. The densification parameter was set to *high*, which downscales each image by a factor of 4 (2 x width, 2 x height) for computational ease, with an *Aggressive* depth filtering approach which is well-suited to aerial data processing (AgiSoft LLC, 2016).

Prior to model optimisation, the GCPs had a average mean error of 0.009 m, 0.006 m, 0.009 m in the x, y and z directions respectively. Following optimisation of the camera model using the GCPs, these errors were slightly reduced to 0.009 m, 0.004 m, and 0.009 m for x, y and z respectively with an average re-projection error across the model of 0.06 pixels. This corresponds to a relative precision of 0.00035:1 m with an RMSE of 0.014 m at a viewing distance of 40 m. To assess the final accuracy of the 3D model, independent check points (ICP) were surveyed using the same Trimble R4 rover unit. ICPs were not used to georeference the model or as part of the camera model optimisation and were located within the cinder track (i.e. inside the area of GCPs) and outside the cinder track (i.e. beyond the area of GCP coverage at the periphery of the model). This allows an understanding of the horizontal and vertical accuracies at the centre of the model where every part of the surface is covered by greater than 9 images and at the edge of the model where the amount of overlap and image coverage begins to tail off. ICPs were not pre-laid targets, given the abundance of distinguishable man-made objects such as cycle path markings, sculptures and roadways. The location of the GCPs are highlighted within red squares on figure 4.6 and dots denote the ICPs. Each point (both GCPs and ICPs) were observed for 5 minutes and baselines were processed using OS Net RINEX data from a nearby (NCAS – Newcastle) station. All processing was performed in the WGS-84 geographic coordinate system (UTM zone 30N).

To assess the impact of lens distortion on model quality and the way in which this can be minimised through data collection approaches, a total of 6 models were created; nadir non-optimised (NNO), nadir optimised (NO), oblique non-optimised (ONO), oblique optimised (OO), combined non-optimised (CNO) and combined optimised (CO). The results of the RMSE of GCPs and ICPs for each model are summarised in table 4.2. Based on previous research, the CO model was assumed to be the most accurate and used as a base for calculating the RMSE and cloud-to-cloud distances with the other 5 models. The CNO model displayed a GCP RMSE of 0.015 m and a significantly higher ICP RMSE of 0.184 m. ICP errors are highest at the peripheries of the model where the number of projections (amount of images a GCP/ICP appears within) are low (0.25 m with 19 projections) and lowest nearer the centre of the survey within the control zone (defined as the area within or near the GCP network) where the number of projections are higher (0.11 m 41 projections). Positional errors for ICPs were greatest in the z-axis with 0.099 m, 0.053 m and 0.145 m for x, y and z respectively.

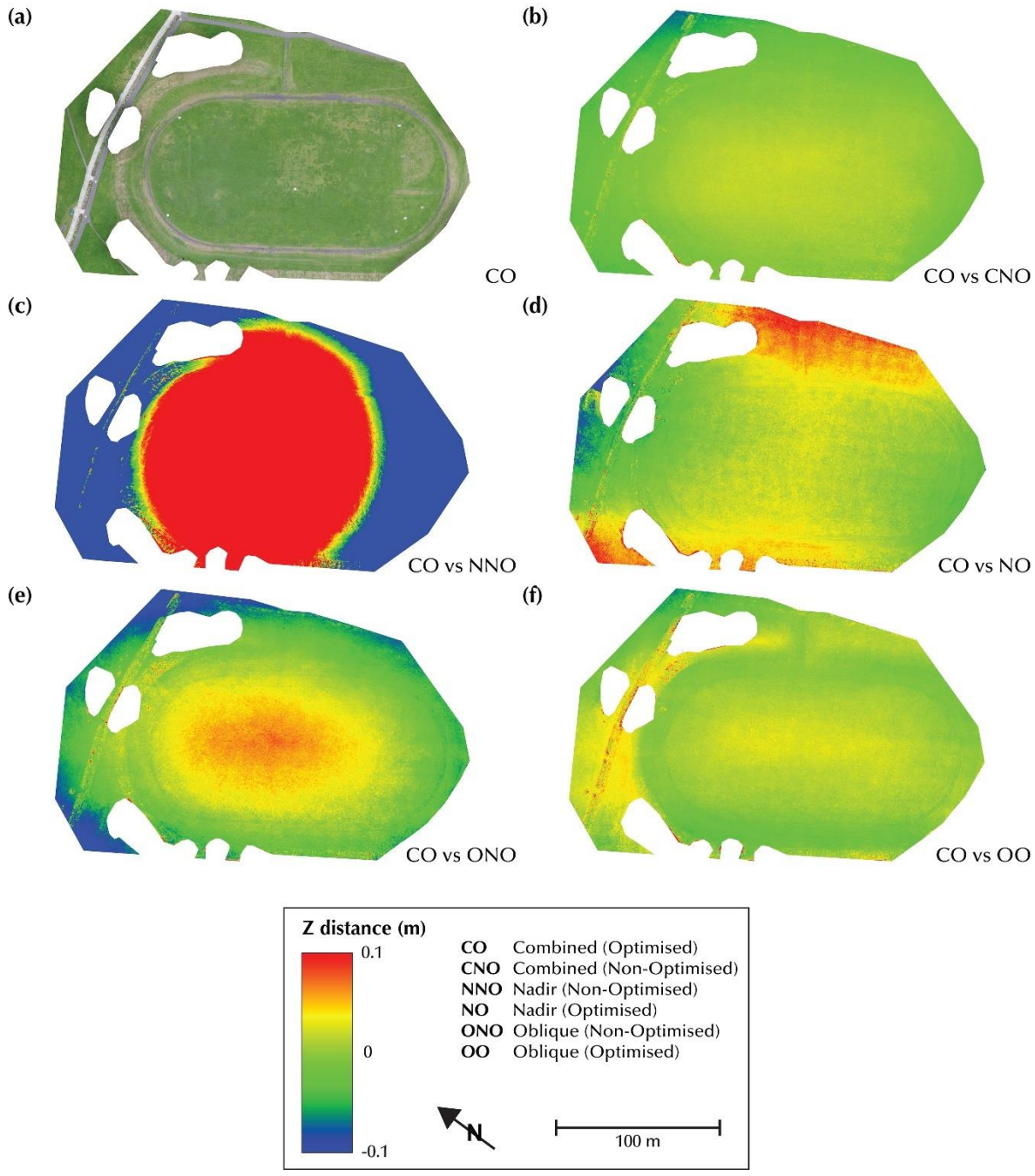

Figure 4.6: Effect of non-linear camera-model deformation and image perspective on model quality. Highlighted using a cloud-to-cloud distance measurement through a single axis (z). (a) City Stadium model with RGB values applied; model created using combination of nadir and oblique imagery and optimised using independent GCPs (CO). Model CO compared with (b) CNO; (c) NNO; (d) NO; (e) ONO and; (f) OO.

Cloud-to-cloud comparison between a model produced using solely 159 nadir images (NNO) and a model produced combining the nadir imagery with 153 oblique images (CNO), without optimisation, was performed to assess the impact of oblique imagery on reducing the level of non-linear model distortions. This was also repeated for both point clouds following optimisation of the camera model (NO & CO). A straightforward cloud-to-cloud comparison along the z component of each cloud was performed to highlight areas of greatest difference, assumed to be the greatest level of distortion/error against a base dataset (CO) (fig. 4.6) and demonstrates the effect of; a)

complimenting nadir imagery (i.e. captured with a 90-degree angle of incidence) with oblique imagery for minimising the level of non-linear distortion caused by inherent lens properties and; b) using a distortion model for correcting lens calibration parameters with a series of GCPs. The accompanying errors of the GCPs and ICPs for each model are given in table 4.2. These results highlight the importance of optimisation, as ICP errors following optimisation for all datasets regardless of data acquisition method are within 0.01 m of each other. This suggests that providing suitable ground control is collected, the distortion from a non-optimal perspective can be largely offset through calibration and optimisation of the camera model.

Table 4.2: GCP and ICP errors for each of the experimental datasets from City Stadium, Newcastle upon Tyne.

	NNO	NO	ONO	OO	CNO	CO
GCP Error (m)	0.290	0.017	0.029	0.020	0.015	0.016
ICP Error (m)	1.476	0.167	0.224	0.161	0.184	0.160

Figure 4.6 also reveals the large concave distortion, commonly referred to as the 'bowl effect', in the non-optimised model created using solely nadir imagery (fig. 4.6 c). The colour scale is kept consistent for all figures shown to emphasise the level of distortion. The same effect can be seen in the non-optimised model created using solely oblique imagery (fig. 4.6 e), though not to the same degree with a much greater area of the model being consistent with the control data. Following optimisation of the camera model for the nadir and oblique datasets, the concave distortion is largely removed. However, there are still issues in both models at the peripheries where image overlap is less than central areas. Both models appear to have an angular distortion running from top to bottom and left to right for the nadir and oblique models respectively. The best result (i.e. the model that produced the least level of distortion compared to the control data) is achieved when combining nadir with oblique imagery (fig. 4.6 b). Despite no optimisation of the camera model, the combination of multiple perspectives appears to largely offset the likelihood of non-linear distortions witnessed in the single-perspective models.

4.4.2 Image Over/Sidelap and Perspective

The number of images collected during a field campaign is ultimately dependent on the logistical capabilities and the availability of computational processing power. The gains achieved from increasing the number of images and thus, increase in the amount of overlap/ side-lap between consecutive images, has been said to reduce substantially once each point of the surface is covered in a three or more frames (Smith, Carrivick and Quincey, 2015). The effect of image

quantity on point cloud density was tested at the Rhone glacier, Switzerland (fig. 4.7). A terrestrial image-set with a far greater percentage of overlap than typically collected was used to produce a series of 3D models, each time reducing the size of the image-set by a factor of 2 and examining the effect that this had of the properties of the generated model. The full image set consisted of 277 images covering a spatial extent of approximately 0.25 km^2, along the NW-facing lateral moraine of the glacier. Models were created with the full (277 images), one-half (139 images), -quarter (70 images), -eighth (35 images) and -sixteenth (18 images) of the original image set. Distances between the camera and the slope were between 150 and 200 m, following the geometry of the glacier, and captured with a 24 MP camera at a fixed 20 mm focal length. This resulted in a ground resolution of approximately 0.04 m/pixel.

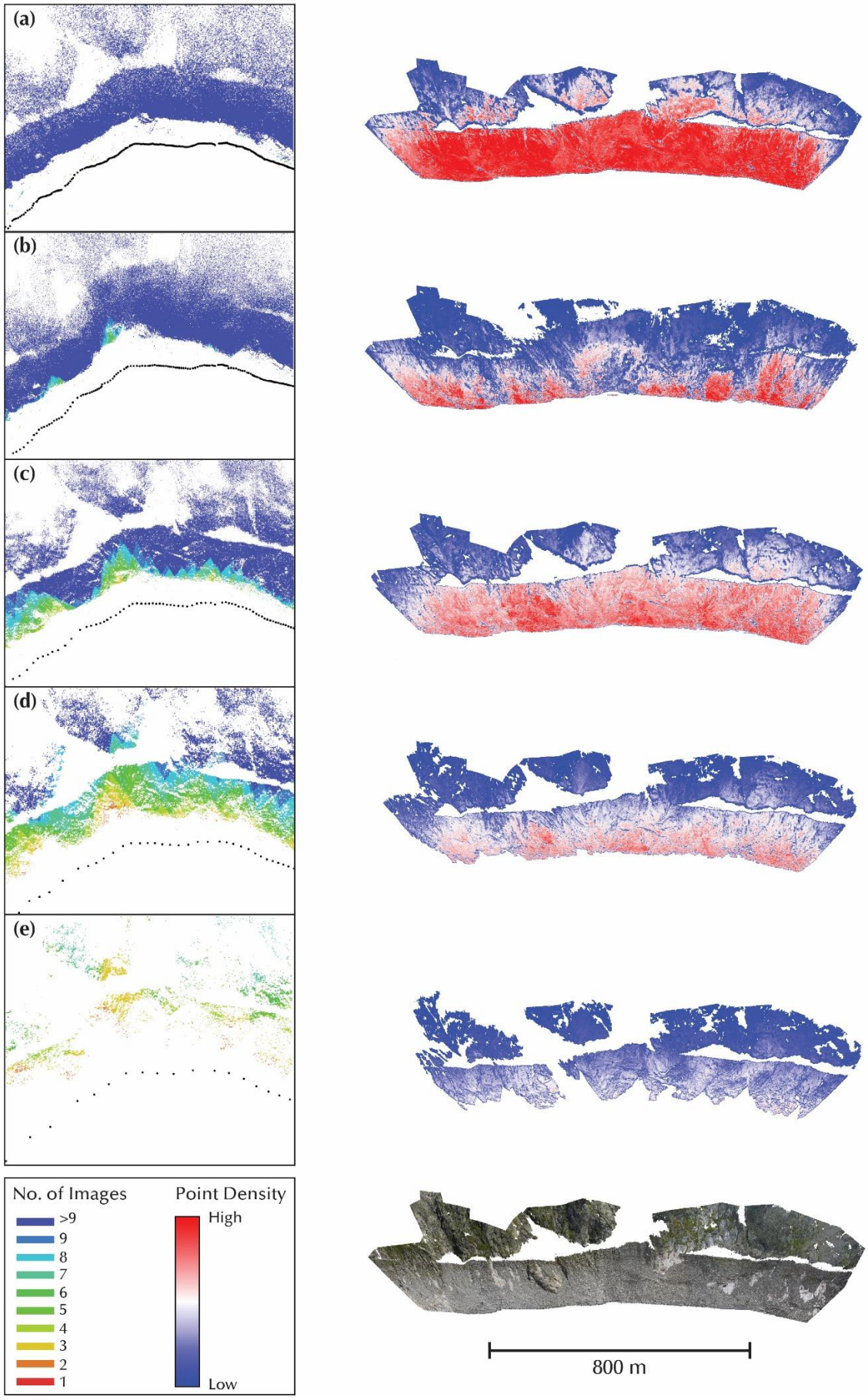

Figure 4.7: Results of the test on the effect of image quantity on point cloud density at the Rhone glacier, Switzerland. (Left) Tie points extracted from images, coloured by number of images they appear in and (Right) point density distributions for (a) full; (b) half; (c) quarter; (d) eighth; (e) sixteenth image-set model.

Point densities (number of points within a 1 m^3 spherical search on each point), and the number of projections of each point are shown in figure 4.7 (a) - (e), with the maximum density of the lowest image-set used as the upper value on the other datasets colour scales for easier comparison. The model created with the full set of images has a high point density across the majority of the model. As can be seen with most survey techniques, the point density deteriorates at the edge of the model, highlighting the importance of ensuring the imagery covers an area beyond that which is to be surveyed to allow for the deterioration in an area that can be cropped from the model. Once the image set is halved (fig. 4.7 b), the distribution of point density becomes disrupted with areas of lower point densities within the main survey area. Interestingly, the model created with just one quarter of the images appears to have a more evenly distributed (and higher) density across the model than the half image-set model, whilst the models created with one eighth and one sixteenth (fig. 4.7 d and e) are poorly distributed and in places, suffering from occlusion and lack of image cover. The number of images covering each tie point (fig. 4.7 left) gradually reduces though even in the model with the least amount of images (fig. 4.7 e), the majority of tie points are still covered in a minimum of 3 images. The results suggest that to achieve the best quality (i.e. evenly distributed point density), ensuring that each point is covered in 9 or more images is an optimal approach. The effect of perspective is also visible in the point densities, as the steep angle of incidence results in poor ground resolution at higher altitudes and subsequently, a deterioration in the point density across all models.

4.4.3 Accuracy and Repeatability

The accuracy and repeatability of SfM-MVS was tested across a rock-slope in the pro-glacial zone of the Bossons glacier. Image sequences were captured on the same day at approximately 11:15 – 11:25 and 12:55 – 13:10 for the first and second surveys respectively, and it is assumed that there was no change between these surveys. 2D slope elevation profiles (along the transects denoted in fig. 4.9 b) and cloud-to-cloud distances between the two SfM-MVS surveys are shown in figures 4.8 and 4.9 respectively. The elevation profiles reveal good alignment between the two point clouds (fig. 4.8). Surface roughness has been computed to assess its influence on the alignment and quality of the model. Sharp breaks in the topography, particularly when sloping away from the camera is shown to result in poorer alignment and model quality, and often distances are greater immediately before or after such a change. It is not possible to establish which of the two models 'truth' without an independent survey method. In some cases, the RGB values suggest small patches of vegetation are the reason for rougher surface values, and greater distances. Large areas of vegetation were manually removed from the point cloud model (using the *segmentation tool* embedded within the CloudCompare (Danielgm.net, 2016) software) to reduce the likelihood of it affecting the alignment quality. Automated workflows for the detection and removal of vegetation

from point cloud models have previously been shown as an effective alternative (e.g. Brodu and Lague, 2012) though it was found that manually removing was less computationally demanding and ultimately consumed less time during the data processing phase of the study. The two same-day point clouds were registered with an RMSE of 0.09 m, which corresponds with a relative precision of approximately 1:100, given that images were captured roughly 90 m from the rock face.

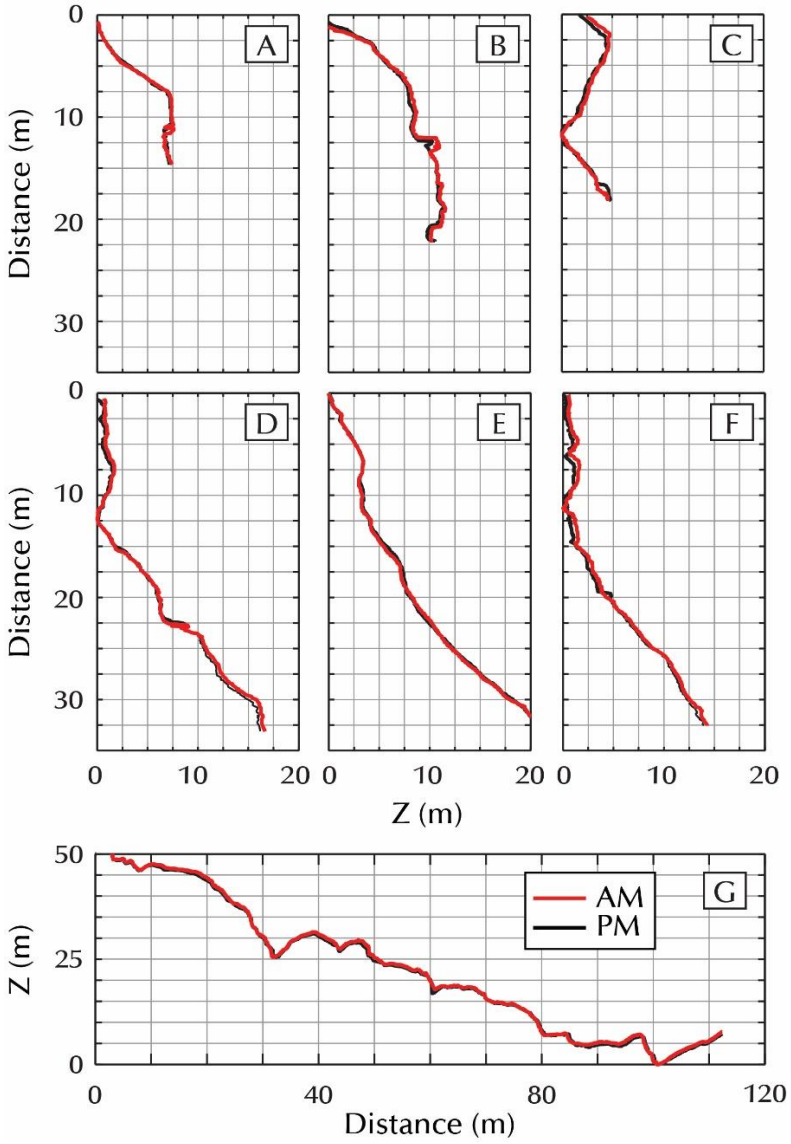

Figure 4.8: Rock-wall surface elevation profiles (Z is perpendicular to the rock-wall), extracted from the same-day point clouds with a swath of 0.1 m. Profile locations are shown in Fig. 4.9 (b). Profiles A to F are vertical from top to bottom and profile G is horizontal running from left to right.

4.4.4 Illumination and Thresholding

A number of authors allude to the detrimental effect of uneven and poor illumination on the quality of 3D reconstructions, yet a full assessment of these influences and thresholding approaches has yet to be adequately addressed in existing work. SfM-MVS relies on strongly

distinguishable patterns and areas of high contrast to identify keypoints in each images, and therefore model quality in areas of heavy shadowing or poorly illuminated surfaces can suffer from inaccurate and incorrect point positioning, or large areas of no-data. In the natural environment, particularly mountain landscapes, the weather can be difficult to predict and not always ideal for surveying but with limited time, there is often little-to-no flexibility whilst operating in the field. Therefore, one principal aim of this test was to quantify the effect of poor illumination, and changes in lighting conditions between successive surveys to understand whether the negative effects can be removed, or at least partially-removed through an effective thresholding technique. Image sets captured between 11:15 – 11:25 and 12:55 – 13:10 allowed enough time to pass for significant changes in the level of illumination across the rock-slope. Image-capture technique (UAS), ground control and other conditions remained the same between the two surveys. Figure 4.9 (a, b) shows a comparison between the models created in the first and second surveys for a section of the surveyed slope form. It can be clearly seen that the second survey is subjected to significant shadowing compared to the first survey, although the intensity of light is very similar. To quantify the difference in lighting conditions between the two surveys, a composite of RGB (RGBc) ((R+G+B)/3) has been used where significantly lower values correspond with shadowed areas (fig. 4.9 c & d). To assess the impact of shadowing on model quality, a simple cloud-to-cloud measurement was computed where no change was expected (fig. 4.9 e).

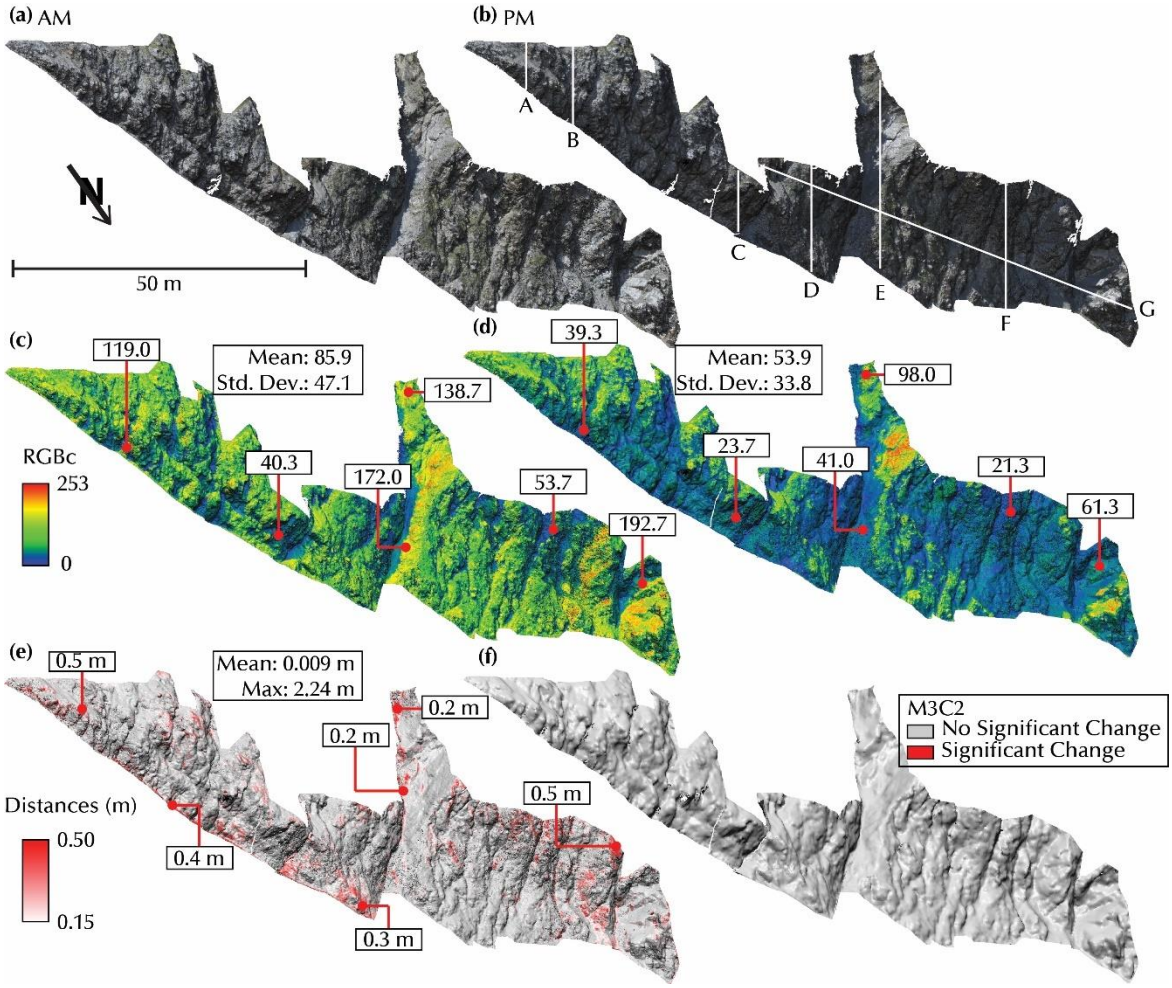

Figure 4.9: (a & b) 3D point clouds with RGB values applied from the same-day imagery, showing a clear difference in lighting conditions and shadowing between the morning (a) and afternoon (b) surveys. Transects in (b) denote cross-section profiles A to G in figure 4. (c & d) RGB composite (RGBc) point clouds ([R+G+B]/3) clearly demonstrating the variation in lighting between the two surveys. (e) Cloud-to-Cloud differencing between the same-day surveys. (f) M3C2 differencing output model. No significant change was identified highlighting the variable thresholding ability of the algorithm to identify areas of poorer alignment quality.

The cloud-to-cloud distances have been plotted against RGBc values (fig. 4.10} a) to highlight any potential relationship between distance and shadowing/poor lighting. The greatest cloud-to-cloud distances, which are assumed to be the greatest level of error between same-day surveys, are located on the points with the lowest RGBc values (i.e. darkest points). Figure 4.10} (b) summarises the results of gradually removing (thresholding) points based on their respective RGBc values and the subsequent RMSE between the two clouds. The result of increasing the threshold (i.e. removing heavily shadowed areas from the model) is shown to increase the alignment quality with a strong polynomial trend ($R^2 = 0.99$). Shadowing is detrimental to model quality and increases the thresholds for change detection in repeat SfM-MVS surveys and is an essential step in driving such thresholds in multi-temporal analyses. Ideally, a relatively consistent level of homogeneous lighting across the slope and at repeat surveys would be the optimal operating conditions however, such surveys are often conducted under time-pressure and in environments where such conditions

are impossible to control and likely to change. This thresholding approach with the RGBc provides a useful tool for removing areas of topographical data that are most likely to be erroneous prior to change detection in environments where lighting cannot be controlled.

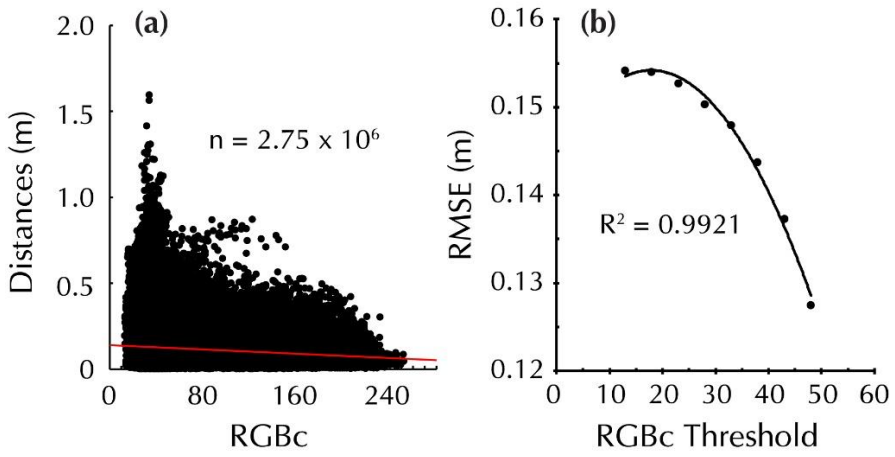

Figure 4.10: (a) Scatter-plot of RGBc vs Cloud-to-Cloud distances, indicating that the greatest distances (assumed to be the greatest error between the same-day surveys) are found on points with the lowest RGBc values (higher level of shadowing). (b) Effect of gradually increasing the RGBc threshold on the RMSE of alignment following ICP registration on one section (ii) of the point cloud. A polynomial trend with an R^2 value of 0.99 is overlain.

4.4.5 Scale vs. Detail

Three surveys from three different perspectives were performed at the Glacier de Bossons in 2014; terrestrial, UAV and helicopter. Terrestrial was shown to produce the models with the greatest point density, as image side-lap was significantly greater than that achieved with the UAV or the helicopter. The GSD was similar between the terrestrial and UAV images, though the UAV permitted the collection of images closer to the rock-slope surface where similar proximity terrestrially would be logistically difficult. The helicopter allowed the greatest scale in the shortest period of time, though the speed of travel and proximity to the slope meant side-lap was significantly lower than the other two perspectives resulting in significantly lower point densities and GSD. The lower GSD is an important consideration for helicopter images as it is not possible to fly closer to the slopes and a higher quality sensor would be beneficial, whilst the lower point density could be accounted for with successive flights along the same slope to ensure a greater amount of side-lap between image sets. A combination of all three, such as the approach adopted in this study, has the benefit of analysing valley-scale distributions whilst also capturing smaller-magnitude failures that have previously been un-accounted for.

4.5 Change Detection

A number of approaches to measuring change between successive topographical datasets have been established (see section 2.12.1). In this study, open-source algorithms and point-cloud data are used to create a 3D workflow where the full geometry of the model is considered throughout change detection and volumetric computation, ensuring that the natural geometry of the slope is preserved throughout the analysis and that change is not omitted or under-estimated as a result of a surface interpolation that is required in other approaches.

4.5.1 Multi-Scale Model to Model Differencing (M3C2)

Distances were computed using the M3C2 algorithm proposed by Lague, Brodu and Leroux (2013). This is a multi-scale model to model comparison technique which can be used to identify areas of significant change, in this case, the focus is loss due to slope failure. The M3C2 algorithm allows rapid analyses of complex surfaces, taking into consideration local surface roughness and alignment errors to calculate a confidence interval for each point of change measured (Lague, Brodu and Leroux, 2013). Change is considered within a cylinder projected through both clouds of a defined length and width (fig. 4.11). At the first stage, the surface normals at each point in the cloud are calculated considering points in a user-defined neighbourhood calculated from a single cloud (typically the earlier date), or by averaging the normals of both clouds. To reduce computational intensity, the M3C2 technique makes use of core points, which are a subset of a full point cloud. Reducing the point cloud does not lessen the accuracy of distance measurements, as despite data only being returned for every core point, the density of the full point cloud is still used to inform the calculations (Barnhart and Crosby, 2013; Lague, Brodu and Leroux, 2013). The length of the projection cylinder can also be defined and this limits the maximum distance considered throughout the computation. The projection scale (i.e. the diameter of the cylinder in which distances are measured for each point) should be given careful consideration to guarantee the distance measurement is independent of the local surface roughness (Stumpf *et al.*, 2014), as all of the points within each cloud that lie within the cylinder are spatially averaged to calculate mean surface positions (Barnhart and Crosby, 2013).

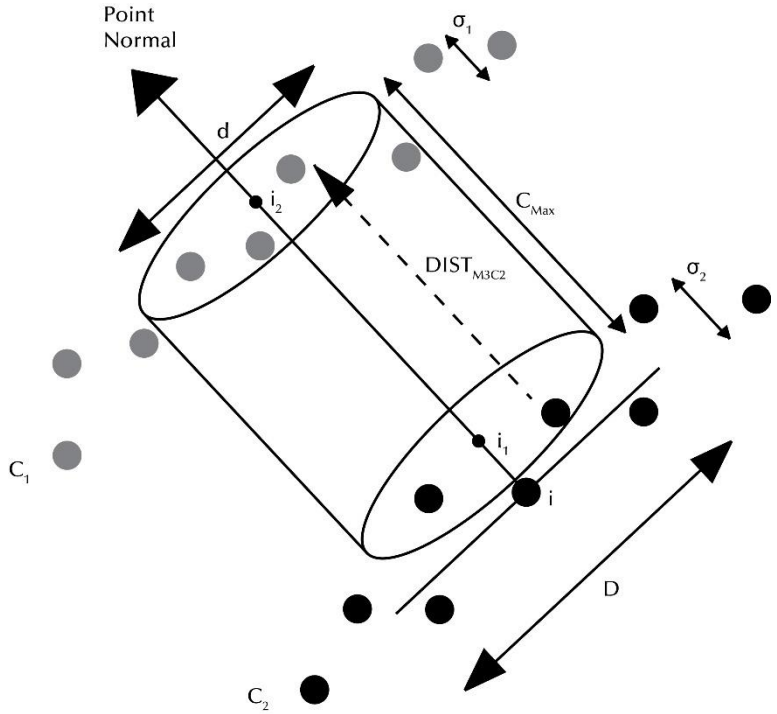

Figure 4.11: Conceptual diagram of the M3C2 technique. The point normal for i is calculated using the scale, D. A cylinder with a diameter d and a user-specified maximum length is used to select points in C_1 and C_2 for the calculation of i_1 and i_2, respectively. $DIST_{M3C2}$ is the distance between i_1 and i_2 and is stored as an attribute of i. The local and apparent roughness of C_1 and C_2 are calculated as $\sigma 1$ and $\sigma 2$, respectively, which are used to calculate the SVCI for i (modified from Barnhart and Crosby (2013), after Lague, Brodu and Leroux (2013)).

4.5.2 Level of Detection (LOD) Threshold

To complement the M3C2 algorithm, Lague, Brodu and Leroux (2013) also proposed a Spatially Variable Confidence Interval (SVCI), which considers the local surface roughness and alignment registration error to calculate whether measured differences are significant. The SVCI is computed and stored as an attribute of each point, defined as

$$LOD_{95\%}(d) = \pm 1.96\left(\sqrt{\frac{\sigma_1(d)^2}{n_1} + \frac{\sigma_2(d)^2}{n_2}} + reg\right)$$

Equation 4.1

where d is the radius of a projection cylinder, reg is the RMSE between the two clouds in the computation and n_1 and n_2 are the two clouds considered. During the test of reproducibility, a trial and error approach to defining M3C2 parameters was adopted to ensure that error was correctly accounted for. Figure 4.9 (f) shows that no area of the detected change was deemed significant (i.e. above the level of detection threshold) for the same-day surveys at the Glacier de Bossons demonstrating that the operating parameters correctly accounted for error and were not deemed significant (i.e. confidence > 95%).

Areas identified as significant change are cross-checked to ensure that no erroneous data is misinterpreted as genuine change, which could affect patterns of size distribution in later analyses. Areas of roughness such as vegetation in small patches on rock-walls, boundaries of survey areas and particularly complex geometries are amongst the causes of some errors and can mostly be identified and removed through a visual clarification. Slope elevation profiles are also used as a rapid approach to check whether the change is genuine or a result of misalignment.

Following the extraction of areas of significant change and cross-checking for accuracy, and to ensure no erroneous data is mistaken as a slope failure, the cloud is broken into separate slope failures (i.e. areas that are believed to have failed as an independent event). To do this, a Connected-Component approach was taken where the point cloud is segmented based upon a user-defined minimum distance. Figure 4.12 shows a section of the Mer de Glace dataset following this stage, where each cluster of points that fulfil the user-defined criteria are separated into their respective component groups. One crucial assumption at this stage, which is a particularly important consideration across sediment-mantled slopes, is that areas of significant change are single slope failures and are counted as such. However, in some cases the total loss could be coalescing failures that are mistakenly counted as one.

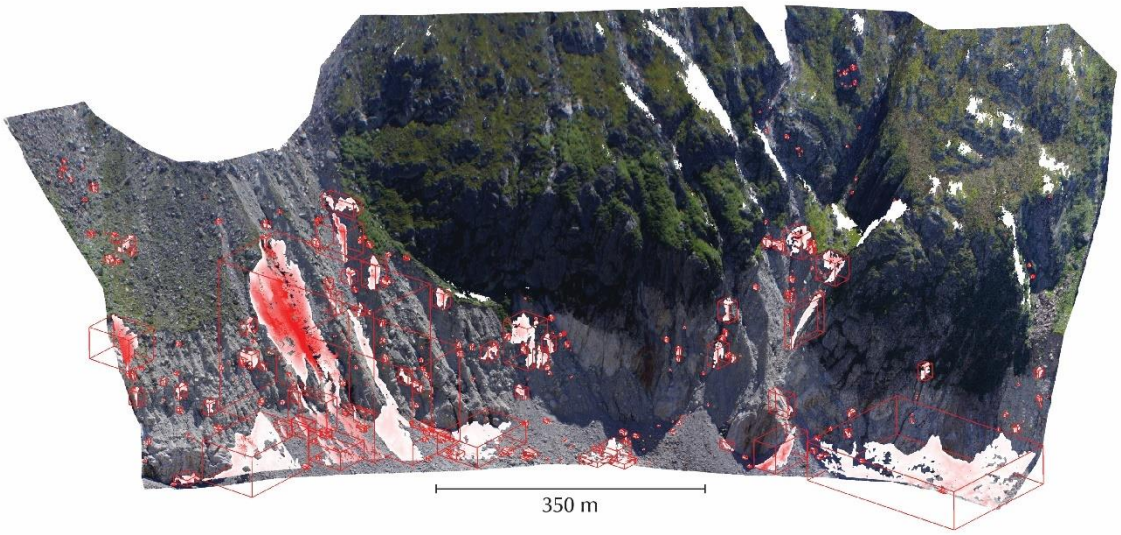

Figure 4.12: Section of Mer de Glace dataset with areas of significant change overlain. These are separated into individual slope failures using Connected Components analysis, and the red bounding boxes denote the individual slope failures used in volume computation and size distribution analysis.

4.5.3 Volume Calculation

An ideal workflow for calculating volume is one that provides an accurate estimate without considerable over- or under-estimation. The aim here is to produce a repeatable workflow that calculates an accurate estimate of volume using the un-edited 3D data that M3C2 outputs in an efficient manner. The advantages of using the M3C2 algorithm for cloud-to-cloud differencing are clear, especially when considering change across complex topography such as that here. However, the measured distances are along a single axis in the direction of the normal orientation (i.e. the cloud-to-cloud distance within a single projection cylinder around each *core point*) and computing the volume of single slope failures with this information is no trivial matter. So far, existing work that exploits the M3C2 algorithm has not thoroughly explained the process of calculating volumetric change with the output data or have used the approach for solely identifying areas of change deemed statistically significant before extracting these areas and performing volume calculations in a more traditional manner (e.g. difference of DEM). Typically this involves raster-based approaches in GIS where depth is often averaged across the failure surface. Given the benefits of M3C2 in identifying distances across complex surfaces, it would be ideal to also consider the calculation of volume using this information and the following sub-section outlines how that is considered in this work.

Prior to using the M3C2 algorithm for 3D change detection, each of the input point clouds were sub-sampled to regular spacing intervals. This has two main advantages; firstly it reduces the computational intensity, and providing the sub-sample distance is chosen sensibly, feature definition is not reduced given the high-density nature of SfM-MVS point clouds. Secondly, as the point cloud is sub-sampled prior to using the M3C2 algorithm, the full cloud can be used without opting to use core points for the distance calculation. The point density between each of the clouds remains fairly consistent which benefits the following workflow for computing volumetric change (fig. 4.13). If the density of the point cloud is known, then the 'surface' around each point based on the projection cylinder radius can be calculated. The M3C2 distance measurement can be used with the radius to calculate the volume of the cylinder at each point. However, a robust cylinder radius will consider not only the core point, but a number of surrounding points as well (fig. 4.13 a) which means there will be a significant amount of overlap between the projection cylinders, and the sum of all projection cylinder volumes would therefore vastly over-estimate the total volume. To ensure there is no overlap between neighbouring cylinders, a correction must be used which is dependent upon the projection scale and point-cloud density. One further issue is presented by surface normals as by default, M3C2 projects distances in the direction of the local surface normal. This is not an issue in areas where the topography is generally planar and change can be measured principally through a single axis (e.g. coastal cliff backwasting) however, more complex surfaces may result in cylinders in opposing projection directions which may intersect with their neighbours.

This isn't a problem if considering solely the single cloud-to-cloud distance but again, could result in a significant over-estimation of volume if the intersecting cylinder areas are considered more than once. The problem of intersecting cylinders was accounted for by recalculating normals for each point cloud prior to the M3C2 algorithm with a fixed orientation (in this case, +Z), using a *plane* local surface model, which is most robust to noise. These normal orientations are then used in the M3C2 parameters, thus constraining the orientation of the projection cylinders within which the cloud-to-cloud distances are considered and removing the possibility of intersecting cylinder volumes. Through a trial and error approach, this was seen to significantly reduce the calculated volume (from the approach which did not use a fixed normal orientation) to a value more in-line with if each slope failure were considered as a geometrical cuboid (i.e. *height x width x mean-depth*), though assumed to be more accurate than a *cuboid* approach as the calculation considers the total variability of measured distances.

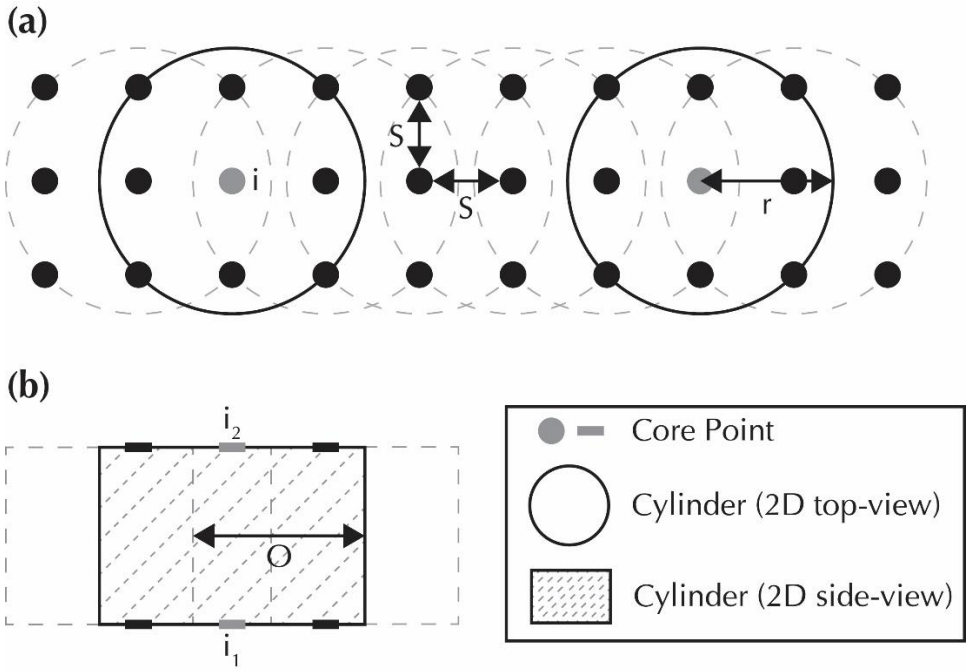

Figure 4.13: Conceptual diagram of the technique used to calculate volume using 3D data. The volume for the cylinder at each point (i) is calculated using the cylinder radius (r). Overlap (O) can be calculated and corrected for using the sub-sampling distance (S) and r. i_1 and i_2 correspond to i_1 and i_2 in figure 4.11}.

Implemented in Matlab for batch-processing of multiple outputs, the volume calculation takes the form:

$$V_C = \frac{(\Pi r^2 \times M3C2_{DIST})}{r^2 \div ss^2}$$

Equation 4.2

where V_C is the volume of the projection cylinder, r is the radius of the projection cylinder, $M3C2_{DIST}$ is the measured distance between point clouds (i_1 and i_2), and ss is the sub-sampling distance. The total volume for each slope failure is therefore calculated as:

$$V_L = \sum_{y=1}^{n} V_{Cy}$$

Equation 4.3

where V_L is the volume of the slope failure, and n is the total number of core points considered in the M3C2 algorithm (i.e. the total volume is the sum of all projection cylinders, after correction for overlap using equation 4.2). The volume of failures (identified using the connected-components approach outlined earlier) are calculated individually through batch processing and the descriptive metrics (height, width, maximum depth and area) of each failure zone are calculated using point coordinates (e.g. $Z_{max} - Z_{min} = Failure\ Height\ (H_L)$).

4.6 Spatial Distribution Analysis

Analyses of the spatial distributions of slope failures are important for considering the underlying drivers. Identification of significant patterns and clustering helps identify key trends and processes. There are two main approaches for examining the spatial distribution of slope failure datasets; the first is qualitative analysis based on their location on an underlying basemap, which can be aided through graded symbology to highlight significant distributions across the study area. The second is a quantitative approach to understand whether the spatial distribution is clustered in a particular area, dispersed, or relative to other factors. The spatial distribution of slope failures are analysed using slope failure area proportion (SFAP) and the slope failure concentration (SFC). SFAP is defined as the percentage of total slope failure area within a given constraint (e.g. slope angle range), whilst SFC is the number of slope failures per square kilometre. These are commonly used metrics within studies of slope failure inventories and are useful for understanding the spatial distribution of slope failures at the local and orogenic scale.

4.7 Size Distribution Analysis

Slope failures are characterised by their geometry, which is useful for identifying potential driving mechanisms based upon failure shape. Width (W_L), height (H_L), maximum depth ($D_L{}^{MAX}$) and mean depth ($D_L{}^{MEAN}$) are calculated based on the 3D point cloud data of each slope failure. W_L for each event is calculated as the difference between $max_{x/y}$ and $min_{x/y}$ whilst the difference between max_z and min_z are used to calculate H_L. M3C2 distances are used to calculate $D_L{}^{MAX}$ and $D_L{}^{MEAN}$. Surface area ($A_L{}^{SURFACE}$) of the slope failure (i.e. 3D area of the slope) is taken to be the sum of the projection cylinder area used to inform the calculation of volume (eqn. 4.2) whilst are area (A_L) is calculated as W_L x H_L.

The magnitude-frequency of the detected slope failures are expressed by way of a cumulative distribution function (CDF) (eqn. 4.8). The CDF is an alternative to the Probability Density Function (PDF) that describes the relative likelihood that a randomly selected slope failure will assume a particular magnitude. The CDF gives the probability that a randomly selected slope failure from the inventory will have a magnitude of equal to or less than a selected value (Hoek, 2000). Whilst a PDF and a CDF essentially convey the same information, their use is partly a matter of taste and convention. Anecdotally, a PDF represents probability with area whilst a CDF represents probability with distances and cognitive neuroscience literature shows that people compare distances faster and more accurately than they compare areas (Cleveland, 1994; Dent, 1999; MacEachren, 2004; Whuber, 2010). Thus, as a graphical tool for reading off probabilities, a CDF is favoured. It is written as;

$$\mathrm{F(x)} \;=\; \mathrm{P(A} \leq \mathrm{x)}$$

Equation 4.4

For example, if A is the magnitude of a randomly selected slope failure, then $F(x)$ is the chance that the magnitude is equal to or less than x (e.g. $F = (100\ m^3) = 0.8$, which means there is an 80 % chance that the randomly selected slope failure has a magnitude equal to or less than 100 m^3, or equivalently a 20 % chance that it will be greater). The CDF is the probability of a slope failure being *at least as extreme* as x, expressed as;

$$\overline{\mathrm{F}}(\mathrm{x}) = \mathrm{P}(\mathrm{A} \geq \mathrm{x}) = 1 - \mathrm{F}(\mathrm{x})$$

Equation 4.5

The Volume-CDF (V_L-CDF) relationships are plotted on a log-log scale with fitted Power-Law (P-L) and Log-Normal (L-N) distributions overlain. The distributions are computed using open-

source code ("poweRlaw", Gillespie (2015)), following a workflow based upon the approach outlined by Clauset, Shalizi and Newman (2009). In practice, it is near-impossible to state with certainty that a quantity is drawn from a power-law distribution, rather the data should be consistent with the hypothesis that x is drawn from a distribution expressed as;

$$\mathrm{p(x)} \propto \mathrm{x}^{-\alpha}$$

Equation 4.6

where α is a constant parameter known as the 'scaling parameter', and typically falls in the range $2 < \alpha < 3$, with occasional exceptions (Clauset, Shalizi and Newman, 2009). It has been found that a number of studies have purported empirical datasets following a power-law distribution which have later been refuted through careful statistical analysis. Stumpf and Porter (2012) state that "the most productive use of power-laws in the real-world will therefore... ...come from recognising their ubiquity (and perhaps exploiting them to simplify or even motivate subsequent analysis) rather than from imbuing them with a vague and mistakenly mystical sense of universality."

Power-law distributions in particular are characterised by their 'heavy-tail' which when compared to the 'bell-curve' of a Gaussian distribution, increases the likelihood of extreme events (Stumpf and Porter, 2012). For continuous data, the power-law distribution has a probability density function (PDF), expressed as;

$$\mathrm{p(x)} = \frac{\alpha - 1}{\mathrm{x_{min}}} \left(\frac{\mathrm{x}}{\mathrm{x_{min}}}\right)^{-\alpha}$$

Equation 4.7

where α > 1 and x_{min} > 0. The cumulative distribution function (CDF) for continuous data is shown as;

$$\mathrm{p(X \leq x)} = 1 - \left(\frac{\mathrm{x}}{\mathrm{x_{min}}}\right)^{-\alpha+1}$$

Equation 4.8

and the moments of a power-law distribution for continuous datasets are;

$$\mathrm{E}[\mathrm{X}^{\mathrm{m}}] = \int_{\mathrm{x_{min}}}^{\infty} \mathrm{x}^{\mathrm{m}}\, \mathrm{p(x)dx} = \frac{\alpha - 1}{\alpha - 1 - \mathrm{m}} \mathrm{x}_{\mathrm{min}}^{\mathrm{m}}$$

Equation 4.9

The estimation of the scaling parameter α is achieved using a maximum likelihood estimator (MLE), which for continuous data is;

$$\hat{\alpha} = 1 + n\left[\sum_{i=1}^{n} ln\frac{x_i}{x_{min}}\right]^{-1}$$

Equation 4.10

where x_i are the observed data values and $x_i \geq x_{min}$ (Muniruzzaman, 1957; Gillespie, 2015). The MLE for α is dependent upon the value of x_{min}, which is often not the minimum data value as the distribution often only follows a power-law for a truncated portion of the full dataset (i.e. the tail-end). x_{min} has commonly been estimated from a visual inspection of the distribution to determine the lower value from which data satisfies a power-law. Several authors have pointed out that this is highly subjective and open to data biases and error (Clauset, Shalizi and Newman, 2009; Virkar and Clauset, 2014; Gillespie, 2015). The Kolmogorov-Smirnov (KS) approach was proposed by Clauset, Shalizi and Newman (2009), to estimate the lower bound, which examines the maximum distance between the dataset and the fitted CDFs;

$$D = \frac{max}{x \geq x_{min}} |S(x) - P(x)|$$

Equation 4.11

where $S(x)$ and $P(x)$ are the CDFs of the data and model respectively (for $x \geq x_{min}$). The estimate chosen for x_{min} is therefore the value that minimises D, removing subjectivity and reducing the likelihood for error (Clauset, Shalizi and Newman, 2009; Gillespie, 2015).

The plausibility of the hypothesis that size distribution of detected slope failures follow either a P-L or L-N distribution is tested using a goodness-of-fit test via a bootstrapping procedure proposed by Clauset, Shalizi and Newman (2009) (Gillespie, 2015). Again, this test is also based on the distance between the data and hypothesised model, and is performed here using the KS statistic (Clauset, Shalizi and Newman, 2009), which implemented in R, returns a p-value where:

$p \simeq 1$: any difference between the data and the model can be explained with statistical fluctuations;

$p \simeq 0$: the model does not provide a plausible fit to the data and another distribution may be more appropriate.

Typically, analyses of the magnitude-frequency of slope failures include data from inventories spanning several orders of time-scales, from a few years to millennia. As the observational data used in this study cover just one year, the inventories of slope failures could misrepresent the probability of large-magnitude events that have previously been shown to occur at lower-frequencies than those of small- to mid-sized events. Therefore, larger magnitudes could skew fitted distributions as outliers and to account for this, two P-L and L-N distributions are fit to each dataset; one that considers the entire range of data, and another that considers only volumes that are smaller than one standard deviation greater than the mean.

The volume-to-surface-area ratio (V/S) is a crucial factor, and when considering spheres of varying radii, larger spheres with larger V/S are more prone to breakage due to the larger pressure applied on the unit surface area and therefore, as an object increases in size it must also reshape itself towards a smaller V/S to avoid crushing under pressure (Li, Lan and Wu, 2014). In terms of secondary slope failures, the effect of *cohesion* has often been discussed in regards to explaining potential driving forces of a rollover in slope failure datasets. Slope failure bodies are subject to three categories of force; gravity ($\mathrm{F_g}$), friction (F_f) and cohesion (F_c), among which gravity is the driving force whilst the other two are resistance forces. Under the principle that cohesion is broadly proportional to the failure surface area, the work of Li, Lan and Wu (2014) found that a decrease in the V/S (i.e. lower-magnitude slope failures) magnifies the resistance effect of cohesion which further results in a decrease in the slope failure frequency, thus they propose that the rollover observed in inventories that consider failures of the slide type (i.e. secondary failures) is since V/S is generally positively correlated with slope failure size (Li, Lan and Wu, 2014). Briefly, failure requires the overall force;

$$\mathrm{F_g} - \mathrm{F_f} - \mathrm{F_c} > 0$$

Equation 4.12

Gravity and friction are proportional to the mass and hence are proportional to slope failure volume (V_L), whereas the cohesion is proportional to the area of the slope failure surface (S). Therefore, slope stability can be associated with a balance between the resultant driving forces (the resultant force of gravity and friction) proportional to V_L and the resistance force (the cohesion) proportional to S and equation 4.12 can be written as;

$$GV_L - CS > 0$$

Equation 4.13

Where G and C are the proportional coefficients with respect to V_L and S respectively and are both related to the mechanical configuration of the slope failure. Therefore, the failure condition is equivalent to;

$$V/S > C/G = T$$

Equation 4.14

where the low threshold of V/S for a failure is denoted by T. Guzzetti *et al.* (2002), are amongst a number of authors who partly attribute the rollover in frequency to a termination in the self-similar power-law scaling applicable to medium-to-large-magnitude slope failures as a result of transitioning from principally friction-controlled (mid-to-large) resistive forcing to cohesion-controlled (small-magnitude). They explain this using the failure criteria (Terzaghi, 1962);

$$\tau_f = \tau_0 + (\rho g h - \mu) f$$

Equation 4.15

where τ_f is the failure shear stress of the slope failure's basal (sliding) surface, τ_0 is the cohesive strength of this surface, ρ is the density of the rock, g is the Earth's gravitational acceleration, h is the depth to the basal surface, μ is the pore pressure in the rock or soil, and f the coefficient of friction on the basal surface. Thus, for small, shallow slope failures, $\rho g h$ is small because h is small and failure is mostly controlled by the cohesive strength. Since the gravitational body force on the basal layer driving the slope failure is proportional to h, the cohesive force will prevent small slope failures (Guzzetti *et al.*, 2002), thus reducing their likelihood which is represented as a rollover in their CDF.

4.8 Structural Analysis

Unstable slopes present a significant hazard for human activities in popular mountain regions. Presently, slope stability assessments are typically limited to disparate and time-consuming site investigations, which are often static, qualitative and restricted to a very localised focus. Regional and network-scale slope stability, slope failure susceptibility and hazard potential modelling is usually conducted within a GIS environment (e.g. Chau *et al.* (2004); Ray and De Smedt, (2009)) with little or no field data. Such work relies on a few basic assumptions and a body of knowledge that is generally accepted amongst engineering geologists and geomorphologists

(Guzzetti *et al.*, 1999). Reliance of regional-scale GIS hazard assessments on historical inventories are prone to several issues including under-sampled areas (particularly remote environments) and low-resolution data (Guzzetti *et al.*, 1999). In this section, the technique for extracting discontinuity information and calculating the stability of slope masses is given. The workflow makes use of open-source code provided by Riquelme *et al.* (2014), Riquelme, Abellán and Tomás (2015) and Riquelme, Tomás and Abellán (2014). Other researchers have produced similar workflows and programs though for continuity and repeatability it was decided that the following workflow would be the most straightforward and has been shown to produce accurate and reliable results. An overview of the technique is given in this section whilst detailed descriptions can be found in Riquelme *et al.* (2014), for discontinuity identification and extraction; Riquelme, Abellán and Tomás (2015), for calculating joint spacing and; Riquelme *et al.* (2016), for an overview of the SMRTool. Combined with SfM-MVS, the workflow presents a rapid and capable solution to acquiring structural data across rock-slopes in environments which previously would have proven logistically challenging.

4.8.1 Joint Identification

To identify and characterise joints, the open-source Discontinuity Set Extractor (DSE) (Riquelme *et al.*, 2014) was utilised which uses bare (i.e. RGB and NxNyNz removed) 3D SfM-MVS point clouds as a raw input. Implemented in Matlab, DSE adopts a 3-step approach; (i) local curvature calculation, (ii) statistical analysis of planes, and (iii) cluster analysis. In the first stage, a K-nearest neighbours (knn) algorithm is applied to each point in the cloud to define a subset of neighbour points. Next, each subset is tested to establish whether it is coplanar (i.e. on the same plane as neighbouring subsets) or not. If it is the latter, the subset will be rejected whilst those subsets found to be coplanar are retained and a best-fit adjustment plane is computed to establish the orientation of each. A normal vector for each plane is converted to a stereographic projection and the density of the poles to that plane is calculated using a kernel density estimation (KDE). A principal orientation is then assigned to every point in the cloud, and those that are not represented receive no assignment. A user-specified cone filter (minimum value for the angle formed by two principle vectors) and maximum poles filter (maximum number of discontinuity sets) define a local maximum as a principal pole. The 'Density-Based Scan Algorithm with Noise' (DBSCAN) (Ester *et al.*, 1996) is used to cluster each discontinuity set before the plane equations are calculated to define the characteristics of each. As an example, figure 4.14 (Riquelme *et al.*, 2014) presents the stereographic projections of the poles of the normal vector of an experimental dataset (a cube, scanned using LiDAR - note that the base of the cube is not represented as it was not in view during the scan) (fig. 4.14 b), whilst the KDE-calculated density functions of the normal vector poles are presented in figure 4.14 (c) and (d), which as expected for a cube, are clustered into three orthogonal discontinuity sets (Riquelme *et al.*, 2014). At this stage, the peaks which reasonably

represent the orientations of the model can be identified using the information from the KDE, and results can be filtered to remove and erroneously represented orientations (Riquelme *et al.*, 2014). A further example, created using data from the rock-slope in the pro-glacial zone of the Glacier de Bossons, is given in figure 4.15.

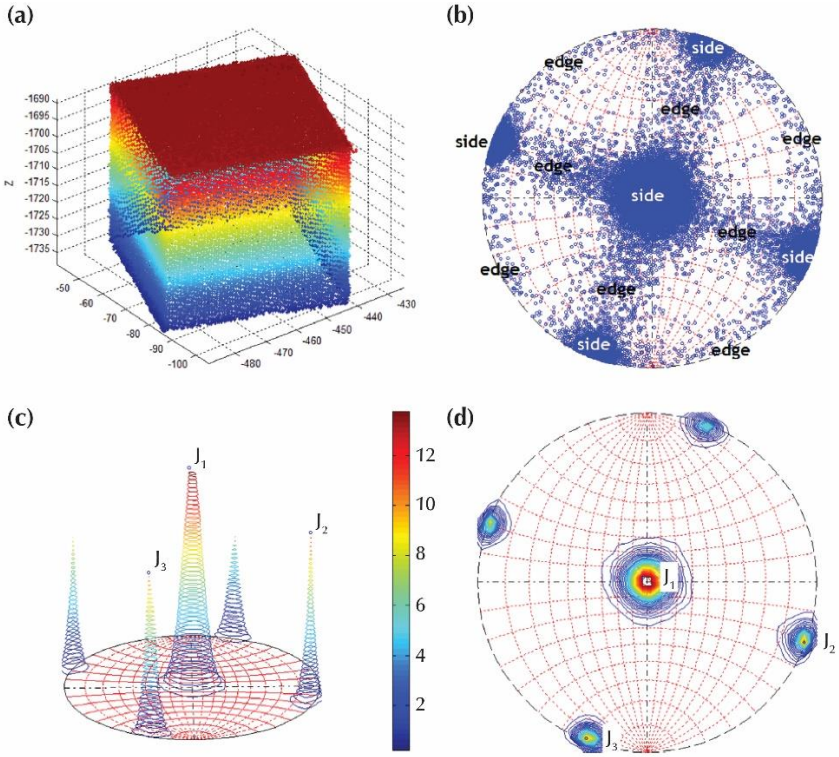

Figure 4.14: Example of DSE applied to experimental dataset (3D model of a cube with 50 mm sides); (a) Raw data 3D view of the cube (60,488 points). Plotted data were scanned at laboratory using a microlidar; (b) Normal vector poles stereographic projection, knn = 15. Side and edge poles zones are labelled.(c) and (d) Density estimation via kernels, isolines each 2%. Note that the identification of the main discontinuity sets is able to filter out the normal vectors calculated at the edges between planes. Modified from Riquelme et al. (2014).

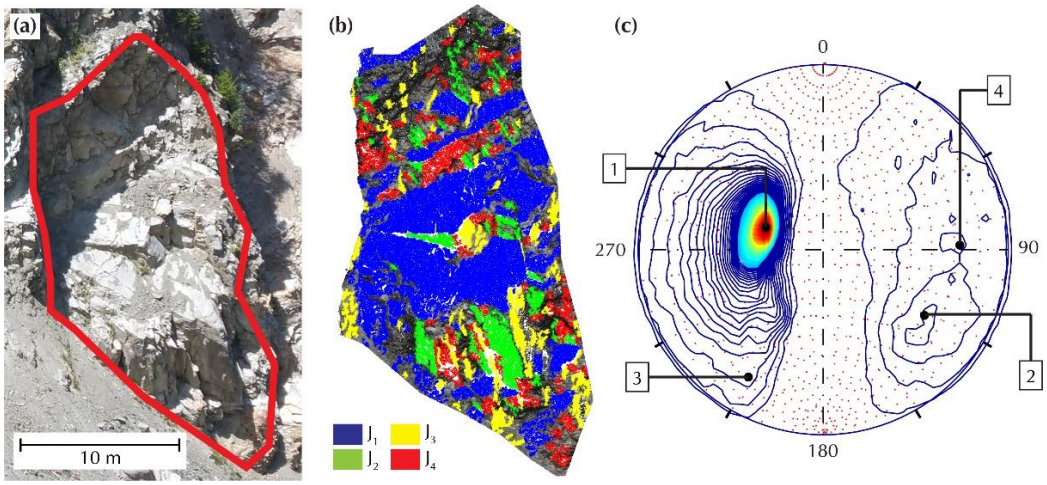

Figure 4.15: (a) Field photograph of section v with model area outlined. (b) Example of a 3D model with discontinuity set assignment to each point (J_1 to J_4) for section v; the points that are not associated to any set are not shown (knn=30,

n_{max}=20%, y_1=20, n_p=4, y_2=30, ppc=100). (d) Pole density function plot and set identification following discontinuity analysis for section v. Discontinuity set numbers highlighted.

4.8.2 Joint Spacing

The computation of joint spacing was performed using the method outlined by Riquelme, Abellán and Tomás (2015), available as open-source code utilising the previously DSE-classified data where each point is associated with an assigned joint cluster. Implemented in Matlab, clusters from each joint set are sorted in ascending order along a virtual scanline and the closest cluster is determined for each. Spacing is calculated as the normal spacing between them (fig. 4.16) (Riquelme, Abellán and Tomás, 2015). The non-parametric distribution of spacings for each joint set is calculated by means of kernel density estimation. Both non-persistent and fully-persistent approaches are considered in this approach (fig. 4.16). The non-persistence spacing values were used in this study to inform the stability assessment. This adds an additional complexity over other approaches which assume full persistence. However, non-persistence utilises the full geometry of the 3D data to consider discontinuity planes which are not necessarily intersected by a scanline and are distributed within the 3D space (Riquelme, Abellán and Tomás, 2015) which significantly increases the reliability of the approach.

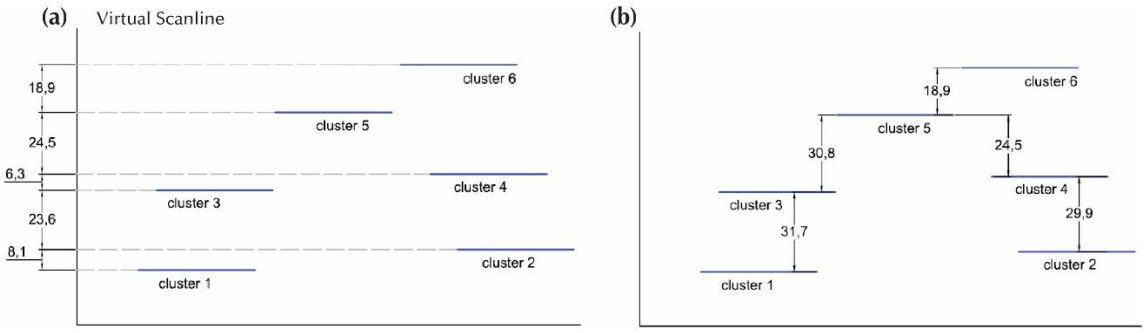

Figure 4.16: Schematic representation for the method of the cluster linking and the discontinuity normal set spacing considering (a) full persistence and (b) non-persistence of the discontinuities. Blue thick lines represent the discontinuities. Modified from Riquelme, Abellán and Tomás (2015).

Figure 4.17 is given as a clear example of how spacing is considered for a synthetic model (a table) with three orthogonal planes (Riquelme, Abellán and Tomás, 2015). DSE is first used to extract the discontinuity sets where J_1 represents the horizontal surfaces of the table and; J_2 and J_3 refer to the vertical planes with three principal orientations identified which correspond to the four rectangular legs and the table top (Riquelme, Abellán and Tomás, 2015). Spacings are calculated for each discontinuity set, measuring distances between each cluster within the set (fig. 4.17 b and d) and are summarised in table 4.3 for J_2. The calculated differences (D_i - D_j) are shown

alongside real distances and show a good agreement with small error values. The algorithm first considers cluster 1 (refer to fig. 4.16 d) whose plane equation shows the lowest D value, before searching for the nearest cluster (in this example, 4) and calculating the distance between the two. This continues in ascending order, according to the D parameter, until all clusters have been considered (Riquelme, Abellán and Tomás, 2015).

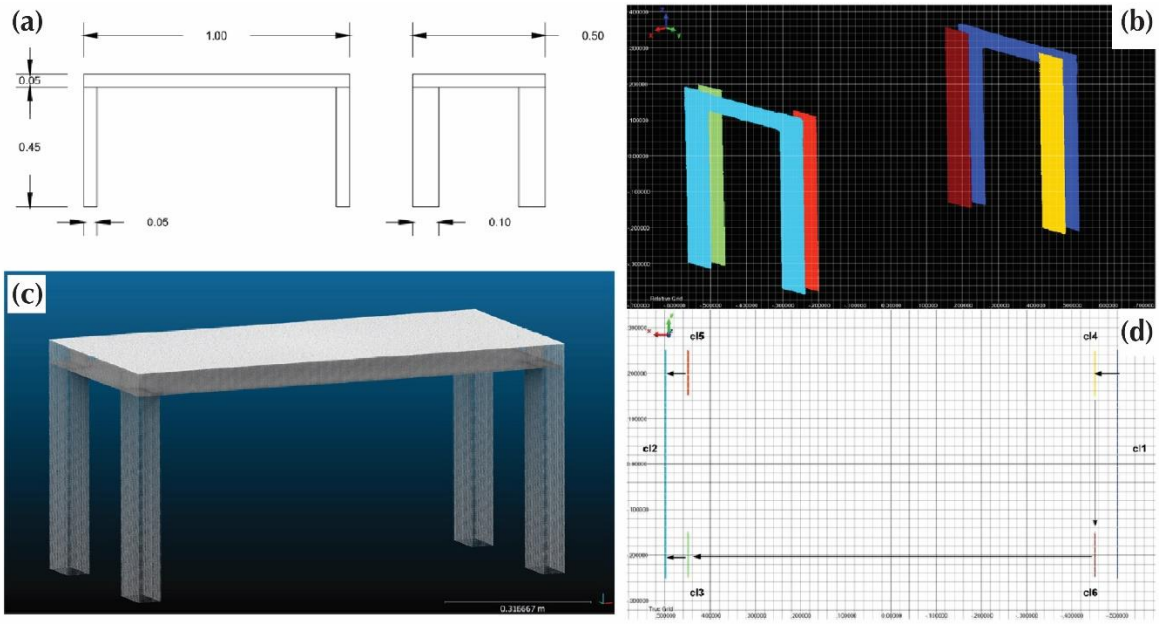

Figure 4.17: Example of technique for calculating joint spacing with experimental dataset (modelled table); (a) Map of the modelled table with dimensions (in metres); (b) point cloud of the modelled table, where all sides are orthogonal;(c) Example of one of the discontinuity sets extracted using the DSE algorithms (Riquelme et al., 2014), made up of six clusters which are individually coloured; (d) top view of the discontinuity set with measurements required for spacing denoted with black arrows (Riquelme, Abellán and Tomás, 2015).

Table 4.3: Results of joint spacing (J_2) analysis for modelled table (Riquelme, Abellán and Tomás, 2015).

Cl_i	Cl_j	D_i (m)	D_j (m)	D_i - D_j (m)	Distance (m)	Abs Error (m)
1	4	-0.4927	-0.4485	0.0442	0.05	0.0058
4	6	-0.4485	-0.4392	0.0093	0.00	0.0093
6	3	-0.4392	0.4603	0.8995	0.90	0.0005
5	2	0.4510	0.5068	0.0558	0.05	0.0058
3	2	0.4603	0.5068	0.0465	0.05	0.0035

4.8.3 Slope Stability (Slope Mass Rating)

Section 2.8.1.1 provided an overview of the Slope Mass Rating (SMR), which derives from the Rock Mass Rating (RMR) and is calculated as;

$$SMR = RMR_b + (F_1F_2F_3) + F_4$$

Equation 4.16

where RMR_b is the basic RMR index (table 2.2) (Bieniawski, 1976) without any correction; F_1, F_2 and F_3 are slope correction factors where F_1 depends on the parallelism between discontinuities and the slope face; F_2 depends on the discontinuity dip and; F_3 depends on the relationship between the slope face and the discontinuity dip. F_4 is a descriptive value that identifies the excavation method (if any) (Romana, 1993).

Table 4.4: Slope Mass Rating (SMR) class descriptions (Romana, 1993).

Class	SMR	Description	Stability	Failures
I	81-100	Very good	Completely stable	None
II	61-80	Good	Stable	Some blocks
III	41-60	Normal	Partially stable	Some joints or many wedges
IV	21-40	Bad	Unstable	Planar or big wedges
V	0-20	Very bad	Completely unstable	Big planar or soil-like

Whilst the SMR ratings detailed in table 4.4 and the required RMR values in table 2.2 are a relatively simplistic categorisation of rock mass strength, as discussed in section 2.8.1.2, mapping discontinuities across a slope is traditionally a time-consuming, labour-intensive and sometimes costly process which can be impeded by limited access in challenging environments. The use of 3D slope data and semi-automated workflows, such as those outlined in this chapter, for the identification and characterisation of slope characteristics allows spatial coverage of an unprecedented scale using consumer-grade technology. Whilst not considered in this study, others have conducted work across the slopes of high-alpine rockwalls such as Aiguille du Midi and the Dru (e.g. Deline *et al.* (2008), Ravanel and Deline (2011) and Matasci *et al.* (2014)) which present significant logistical challenges for qualitative analyses of slope stability. However, remote sensing campaigns (such as terrestrial laser scanning or digital photogrammetry) are significantly more achievable and a workflow such as that presented here would be of great use to characterising the stability of such challenging environments.

The SMR index is calculated using the open-source code; SMRTool (fig. 4.18) (Riquelme, Tomás and Abellán, 2014). The required inputs for calculation of the SMR are (i) the orientation of the slope; (ii) the excavation method (if applicable); (iii) the orientation of each of the joint sets (extracted using the method outlined in section 4.8.1); and (iv) the RMR_b value (Riquelme, Tomás

and Abellán, 2014). The DSE-classified data for (i) and (iii) is correct globally as the SfM-MVS data are georeferenced to a global coordinate system (WGS84 UTM Zone 32N). Some information for the calculation of RMR_b for each discontinuity set was extracted from the 3D point clouds however, some parameters require extra information that cannot be obtained this way. As a result, this information was obtained from visual analysis of the slope (also possible with model when RGB values are applied) and the RocProp 2.0 rock properties database (version 5.001) (RocScience, 2014). SMRTool automatically calculates the adjustment/correction factors (Tomás, Delgado and Serón, 2007) as well as the corresponding wedge for each couple of discontinuity sets (Riquelme, Tomás and Abellán, 2014; Riquelme *et al.*, 2016). It also calculates the possible mode of failure for each joint set and as an aid to understanding, creates a conceptual cross-section where the joint set intersects the slope (fig. 4.18).

Following the calculation of the SMR for each joint set using SMRTool, the rating is stored as an attribute of each point in the joint set which allows the variability of the index across the rock-wall to be mapped in GIS. Differences between pre- and post-large failure analysis of stability, quantified using the SMR offers a unique insight into the structural variability and possible drivers of change across recently de-glaciated slopes. As discussed earlier in section 2.8.1.1, the rock mass strength (measured using the SMR) has been shown to vary inversely with rockwall recession rate (Moore *et al.*, 2009). Recently-deglaciated rockslopes, such as those presented in this thesis, are thought to more vulnerable to instability through mechanical processes such as debuttressing (a loss of support), permafrost degradation and cyclical freeze-thaw action (Kenner *et al.*, 2011). Comparisons between the stability and erosion rates of the rockwalls studied here and those in other (non-glaciated) environments may also further our understanding of whether rockwall recession is characteristic of the decadal to centennial period following deglaciation. This analysis was performed across the rock-slope in the pro-glacial zone of the Glacier de Bossons, using point cloud data created using imagery from terrestrial and UAV surveys. Using historic imagery, it is estimated that the rockwall became exposed through deglaciation between 1990 – 2000 (Nussbaumer and Zumbühl, 2012). The full-valley surveys of Argentière and Mer de Glace were captured at too great a distance from the high-altitude rock-walls and as such, the photogrammetric workflow is incapable of resolving the detailed structural information required for this analysis.

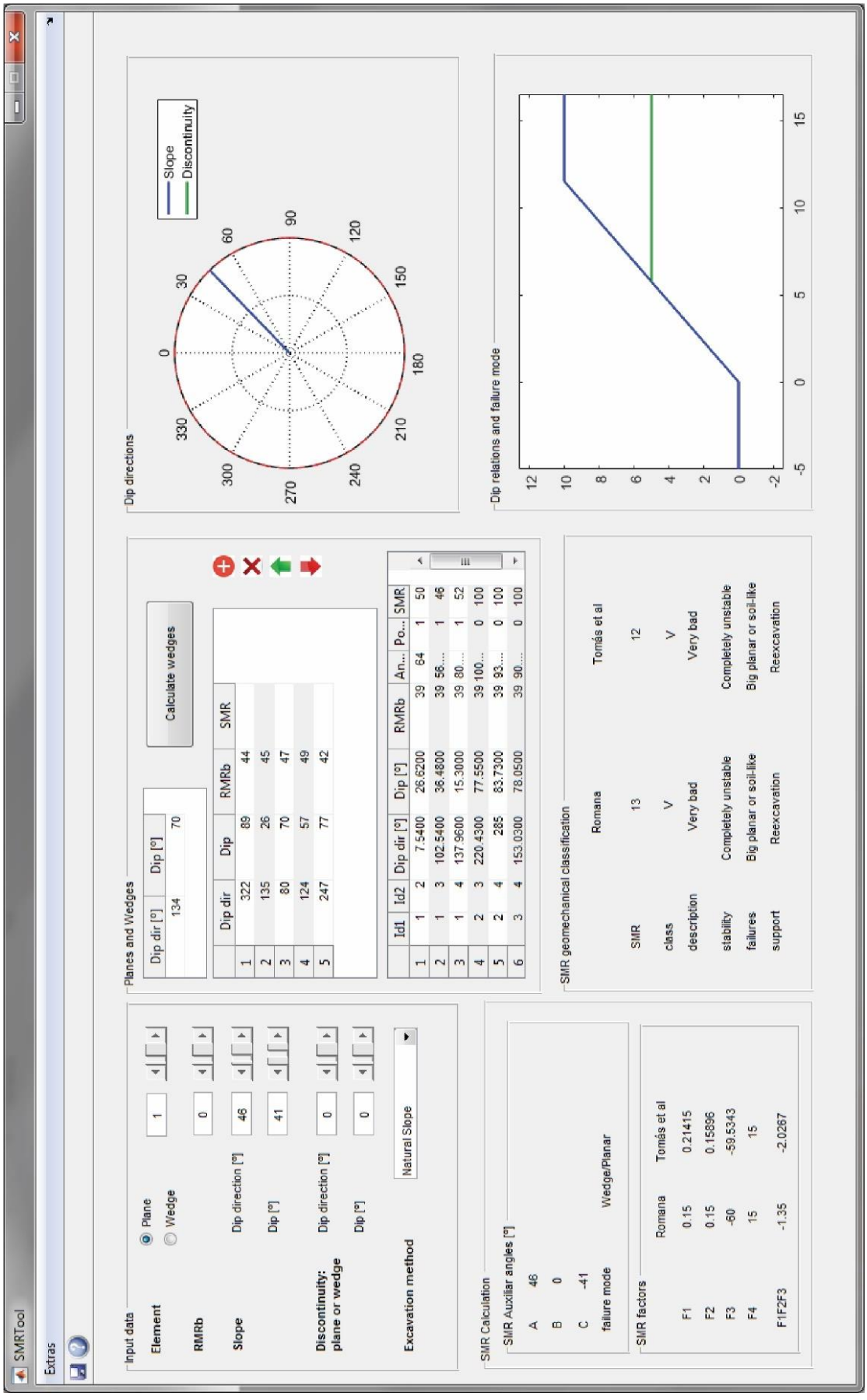

Figure 4.18: Screenshot of the SMRTool interface where user-input parameters are used to calculate to SMR of rock masses.

4.9 Mont Blanc Massif Data

SfM-MVS photogrammetry was used to create models at five sites; Glacier d'Argentière (fig. 4.19), Mer de Glace (fig. 4.20), Glacier de Bossons (fig. 4.23), Ghiacciaio del Miage (fig. 4.22) and Pre de Bard (fig. 4.21). This section provides an overview of each of the site models and outlines the LOD thresholds in preparation for the presentation of results in the following chapter. The models were created using images from a terrestrial, UAV and helicopter perspective. Following the creating of a 3D point cloud for each site using the SfM-MVS workflow outlined in section 4.4, the models were cropped into sections for change detection analysis in order to ease computational intensity. These sections are denoted by the blue boxes on figures 4.19 to 4.23. Sectioning also had the added benefit of ensuring the LOD threshold was minimised as rockslopes were separated from sediment-mantled slopes, and areas such as the higher alpine rockwalls (HARW) where model resolution limited detectable failures did not affect sections of slope where resolution was considerably higher (and thus, a lower LOD threshold). Section numbers denoted within or near the blue boxes at each site on figures 4.19 to 4.23 correlate to the LOD thresholds given in tables 4.5 to 4.9.

As outlined in section 4.5.2, the LOD threshold is a Spatially Variable Confidence Interval (SVCI), which considers the local surface roughness and alignment registration error (RMSE). The tables in section 4.5.2 summarise the LOD threshold for each of the models used in this study. As mentioned in the previous paragraph, models were separated into sections following georeferencing based on their characteristics (i.e. moraine vs. rock-slope), natural separation (i.e. where snow or vegetation created a natural divide) or along distinct geological boundaries (i.e. along principle joints). This allowed more accurate alignments between sections (linear movements in orientation and space only, no adjustments to scale) and reduced computational intensity during change analysis. The values in the tables below are those which are referred to in the following chapter when a detected failure is said to be 'above the LOD threshold'. For each section, the LOD threshold and slope-type is given (R-S = rock-slope, U-S = unconsolidated-sediment, M = mixed).

At the Glacier d'Argentière site, LOD thresholds vary from a maximum of 4.55 m on the NE-facing slope in section 6, to a minimum of 0.23 m on the NE-facing slope in section 14. Section 6 on the NE-slope (fig. 4.19 lower) represents a section of HARW and poor (i.e. high) thresholds are a consequence of; i) a greater distance between the sensor (camera in helicopter) and the slope surface and; ii) poor illumination across the slope which hampers the capability of image-matching algorithms. Similarly, across the slopes of the Mer de Glace the LOD threshold is variable with a maximum of 3.14 m on the SW-facing slope (fig. 4.20 upper) in section 4 and a minimum of 0.48 m on the NE-facing slope (fig. 4.20 lower) in section 9. Section 4 on the SW-slope represents an area of rockwall above the LIA trimline with a high surface-roughness caused by vegetation whilst section

9 on the NE-slope is an area of rockslope exposed over the last few decades following the degradation of the Mer de Glace. At the Glacier de Bossons, a terrestrial and UAV survey site, shorter distances between the sensor and the slope are reflected in relatively low LOD thresholds across the surveyed area (ranging from 0.11 to 0.29 m) which has implications for scale-dependency of quantified failures. This is discussed further in chapter 6. With the exception of section 4 at the Ghiacciaio del Miage, the sections at this site and Pre de Bard are also relatively lower than the full-valley surveys as a consequence of shorter distances and a greater level of overlap/sidelap between successive images. The higher LOD threshold for section 4 at the Ghiacciaio del Miage is the result of poor illumination in the repeat survey making the identification of correlating ground control a particularly difficult task.

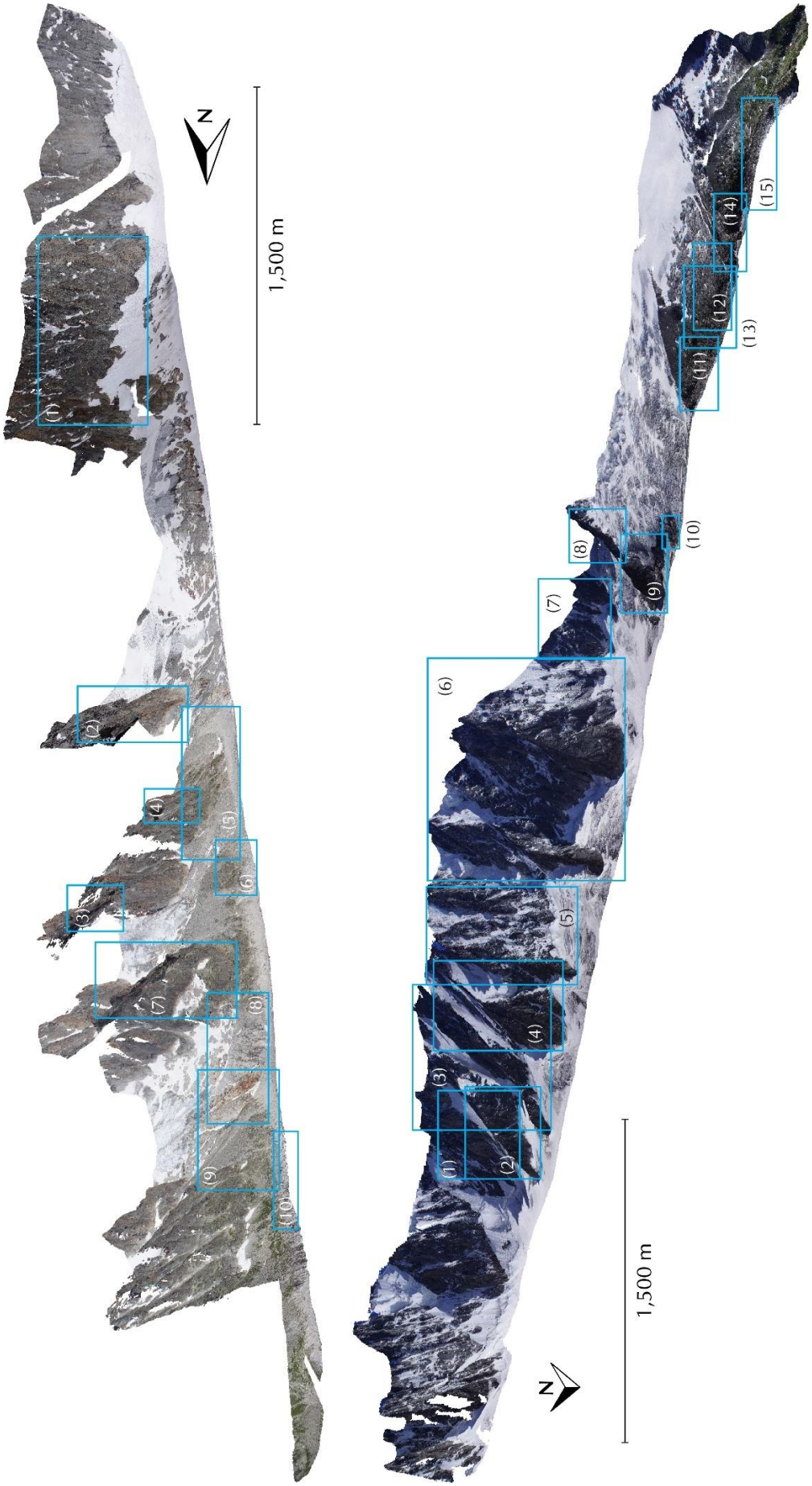

Figure 4.19: Overview of the model and location of each processing section: Glacier d'Argentière

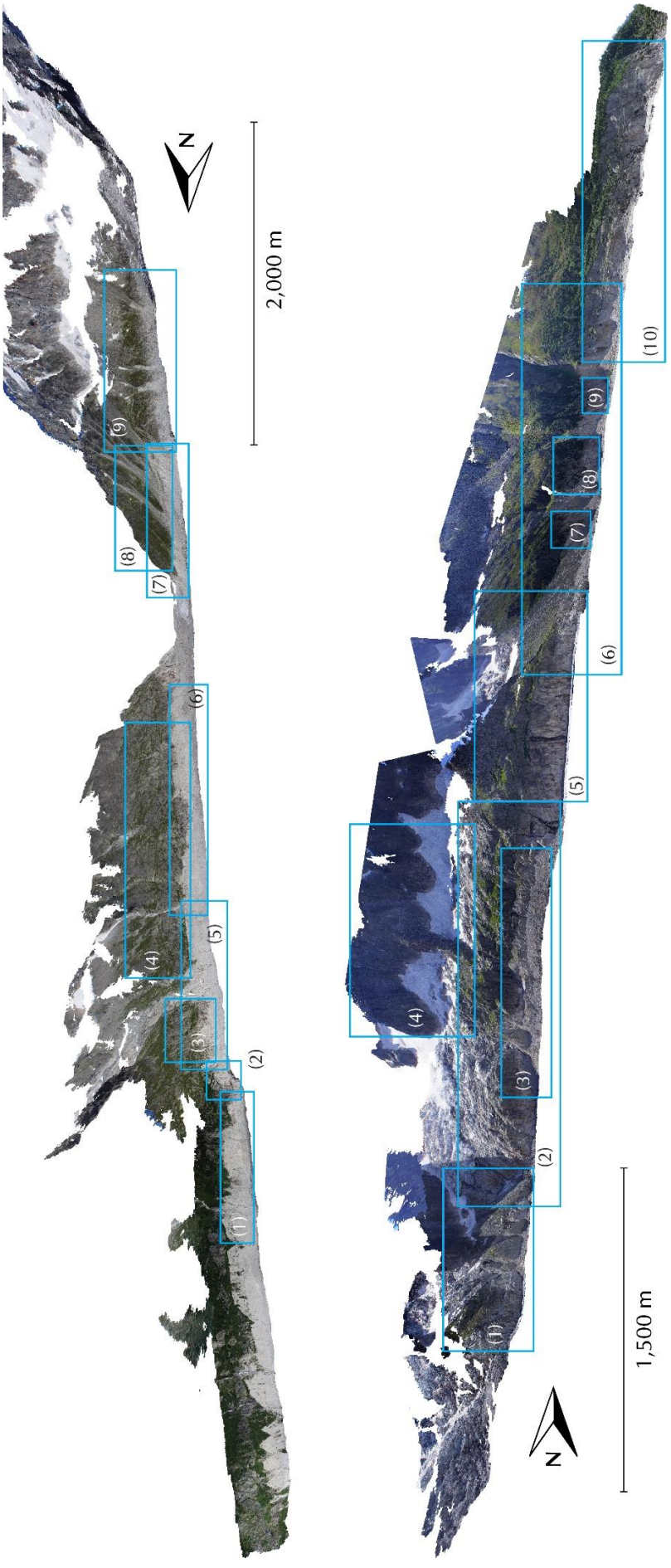

Figure 4.20: Overview of the model and location of each processing section: Mer de Glace

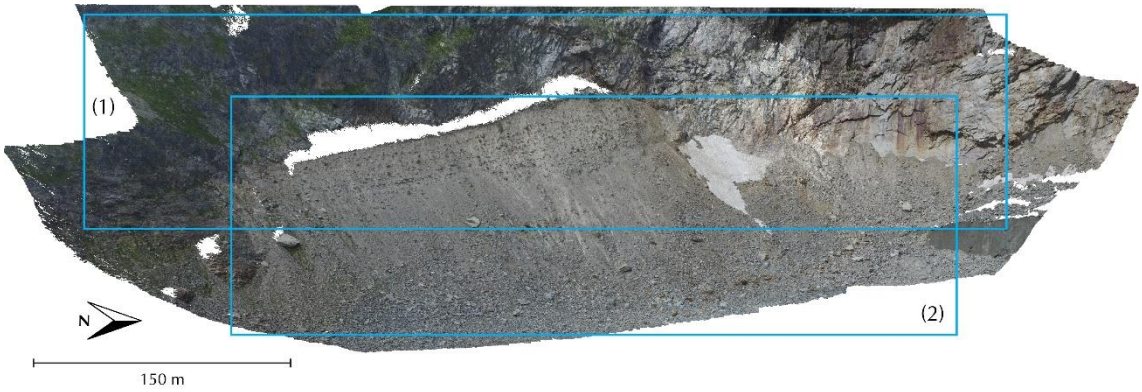

Figure 4.21: Overview of the model and location of each processing section: Pre de Bard.

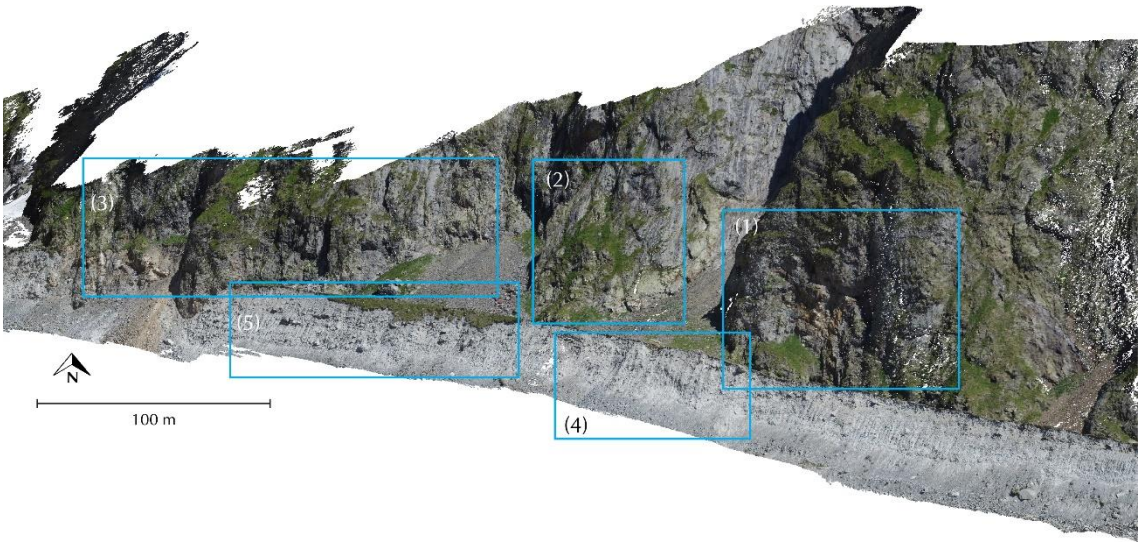

Figure 4.22: Overview of the model and location of each processing section: Ghiacciaio del Miage.

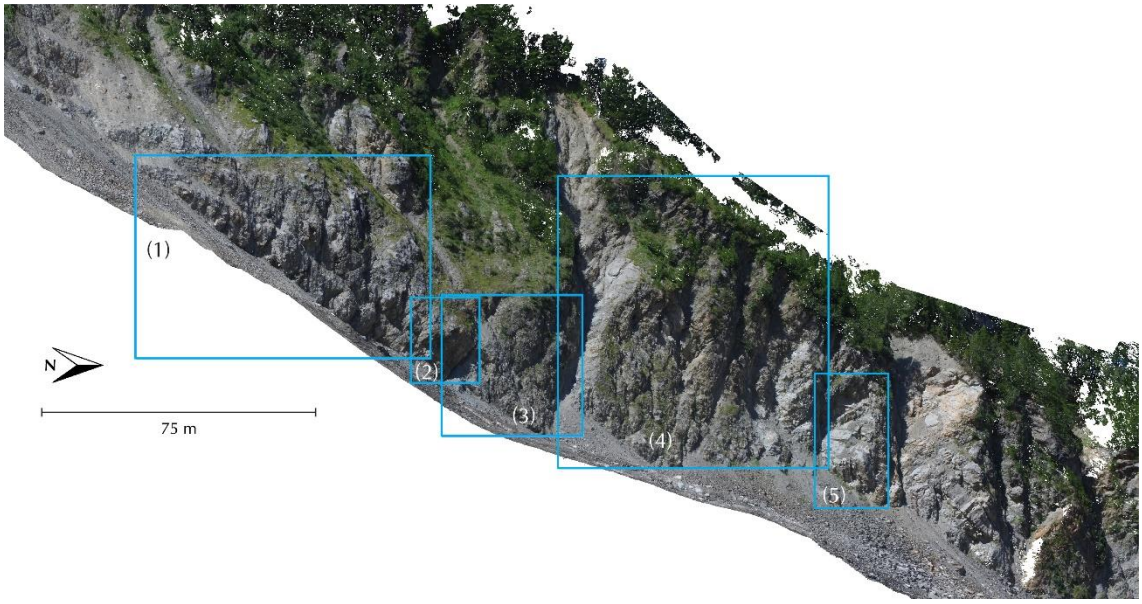

Figure 4.23: Overview of the model and location of each processing section: Glacier de Bossons.

4.9.1 Level of Detection Thresholds

Table 4.5: Summary of LOD thresholds and slope-type: Glacier d'Argentière.

NE-Slope			SW-Slope		
Section	LOD Threshold (m)	Slope-Type	Section	LOD Threshold (m)	Slope-Type
1	0.71	R-S	1	1.19	R-S
2	0.94	R-S	2	1.39	R-S
3	2.46	R-S	3	1.45	R-S
4	0.75	R-S	4	0.65	R-S
5	1.21	R-S	5	0.45	U-S
6	4.55	R-S	6	0.31	R-S
7	0.67	R-S	7	1.70	R-S
8	0.84	R-S	8	0.46	R-S
9	3.14	R-S	9	0.75	U-S
10	0.76	R-S	10	0.49	R-S
11	0.29	R-S			
12	0.26	R-S			
13	0.37	U-S			
14	0.23	R-S			
15	0.33	U-S			

Table 4.6: Summary of LOD thresholds and slope-type: Mer de Glace.

NE-Slope			SW-Slope		
Section	LOD Threshold (m)	Slope-Type	Section	LOD Threshold (m)	Slope-Type
1	1.13	M	1	2.77	M
2	0.89	R-S	2	0.75	R-S
3	1.45	U-S	3	0.50	R-S
4	1.12	R-S	4	3.14	R-S
5	0.67	R-S	5	1.90	U-S
6	1.54	U-S	6	1.94	U-S
7	0.70	R-S	7	1.57	U-S
8	0.65	R-S	8	0.76	M
9	0.48	R-S	9	1.67	M
10	0.74	R-S			

Table 4.7: Summary of LOD thresholds and slope-type: Glacier de Bossons.

Section	LOD Threshold (m)	Slope-Type
1	0.29	R-S
2	0.27	R-S
3	0.11	R-S
4	0.17	R-S
5	0.23	R-S

Table 4.8: Summary of LOD thresholds and slope-type: Ghiacciaio del Miage.

Section	LOD Threshold (m)	Slope-Type
1	0.49	R-S
2	0.29	R-S
3	0.53	R-S
4	2.00	U-S
5	0.62	U-S

Table 4.9: Summary of LOD thresholds and slope-type: Pre de Bard.

Section	LOD Threshold (m)	Slope-Type
1	0.32	R-S
2	0.29	U-S

4.10 Summary

This chapter outlines;

i) the workflow for taking photographs on Alpine slopes and using the SfM-MVS photogrammetric technique to create accurate 3D models;
ii) the steps taken to understand sources of error during the creation of 3D models using SfM-MVS and the approach taken to ensure these do not propagate through to the final results through the effective use of thresholding;
iii) using the multi-scale point cloud comparison algorithm, M3C2, to detect areas of significant change between consecutive surveys and calculate volume using the 3D data output;
iv) using open-source code to analyse the geological structure of a rock-slope for the purpose of stability assessment;
v) the statistical approach for examining the size distribution of detected slope failures and determining its significance;
vi) the use of GIS to analyse the spatial distribution of slope failures in order to identify any patterns across the study are.

In terms of the SfM-MVS workflow presented here, a number of technical and conceptual advances are made. For example, this is the first use of multi-scale (single slope to valley-wide) surveys utilising images captured from several platforms (terrestrial, UAS and helicopter). The

benefits of such an approach are; i) the ability to create high-resolution models of slopes above and around wasting glaciers with an aim of quantifying slope processes at a fraction of the cost of traditional approaches such as TLS; ii) the combination of smaller surveys captured using terrestrial and UAS imagery with larger surveys utilising helicopter-captured imagery offers valuable insights into slope failure distributions across much wider scales, and; iii) identifying key caveats of the SfM-MVS techniques such as a negative relationship between distance from slope/ percentage image overlap and model quality (though the former is a caveat of most survey techniques), and issues associated with surface roughness, illumination and model-to-model alignment. A novel approach to dealing with poor illumination using a composite of the RGB values across the point cloud is proposed and appears to be effective at reducing the RMSE following cloud-to-cloud alignment. A unique method of calculating volume using the output from a multi-scale model-to-model comparison algorithm (M3C2) is promising and appears to generate volume estimates in-line with other approaches. However, thorough field testing and quantification would be required to accurately assess levels of error in volume estimates – this is discussed further in chapter 7 as a suggestion for future work.

The use of a statistical approach to calculating the magnitude-frequency and goodness-of-fit for fitted P-L and L-N models is a more thorough approach than has previously been demonstrated in the literature and removes any element of subjectivity, bias or error by providing a statistical validation of how well the size distribution of failures follows either or neither of the models. This has important implications for our understanding of slope processes and hazard prediction which are discussed further in chapters 5 and 6. Using the models for change analysis and structural analysis generates another dimension of knowledge and will offer unique insights into possible driving mechanisms of change across rockslope failures (i.e. structural controls on primary slope failure events). The following chapter will present the results obtained from performing the methods outlined in this chapter.

5 Results

5.1 Introduction

SfM-MVS data were collected across the slopes above and around five glaciers in the Mont Blanc massif, the first such attempt to quantify slope failure activity across such a scale; two full-valley surveys conducted using imagery captured from a helicopter and more-detailed surveys across slopes at four of the five sites, conducted using a combination of terrestrial and UAV imagery. This chapter presents the results of change detection analysis across these five sites in the Mont Blanc massif, in the order of; Argentière, Mer de Glace, Bossons, Miage and Pre de Bard. Change detection processing highlighted areas of significant differences, above the LOD threshold outlined in the previous chapter (section 4.9.1). An overview of the detected slope failures at each site is given and their spatial and size distributions are presented. The events are combined and presented as collective inventories of primary and secondary slope failures and range-scale spatial and size distributions are presented. Data were obtained using the methods outlined in the previous chapter, whilst the implications of the results presented here are discussed in the next chapter.

As sites are presented individually, some important considerations are given in this section that apply across sections 5.2 to 5.7. It is worth noting (with all sites), that the mean volume estimates do not square with the mean width, height and depth estimates as would be expected with cuboid volume. This is partly a function of the methodological approach and the nature of the slope failures. As outlined in section 4.7, width and height are calculated using the minimum *x*,*y* and *z* values subtracted from the maximum values for each slope failure and thus represent the maximum of both metrics (e.g. slope failure ARG 1 from the inventory – see appendix 1, section 8.2 – has a width of 18.49 m and a height of 9.28 m at its greatest points). As well as this, the mean depth values, calculated as an average of the measured distances along a single axis perpendicular to the slope, mask the variability of the failure scar surface. For example, slope failure MDG 197 from the inventory – see appendix 1, section 8.2 – has a mean depth of 4.02 m but a closer look at all of the measured distances reveals a maximum distance of 41.26 m. This variability in failure depth is partly responsible for discrepancies between W_L x H_L x D_L volume estimates and measured V_L estimates. It is assumed that the V_L estimates calculated using the method outlined in section 4.5.3 are more reliable as they consider the full geometry of the slope failure surface.

Using the method outlined in section 4.5.2 (connected components), individual failures are identified based on their proximity to other areas of loss as defined by a user-specified minimum distance. This raises several important considerations; i) it is assumed that areas of significant change are single slope failures and are counted as such. As the sampling interval is one year for most surveys, it is possible that the number of detected events does not represent the number of discrete slope failures. For example, primary slope failures will likely lead to subsequent failures

from the same destabilised site. Similarly, measurements of single large secondary slope failures could in fact be comprised of many smaller coalescing failures; ii) as a consequence of point (i), it is important to note that magnitude may be overestimated (i.e. measuring multiple failures as one) and frequency may be underestimated (i.e. sampling interval of one year is not sufficient to detect discrete failure events). As outlined in section 4.7, larger magnitudes could skew fitted distributions and therefore, two P-L and L-N distributions are fit to each dataset; one that considers the entire range of data, and another that considers only volumes that are smaller than one standard deviation greater than the mean (failures ≤ σ_1). This is a crucial assumption, but one that could go some way to reducing the likelihood of measuring coalescing or same-site repeat failures as a single event. Nevertheless, the consequence of overestimating the magnitude and underestimating the frequency will be discussed further in chapter 6.

5.1.1 Chapter Objectives

The objectives of this chapter are to;

1) Outline the results of change detection analysis across the five sites of the Mont Blanc massif.
2) Present the key patterns of spatial distribution of the detected slope failures.
3) Explore the relationships between slope failure geometries and their size distributions.
4) Present the results of site- and range-scale (combined) analyses to identify regional signals and drivers of change.

5.2 Glacier d'Argentière (Annual, Helicopter vs. Helicopter)

The annual surveys of the Glacier d'Argentière account for change from the 6th August 2014 to the 30th June 2015 (329 days inclusive), across the full length of the glacial valley. The surveys of the NE- and SW-facing slopes above the Glacier d'Argentière covered lengths of roughly 7 and 9 km, and heights of 1.5 and 2 km. This resulted in areas of approximately 10.5 and 18 km^2 respectively yielding point-clouds well in-excess of 160 and 200 million points with an average point density of approximately 25 pts/ m^3.

A total of 10 primary (i.e. from bedrock) and 196 secondary (i.e. from moraines, scree slopes, and other non-bedrock slopes) slope failures above the level-of-detection threshold (table 4.5) were identified between 2014 and 2015 spanning several orders of magnitude. They resulted in a total volumetric loss of 1.3 x 10^2 m^3 and 5.5 x 10^3 m^3 respectively.

5.2.1 Spatial Distribution

The location and distribution of volume (V_L) of the primary- and secondary-type slope failures are given in figure 5.1. They are clustered in areas where there is slope-glacier contact. There were no failures that exceeded the LOD threshold across high-altitude rockwalls. Secondary failures are detected in three areas; (i) across the lateral margins of the NE-facing slope near the terminus of the glacier; (ii) along the lateral moraine of the receded tributary glacier, the Glacier du Chardonnet and; (iii) at the lateral margin of the glacier on the SW-facing slope, near to the Glacier des Amethysts.

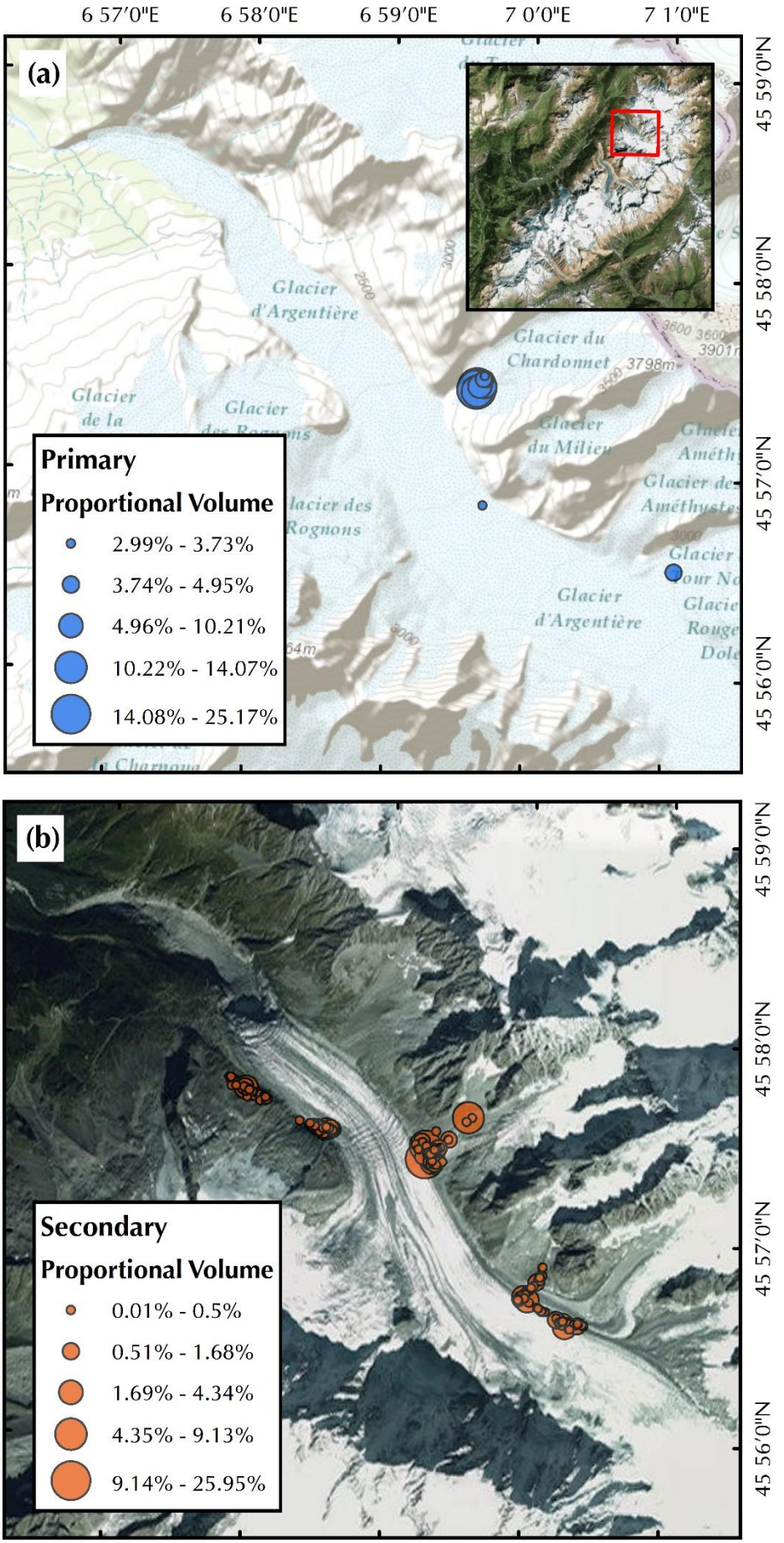

Figure 5.1: Maps showing the location of detected primary (a) and secondary (b) slope failures at the Glacier d'Argentière using change analysis of annual topographic datasets. Failure volumes are shown as a percentage of their respective totals. Inset on (a) for reference. Basemap data from ESRI.

The probability density functions (PDF) for secondary slope failures (too few primary failures were recorded for a meaningful density function) were calculated for failure altitude, pre-failure slope angle, and failure aspect and are shown in figure 5.2 (a, b & c respectively). Maximal densities occur at an altitude of approximately 2,500 m a.s.l. across slopes at a pre-failure angle of 35-40° with a predominantly SW aspect.

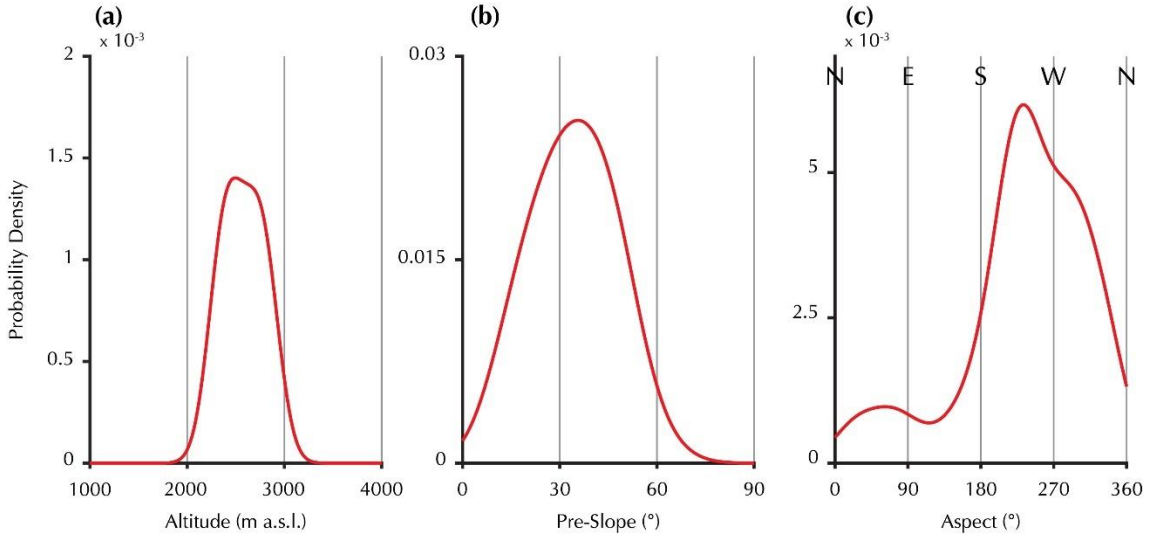

Figure 5.2: Probability density functions for (a) slope failure altitude; (b) pre-failure slope angle and; (c) slope failure aspect from the inventory of secondary failures at the Glacier d'Argentière site. The probability of failure for a horizontal slope in (b) is shown as > 0 – this is an artefact of the statistical process and not a real probability.

Examples of detected secondary failures on the SW- and NE-facing slopes are given in figures 5.3 and 5.4 respectively. On the SW-facing slope (fig. 5.3), failures can be seen to cluster around the ridge of the lateral moraine of the receded Glacier du Chardonnet, with further losses from the debris cones at the base of the gullied sediment-mantled slope. On the NE-facing slope (fig. 5.4), failures are randomly distributed across the slope, below the ridge-line of the lateral moraine. No failures above the LOD threshold were detected on the rockslopes above the ridge-line. In both examples, debris falls straight onto the surface of the glacier, or is stored at the base of the slopes in debris cones.

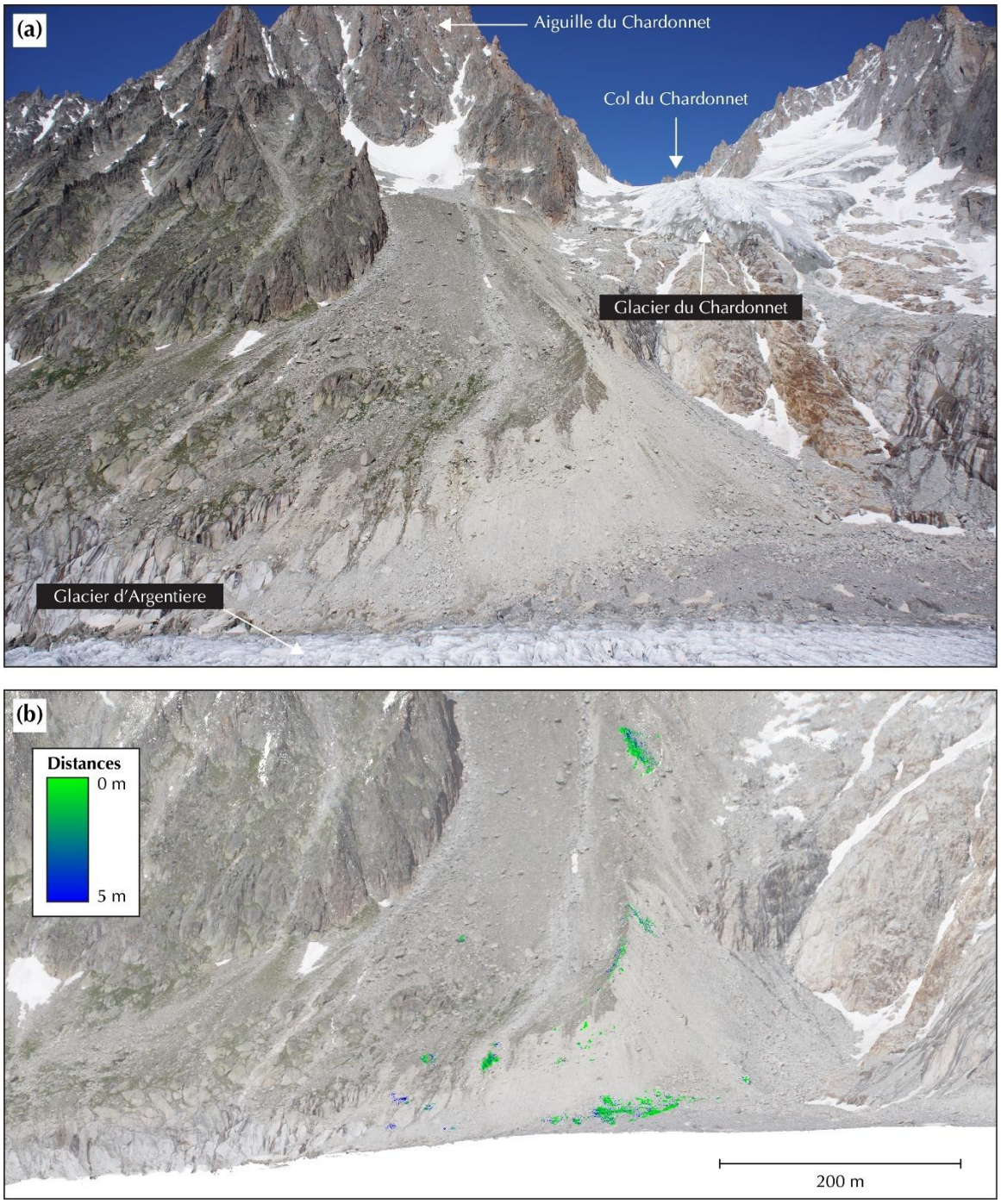

Figure 5.3: Example of the measured distances above the level-of-detection threshold (~ 0.75 m) at section 9 of SW-facing slope of the Glacier d'Argentière dataset. (a) Field photography for context of location with key features labelled and; (b) post-failure point cloud overlain with measured distances in areas deemed significant by the M3C2 change detection technique.

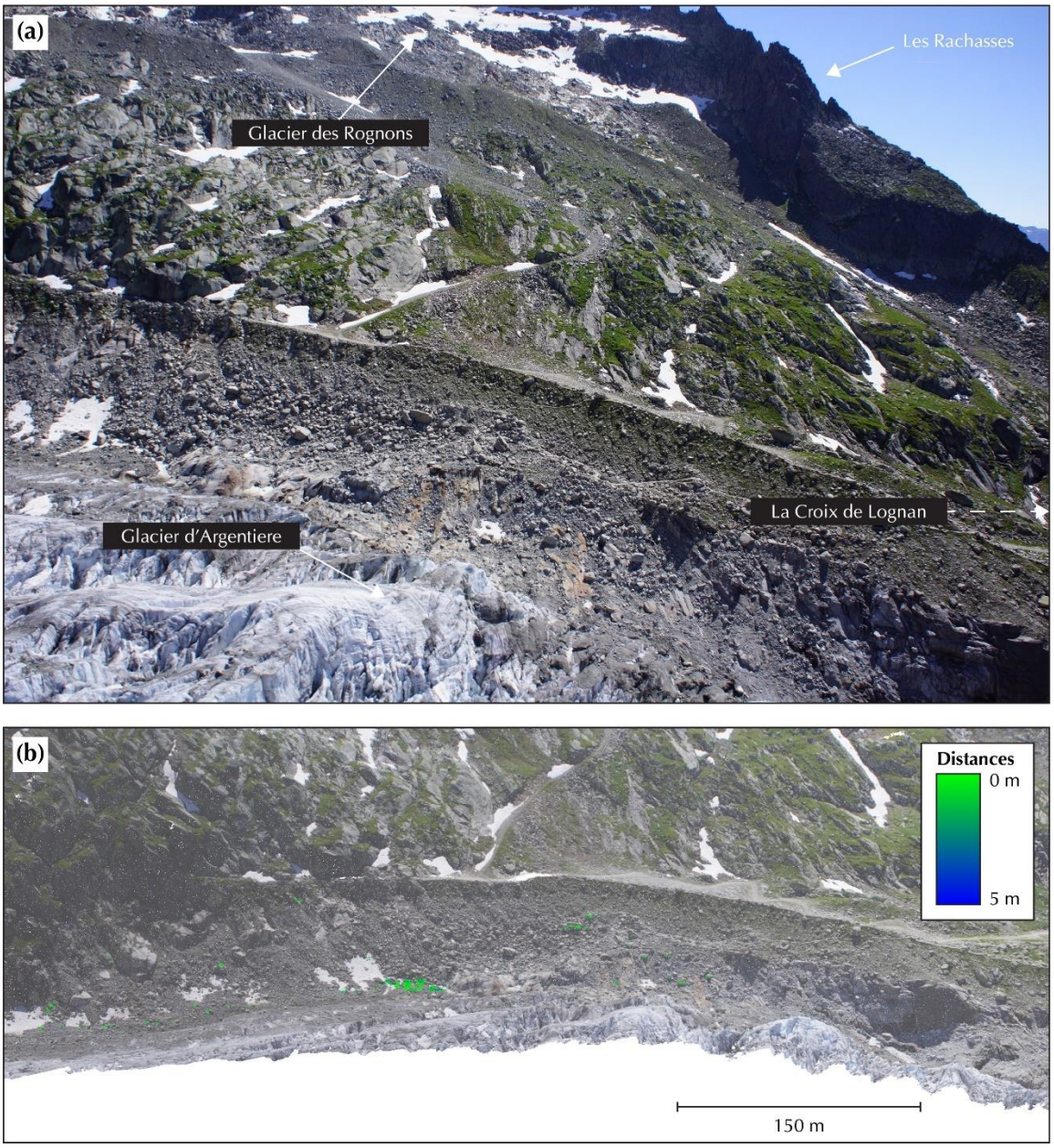

Figure 5.4: Example of the measured distances above the level-of-detection threshold (~ 0.33 m) at section 15 of the NE-facing slope of the Glacier d'Argentière dataset. (a) Field photography for context of location with key features labelled and; (b) post-failure point cloud overlain with measured distances in areas deemed significant by the M3C2 change detection technique.

The mean depth of each secondary slope failure is plotted against the pre-failure slope angle in figure 5.5. The largest mean depth, approximately 2.4 m, is found on the pre-failure slope with the steepest gradient.

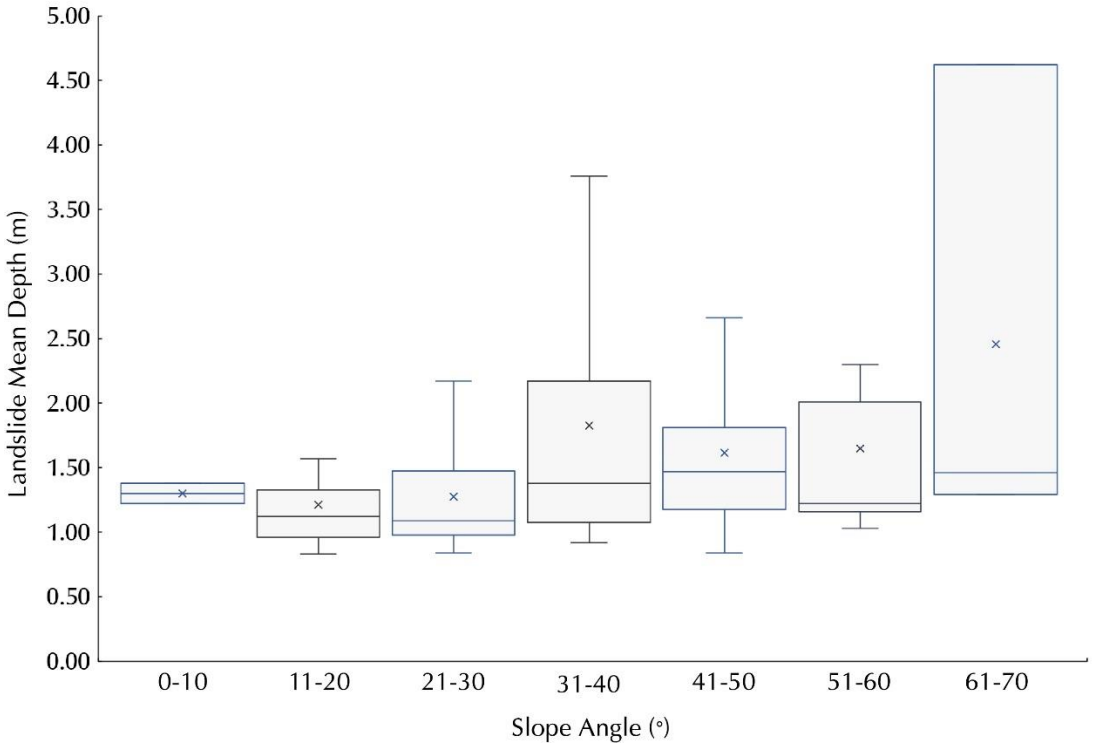

Figure 5.5: Box and whisker chart showing the mean slope failure depth against increasing slope angles for secondary failures at the Glacier d'Argentière site. Crosses denote the mean depth values within each slope angle range, whilst whiskers denote range.

5.2.2 Size Distribution

Tables 5.1 and 5.2 summarise the descriptive statistics for the primary and secondary inventories of slope failures from the Argentière dataset. Primary and secondary failures have a similar mean depth of 1.57 and 1.55 m, whilst secondary slope failures are shown to have the largest mean volume (V_L) and area (A_L). Primary and secondary failures cover a total area of 2.5 x 10^{-2} and 1.1 x 10^{-2} km^2 respectively. The 90th percentile of primary slope failures ($\leq$ 27.45 m^3; n = 9) account for 74.83 % of the total primary failure volume (9.36 x 10^1 m^3) whilst the upper 1 % ($\geq$ 31.07 m^3; n = 1) represent 25.17 % of the total (3.14 x 10^1 m^3). The 90th percentile of secondary slope failures ($\leq$ 46.75 m^3; n = 176) account for 28.17 % of the total secondary failure volume (1.56 x 10^3 m^3) whilst the upper 1 % ($\geq$ 430.10 m^3; n = 2) represent 35.09 % of the total (1.93 x 10^3 m^3).

Table 5.1: Descriptive statistics of the inventory of primary slope failures from the Glacier d'Argentière dataset.

	V_L (m^3)	W_L (m)	H_L (m)	D_L (m)	A_L (m)
Mean	12.50	5.01	4.07	1.57	24.72
Median	8.06	4.89	4.04	1.40	18.83
SD	9.83	2.86	2.01	0.69	21.73
Range	27.73	9.68	4.94	2.41	63.52
Minimum	3.74	0.86	1.40	0.93	1.49
Maximum	31.47	10.54	6.34	3.34	65.02

Sum	125.03	50.12	40.65	15.66	247.24

Table 5.2: Descriptive statistics of the inventory of secondary slope failures from the Glacier d'Argentière dataset.

	V_L (m^3)	W_L (m)	H_L (m)	D_L (m)	A_L (m)
Mean	28.16	5.76	3.69	1.55	57.55
Median	6.3	2.96	2.1	1.25	5.41
SD	114.68	8.02	5.09	0.83	210.73
Range	1,432.20	63.2	37.97	6.41	1,816.78
Minimum	0.28	0.32	0.09	0.83	0.04
Maximum	1,432.48	63.52	38.06	7.24	1,816.82
Sum	5,519.81	1,128.38	723.14	303.69	11,280.59

The measured volumes of detected slope failures were used to construct magnitude-frequency relationships by way of Cumulative Distribution Functions and these are shown in figure 5.6 for primary (a & b) and secondary (c & d) events. Maximum likelihood power-law and log-normal distributions have been fitted to the data. The MF distribution of the primary slope failures is characterised by a heavy-tailed power-law with a scaling exponent (α) of 2.06 for both the full (fig. 5.6 a) and truncated ($\leq \sigma_1$, α = 2.84) (fig. 5.6 b) datasets, although given the sparsity of data, the distribution cannot be considered a statistically valid assessment. The P-L is shown to fit the data above a lower bound of 3.74 m^3 ($\leq \sigma_1$, x_{min} = 4.67 m^3). A *hummock* in the data at 6.19 m^3 is visible and is also the lower bound for a L-N, although this is not a suitable fit to the data. The MF distribution of the secondary slope failures is also characterised by a heavy-tailed power-law with a lower scaling exponent (α) of 1.77 for both the full (fig. 5.6 c) and truncated (≤ σ_1, α = 1.90) (fig. 5.6 d) datasets. The P-L is shown to fit the data above a lower bound of 4.36 m^3 (≤ σ_1, x_{min} = 4.36 m^3), although a L-N is shown to fit the data from a lower bound of 4.17 m^3 (≤ σ_1, x_{min} = 1.01 m^3), more closely resembling the heavier tail in the distribution of data. Statistical suitability analyses of the fitted distributions agree that the L-N is a better fit to the data with a goodness-of-fit (*gof*) of 0.64. The scaling exponents of the L-N, fitted to the secondary failures' MF distribution are -0.97, 2.48 (≤ σ_1, α = 1.74, 1.30).

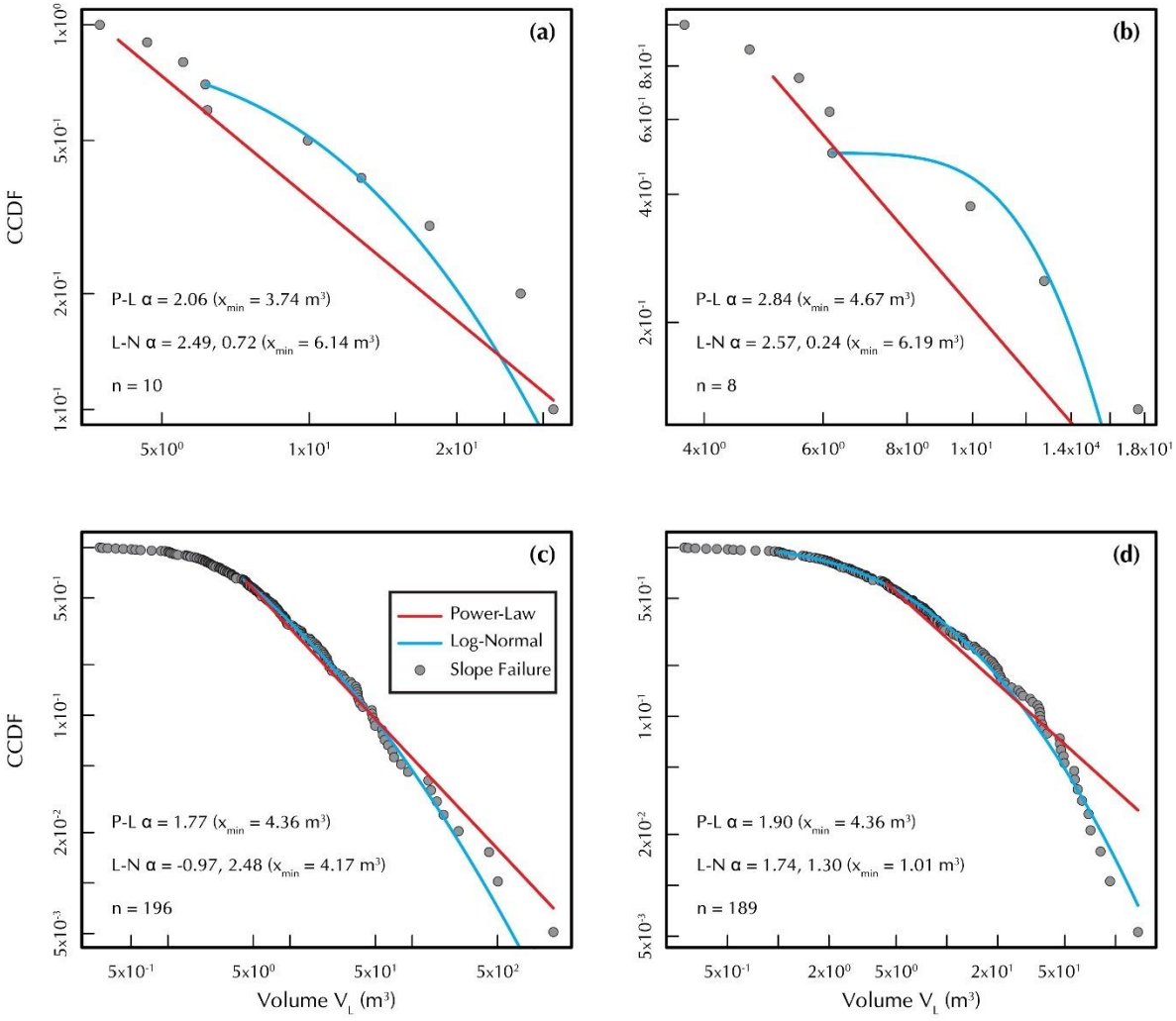

Figure 5.6: Cumulative Distribution Functions (CDF) for Glacier d'Argentière. Primary (a & b) and Secondary (c & d) slope failures are plotted against their CDF with their maximum likelihood power-law (red) and log-normal (blue) fit. Scaling exponents (α) and rollover values (x_{min}) are given on each graph. (a) and (c) are calculated considering the full inventory of slope failures at the site, whilst (b) and (d) are calculated considering only values less than σ_1 greater than the mean (see tables 5.1 and 5.2 for Argentière inventory statistics and table 5.11 for a summary of distribution characteristics).

5.3 Mer de Glace (Annual, Helicopter vs. Helicopter)

The annual surveys of the Mer de Glace account for change from the 6th August 2014 to the 30th June 2015 (329 days inclusive), across the full length of the glacial valley. The surveys of the NE- and SW-facing slopes above the Mer de Glace covered lengths of roughly 7 and 12 km, and heights of 1.5 and 1.5 km. This resulted in areas of approximately 10.5 and 18 km^2, yielding point-clouds in excess of 190 and 210 million points.

A total of 14 primary and 481 secondary slope failures above the level-of-detection threshold (table 4.6) were identified between 2014 and 2015 spanning several orders of magnitude. They resulted in a total volumetric loss of 1.0 x 10^3 m^3 and 3.6 x 10^5 m^3 respectively.

5.3.1 Spatial Distribution

The location and distribution of volume (V_L) of the primary- and secondary-type slope failures are given in figure 5.7. Primary slope failures are clustered in areas of slope-glacier contact where the LOD threshold is low enough to detect them whilst secondary failures reflect the distribution of sediment-mantled slopes across the entire length of the glacier on both the NE- and SW-facing slopes. The largest detected secondary failures are clustered in the lower regions of the glacier around the area where the glacier meanders from NW to N.

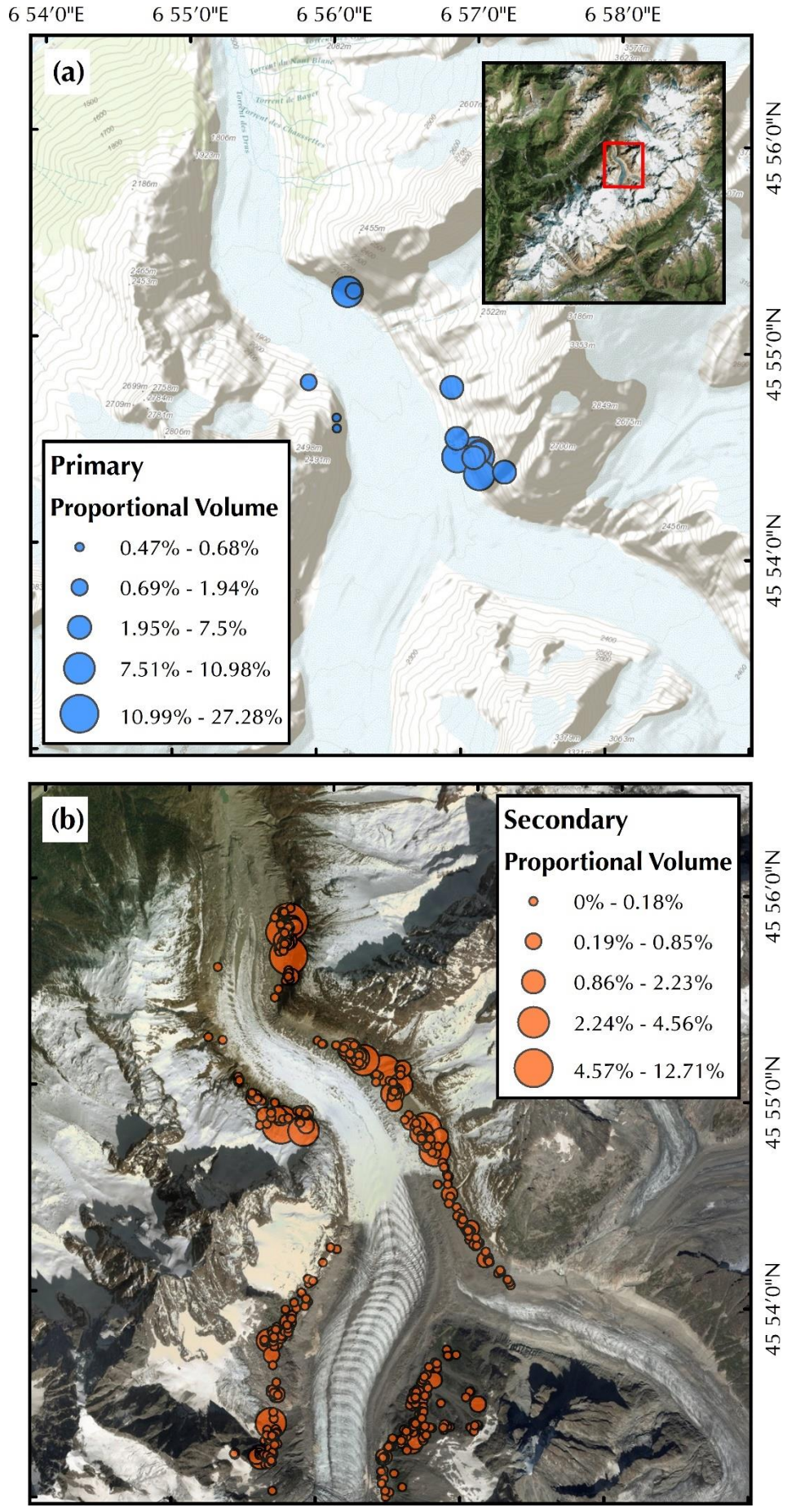

Figure 5.7: Maps showing the location of detected primary (a) and secondary (b) slope failures at the Mer de Glace using change analysis of annual topographic datasets. Failure volumes are shown as a percentage of their respective totals. Inset on (a) for reference. Basemap data from ESRI.

The probability density functions (PDF) for secondary slope failures (too few primary failures were recorded for a meaningful density function) were calculated for failure altitude, pre-failure slope angle, and failure aspect and are shown in figure 5.8 (a, b & c respectively). Maximal densities occur at an altitude of approximately 2250 m a.s.l. across slopes at a pre-failure angle of 45-50° with a predominantly SW aspect.

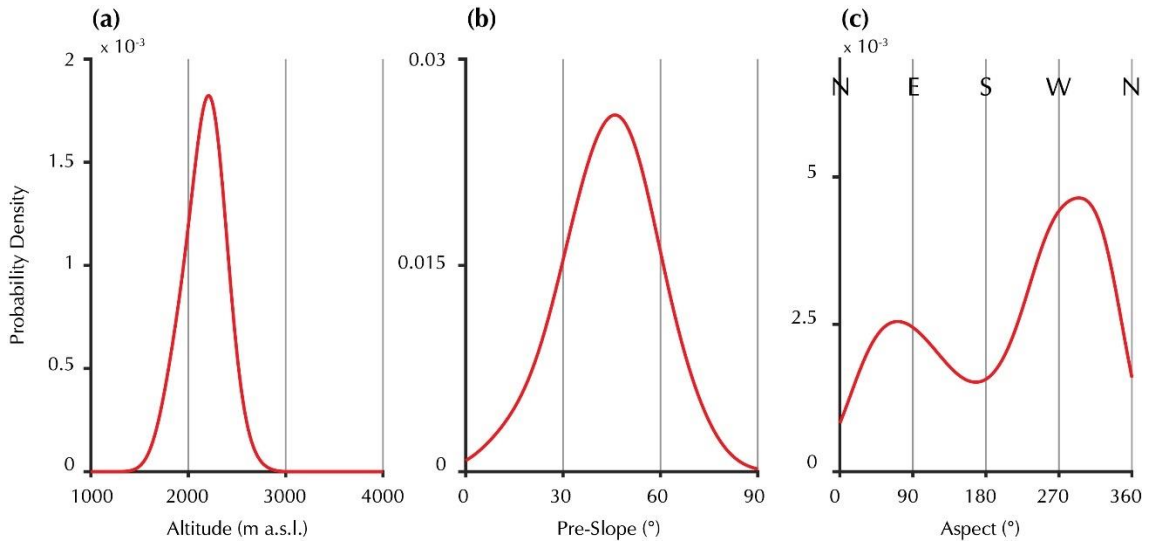

Figure 5.8: Probability density functions for (a) slope failure altitude; (b) pre-failure slope angle and; (c) slope failure aspect from the inventory of secondary failures at the Mer de Glace site. The probability of failure for a horizontal slope in (b) is shown as > 0 – this is an artefact of the statistical process and not a real probability.

Examples of detected secondary failures on the NE- and SW-facing slopes are given in figures 5.9 and 5.10 respectively. On the NE-facing slope (fig. 5.9), failures can be seen to occur predominantly towards the top of the sediment-mantled slopes with greatest losses occurring in areas of water-flow (as visible on the photograph) and where the debris layer sits on-top of glacially-smoothed rockwall. On the SW-facing slope (fig. 5.10), failures are also seen to occur principally along the top of gullied slopes whilst secondary ridge-lines create *zones* of failures at decreasing heights towards the glacier surface.

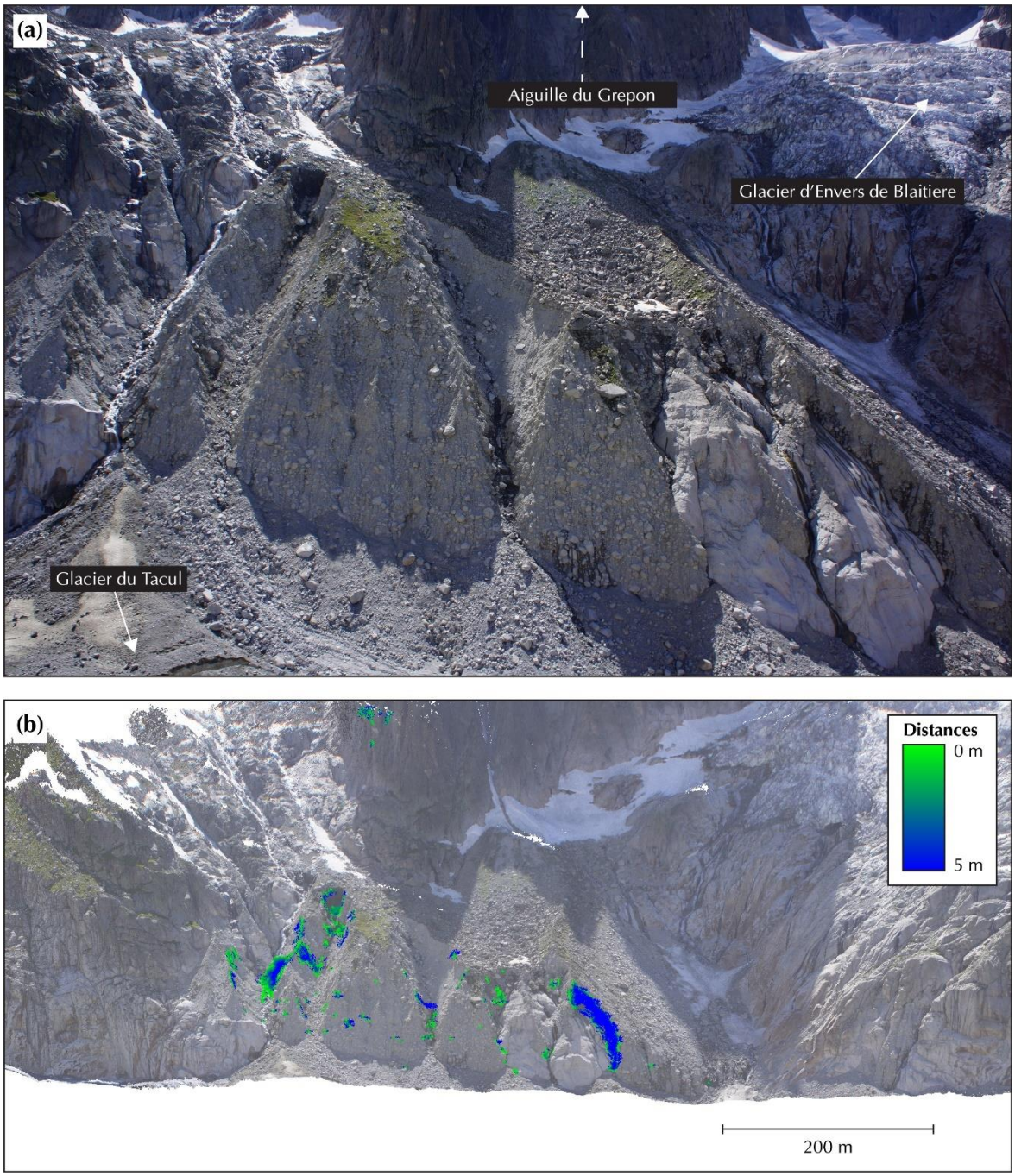

Figure 5.9: Example of the measured distances above the level-of-detection threshold (~ 1.13 m) at section 1 of NE-facing slope of the Mer de Glace dataset. (a) Field photography for context of location with key features labelled and; (b) post-failure point cloud overlain with measured distances in areas deemed significant by the M3C2 change detection technique.

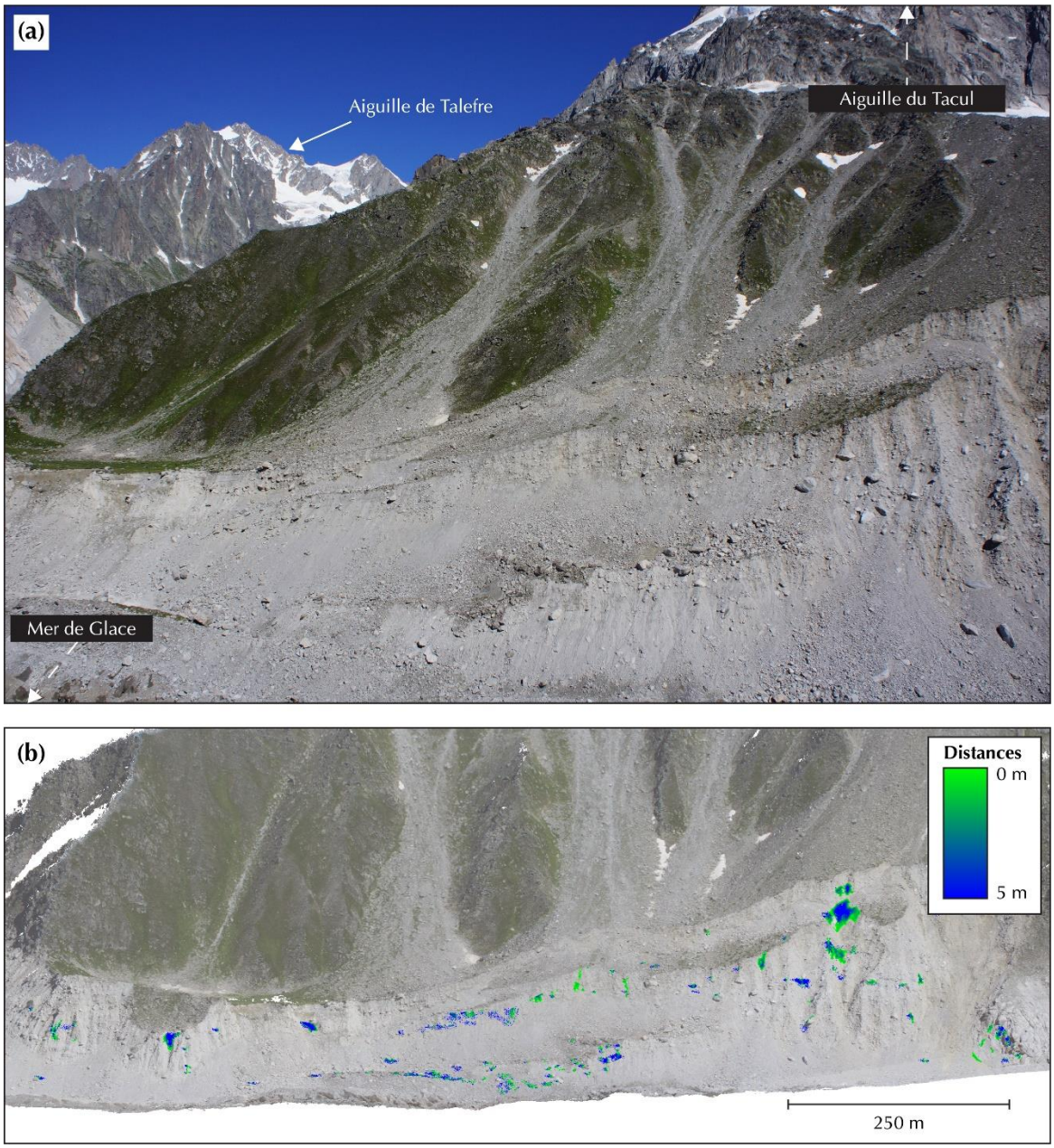

Figure 5.10: Example of the measured distances above the level-of-detection threshold (~ 1.57 m) at section 7 of SW-facing slope of the Mer de Glace dataset. (a) Field photography for context of location with key features labelled and; (b) post-failure point cloud overlain with measured distances in areas deemed significant by the M3C2 change detection technique.

To test for a time-dependent response to the removal of ice, height above the ice was used as a proxy for exposure time (i.e. time passed since the glacier was *n* metres higher than present day) across a section of the slope above the Mer de Glace where glacial thinning and retreat is well constrained by previous work (Berthier and Vincent, 2012). Figure 5.11 (a) displays the areas of significant loss (i.e. change above the level-of-detection threshold) across a section of the slope identified in figure 5.11 (b). Figure 5.11 (c) shows the percentage of total loss against the height above the ice with previous glacier heights denoted with dashed lines. Dates are estimated based upon the thinning rates calculated by Berthier (2004), and assume no change in rate between 2008 and 2015 from 4.0 m a^{-1}. The highest proportion of slope failure activity occurs on areas of the slope that have been exposed the longest (> 36 years) with two peaks representing approximately 70 % of the total sediment loss, but no clear downward trend exists with a secondary peak in the area of the slope exposed between 2000 and 2008 representing just over 10 % of the total volume loss detected. The lack of downward trend could indicate secondary failures are not time-dependent or driven by time since becoming exposed (i.e. deglaciation) but by other processes (e.g. slope steepness). This is discussed further in section 6.3.1.

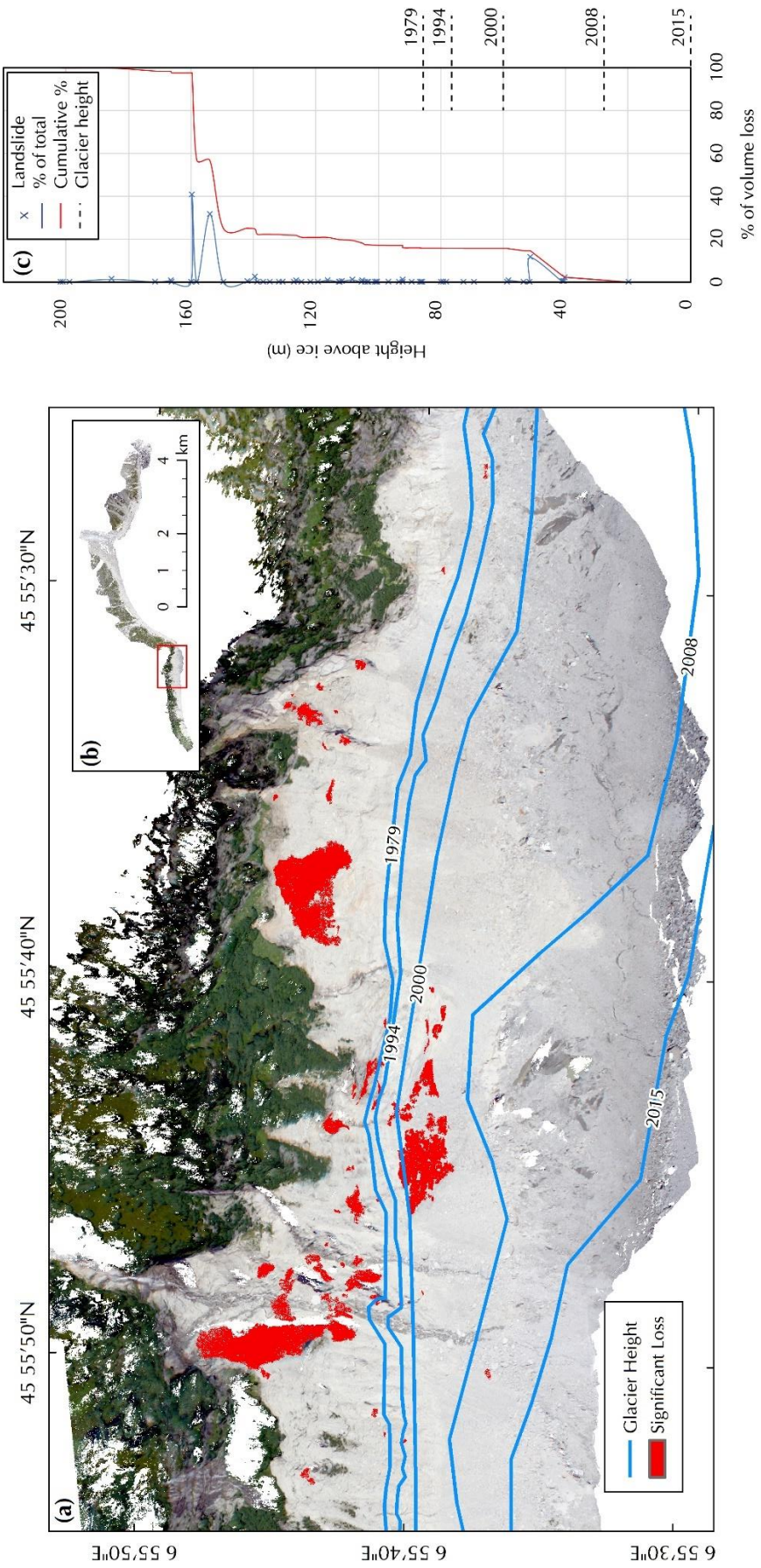

Figure 5.11: (a) Significant change overlain across a section of lateral moraine at the Mer de Glace where the previous ice height is well constrained in earlier work. Blue lines denote height of ice and red denotes the area of change above the level-of-detection threshold. Inset (b) for location along the SW-facing slope. (c) Proportion and combined total of volume loss against height above the ice surface. Dashed lines denote previous ice heights determined using rates calculated in previous work.

The mean depth of each secondary slope failure is plotted against the pre-failure slope angle in figure 5.12. The largest mean depth, approximately 5.7 m, is found on the pre-failure slope with the shallowest gradient. The largest range of depths, including the deepest as indicated by the upper whiskers, are found on the steeper pre-failure slopes in excess of 50°.

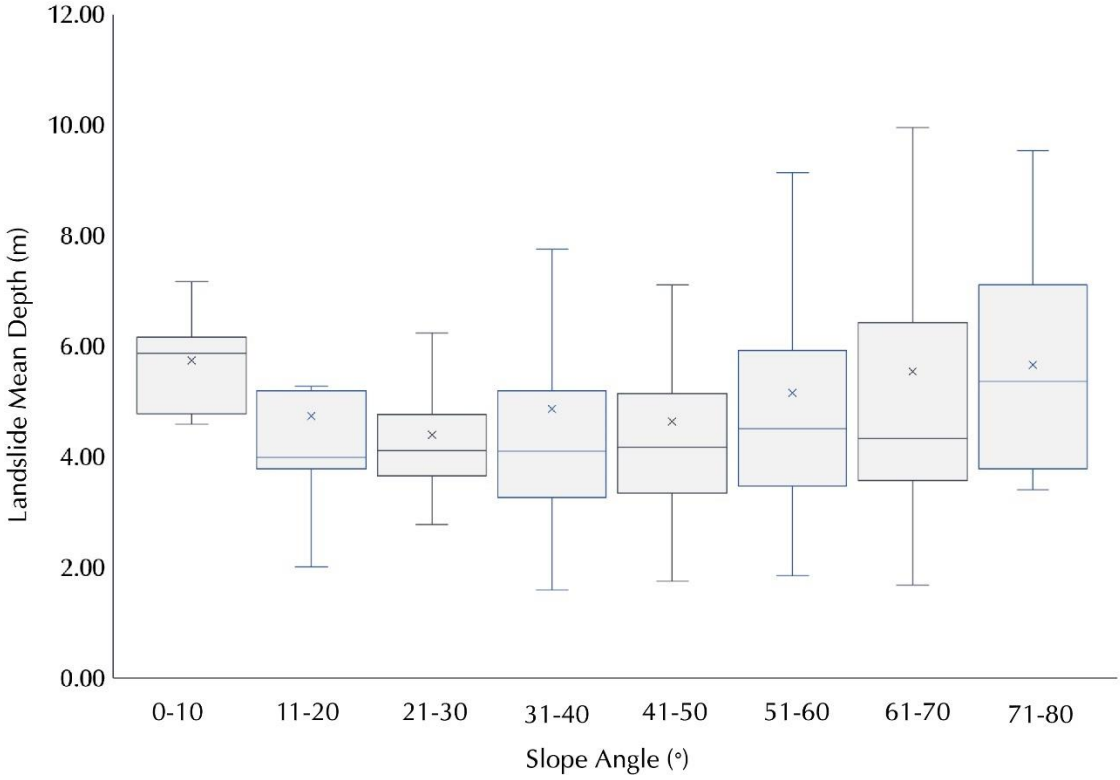

Figure 5.12: Box and whisker chart showing the mean slope failure depth against increasing slope angles for secondary failures at the Mer de Glace site. Crosses denote the mean depth values within each slope angle range, whilst whiskers denote range.

5.3.2 Size Distribution

Tables 5.3 and 5.4 summarise the descriptive statistics for the primary and secondary inventories of slope failures from the Mer de Glace dataset. Primary and secondary failures have mean depths of 5.66 and 4.92 m respectively, whilst secondary slope failures are shown to have the largest mean V_L and A_L. Primary and secondary failures cover a total area of 4.8 x 10^{-2} and 1.1 x 10^{-1} km^2. The 90th percentile of primary slope failures (≤ 113.18 m^3; n = 12) account for 61.74 % of the total primary failure volume (6.43 x 10^2 m^3) whilst the upper 1 % (≥ 262.35 m^3; n = 1) represent 27.28 % of the total (2.84 x 10^2 m^3). The 90th percentile of secondary slope failures (≤ 969.75 m^3; n = 433) account for 15.31 % of the total secondary failure volume (5.51 x 10^4 m^3) whilst the upper 1 % (≥ 13,481.40 m^3; n = 2) represent 42.95 % of the total (1.55 x 10^5 m^3).

Table 5.3: Descriptive statistics of the inventory of primary slope failures from the Mer de Glace dataset.

	V_L (m^3)	W_L (m)	H_L (m)	D_L (m)	A_L (m)
Mean	74.48	6.06	5.55	5.66	34.25
Median	64.03	5.80	5.38	6.86	29.65
SD	70.00	2.07	1.60	2.32	17.34
Range	279.52	8.70	6.05	6.63	66.60
Minimum	4.93	3.56	2.43	1.74	13.26
Maximum	284.45	12.26	8.48	8.37	79.86
Sum	1,042.66	84.80	77.70	79.25	479.56

Table 5.4: Descriptive statistics of the inventory of secondary slope failures from the Mer de Glace dataset.

	V_L (m^3)	W_L (m)	H_L (m)	D_L (m)	A_L (m)
Mean	748.54	10.98	9.83	4.92	237.32
Median	61.85	7.29	5.84	4.25	38.51
SD	3,684.49	12.51	12.21	3.15	793.95
Range	45,776.36	98.45	89.61	30.19	8,218.04
Minimum	3.09	0.67	0.29	1.59	0.31
Maximum	45,779.46	99.12	89.90	31.79	8218.35
Sum	360,049.90	5,282.56	4,726.79	2,365.51	114,151.43

The measured volumes of detected slope failures were used to construct magnitude-frequency relationships by way of Cumulative Distribution Functions and these are shown in figure 5.13 for primary (a & b) and secondary (c & d) events. Maximum likelihood power-law and log-normal distributions have been fitted to the data. The MF distribution of the primary slope failures is characterised by a heavy-tailed power-law with a scaling exponent (α) of 3.33 for both the full (fig. 5.13 a) and truncated (≤ σ_1, α = 4.50) (fig. 5.13 b) datasets, although given the sparsity of data, the distribution cannot be considered a statistically valid assessment. The P-L is shown to fit the data above a lower bound of 59.40 m^3 for both. A break in the distribution of data at 20.22 m^3 is visible, and the lower bound for a L-N matches that of the P-L. The MF distribution of the secondary slope failures is also characterised by a heavy-tailed power-law with a lower scaling exponent (α) of 1.73 for both the full (fig. 5.13 c) and truncated (≤ σ_1, α = 2.93) (fig. 5.13 d) datasets. The P-L is shown to fit the data above a lower bound of 167 m^3 (≤ σ_1, x_{min} = 1,048 m^3), although a L-N is shown to fit the data from a lower bound of 14.70 m^3 (≤ σ_1, x_{min} = 10.30 m^3), more closely resembling the distribution of data. Statistical suitability analyses of the fitted distributions agree that the L-N is a better fit to the data with a *gof* value of 0.50. The scaling exponents of the L-N, fitted to the secondary failures' MF distribution are 2.18, 2.81 (≤ σ_1, α = 3.61, 1.95).

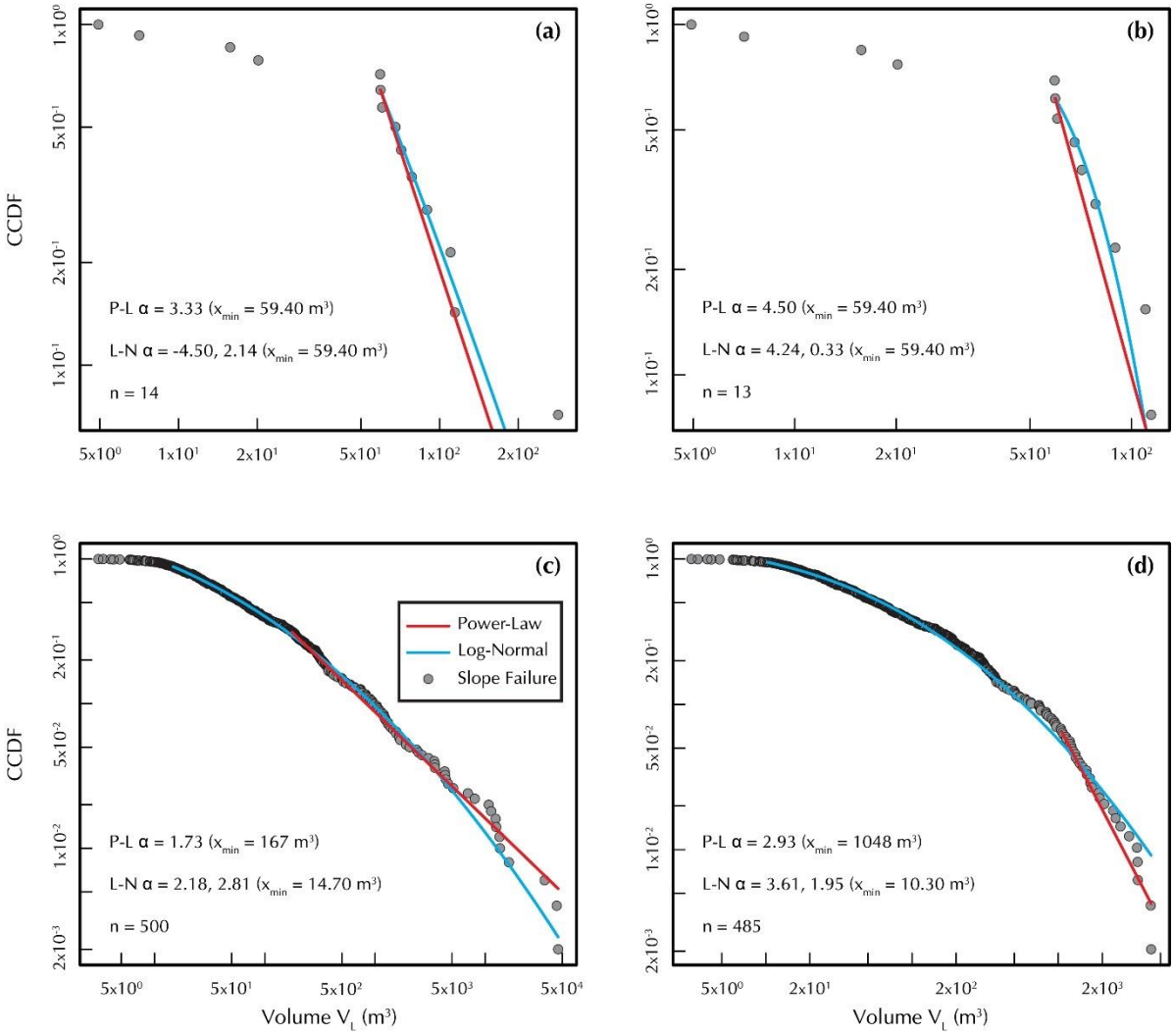

Figure 5.13: Cumulative Distribution Functions (CDF) for Mer de Glace. Primary (a & b) and Secondary (c & d) slope failures are plotted against their CDF with their maximum likelihood power-law (red) and log-normal (blue) fit. Scaling exponents (α) and rollover values (x_{min}) are given on each graph. (a) and (c) are calculated considering the full inventory of slope failures at the site, whilst (b) and (d) are calculated considering only values less than σ_1 greater than the mean (see tables 5.3 and 5.4 for Mer de Glace inventory statistics and table 5.11 for a summary of distribution characteristics).

5.3.3 Intra-Annual, (Terrestrial vs. UAV)

The intra-annual surveys of the Mer de Glace account for change from the 6th June to the 22nd August 2014 (78 days inclusive), across a smaller section of the SW-facing slope. 134 secondary failures were detected with a total volume of 2.8 x 10^4 m^3. Table 5.5 summarises the descriptive statistics for the inventory of secondary slope failures from the Mer de Glace intra-annual dataset. No primary slope failures were detected during this period. Slope failures are shown to have mean V_L and A_L of 209.26 m^3 and 70.90 m^2 with a mean depth of 2.26 m. Failures cover an area of 9.5 x 10^3 m^2. The 90th percentile of secondary slope failures (≤ 254.91 m^3 / *n* = 120) account for 13.89 % of the total secondary failure volume whilst the upper 1 % (≥ 2,984.76 m^3 / *n* = 2) represent 57.39 % of the total (1.61 x 10^4 m^3).

Table 5.5: Descriptive statistics of the inventory of secondary slope failures from the Mer de Glace intra-annual dataset.

	V_L (m^3)	W_L (m)	H_L (m)	D_L (m)	A_L (m)
Mean	209.26	4.94	4.20	2.26	70.90
Median	19.45	2.06	2.30	2.23	4.47
SD	1,162.73	11.56	5.82	0.29	386.27
Range	12,844.23	115.60	36.42	1.36	4,275.21
Minimum	2.38	0.64	0.36	1.85	0.31
Maximum	12,846.61	116.24	36.78	3.22	4,275.52
Sum	28,040.26	662.28	562.78	303.15	9,500.18

The measured volumes of detected slope failures were used to construct magnitude-frequency relationships by way of Cumulative Distribution Functions and these are shown in figure 5.14 for secondary (a & b) events. Maximum likelihood power-law and log-normal distributions have been fitted to the data. The MF distribution of the secondary slope failures is characterised by a heavy-tailed power-law with a scaling exponent (α) of 1.82 for the full (fig. 5.14 a) dataset, although the P-L for the truncated (≤ σ_1, α = 5.47) (fig. 5.14 b) data is not a good fit. The P-L is shown to fit the data above a lower bound of 47.10 m^3 (≤ σ_1, x_{min} = 294 m^3), although a L-N is shown to fit the data from a lower bound of 2.62 m^3 (≤ σ_1, x_{min} = 10.90 m^3), more closely resembling the distribution of data. The scaling exponents of the L-N, fitted to the secondary failures' MF distribution are 1.56, 2.55 (≤ σ_1, α = 3.44, 1.38).

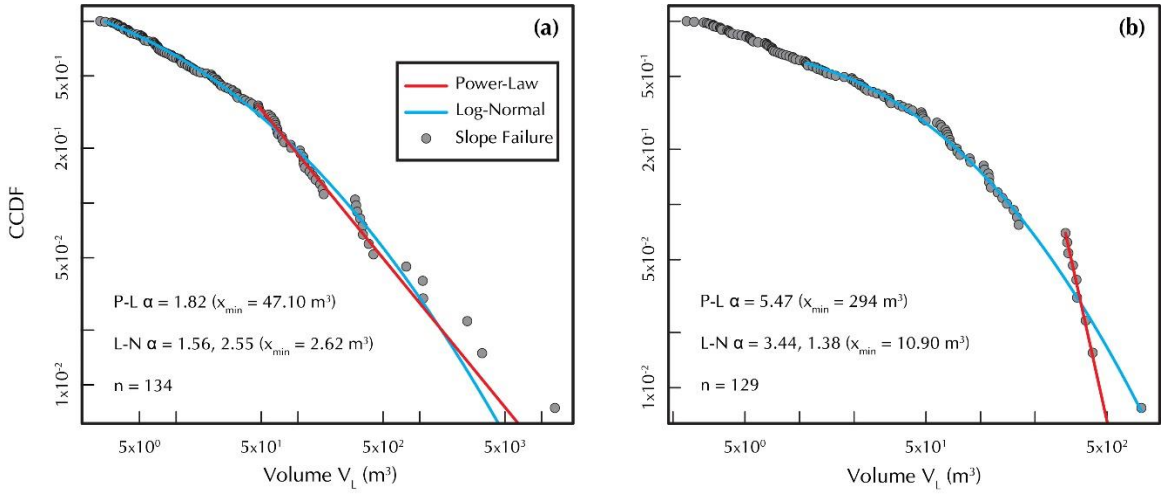

Figure 5.14: Cumulative Distribution Functions (CDF) for Mer de Glace. Secondary (a & b) slope failures are plotted against their CDF with their maximum likelihood power-law (red) and log-normal (blue) fit. Scaling exponents (α) and rollover values (x_{min}) are given on each graph. (a) are calculated considering the full inventory of slope failures at the site, whilst (b) are calculated considering only values less than σ_1 greater than the mean (see table 5.5 for intra-annual Mer de Glace inventory statistics and table 5.11 for a summary of distribution characteristics).

5.4 Glacier de Bossons (Annual, Terrestrial vs. UAV)

The annual surveys of the Glacier de Bossons account for change from the 16th August 2014 to the 29th June 2015 (318 days inclusive), across a section of rockslope in the proglacial zone. The survey of the NE-facing rockslope in the proglacial zone of the Glacier de Bossons covered a length of approximately 200 m, and a height of 96 m. This resulted in an area of approximately 6.1 x 10^3 m^2 yielding a point-cloud of 2.7 million points with an average point density of approximately 35 pts/ m^3.

A total of 19 primary slope failures above the level-of-detection threshold (table 4.7) were identified between 2014 and 2015 spanning several orders of magnitude. They resulted in a total volumetric loss of 2.8 x 10^2 m^3. A face-averaged retreat rate of 52.39 mm a^{-1} is calculated by dividing this volume by the area of the surveyed slope (6116 m^2) and the monitoring period duration (317 days).

5.4.1 Spatial Distribution

The location and distribution of detected change above the LOD threshold across the Glacier de Bossons site are given in figure 5.15.

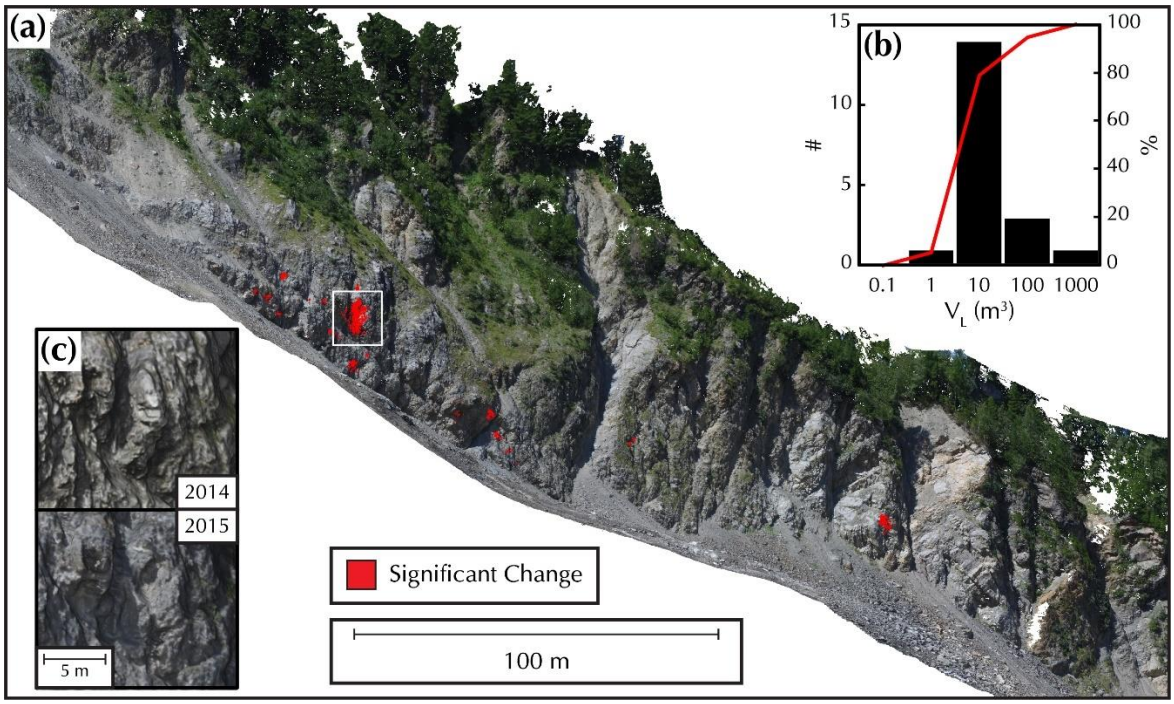

Figure 5.15: (a) Glacier de Bossons point cloud dataset created using SfM-MVS with RGB values. Areas of significant change overlain in red. (b) Histogram of magnitude-frequency for detected slope failures at the Glacier de Bossons site, with cumulative percentage denoted by the red line on the secondary axis. (c) Inset close-up of area outlined with white box in (a) showing datasets from pre- and post- the largest single detected slope failure in the dataset referred to in section 5.4.3.

The frequency of slope failures in regards to the pre-failure slope angle at the Glacier de Bossons site is shown in figure 5.16. No failures are shown to occur across slopes shallower than 50° whilst the maximal frequencies are across areas of the rockslope in excess of 80°.

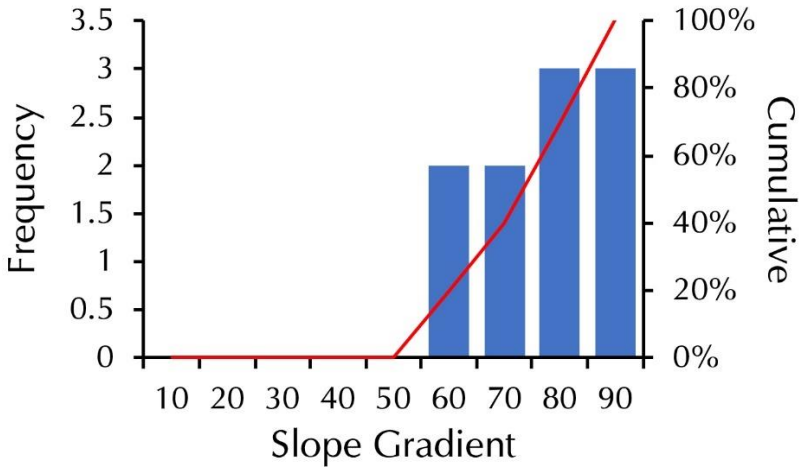

Figure 5.16: (left axis) Frequency and cumulative frequency (right axis) of slope gradients for the detected primary failures at the Glacier de Bossons site. Red line denoting cumulative frequency overlain.

5.4.2 Size Distribution

Table 5.6 summarises the descriptive statistics for the inventory of primary slope failures from the Bossons dataset. Slope failures are shown to have mean V_L and A_L of 14.85 m^3 and 10.06 m^2 with a mean depth of 1.17 m. Failures cover a total area of 1.9 x 10^2 m^2. The 90th percentile of primary slope failures (≤ 17.59 m^3; *n* = 17) account for 26.93 % of the total primary failure volume (7.56 x 10^1 m^3) whilst the upper 1 % (≥ 150.64 m^3; *n* = 1) represent 62.87 % of the total (1.77 x 10^2 m^3).

Table 5.6: Descriptive statistics of the inventory of primary slope failures from the Glacier de Bossons dataset.

	V_L (m^3)	W_L (m)	H_L (m)	D_L (m)	A_L (m)
Mean	14.85	2.47	2.61	1.17	10.06
Median	3.63	2.21	1.95	1.13	3.81
SD	39.91	1.84	2.35	0.45	19.82
Range	177.24	7.67	10.34	1.90	88.59
Minimum	0.15	0.51	0.52	0.43	0.27
Maximum	177.38	8.18	10.86	2.33	88.86
Sum	282.14	46.86	49.54	22.24	191.21

The measured volumes of detected slope failures were used to construct magnitude-frequency relationships by way of Cumulative Distribution Functions and these are shown in figure

5.17 for primary (a & b) events. Maximum likelihood power-law and log-normal distributions have been fitted to the data. The MF distribution of the primary slope failures is characterised by a heavy-tailed power-law with a scaling exponent (α) of 1.76 for both the full (fig. 5.17 a) and truncated (≤ σ_1, α = 1.91) (fig. 5.17 b). The P-L is shown to fit the data above a lower bound of 1.48 m^3 for both. A break in the distribution of data at 0.15 m^3 is visible, and the lower bound for a L-N matches that of the P-L for the full dataset but increases to 2.35 m^3 for the truncated data. Statistical suitability analyses of the fitted distributions show that the P-L and L-N are suitable fits to the data with *gof* values of 0.87 and 0.99. The scaling exponents of the L-N, fitted to the primary failures' MF distribution are -1.55, 2.46 (≤ σ_1, α = 1.49, 0.94).

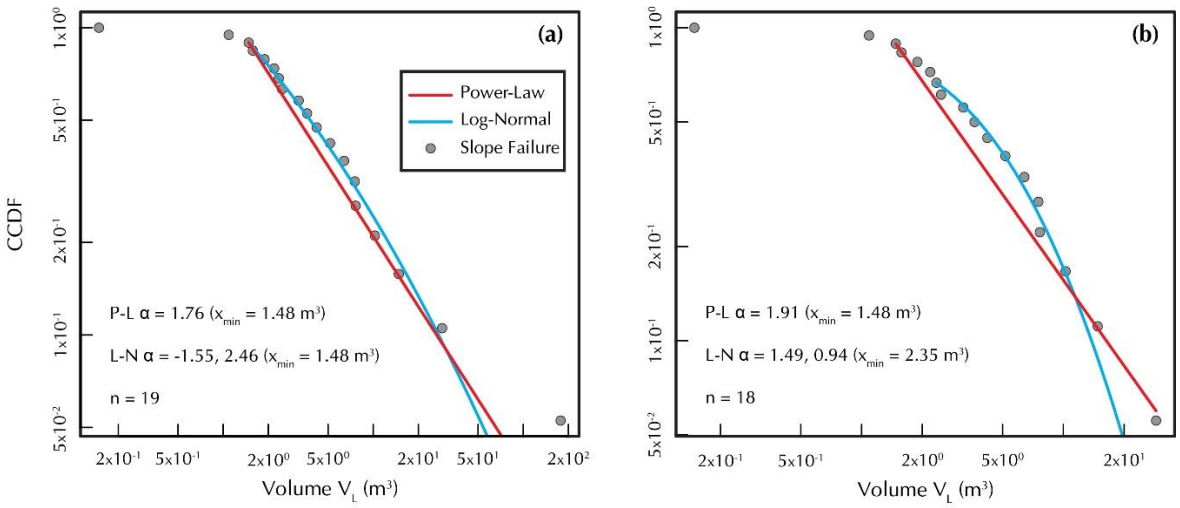

Figure 5.17: Cumulative Distribution Functions: Glacier de Bossons]{Cumulative Distribution Functions (CDF) for Glacier de Bossons. Primary (a & b) slope failures are plotted against their CDF with their maximum likelihood power-law (red) and log-normal (blue) fit. Scaling exponents (α) and rollover values (x_{min}) are given on each graph. (a) are calculated considering the full inventory of slope failures at the site, whilst (b) are calculated considering only values less than σ_1 greater than the mean (see table 5.6 for Bossons inventory statistics and table 5.11 for a summary of distribution characteristics).

5.4.3 Structural Analysis

Structural analysis of the proglacial rockslope was performed and examples of the extracted joints for each of the sections are given in figure 5.18. Sections 1 to 5 represent areas of bedrock at an average altitude of 1481, 1460, 1452, 1464 and 1433 m a.s.l. respectively (taken as the centre point of a 3D bounding box). Principal joints with maximal densities of 36, 23, 37, 33 and 30 % towards 48/054, 53/045, 68/027, 60/052 and 35/103 were identified across the slope. The discontinuity spacing, rock strength parameters and bedrock conditions through visual observations of field photographs and data, were used to determine a SMR for the assessment of bedrock stability.

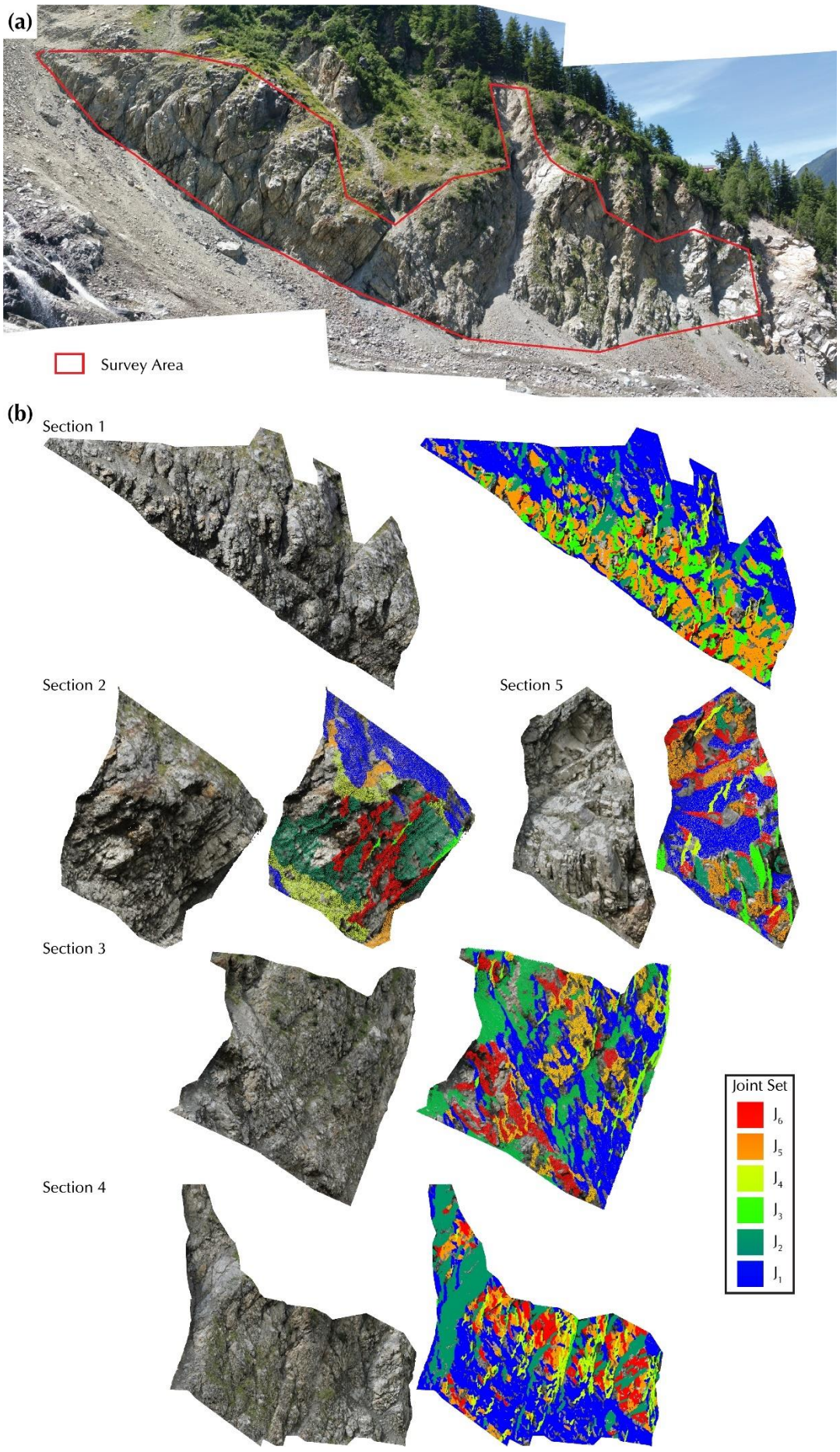

Figure 5.18: (a) The bedrock at the Glacier de Bossons fieldsite. Extracted survey area highlighted. (b) Examples of discontinuity sets extracted for each section of the bedrock at Glacier de Bossons. Colours denote individual sets.

The SMR is applied to the point cloud as a scalar field, and its distribution across the rockslope is shown in figure 5.19. All sections of the slope are classified from I to IV (very good to bad), with no areas classified as V (very bad). However, there are only two classifications of IV for J_1 on section 1 and J_6 on section 2 of the slope, whilst all others are considered as I, II and III (very good, good and normal) indicating a mix of completely stable, stable and partially stable rockwall. The largest detected failure (177.38 m^3) detached from section 1 (fig. 5.19 d) at the v-shaped intersection between J_2 and J_4 which are both classified with a SMR of II (good). However, the auxiliary angles calculated by examining the orientation of the slope with respect to the discontinuities correctly suggested a wedge-type failure mode for J_2. No significant change in the SMR classification was found to occur across the rockslope following this failure.

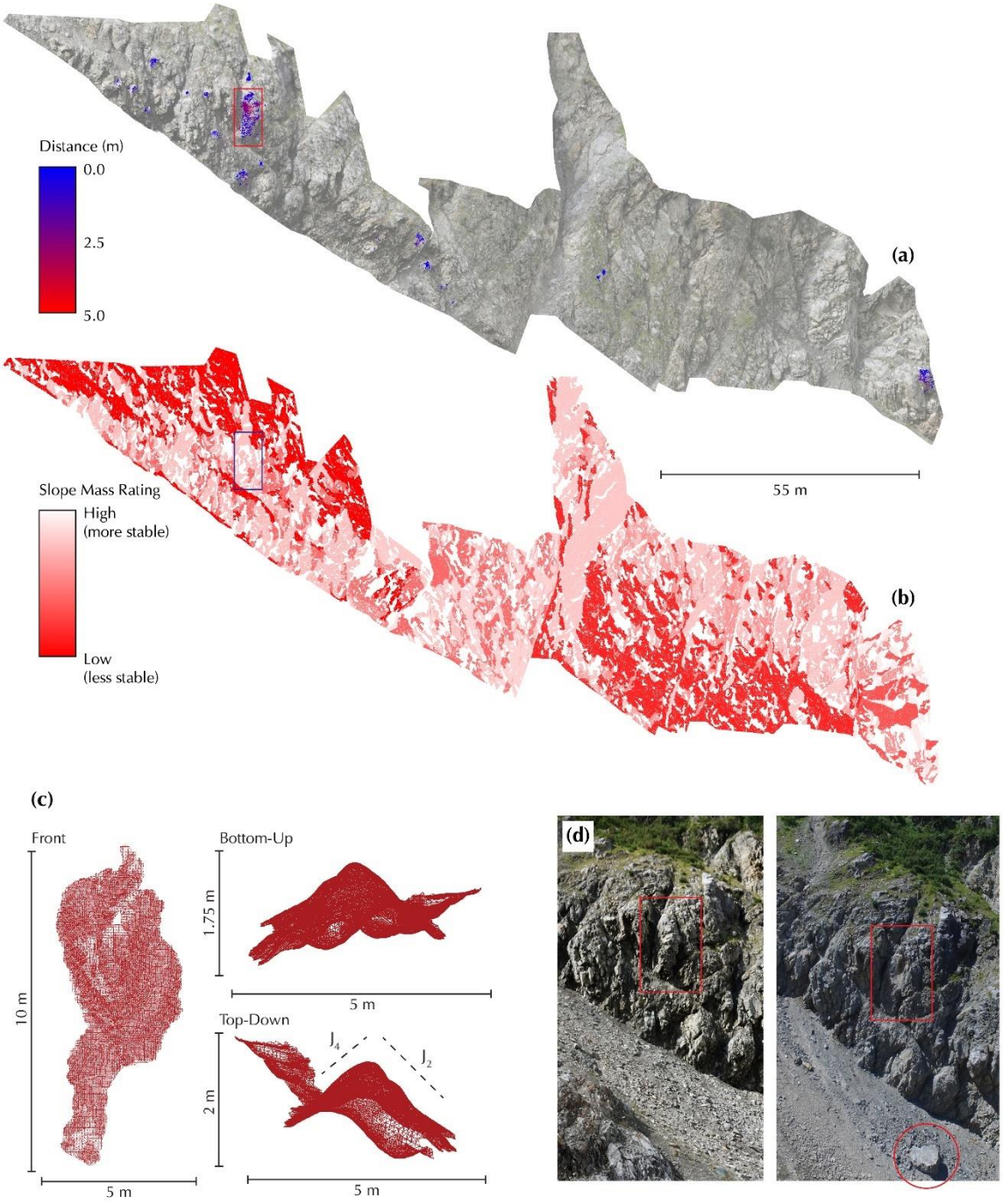

Figure 5.19: (a) Point cloud model of the rockslope in the proglacial zone of the Glacier de Bossons with difference (above the level-of-detection threshold) overlain. (b) Slope mass rating of the extracted joint sets as a scalar on the Glacier de Bossons point cloud model. (c) Volumetric mesh of the largest detected failure at the Bossons site, location is denoted by a box in (a) and (b), from three perspectives. J_1 and J_3 are identified in the top-down view. (d) Field photographs highlighting the area of the largest failure, pre- and post-failure. Red squares denote failure area whilst the assumed deposit is denoted by a red circle.

5.5 Ghiacciaio del Miage (Annual, UAV vs. UAV)

The annual surveys of the Ghiacciaio del Miage account for change from the 3rd July 2014 to the 9th July 2015 (366 days inclusive), across a section of lateral moraine above the glacier surface. The survey of the SW-facing slope above the Ghiacciaio del Miage covered a length of approximately 350 m, and a height of 133 m. This resulted in an area of approximately 3.8 x 10^4 m^2 yielding a point-cloud of 4.2 million points with an average point density of approximately 89 pts/ m^3.

A total of 12 secondary slope failures above the level-of-detection threshold (table 4.8) were identified between 2014 and 2015 spanning several orders of magnitude. They resulted in a total volumetric loss of 6.0 x 10^2 m^3.

5.5.1 Spatial Distribution

The location and distribution of detected change above the LOD threshold across the Ghiacciaio del Miage site are given in figure 5.20.

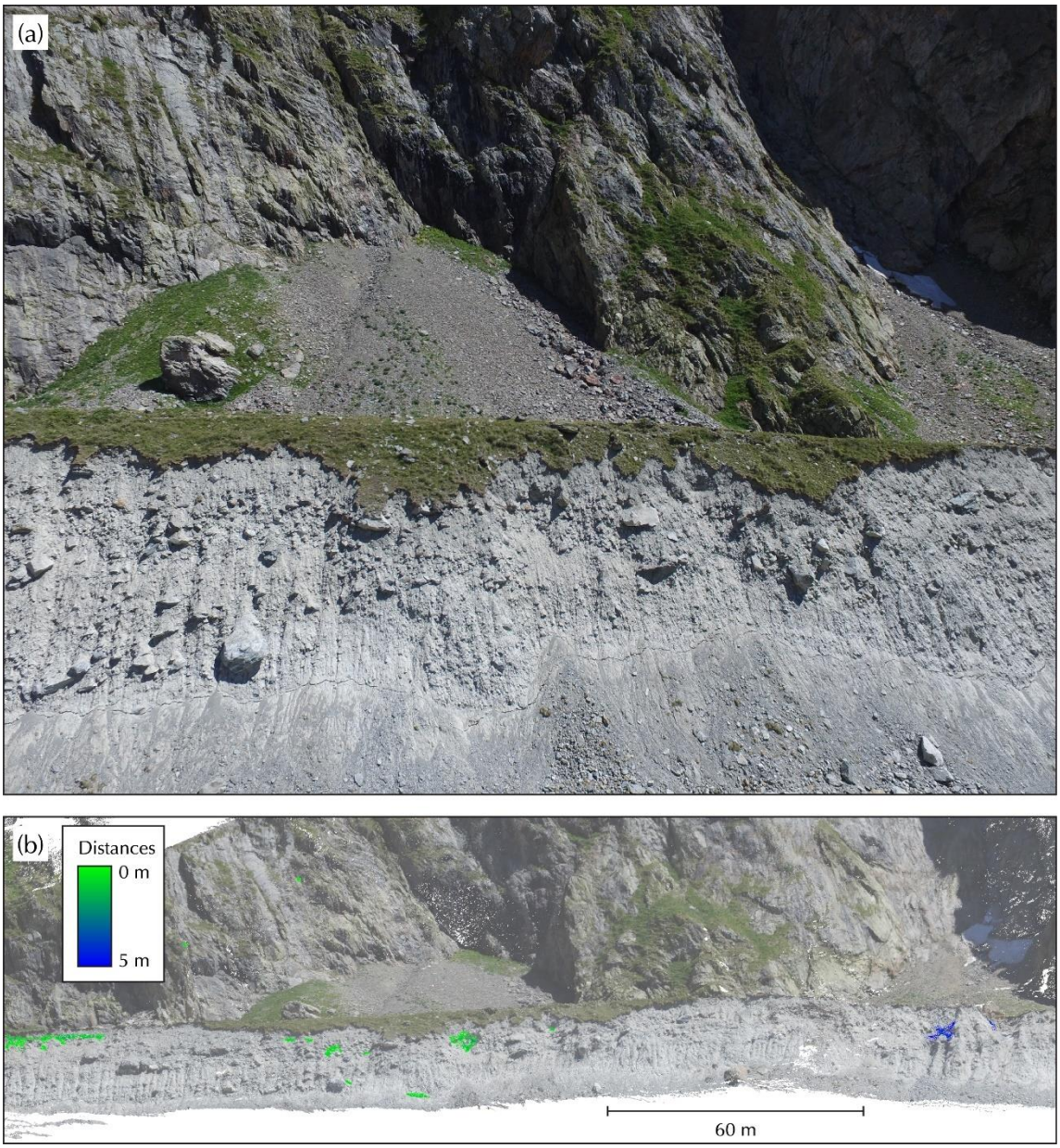

Figure 5.20: (a) Field photograph of the lateral moraine above the Ghiacciaio del Miage; (b) post-failure point cloud overlain with measured distances in areas deemed significant by the M3C2 change detection technique.

The frequency of slope failures in regards to the pre-failure slope angle at the Ghiacciaio del Miage site is shown in figure 5.21. One failure is shown to occur across a shallow slope in the 0-10° range, whilst the maximal frequencies are across areas of the lateral moraine in the range of 40-50°. No more slope failures occur once the lateral moraine is in excess of 60-70°.

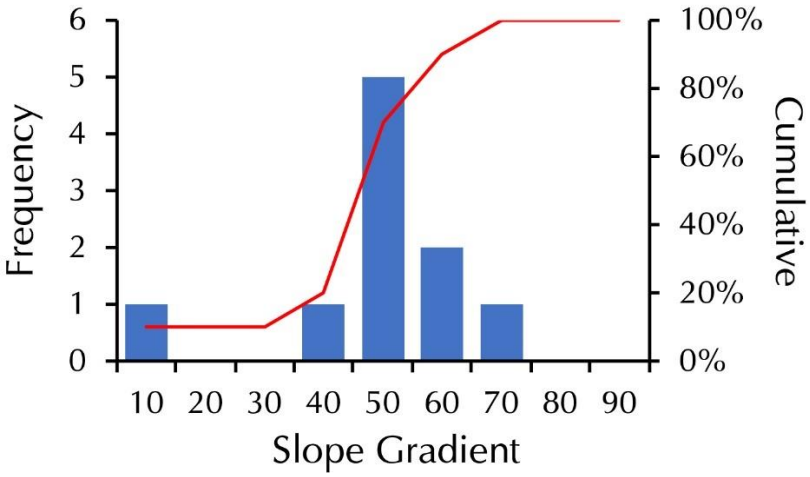

Figure 5.21: (left axis) Frequency and cumulative frequency (right axis) of slope gradients for the detected secondary failures at the Ghiacciaio del Miage site. Red line denoting cumulative frequency overlain.

5.5.2 Size Distribution

Table 5.7 summarises the descriptive statistics for the inventory of secondary slope failures from the Miage dataset. Slope failures are shown to have mean V_L and A_L of 50.18 m^3 and 19.10 m^2 with a mean depth of 2.11 m. Failures cover a total area of 2.3 x 10^2 m^2. The 90th percentile of secondary slope failures (≤ 133.38 m^3; *n* = 10) account for 43.75 % of the total secondary failure volume (2.63 x 10^2 m^3) whilst the upper 1 % (≥ 194.99 m^3; *n* = 1) represent 33.58 % of the total (2.02 x 10^2 m^3).

Table 5.7: Descriptive statistics of the inventory of secondary slope failures from the Ghiacciaio del Miage dataset.

	V_L (m^3)	W_L (m)	H_L (m)	D_L (m)	A_L (m)
Mean	50.18	4.15	2.95	2.11	19.10
Median	22.17	2.70	1.93	1.65	7.82
SD	63.44	4.54	2.33	1.18	30.65
Range	197.79	16.15	6.48	3.36	103.95
Minimum	4.43	0.96	0.70	1.37	0.69
Maximum	202.22	17.11	7.18	4.73	104.63
Sum	602.14	49.84	35.35	25.29	229.25

The measured volumes of detected slope failures were used to construct magnitude-frequency relationships by way of Cumulative Distribution Functions and these are shown in figure 5.22 for secondary (a & b) events. Maximum likelihood power-law and log-normal distributions have been fitted to the data. The MF distribution of the secondary slope failures is characterised by a heavy-tailed power-law with a scaling exponent (α) of 1.71 for both the full (fig. 5.22 c) and truncated (≤ σ_1, α = 2.75) (fig. 5.22 d) datasets. The P-L is shown to fit the data above a lower bound of 7.19 m^3 (≤ σ_1, x_{min} = 20.10 m^3), although a L-N is shown to fit the data from a lower bound of 4.43 m^3 for both, more closely resembling the distribution of data. Statistical suitability analyses of the fitted distributions show that neither the P-L or L-N are a strong fit to the data with *gof* values of 0.50 and 0.26. The scaling exponents of the L-N, fitted to the secondary failures' MF distribution are 3.11, 1.31 (≤ σ_1, α = 2.88, 0.91).

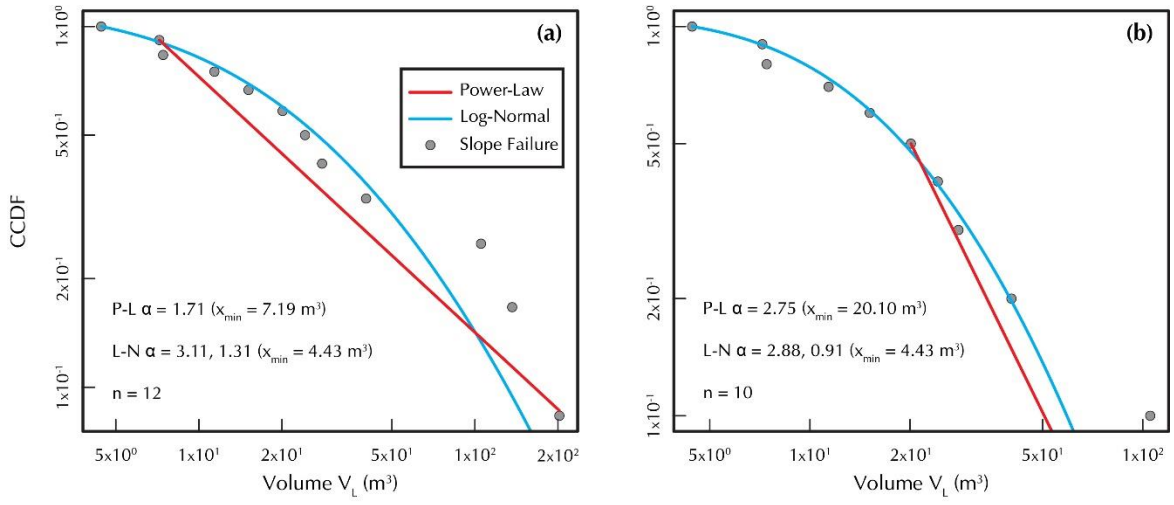

Figure 5.22: Cumulative Distribution Functions (CDF) for Ghiacciaio del Miage. Secondary (a & b) slope failures are plotted against their CDF with their maximum likelihood power-law (red) and log-normal (blue) fit. Scaling exponents (α) and rollover values (x_{min}) are given on each graph. (a) are calculated considering the full inventory of slope failures at the site, whilst (b) are calculated considering only values less than σ_1 greater than the mean (see table 5.7 for Miage inventory statistics and table 5.11 for a summary of distribution characteristics).

5.6 Pre de Bard (Annual, Terrestrial vs. UAV)

The annual surveys of the Pre de Bard account for change from the 18th August 2014 to the 5th July 2015 (322 days inclusive), across a section of lateral moraine in the proglacial zone. The survey of the NE-facing slope in the proglacial zone of the Pre de Bard covered a length of approximately 600 m, and a height of 300 m. This resulted in an area of approximately 1.7 x 10^5 m^2 yielding a point-cloud of 5.6 million points with an average point density of approximately 110 pts/ m^3.

A total of 34 secondary slope failures above the level-of-detection threshold (table 4.9) were identified between 2014 and 2015 spanning several orders of magnitude. They resulted in a total volumetric loss of 2.2×10^2 m^3.

5.6.1 Spatial Distribution

The location and distribution of detected change above the LOD threshold across the Pre de Bard site are given in figure 5.23.

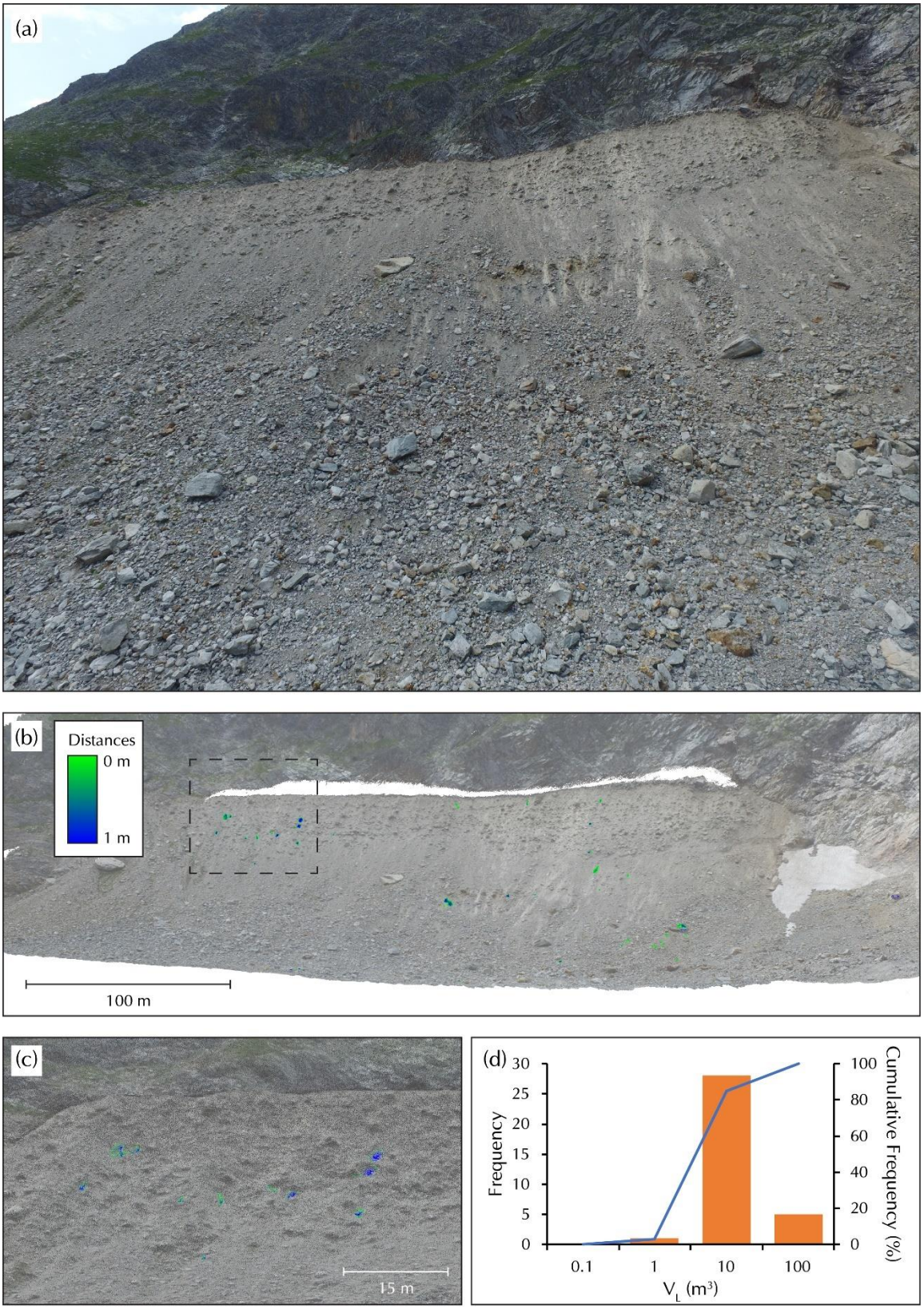

Figure 5.23: (a) Field photograph of the lateral moraine in the proglacial zone of the Pre de Bard glacier; (b) post-failure point cloud overlain with measured distances in areas deemed significant by the M3C2 change detection technique; (c) detailed view of the area denoted in (b) and; (d) frequency of detected slope failures at the Pre de Bard site.

The frequency of slope failures in regards to the pre-failure slope angle at the Pre de Bard site is shown in figure 5.24. Maximal frequencies are across areas of the lateral moraine in the range of 40-50°. No more slope failures occur once the lateral moraine is in excess of 50-60°.

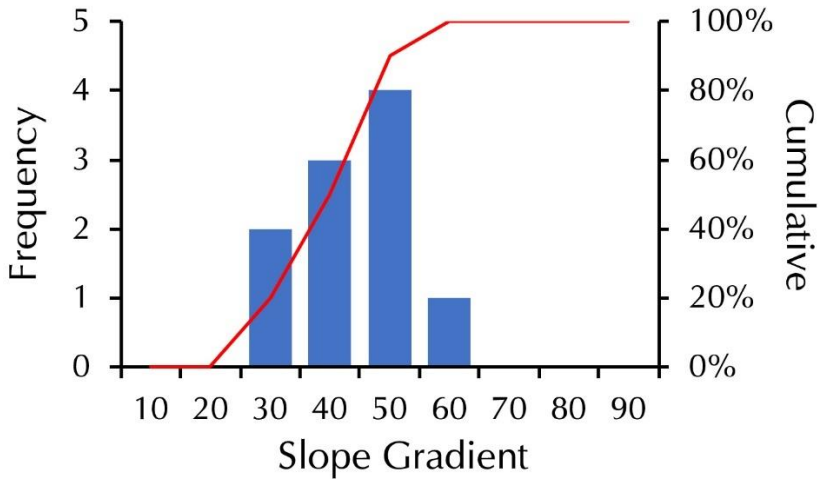

Figure 5.24: (left axis) Frequency and cumulative frequency (right axis) of slope gradients for the detected secondary failures at the Pre de Bard site. Red line denoting cumulative frequency overlain.

5.6.2 Size Distribution

Table 5.8 summarises the descriptive statistics for the inventory of secondary slope failures from the Miage dataset. Slope failures are shown to have mean V_L and A_L of 6.40 m^3 and 5.68 m^2 with a mean depth of 0.77 m. Failures cover a total area of 1.9 x 10^2 m^2. The 90^{th} percentile of secondary slope failures (≤ 14.82 m^3; *n* = 30) account for 51.23 % of the total secondary failure volume (1.11 x 10^2 m^3) whilst the upper 1 % (≥ 31.19 m^3; *n* = 1) represent 14.81 % of the total (3.22 x 10^1 m^3).

Table 5.8: Descriptive statistics of the inventory of secondary slope failures from the Pre de Bard dataset.

	V_L (m^3)	W_L (m)	H_L (m)	D_L (m)	A_L (m)
Mean	6.4	2.15	2.06	0.77	5.68
Median	3.13	1.59	1.77	0.73	2.72
SD	8.09	1.48	1.37	0.18	7.35
Range	32.01	6.57	6.15	0.94	27.95
Minimum	0.2	0.17	0.2	0.61	0.03
Maximum	32.21	6.73	6.34	1.56	27.99
Sum	217.51	73.03	69.89	26.19	193.23

The measured volumes of detected slope failures were used to construct magnitude-frequency relationships by way of Cumulative Distribution Functions and these are shown in figure 5.25 for secondary (a & b) events. Maximum likelihood power-law and log-normal distributions have been fitted to the data. The MF distribution of the secondary slope failures is characterised by a heavy-tailed power-law with a lower scaling exponent (α) of 2.04 for both the full (fig. 5.25 c) and truncated (≤ σ_1, α = 2.52) (fig. 5.25 d) datasets. The P-L is shown to fit the data above a lower bound of 1.94 m^3 (≤ σ_1, x_{min} = 1.93 m^3), and a L-N is shown to fit the data from a lower bound of 1.99 m^3 for both. Statistical suitability analyses of the fitted distributions show that both the P-L and L-N are a similarly suitable fit to the data with *gof* values of 0.60 and 0.64 but that the L-N more closely resembles the distribution of data. The scaling exponents of the L-N, fitted to the secondary failures' MF distribution are -0.06, 1.57 (≤ σ_1, α = 1.08, 0.69).

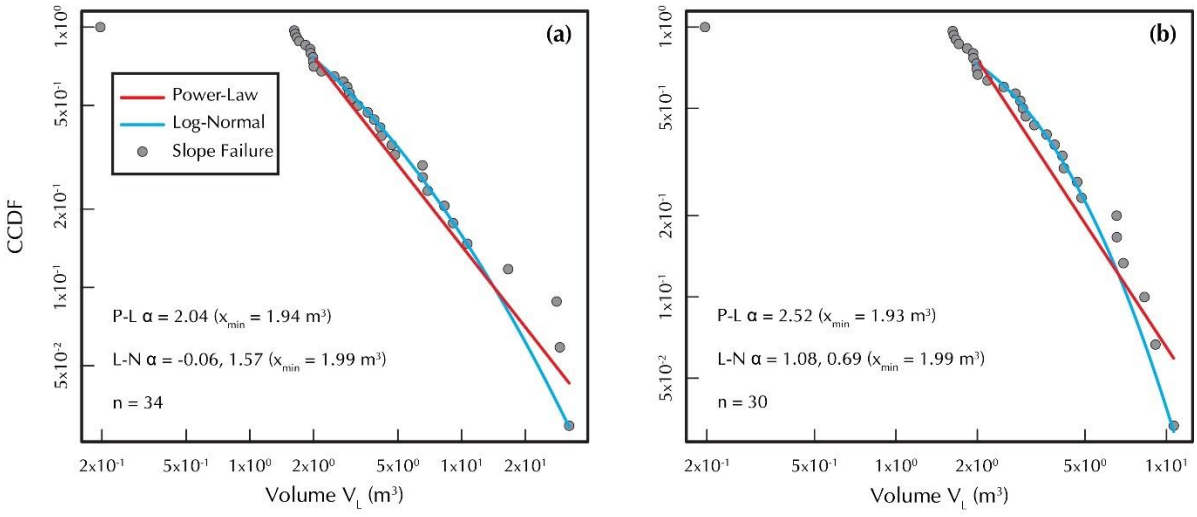

Figure 5.25: Cumulative Distribution Functions (CDF) for Pre de Bard. Secondary (a & b) slope failures are plotted against their CDF with their maximum likelihood power-law (red) and log-normal (blue) fit. Scaling exponents (α) and rollover values (x_{min}) are given on each graph. (a) are calculated considering the full inventory of slope failures at the site, whilst (b) are calculated considering only values less than σ_1 greater than the mean (see table 5.8 for Pre de Bard inventory statistics and table 5.11 for a summary of distribution characteristics).

5.7 Combined Analysis Results

The combined inventories of detected primary and secondary slope failures can be found in Appendix 1.

5.7.1 Spatial Distribution

Radar graphs showing the aspect of surveyed slopes (blue line) and detected slope failures (orange line) are presented in figure 5.26. The aspect of the detected slope failures is shown as the percentage of total slope failure area (SFAP as defined in section 4.6) (e.g. figure 5.26 (a) shows that

approximately 52 % of the total area of all detected primary slope failures at the Glacier d'Argentière faced W). The highest SFAP for both primary and secondary slope failures at both Argentière and Mer de Glace are in a SW to WNW direction (fig. 5.26 a, b, c & d), whilst the majority of pre-failure slope area is shown to be in the N to NE direction. At Bossons and Pre de Bard (fig. 5.26 e & g) where only a single slope in NE aspect was surveyed, the SFAP reflects this however, the largest SFAP at the Miage (fig. 5.26 f) is similar to the Argentière and Mer de Glace in the SSW direction.

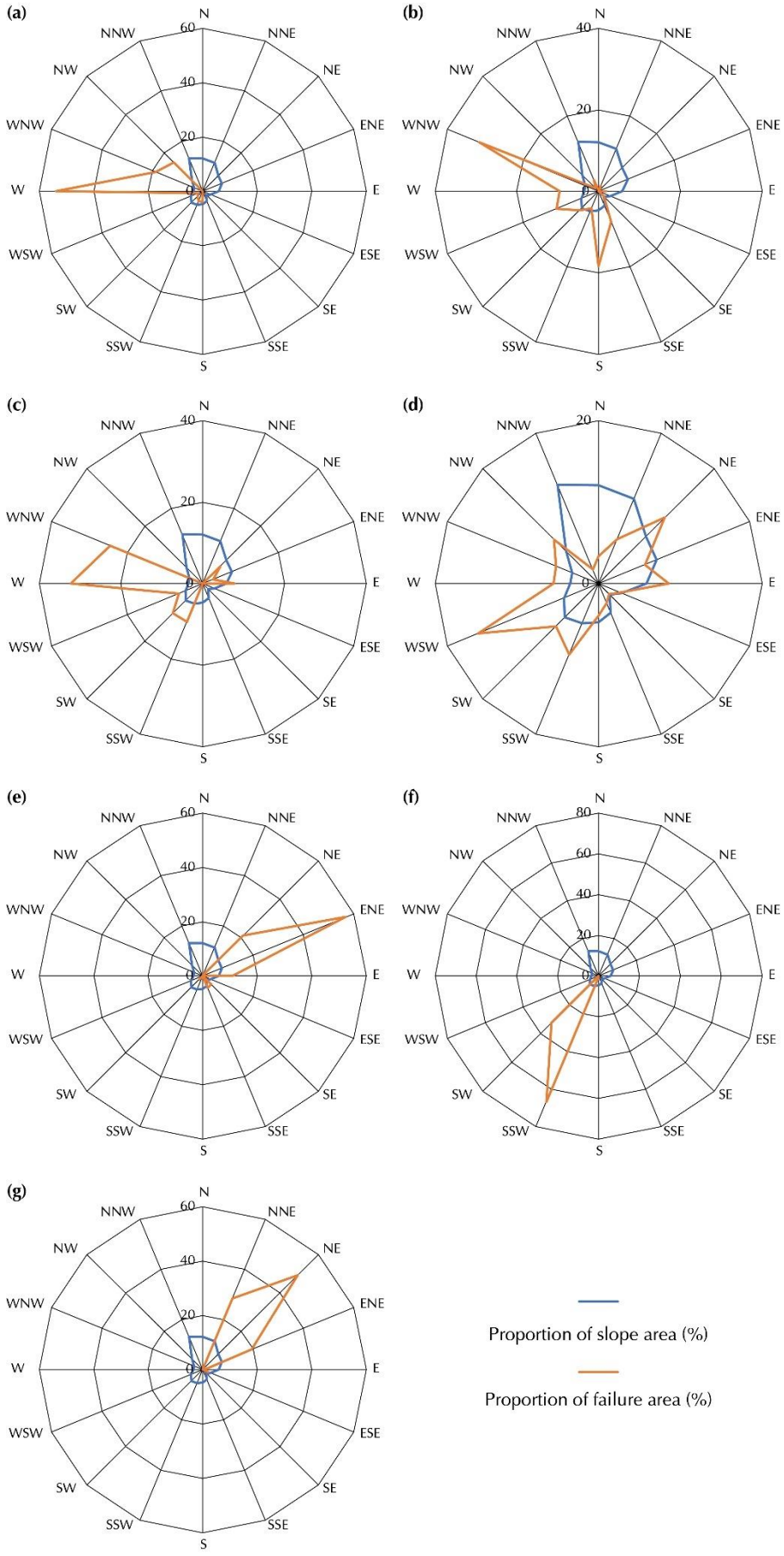

Figure 5.26: Radar graphs showing the aspect of; i) the slope surface area denoted by the blue line and; ii) the proportion of total slope failure area denoted by the orange line for; (a) & (b) Glacier d'Argentière primary and secondary slope failures respectively; (c) & (d) Mer de Glace primary and secondary slope failures respectively; (e) Glacier de Bossons; (f) Ghiacciaio del Miage and; (g) Pre de Bard.

The probability density functions (PDF) for primary and secondary slope failures were calculated for failure altitude, pre-failure slope angle, and failure aspect and are shown in figure 5.27 (left and right for primary and secondary respectively). Primary slope failures were measured across altitudes ranging from 1,429 m a.s.l. to 3,033 m a.s.l. with maximal densities of primary slope failures occurring at an altitude of approximately 1,500 m a.s.l. across slopes at a pre-failure angle of 70-80° with a predominantly ENE aspect. Secondary slope failures were measured across altitudes ranging from 1,759 m a.s.l. to 2,890 m a.s.l. with maximal densities of secondary slope failures occurring at an altitude of approximately 2,250 m a.s.l. across slopes at a pre-failure angle of 40-50° with a predominantly SW aspect. Whilst slope aspect and pre-slope angle offer valuable insights into the driving processes of slope failures, altitude may only serve to reflect site location with densities driven by the altitude of surveys performed. The processes responsible for the spatial distribution of detected slope failures is discussed further in section 6.3.

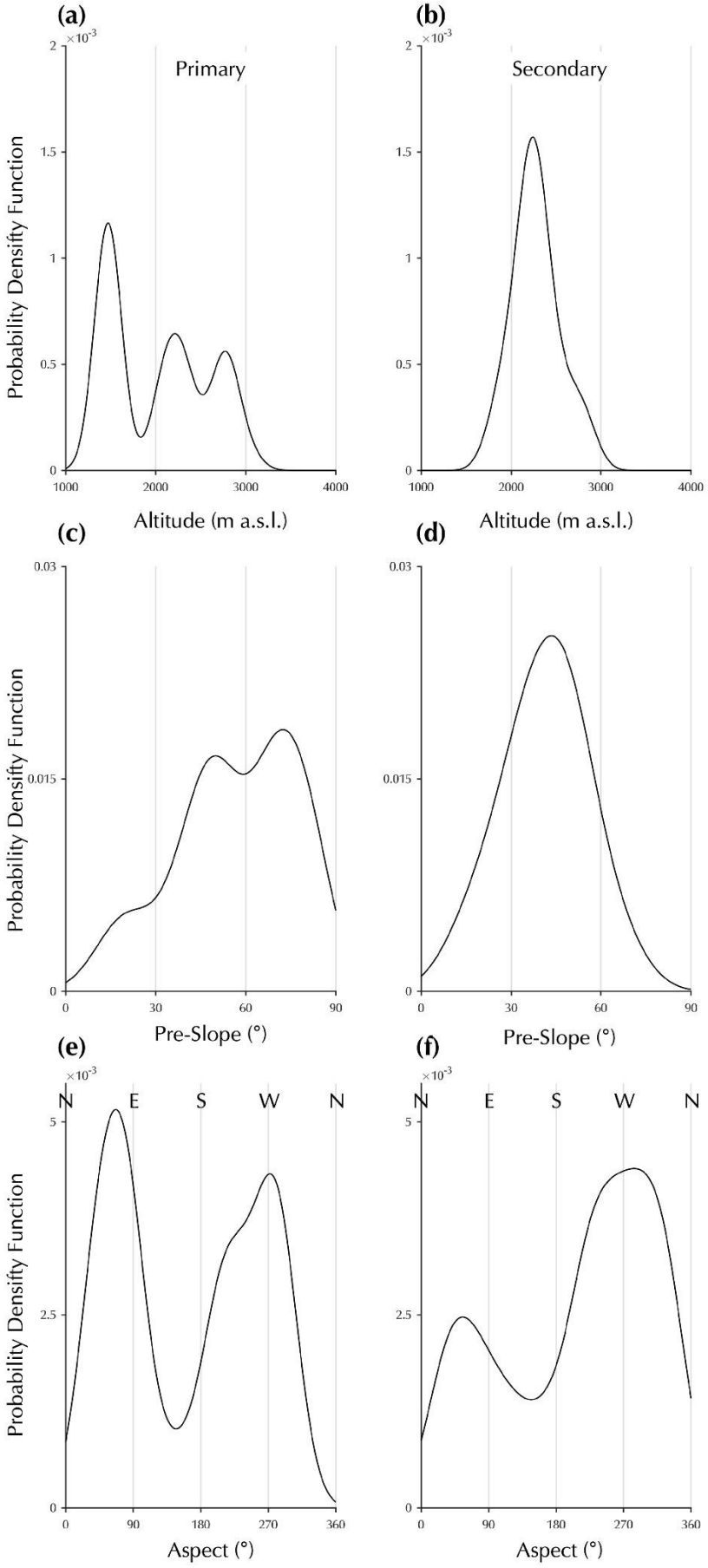

Figure 5.27: Probability density functions for (a & b) slope failure altitude; (c & d) pre-failure slope angle and; (e & f) slope failure aspect from the combined inventories of primary (left) and secondary (right) failures. The probability of failure for a horizontal slope in (c) and (d) is shown as > 0 – this is an artefact of the statistical process and not a real probability.

In figure 5.28, SFAP is plotted for each gradient bin (increasing from shallow in ranges of 10° to vertical) on top of the proportion of total slope area at each angle for all of the sites. The maximum SFAP (denoted by orange and blue line for primary and secondary respectively) are consistently at shallower angles for secondary slope failures than those of primary slope failures, however, this is not true for Mer de Glace (5.28 5.28 b). SFAP does not appear to be driven by the proportional availability of slope area at each gradient.

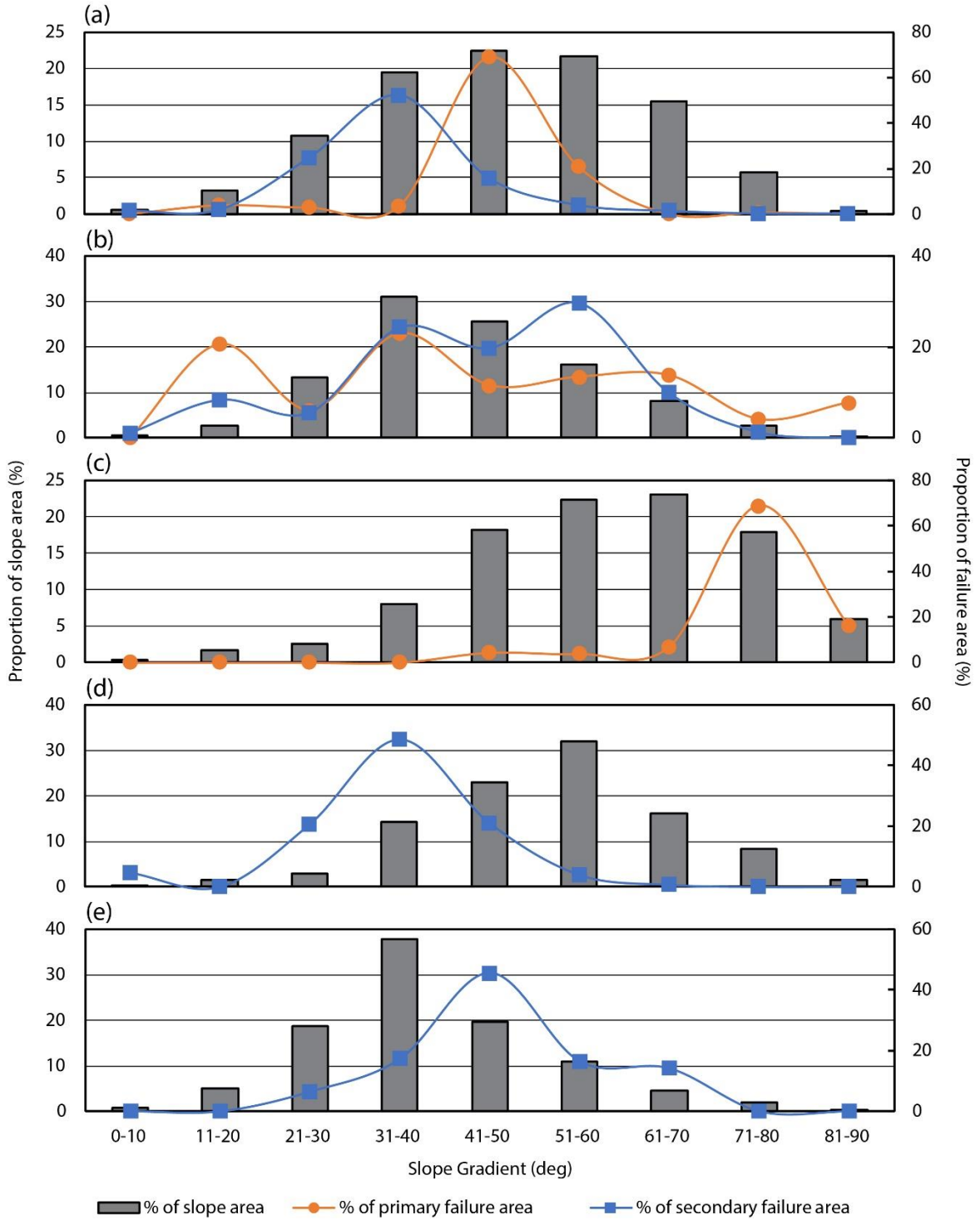

Figure 5.28: Relationships between distribution of slope gradient and slope failure area for; (a) Glacier d'Argentière primary and secondary slope failures; (b) Mer de Glace primary and secondary slope failures; (c) Glacier de Bossons; (d) Ghiacciaio del Miage and; (e) Pre de Bard.

SFAP and SFC are plotted against slope angle for all sites in figure 5.29. Secondary slope failures at Argentière, Mer de Glace and Miage (fig. 5.29 b, d & f) are highest in concentration at much shallower angles than where the maximum SFAP is found. The SFC at the Pre de Bard site (fig. 5.29 g)is maximal at the same angle where the greatest SFAP is found. Highest SFC at Bossons is actually shown to be across areas of the slope that are steeper than where maximum SFAP is found (fig. 5.29 e). Specifically, the largest SFAP are distributed between the ranges of 41-50°, 31-40° and 71-80° for primary slope failures at Argentière, Mer de Glace and Bossons respectively whilst distributions of SFAP are largest in the ranges of 31-40°, 51-60°, 31-40° and 41-50° for Argentière, Mer de Glace, Bossons, Miage and Pre de Bard (fig. 5.29 a to f). SFC is highest (> 1 x 10^4 slope failures/ km^2) at Pre de Bard across the gentlest area of slope (0-10°), although only accounts for 5 % of SFAP.

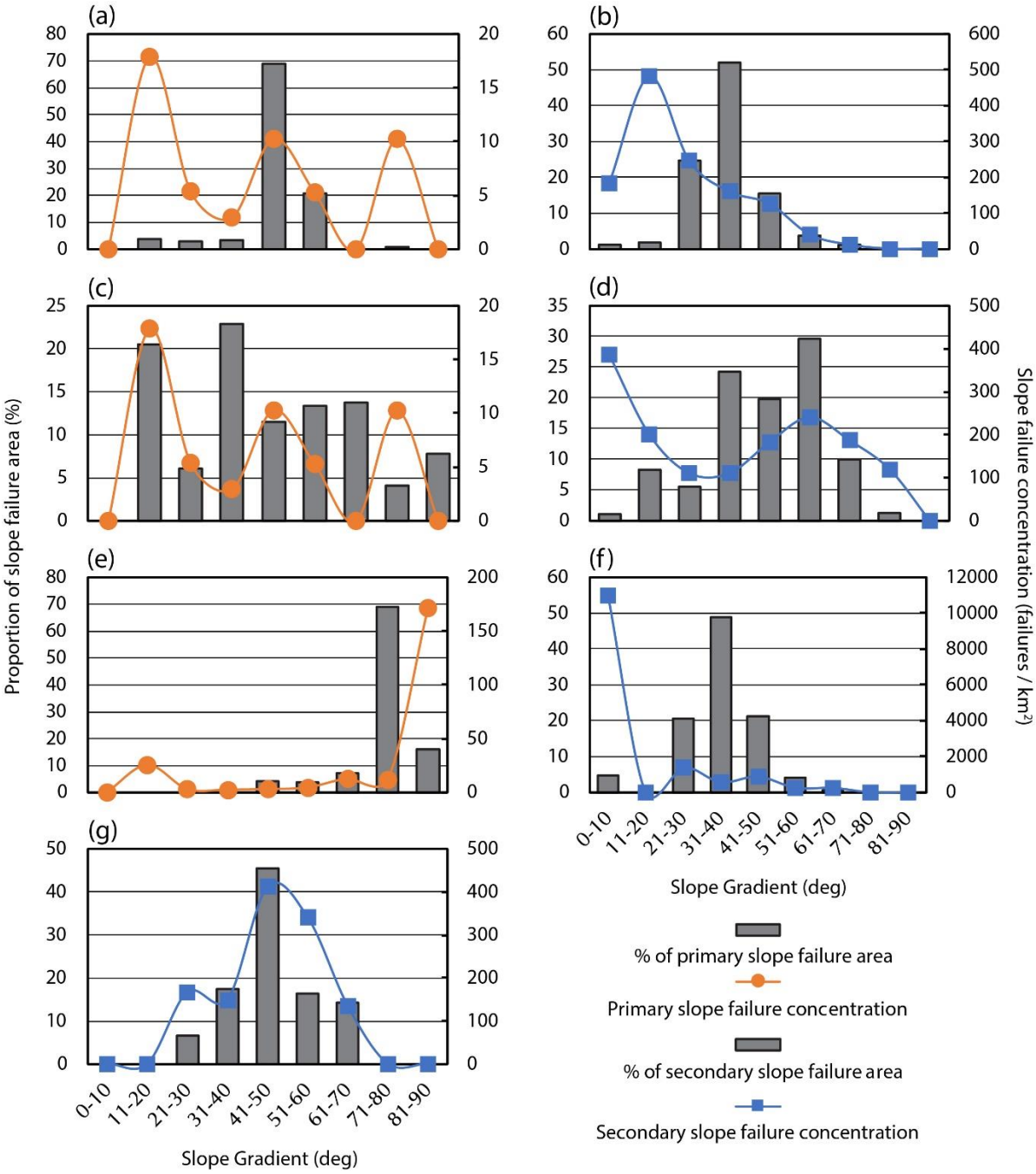

Figure 5.29: Relationships between distribution of slope gradient and slope failure concentration for; (a) & (b) Glacier d'Argentière primary and secondary slope failures respectively; (c) & (d) Mer de Glace primary and secondary slope failures respectively; (e) Glacier de Bossons; (f) Ghiacciaio del Miage and; (g) Pre de Bard.

The mean width, height and depth of slope failures at each of the sites are summarised in figure 5.30. The slope failures detected at the Mer de Glace (both primary and secondary) are consistently the widest, tallest and deepest when compared to the other sites which are typically less than 6 m wide and tall, and less than 2 m deep. It is impossible with these data to say with any degree of certainty whether the individual events detected at the Mer de Glace are single failures that are characteristically larger than those at other sites, or whether the measured distances are several smaller coalescing events. As reviewed in section 2.5.2, failures across sediment-mantled slopes have previously been shown to be dominantly debris flows and debris slides, the rapid downslope flow of poorly sorted sediment and water. In these cases, individual secondary failure events are not necessarily discrete boulder falls (see section 2.2.1) and analysis of width, depth and height will serve to develop our understanding of slope profile development following exposure by deglaciation (e.g. through slope gullying). The implications of these findings on the modification of slope form are discussed in more detail in section 6.5.

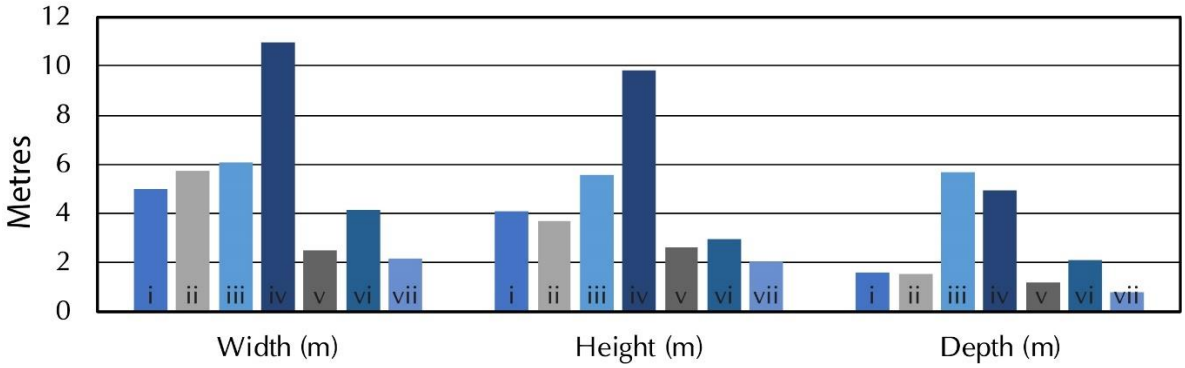

Figure 5.30: Average width, height and depth of slope failures at Argentière (primary) (i), Argentière (secondary) (ii), Mer de Glace (primary) (iii), Mer de Glace (secondary) (iv), Bossons (primary) (v), Miage (secondary) (vi) and Pre de Bard (secondary) (vii).

5.7.2 Size Distribution

Tables 5.9 and 5.10 present descriptive statistics for volume (V_L), width (W_L), height (H_L), depth (D_L) and area (A_L) of slope failures in the combined inventories for primary and secondary types respectively. Primary slope failures represent a total volumetric loss of 1.4 x 10^3 m^3 comprised of 43 single events varying in size across three orders of magnitude. The inventory exhibits a mean slope failure volume of 33.72 m^3 with roughly cuboid-like average dimensions of 4.23 x 3.90 m with a mean depth of 2.72 m. The largest 10 % of primary slope failures (*n* = 4; 9.30 % of total) produce a little under half (47.35 %) of the total slope failure volume whilst the smallest 50 % (*n* = 22; 51.16 % of total) account for just 6.15 % of the total volume. Secondary slope failures exhibit similar behaviour and have a total volumetric loss of 3.7 x 10^5 m^3 comprised of 723 single events varying in size across five orders of magnitude. The inventory of secondary slope failures has a significantly

higher mean volume than that of primary slope failures at 506.76 m^3 and a slightly greater mean depth of 3.76 m. The smallest 20 % of secondary slope failures (*n* = 713; 98.62 % of total) represent the highest frequency but account for less than half (41.27 %) of the total geomorphic work whilst the largest 10 % of secondary slope failures (*n* = 2 / 0.28 % of total) are responsible for almost one quarter (24.61 %). The inventories for both primary and secondary slope failures are positively skewed (i.e. tail of the frequency distribution is larger to right / larger-magnitudes) and hold kurtosis values that indicate both are leptokurtic whilst the distribution of secondary slope failure volumes possesses heavier tails (i.e. greater kurtosis value) than that of primary (tables 5.9 & 5.10). As would be expected with a skewed distribution, the mean V_L for both primary and secondary slope failures is significantly larger than the median, and the latter is a better measure of the centre (i.e. more valid representation of typical magnitude) of both distributions. The median V_L of primary and secondary slope failures is 7.64 m^3 and 30.07 m^3 respectively. The implications of this are discussed further in section 6.4.

Table 5.9: Descriptive statistics of the inventory of primary slope failures from the combined inventory data.

	V_L (m^3)	W_L (m)	H_L (m)	D_L (m)	A_L (m)
Mean	33.72	4.23	3.90	2.72	21.35
Median	7.64	3.66	3.46	1.56	13.26
SD	55.15	2.68	2.39	2.48	21.87
Kurtosis	10.11	0.79	0.09	-0.05	1.62
Skewness	2.90	0.79	0.67	1.26	1.36
Range	284.30	11.75	10.34	7.94	88.59
Minimum	0.15	0.51	0.52	0.43	0.27
Maximum	284.45	12.26	10.86	8.37	88.86
Sum	1,449.83	181.77	167.89	117.16	918.01

Table 5.10: Descriptive statistics of the inventory of secondary slope failures from the combined inventory data.

	V_L (m^3)	W_L (m)	H_L (m)	D_L (m)	A_L (m)
Mean	506.76	9.04	7.68	3.76	174.07
Median	30.07	6.01	4.53	3.51	26.85
SD	3,024.11	11.40	10.75	3.08	662.70
Kurtosis	154.50	18.01	24.36	26.10	75.11
Skewness	11.64	3.70	4.27	3.91	8.05
Range	45,779.26	98.95	89.81	31.17	8,218.32
Minimum	0.20	0.17	0.09	0.61	0.03
Maximum	45,779.46	99.12	89.90	31.79	8,218.35
Sum	366,389.36	6,533.80	5,555.17	2,720.68	125,854.50

The measured volumes of detected slope failures in the combined inventory were used to construct magnitude-frequency relationships by way of Cumulative Distribution Functions and these are shown in figure 5.31 for primary (a) and secondary (b) events. Maximum likelihood power-law and log-normal distributions have been fitted to the data.

The power-law and log-normal can only be fitted across a truncated portion of the primary slope-failure volumes, both from a minimum value of approximately 60 m^3 with scaling exponents of 3.02 and 4.02, 0.79 respectively. There is a clear break between the upper magnitude values and the lower-magnitudes where the distribution begins to roll on the primary slope failure data. The 32 events that fall below the rollover were extracted and their magnitude-frequency are inset on figure 5.31 (a), shown to be well-described by their own log-normal fit. The secondary slope failures (fig. 5.31 b) are shown to follow a much more continuous distribution across a wider range of magnitudes with small perturbations in the upper-values where the frequency of events begins to tail off (inset on fig. 5.31 b). A log-normal is a better fit across a wider range of magnitudes and is true for all events over 13.8 m^3 whilst the power-law can only be fitted to the distribution above a minimum bound of 167 m^3. The scaling exponent of the power-law (α) is 1.75, whilst for the log-normal is 1.32, 2.99.

The break in the distribution of primary slope failures between larger and smaller magnitudes may suggest an element of scale-dependency. Larger surveys are more likely to yield higher magnitude events whilst lower-resolution surveys (as a consequence of distance to the surveyed slope) are limited by a higher detection threshold (LOD). For example, the higher resolution survey conducted at the Glacier de Bossons accounts for the majority of the events in the lower portion of figure 5.31 a, whilst the only other rockslope surveys conducted were across the Glacier d'Argentière and Mer de Glace which were of significantly lower resolution (though larger-scale) as a result of capturing images from a Helicopter. As such, only mid- to large-magnitude events could were detectable across the larger-scale surveys, possibly skewing their probability in the distribution. Such scale-dependencies or site-specific distributions are not true for the combined inventory of secondary slope failures as surveys of varying scale and resolution were conducted across slopes at all sites. The implications of such scale- and site-dependencies on the transferability of the devised distributions is discussed further in section 6.4.

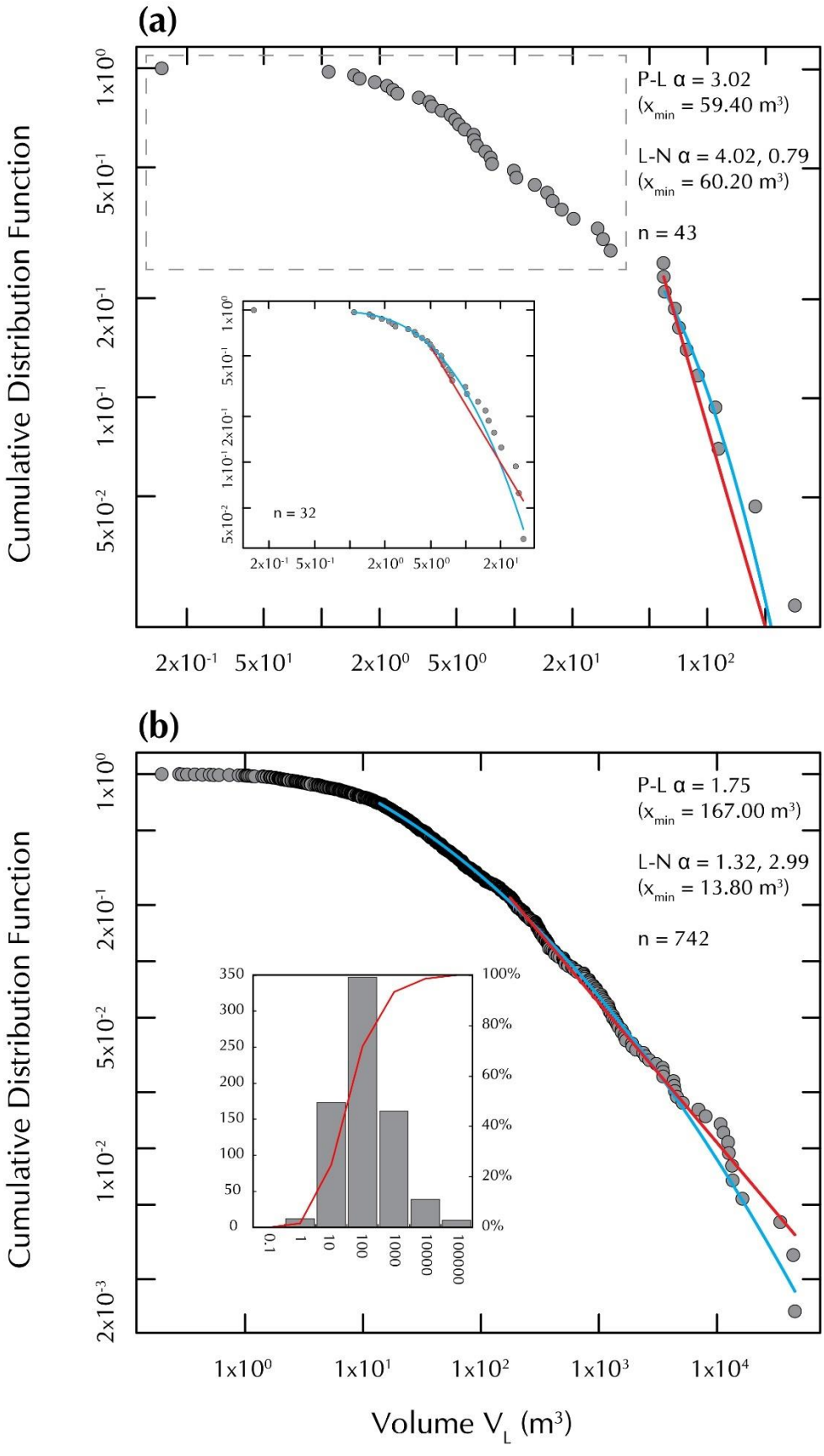

Figure 5.31: Cumulative Distribution Functions (CDF) for the combined inventory of slope failures. Primary and Secondary (a & b respectively) slope failures are plotted against their CDF with their maximum likelihood power-law (red) and log-normal (blue) fit. Scaling exponents (α) and rollover values (x_{min}) are given on each graph. Inset on (a): the lower group of failures (i.e. events below the rollover value) highlighted within the grey dashed box with a power-law and log-normal distribution fit to the data. Inset on (b): histogram to show the frequency distribution of secondary slope failures in the combined inventory. Grey bars represent the frequency on the primary axis and the red line denotes cumulative percentage contribution on the secondary axis.

The statistical characteristics of the power-law and log-normal distributions fitted to the magnitude-frequencies of failures detected at each site are summarised alongside those of the combined inventory in table 5.11. P-L scaling exponents at sites where both primary and secondary slope failures were detected (Argentière and Mer de Glace annual surveys) are shown to be smaller for the latter, although the exponent of the P-L for secondary slope failures detected in the Mer de Glace intra-annual data is the largest of all sites. P-L distributions can be fitted across the data from a lower minimum bound (x_{min}) than the L-N for primary slope failures at all sites, whilst the opposite is true for secondary slope failures. This pattern is also reflected when events are considered collectively.

Table 5.11: Summary of scaling exponents (α) and rollover values (x_{min}) for the inventories of slope failures from each site and the combined inventory.

		Power-Law		Log-Normal	
		α	x_{min} (m^3)	α	x_{min} (m^3)
Primary	Argentière	2.84	4.67	2.57, 0.24	6.19
	Mer de Glace	4.50	59.40	4.24, 0.33	59.40
	Bossons	1.91	1.48	1.49, 0.94	2.35
Secondary	Argentière	1.90	4.36	1.74, 1.30	1.01
	Mer de Glace	2.93	1,048.00	3.61, 1.95	10.30
	Mer de Glace (intra-annual)	5.47	294.00	3.44, 1.38	10.90
	Miage	2.75	20.10	2.88, 0.91	4.43
	Pre de Bard	2.52	1.93	1.08, 0.69	1.99
Combined	Primary	3.02	59.40	4.02, 0.79	60.20
	Secondary	1.75	167.00	1.32, 2.99	13.80

The cumulative proportions of slope failure area and volume for primary and secondary slope failures are shown in figure 5.32. The curves for primary slope failures (fig. 5.32 a & b) have gentler slopes suggesting less of an imbalance between the volume of material produced by smaller- and larger-magnitude slope failures whilst the steeper curves of the secondary slope failure area and volume (fig. 5.32 c & d) indicate that the less-frequent, larger-magnitude events are responsible for the greatest proportion of geomorphic work. However, this is not a straightforward conclusion and relies heavily on the assumptions explained in section 5.1, whereby some of the larger failures may be mass movement events characterised by a larger number of discrete failures that have coalesced and measured as a single event. The validity of the apparent contribution of large-magnitude events to the size distribution is discussed further in section 6.4.

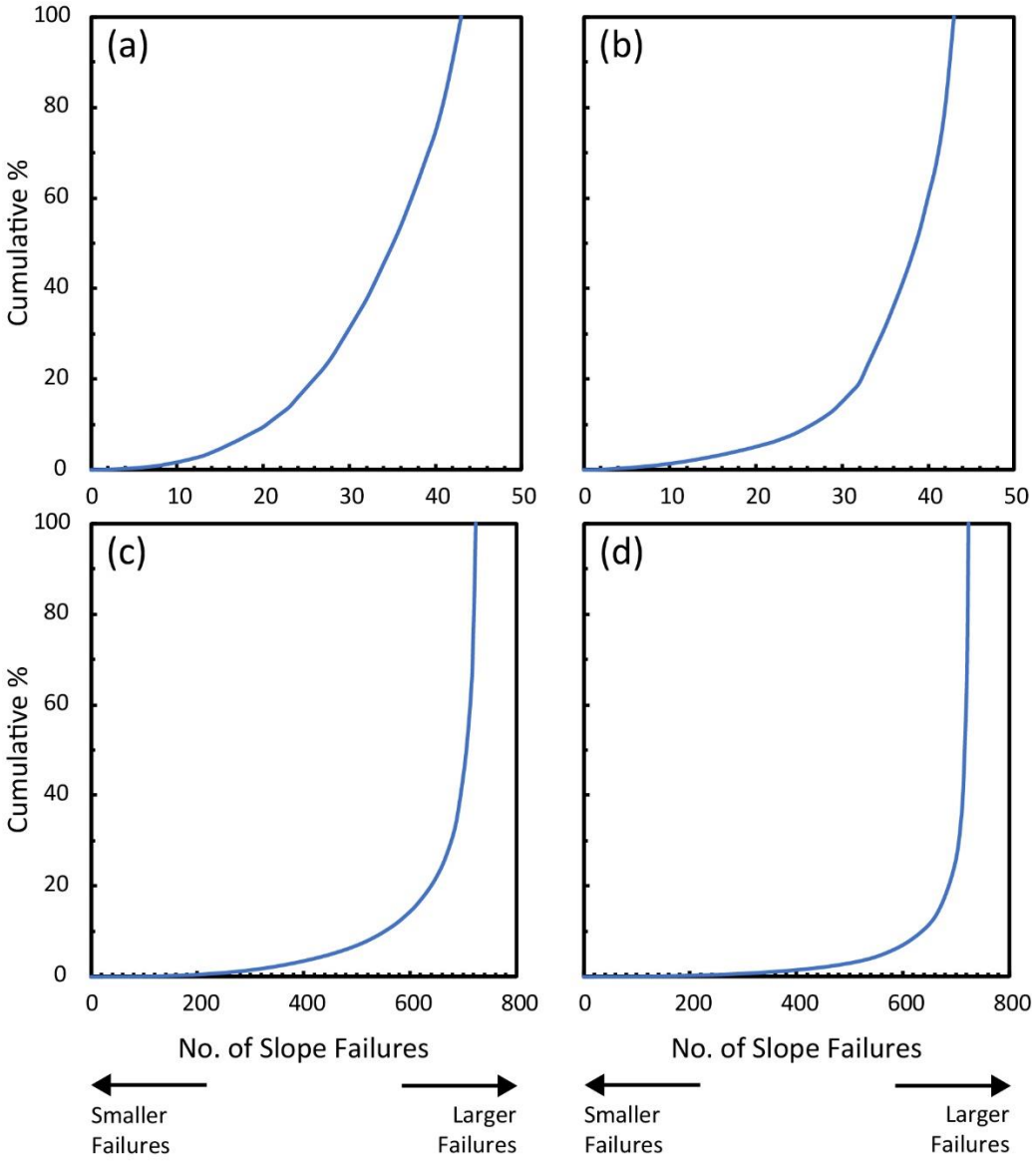

Figure 5.32: Cumulative proportion of slope failure area and volume for primary (a & b respectively) and secondary (c & d respectively) slope failures in the Mont Blanc massif versus slope failure rank (i.e. slope failures in size order).

The relationship between volume and the volume-to-surface-area ratio (V/S) is presented in figure 5.33 for secondary failures. As previously mentioned, the inventory of secondary slope failures observed at all sites (n = 723) is well-defined by a power-law with an exponent a = 1.75 above a lower bound (x_{min}) of 167 m^3 using the method proposed by Clauset, Shalizi and Newman (2009), (fig. 5.31 b). The lower bound defines the region of power-law behaviour and thus, the slope failures with volumes greater than x_{min} (n = 167) can be accepted as representative data that are hardly affected by the probability that V/S exceeds T (the low threshold of V/S for a failure is denoted by T). The empirical data larger than x_{min} produce a power-law relationship between the V/S and the V_L (fig. 5.33);

$$V/S = 0.08{V_L}^{0.16}$$

Equation 5.1

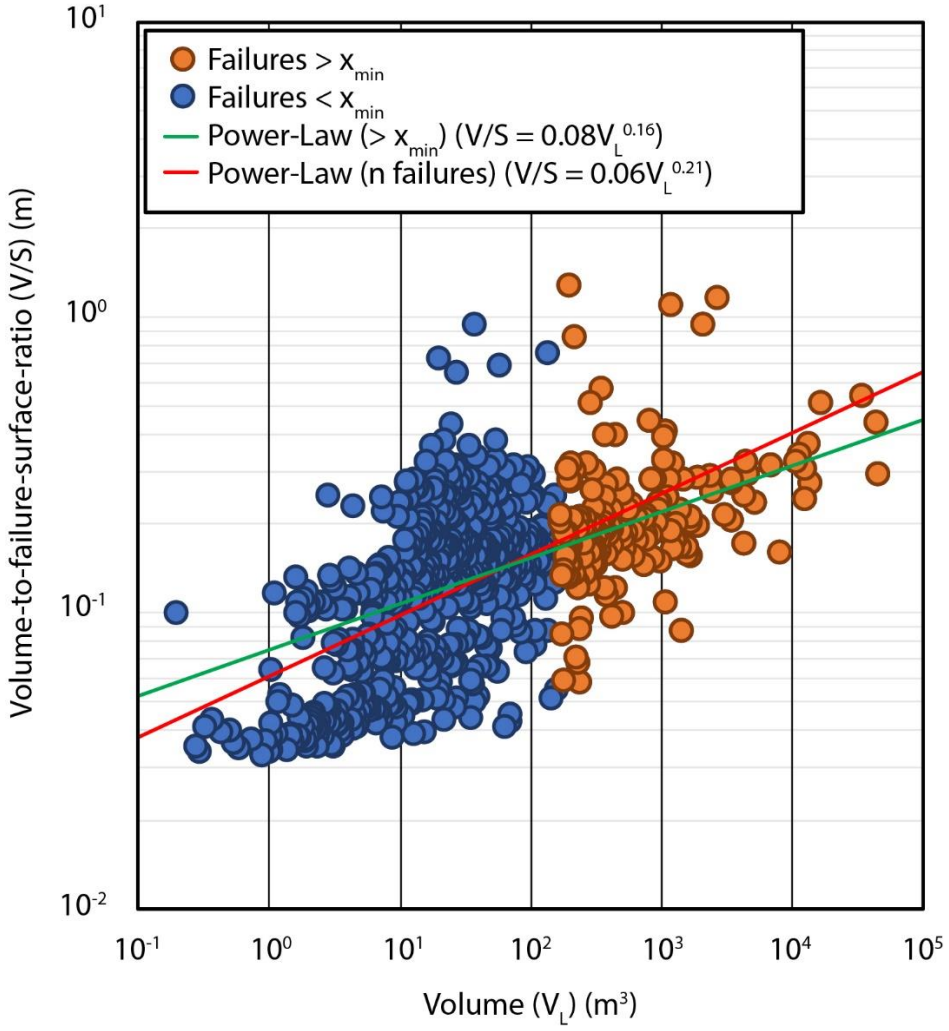

Figure 5.33: The relationship between the volume-to-surface-area ratio (V/S) and the volume (V_L) for the secondary slope failure inventory is shown. Linear fits of the logarithmically transformed values of the empirical data in its entirety and selectively across data larger than the lower bound of the power-law tail (x_{min}) shown in fig. 5.31 are also presented.

5.8 Modification of Slope Form

Secondary failures are the dominant type detected in this study, resulting in a significant modification of the slope form. Examples of areas where this is occurring are given here, whilst the implications are discussed in the following chapter. The most conspicuous sign of sediment reworking above and around the glaciers at the study sites is in the form of closely spaced (often intersecting) gullies which incise the lateral moraines. Examples of these at the Glacier d'Argentière and Mer de Glace are given in figure 5.34.

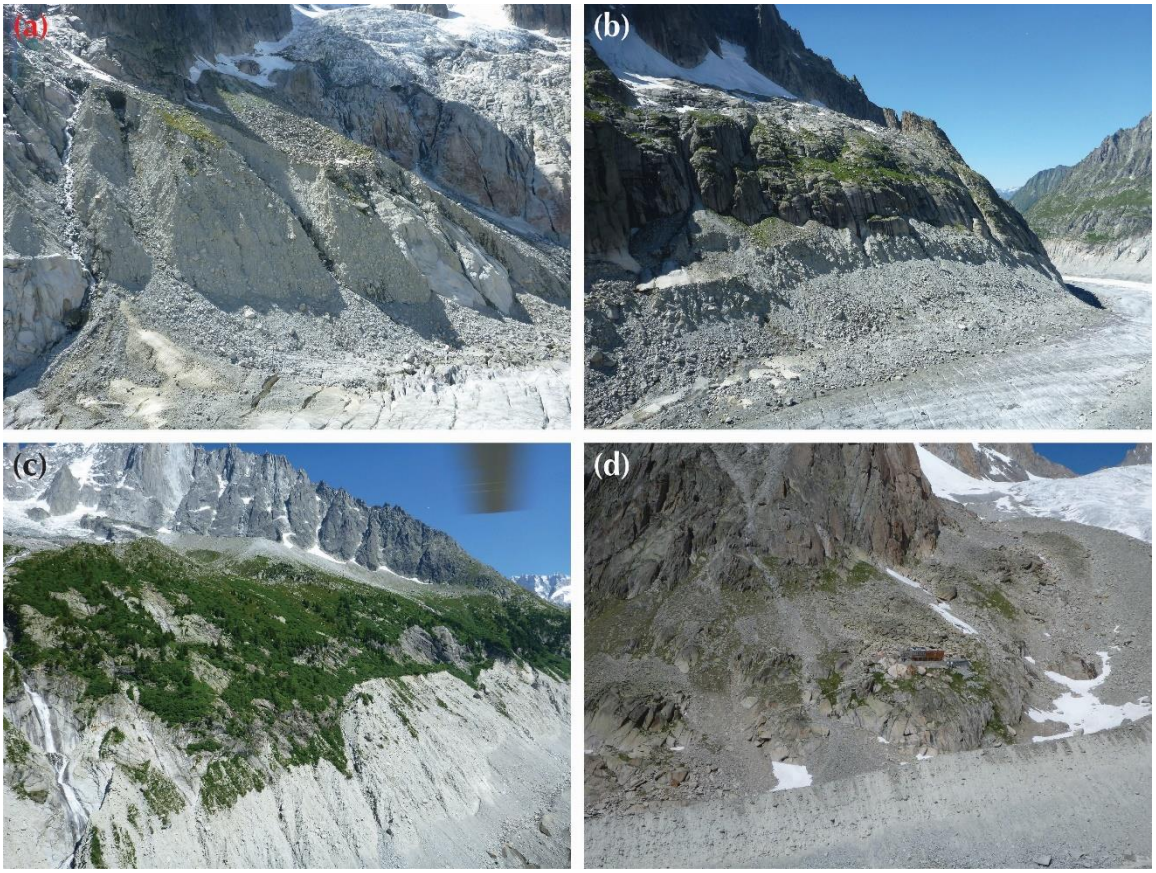

Figure 5.34: Field photographs taken above (a) to (c) Mer de Glace and (d) Glacier d'Argentière glaciers in the Mont Blanc massif, showing steep-sided gullied lateral moraines.

A secondary slope failure across the NE-facing slope of the Mer de Glace is shown in figure 5.35. The failure in the centre of the figure (denoted with a dashed red line) measures approximately 100 x 200 m and had a volume of 4.8 x 10^4 m^3 representing a significant remobilisation of material from the sediment-mantled lateral moraine above the glacier surface. The upper limit of the failure is controlled by the break of the slope and there are not enough data to say whether this is a single failure or several coalescing failures during the observation period. There is also visual evidence of water flowing across the moraine surface post-failure.

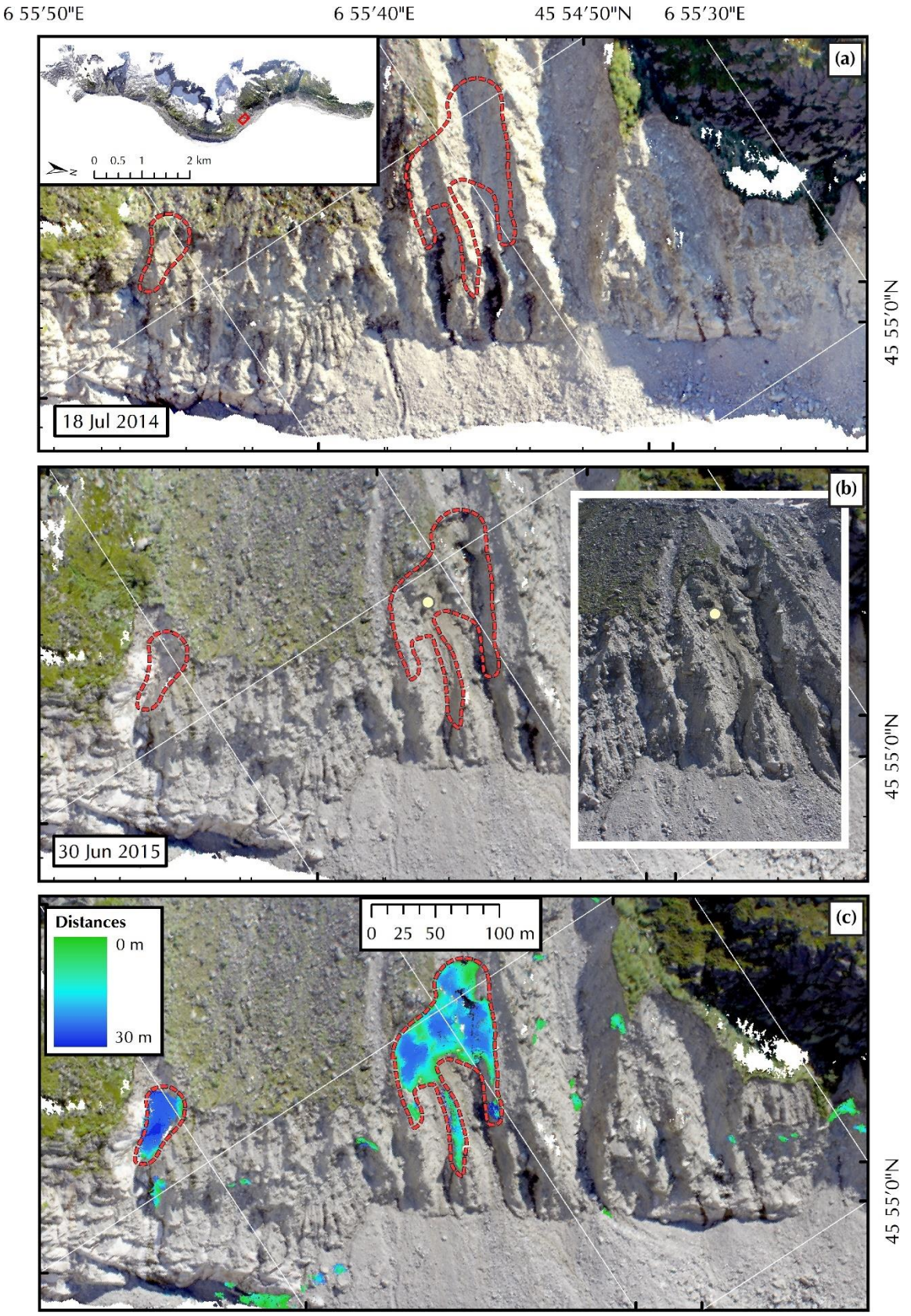

Figure 5.35: An example of two large failures along the lateral moraine of the NE-facing slope of the Mer de Glace. Slope failures are denoted by dashed red. Pre- (a) and post-event (b) point cloud shown with M3C2 distances overlain (c). Inset on (a) for location reference and field photograph inset on (b) showing post-event slope. Yellow circle placed for reference marker between point cloud data and field photograph. Darkened area of slope and channelling post-event are visible indication of water flow.

An example of slope modification, gully lengthening and deepening is given in figure 5.36. This is the same failure presented in figure 5.35. The DEM highlights a steepened section of lateral moraine between the range of 51-80° that failed. The post-failure slope was significantly shallower, between 21-40°. As well as the shallowing of slope angle, the height/ length of the gully increased by roughly 50 m and deepened by up to 10 m.

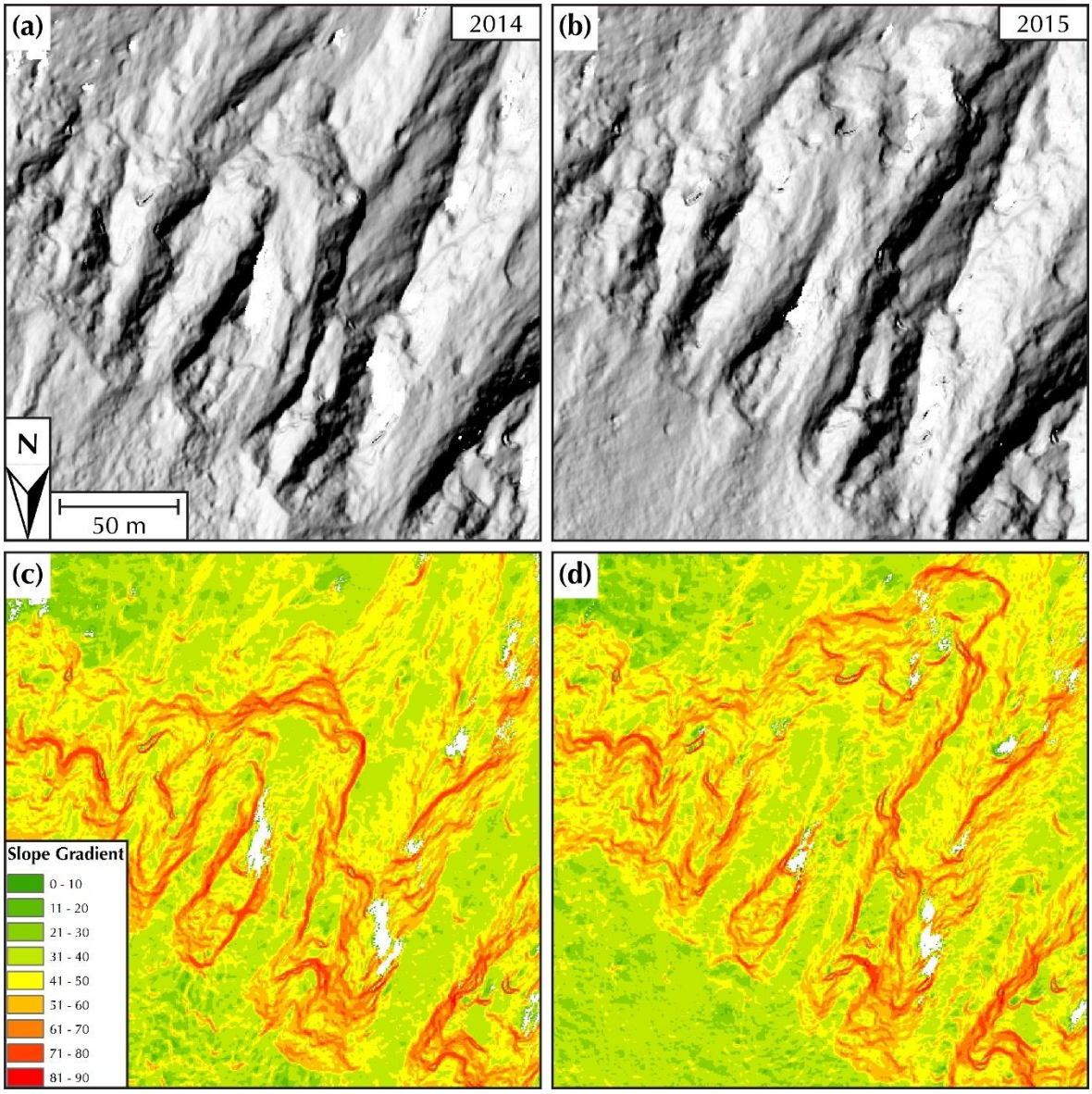

Figure 5.36: Digital elevation models (0.5 m resolution) created using point cloud data from the Mer de Glace dataset. Example of secondary failure along the lateral moraine of the NE-facing slope resulting in significant modification of slope form. (a) and (b) are hill-shaded DEMs for context where the change in form can be easily identified. (c) and (d) demonstrate the adjustment of slope angle and gully lengthening post-failure.

Observations of failures from sediment-mantled slopes such as those shown in figures 5.35 and 5.36 are useful for understanding how such patterns might change slope form. Extrapolating the results from relatively short-term surveys such as those here will allow a better understanding of

slope profile development, gully evolution and sediment dynamics during the period of deglaciation. A geomorphological interpretation of the role of detected slope failures in the modification of slope form and the implications of this are discussed further in section 6.5.

5.8.1 Retreat Rates

Table 6.3 summarises the erosion rates (calculated as the total volume of change across the surface area over the observation period) for the sediment-mantled slopes surveyed at Argentière, Mer de Glace, Miage and Pre de Bard. The first three are rates across slopes above actively wasting glaciers whilst the Pre de Bard has been completely deglaciated for several decades (fig. 6.13).

Table 5.12: Erosion rates across sediment-mantled slopes.

Site	Erosion Rate (mm a^{1})
Argentière	9.51
Mer de Glace	320.00
Miage	122.19
Pre de Bard	4.19

Whilst primary failures across rockslopes at Argentière, Mer de Glace and Bossons where detected, the LOD threshold was insufficiently low enough to detect smaller-magnitude failures and thus, rockslope retreat rates were only calculated for the Bossons site where the survey was of a high-enough quality to capture a full range of magnitudes. A total surface area of approximately 6116 m^2 was assessed for 3D topographical change. The total volume loss between the two annual survey dates (317 days) across the study area was 282.14 m^3. This produces a face-averaged retreat rate of 52.39 mm a^{-1} for the Bossons site.

5.9 Summary

This chapter has presented the results of change detection analysis across five sites at the Mont Blanc massif. The spatial and size distributions of 43 primary and 723 secondary slope failures ranging across several orders of magnitude have been given, highlighting key characteristics and regional signals from each. Secondary slope failures are the most frequently detected type, highlighting the importance and contribution of the steep-sided sediment-mantled slopes above and around actively thinning and retreating glaciers to the alpine sediment budget. The magnitude-frequencies of detected slope failures indicated that despite a P-L providing a good fit across a truncated potion of some data, a L-N is often more suitable fit across a wider range, providing a

better model for the understanding, predictability and extrapolation of slope failure distributions. As outlined in section 2.8.3, calculating the best fit to the magnitude-frequency distribution of slope failure volumes has important implications, such as; i) understanding the physical processes (i.e. slope failure processes) that drive their generative models; ii) assessing the land system response to changes in the cryosphere (specifically, deglaciation and the modification of slope form), and; iii) facilitating statistical extrapolations about the probable likelihood of future events. Qualitatively, compared to a P-L, the slope of a L-N distribution can be seen to lessen the probability of magnitudes at both ends of the spectrum (i.e. the probability of small-magnitude failures flattens, and the probability of larger magnitudes negatively skews away from the extrapolation of a P-L). A better fit to a L-N raises a number of issues regarding the representation of both small- and large-magnitude failures in inventories previously shown to be best characterised by a P-L. This is in-turn has important consequences on knowledge of geomorphic processes and potential hazards in deglaciating catchments. Thoughts on the processes and drivers of change, as well as the implications of the results on our wider understanding of sediment budgets and slope failure distributions are discussed in the following chapter.

6 Discussion

6.1 Introduction

This study has provided an investigation into the distribution of failures above and around glaciers in the Mont Blanc massif, European Alps. It has produced a new failure inventory of primary and secondary slope failures using innovative high-resolution topographical analysis. The combined inventories of detected primary and secondary slope failures can be found in Appendix 1. The results presented here have bridged a gap where previously there was a scarcity of quantitative data, providing insights into size distributions, controls and drivers of change that are only possible as a result of such a scale. As well as this, the use and development of SfM-MVS highlighted a number of key caveats and an effective method for filtering erroneous data as a result of poor illumination was devised. The purpose of this discussion chapter is to draw together and interpret the observations and results presented in earlier chapters, making the novel contribution to the subject clear, discuss the wider implications of the findings and indicate avenues for future working directions. As a reminder of the principle research aim of this thesis; Understand the spatial and size distributions of slope failures above and around wasting glaciers. The following objectives will be addressed; (i) explore the potential drivers and controls of short-term slope failures using their spatial distributions and through structural analysis of a recently deglaciated rockslope; (ii) analyse the effect of observed failure activity on the modification of slope form and mobilisation of sediment within the landsystem. Developing a conceptual model of a sediment yield and a deglaciating landsystem that considers the implications of these findings alongside existing knowledge.

The chapter will first discuss the methodological development and use of SfM-MVS photogrammetry, an innovative photogrammetric workflow that has received a considerable amount of attention in recent years (section 6.2). The spatial and size distributions of detected slope failures will then be examined (sections 6.3 and 6.4) before using these to determine possible drivers and controls (section 6.3.1). The implications of these findings on the mountain sediment budget will then be discussed, identifying possible geomorphological and glaciological consequences of the detected failures (section 6.5). Finally, two conceptual models based on the results and current understanding of the discipline will be presented (section 6.6); (i) a theoretical model of sediment yield through the early stages of the paraglacial period and; (ii) a valley scale time series schematic of slope failure processes and derived landforms in response to retreating glaciers.

6.1.1 Chapter Objectives

The objectives of this chapter are to;

1) Discuss the approach and development of the SfM-MVS technique and 3D change detection for creating topographic models; the advantages, disadvantages and implications for future uses.
2) Use the analysis of the spatial distribution of slope failures to determine potential drivers and controls of slope failures across slopes above and around retreating glaciers.
3) Explore the size distribution results and identify whether the rollover in probability of small magnitude slope failures is driven by physical processes or a manifestation of survey technique.

6.2 Structure from Motion Photogrammetry

As others have previously stated; the SfM-MVS technique represents a democratisation of high resolution 3D geospatial data by making the collection of these data available to "the masses" (e.g. Bemis *et al.*, 2014; Smith, Carrivick and Quincey, 2015). Even through the course of this study, SfM-MVS has seen a significant rise (fig. 2.11) in the number of applications with its continual appraisal and improvement (e.g. Immerzeel *et al.*, 2014; Tonkin *et al.*, 2015; Dewez, Leroux and Morelli, 2016 amongst others). SfM-MVS photogrammetry was used to create high resolution topographical models of slopes above and around glaciers in the Mont Blanc massif, and the results demonstrate that the approach can produce topographic data at the valley scale. The technique has several clear advantages over other approaches;

a) SfM-MVS workflows that are capable of producing topographical datasets of comparable accuracy to laser-based technologies, and in some cases producing point clouds far denser;
b) a reduction in the time required for data collection across large survey scales. For example, James and Robson (2012) notes an 80 % reduction for a 50 m long section of coastal cliff;
c) standard workflows that remove the necessity for either photogrammetry expertise or costly surveying equipment, and;
d) adaptable and particularly well suited to extreme environments where the use of more traditional survey technologies would present significant logistical challenges.

6.2.1 Survey Scales

This study has shown that SfM-MVS applied at the valley scale, using images captured from a helicopter, can produce models of high spatial resolution, and when combined with detailed surveys from terrestrial and UAV imagery offers a unique insight into the spatial distribution of geomorphological activity across such scales. This extends the practical reach of SfM-MVS beyond that proposed by Bangen *et al.* (2014) to a level similar to that of single and multi-beam SONAR (SBS/MBS) (fig. 6.1). Whilst others more recently have demonstrated the use opportunistic helicopter flights for SfM-MVS data capture (Girod *et al.*, 2017), the work here presents the first example of targeted surveys performed at the valley scale where surveys have been flown with the specific intention of capturing appropriate image sets with high quality consumer grade camera equipment. As well as this, airborne imagery was combined with accurate terrestrial ground control to achieve an alignment quality capable of detecting volumes to 0.28 m^3, providing a first of its kind analysis of valley scale spatial distribution and process information, that when combined with the detailed site surveys, present a unique insight into the slope response to deglaciation at the range scale.

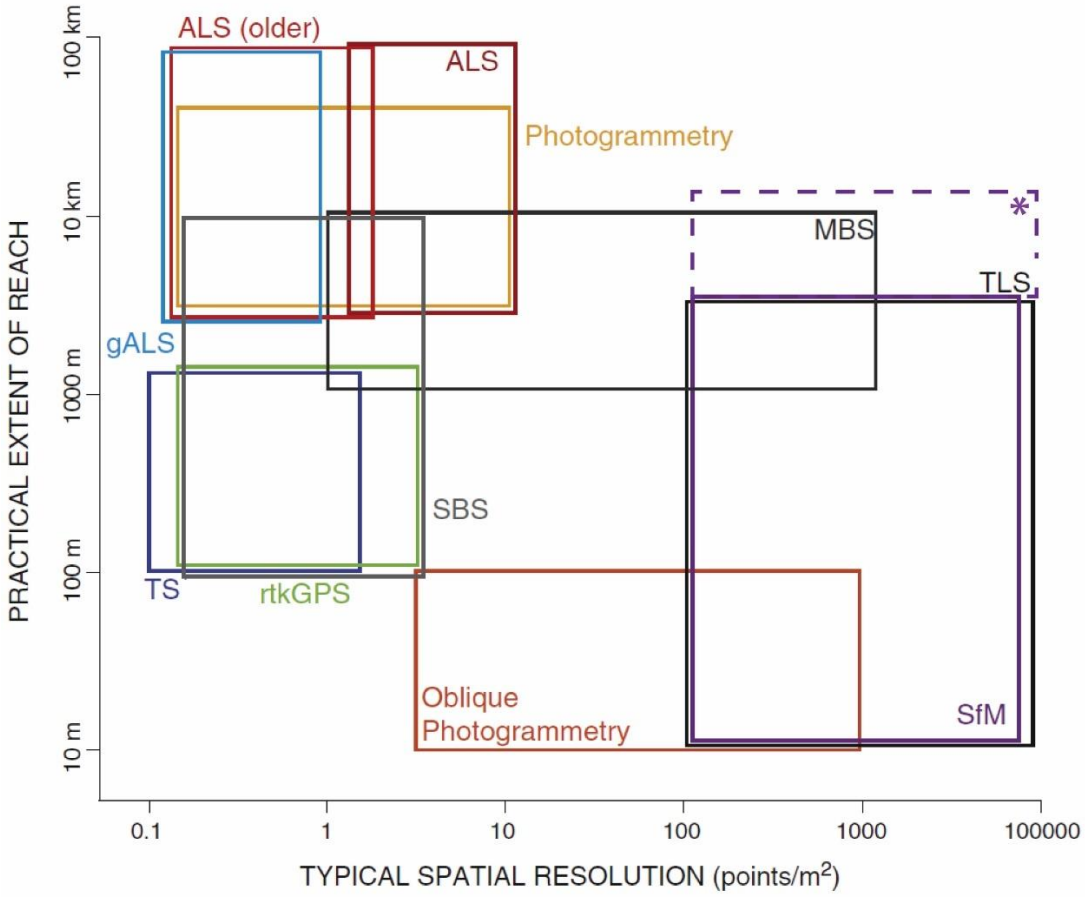

Figure 6.1: Conceptual diagram of the typical survey point spatial resolution versus practical survey reach extent for Airborne LiDAR Surveys (ALS), green ALS (gALS), Total Station (TS), real time kinematic (RTK) GPS, single beam SONAR (SBS), multi beam SONAR (MBS), photogrammetry, oblique photogrammetry, Structure from Motion (SfM), and

Terrestrial Laser Scanning (TLS). Asterix denotes extended practical reach of SfM-MVS (dashed purple box) demonstrated in this study. Adapted from Bangen et al. (2014).

6.2.2 Terrestrial and Airborne Imagery

At the Glacier de Bossons, an elevated slope surface adjacent to the surveyed slope meant that terrestrial imagery could produce slope coverage of comparable perspective to if the camera were elevated, though at other sites, steep high-altitude slopes were more challenging. The use of an Unmanned Aerial Vehicle (UAV) and helicopter greatly increase the achievable scale of SfM-MVS and in many ways are superior to conventional ground based topographical surveying that would traditionally take a number of days or weeks to gather the same level of detail across such scales. Despite model resolution being reduced through an increased distance away from the slope and smaller percentage of overlap between consecutive images, these issues are easily solved in future campaigns and not a general caveat of the SfM-MVS technique. The use of an elevated sensor position reduces the impact of variable ground sampling distance (GSD) as a result of steep topography from a terrestrial perspective (e.g. 4.4.2) and therefore, point density remains more consistent across higher altitude slopes (e.g. section 4.4.2). Whilst a lower point density does not generally mean a lower model quality, a greater GSD results in unclear imagery where smaller slope features are indistinguishable which means they cannot be modelled using SfM-MVS. At first glance, some of the RMSE values, and thus the LOD thresholds (section 4.9.1), for sections of High-Altitude Rock Walls (HARW) in the full valley surveys seem particularly large however, the images from a helicopter platform were captured from up to 3 km away from the surface, therefore RMSE values up to 3 m are expected given the high GSD and achievable precisions discussed below in section 6.2.3. This caveat is easily overcome, and not an issue with the technique but rather the data collection approach. Future work would benefit from several flight paths for each slope which would allow a closer proximity; one that would capture the base of the slope at the glacier: slope interface; one to capture the middle region of slope and; one to capture the HARW. One clear contradiction of the use of a helicopter are the cost benefits of utilising an SfM-MVS technique being diminished, particularly if several flight paths are required. The UAV approach compliments the SfM-MVS technique in that consumer grade low cost UAVs are now capable of operating in a wide range of challenging environments, allowing a better perspective and greater scale of coverage whilst not requiring high capital investment. For geosciences, the simultaneous development of SfM-MVS and drone technology to a point where both are easily usable and accessible has resulted in an explosion of applications across a wide range of sub disciplines (e.g. Woodget *et al.*, 2014; Tonkin *et al.*, 2015; Brun *et al.*, 2016; Bühler *et al.*, 2016; Chesley *et al.*, 2017).

6.2.3 Methodological Development

A number of studies have now shown that SfM-MVS workflows are capable of producing topographical datasets of comparable accuracy to laser based technologies, and in some cases producing point clouds far denser (e.g. Fonstad *et al.*, 2013; Lucieer, Jong and Turner, 2013; Tonkin *et al.*, 2014; Brun *et al.*, 2016; Wilkinson *et al.*, 2016). Most of this work has arisen through the course of this study and as such, some of the developments discussed below are echoed by others. Nevertheless, they represent important considerations that any users of SfM-MVS should account for and highlight a number of caveats. Pre-field methodological testing revealed a systematic distortion in the form of a central convexity, exacerbated through the use of solely nadir imagery and lack of ground control (fig. 4.6). This nonlinear distortion was largely removed through the addition of images at an oblique angle to the surveyed surface, and it was observed that optimising the camera alignment based on well distributed GCPs using the Brown Conrady lens distortion approach also improved model quality on datasets comprising of solely nadir and oblique images respectively. This distortion is commonly referred to in the literature, often as the *bowl effect* (e.g. Immerzeel *et al.*, 2014; Kaiser *et al.*, 2014; Leon *et al.*, 2015; Brunier *et al.*, 2016; Peppa *et al.*, 2016). The most accurate results were found when using both a combination of nadir and oblique images as well as an optimisation workflow, reducing the RMSE to 0.01 m using images captured at 50 m from the surface. That is, a relative precision of 1:5000 where cm scale accuracy is achievable at viewing distances of 50 s of metres using a consumer grade UAV and camera equipment. James and Robson (2012) suggest a relative precision of 1:1000 and thus, the results of pre-field testing here imply that similar levels of precision are achievable at distances five times greater. However, the images (collected during the pre-field testing period) were captured under particularly propitious conditions in that the scene (City Stadium – a local cinder track) was relatively well illuminated, with strong shadowing prevented by a thin layer of cloud on an otherwise bright day. The scene was relatively flat and un-complex which allowed an even spread of ground control and images were captured in a controlled non-constrained setting where several flights with different camera parameters were possible. In the reality of fieldwork, it is unlikely that such a perfect situation as this would be possible and as such, a relative precision within the range of 1:1000 to 1:5000 should be expected. Other causes of poor surface representation in the data and alignment disagreement between successive datasets were identified as vegetation and sharp changes in slope topography. Vegetation is commonly noted as a cause of poor model generation from both photogrammetric and laser based topographical surveying (e.g. Tonkin *et al.*, 2014) owing to it sporadic nature and is mostly dealt with by manually trimming data to remove areas of vegetation and verification of change in areas where vegetation persists. Others have tried algorithm approaches to classifying 3D data based on surface roughness patterns to automatically categorise and filter vegetation from datasets (e.g. Brodu and Lague, 2012). Pre-field testing also highlighted that alignment of successive

data was of poorer quality where sharp changes away from the sensor, highlighted with cross sections in figure 4.8. This was mostly dealt with by ensuring an even spread of GCPs across surfaces of variable aspect and gradient, whilst the LOD threshold also accounted for these minor alignment problems.

Following the first season of data collection, model alignment was of poorer quality across the upper parts of all surveyed slopes, away from where GCPs had been placed at the base of slopes and manually registered using dGPS. Accessing these higher areas for manual GCP placement would be difficult or dangerous and as such, a reflectorless total station was utilised during the second field season. Distinguishable bedrock features were used as GCPs and this allowed a much better spread of control across the surveyed slope, though was restricted in distance. Although the alignment of slopes up to 500 m above the surface of the glacier and valley floor were greatly improved, HARW were beyond the range of the equipment and as such, relied on registration using GCPs at much lower altitudes. This resulted in higher LOD thresholds across these slopes and goes some way to explaining why no primary failures above the LOD threshold were detected. Importantly, this highlights an issue with internal model consistency and suggests that a deterioration in model quality can be expected across areas that aren't well constrained with ground control; a major caveat to the technique and an important consideration for control placement in future applications. Generally, alignment was of poorer quality at greater distances away from the area of control, though separation of the slope into processing sections and section-based adjustment through point to point and ICP registration reduced cloud to cloud distances. Alignments were restricted to adjustments in orientation and space with no allowance for linear re scaling. In all cases, multi temporal slope sections were comparably scaled following alignment suggesting that the deterioration in model quality away from an area of control is not nonlinear but rather constrained to an issue with model orientation and location, which means the camera model optimisation operates consistently between successive datasets providing ground control is also consistent. HARW will always present a significant challenge for an SfM-MVS workflow that relies on manually registered ground control, though significant developments in the use of SfM-MVS have resulted in an approach referred to as direct georeferencing (DG) (Rizaldy and Firdaus, 2012; Turner, Lucieer and Wallace, 2014; Carbonneau and Dietrich, 2016). That is, georeferencing in the absence of ground control points with priori knowledge of the location and orientation of the sensor as well as the camera calibration parameters. DG has been shown to produce results of comparable quality to models created using traditional GPS or TS registered GCPs (Carbonneau and Dietrich, 2016). This approach will be very well suited to research in challenging environments where manual GCP placement is difficult, as well as cases where rapid repeat monitoring data are required and manual GCP placement would significantly increase the time required, offering a potential solution for future topographical research across HARW. Despite this caveat, the RMSE

were not sufficiently high enough across HARW to potentially mask medium to large magnitude failures behind the detection threshold and rock walls at lower altitudes were well constrained with improved alignment quality though were structurally very different. This is explained more in section 6.3.2.

Another novel outcome from the methodological development, was a demonstration of the adverse effect on model quality from poorly illuminated sections of slope. To test the effect of variations in illumination between successive surveys on accuracy and repeatability, a simple approach was taken whereby two surveys were conducted across the same rock slope (Glacier de Bossons) late morning and early afternoon, allowing enough time to pass for the incidence angle of the Sun to significantly change the areas of shadowing across the face. Elevation profiles between the two clouds revealed good alignment across the majority of the surface though sharp changes in the topography away and toward the camera appeared to cause a number of problems, which were largely overcome when GCPs were placed on the opposing faces. A 'rounding off'/smoothing of rock wall areas, similar to those found by Wilkinson *et al.* (2016), in some parts of the model that were constructed using images captured farther away from the surface highlighted potential image resolution (i.e. GSD) problems. As would be expected with an image matching approach to topographic construction, areas obscured by poor lighting are typically poorly reconstructed however, operating within an uncontrolled environment such as the Alps requires a suitable approach for overcoming this shortfall as it is not always the case that surveys can only be conducted under the most favourable of conditions. Stöcker, Eltner and Karrasch (2015) find that during an SfM-MVS survey of a gully system, sunny weather induced shadowing, especially in the gully bed which lead to a reduction in contrast and data gaps whilst on a later date where lighting was more diffuse, the difference resulted in less shadowing and higher contrast across the entire area and thus, the reliability of their models was increased. Here, cloud to cloud differencing (where measured change was assumed to be error) highlighted maximal distances in areas of highest shadowing, determined by means of compositing the red, green and blue (RGBc) layers of each point into a new scalar field. The same scalar field was then shown to be a suitable tool for filtering by its value to reduce the number of erroneously placed points. Of course, filtering such points is at the expense of survey coverage however, this approach is the first example of a standardised workflow for simply removing potentially erroneous data. Filtering by a fixed value of $RGBc^{40}$ across all sites ensured that point removal was non-subjective. Whilst areas of failure within the shadows may be lost, and the general advice to capture image sets in well illuminated conditions still stands, this is the first attempt to provide a relatively straightforward approach to dealing with heavy shadowing which is almost inevitable and thus reducing the likelihood of error propagating through to final analyses. Others simply propose that surveys are conducted under favourable conditions

such as; (i) ensuring homogeneous lighting conditions and; (ii) avoiding areas of particularly heavy shadowing or high reflectivity (e.g. Bemis *et al.*, 2014).

6.2.4 Change Analysis

There are many established methods for measuring change and calculating distances between successive topographic surveys. One of the most recently developed approaches, utilising the M3C2 algorithm (Lague, Brodu and Leroux, 2013), was used in this study and was shown to be particularly useful for considering change across surfaces of particularly complex topography and with datasets that suffered from patches of noise in localised areas, caused by vegetation and poor image quality at greater distances from the sensor (e.g. across HARW). With sensible and informed parameter selection, the results presented in this thesis have shown that the algorithm is capable of highlighting areas of significant difference above a level of detection threshold that was manually verified to be genuine change using elevation profiles and comparisons of successive image sets. This was capable of detecting significant volumetric change (i.e. above the level of detection threshold) down to 0.20 m^3 (with an area of 0.03 m^2). By using this approach, data can be operated upon in raw point cloud format, removing the necessity for meshing or 'gridding' for traditional 2/2.5D approaches. There are an increasing number of examples where the M3C2 algorithm has been used in existing work for establishing cloud to cloud distances between multi temporal datasets (e.g. Benjamin, Rosser and Brain, 2016; Brun *et al.*, 2016; Dewez, Leroux and Morelli, 2016) however, there are no examples where these distances have then been used to calculate an approximate volume based on derived measurements. Often, users will extract areas identified as significant change (above the LOD threshold) and use other approaches for calculating volume, adding an additional layer of complexity in an already extensive processing workflow. In this research, combining the M3C2 algorithm with an original approach to estimating failure volume based upon measurement cylinders (based on online discussions (CloudCompare, 2017)) that could be implemented in programming software, produced a semi-automated workflow capable of efficiently generating failure inventories based on multi temporal topographical datasets.

6.3 Spatial Distribution of Slope Failures

Previous work has suggested that topographic survey data to date have typically been spatially restricted providing little baseline data from which short term geomorphological changes can be assessed (Carrivick and Heckmann, 2017). The data in this study cover recently deglaciated slopes in the pro glacial zone, as well as slopes above actively thinning and retreating glaciers, including geomorphological landforms that within the sediment cascade, act as interruptions and secondary stores in the connectivity of alpine sediment budgets. The spatial distribution of slope

failures is important for determining their potential controls, which are discussed in more detail in the following section (6.3.1). In general, secondary failures are shown to occur across slopes that have a shallower gradient than those where primary events are detected, though in the case of Argentière, Mer de Glace and Miage, maximum failure concentrations (i.e. number of individual detected failure events) are found at lower gradients than where the largest volume of material is lost (i.e. greater volumes, though lower frequencies, are detected across steeper slopes). Primary slope failures don't display any clear pattern of spatial distribution in regard to slope gradient, but at Argentière and Bossons, the maximum proportion of primary failure area is found at steeper gradients than secondary events. There is significant variability between the distribution of failures at the valley and range scale which suggests that slope specific surveys on their own are not suitable for extrapolating slope response to wider scales.

6.3.1 Controls and Drivers

First, the spatial distribution and what this may suggest about the controls and drivers of secondary failures (the most prevalent failure activity during the observation period) will be discussed. The potential controls of primary failures are discussed in relation to rock wall structure in the following section (6.3.2). Significant modification of the slope form immediately following the removal of buttressing ice is shown principally through the a high frequency of small magnitude slope failures which are controlled by gradient, sediment availability and water supply (Curry, 2000). The frequency of slope gradient above 30˚ (fig. 5.28) suggests that the majority of slope area for the Mer de Glace, Argentière, Miage and Pre de Bard meets the prerequisite for extensive slope adjustment through sediment remobilisation proposed by Curry (2000), and it is upon slopes with a pre-failure gradient above this, that the maximal frequency of secondary failures are shown to occur (figs. 5.2, 5.8 and 5.27).

The spatial and size distributions of slope failures are important for establishing potential controls and driving mechanisms. Maximal densities of secondary failures were found to occur on SW facing slopes. Rainfall has been shown to be a major driving mechanism in events such as debris slides, falls and avalanches (Hürlimann, Abancó and Moya, 2012). If this were the principle driver for the majority of secondary failures detected across sediment-mantled slopes, the highest frequency of failure activity would be expected around the wettest months (i.e. May and June) each year (fig. 6.2 a). Mattson and Gardner (1991) observed 25 mass wasting events from lateral moraines over two years, noting that 68 % of these occurred during or shortly after periods of rainfall accounting for 83 % of the total mass lost. They also found that a lesser magnitude (14 % of total loss) occurred at periods of warm clear weather that are most conducive to ablation and production of melt water (Mattson and Gardner, 1991). Considering the data with circumspection,

it is difficult to interpret distributions from such a short sampling period and further work would benefit from longer temporal scales and in-situ measurements of meteorological factors such as precipitation, temperature and insolation.

Insolation of sediment-mantled slopes can degrade sub-surface ice, and removal of overlying sediments can further accelerate this melting (Ballantyne, 2002b). The insolation of the slopes above the Mer de Glace were modelled using GIS to derive incoming solar radiation (measured in watt hours per square metre) (fig. 6.3 b). The solar radiation tool calculates insolation across a landscape (using a DEM as an input) based on methods from the hemispherical view shed algorithm developed by Rich *et al* (1994). It can be seen that the largest area of slope with the highest level of insolation is found on the SW facing slope, correlating well with where maximal densities of secondary slope failures are found, whilst the least amount of insolation is observed across the lower half of the NE facing slope (fig. 6.3 b). The permafrost zonation index (PZI) derived by Gruber (2012), (fig. 6.3 (a)) indicates that the majority of the SW facing slope is within the PZI fringe, where there could be sub-surface permafrost under conservative estimates. The global PZI indicates to what degree permafrost can exist, and ranges from 'only in the most favourable of conditions' to 'nearly everywhere' indicated by yellow to blue colour grading on figure 6.3 (Gruber, 2012). Much of the NE facing slope, where lower densities of secondary failures were observed is not within the PZI. Again, this is highly speculative and without in-situ measurements of independent variables, any interpretations of controls and drivers are tentative at best and at worst, false.

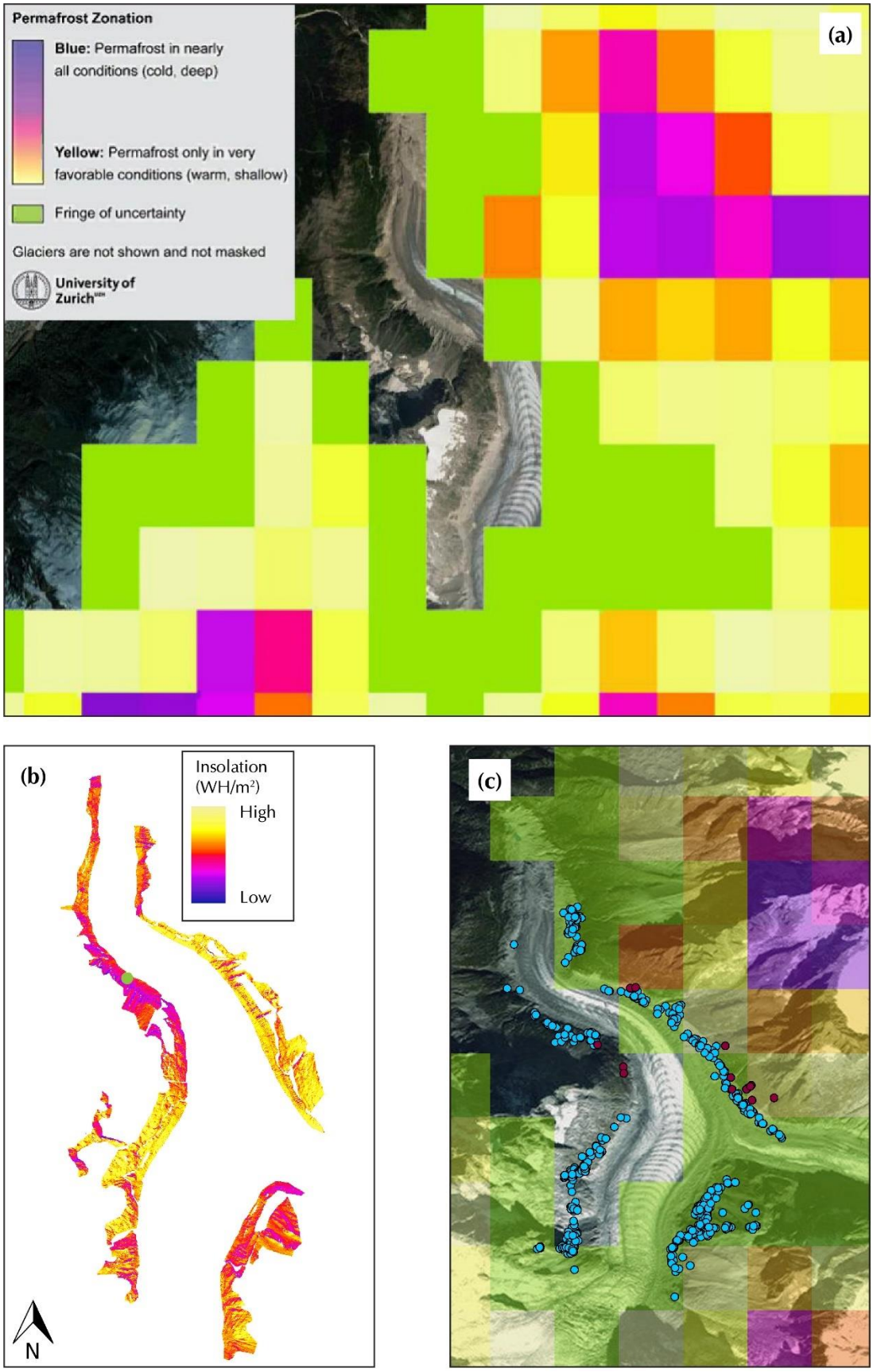

Figure 6.2: Permafrost zonation index (PZI) for the Mer de Glace with legend for reference. (from Gruber (2012); (b) Insolation of slopes calculated using GIS and DEM produced using SfM-MVS photogrammetry for Mer de Glace. Total insolation over one year (2017 used) with inset legend and; (c) Contextual map of the Mer de Glace with slope failure overlain (Red = primary, Blue = secondary). (Satellite imagery: Google Earth).

The NE facing slope receives some of the lowest levels of radiation over the course of one year where the large secondary failure detailed in figure 5.35 occurred (denoted by green circle on figure 6.3 (b)). However, following the failure shown in figure 5.35, the scar sediments were visibly wet, suggesting sub-surface flow as a possible driver. Several hundred metres above this area of lateral moraine lay a thawing patch of snow and ice and it is assumed that this was the source of water percolating through the lateral moraine thus decreasing the stability of the slope beneath the surface, agreeing with the earlier mentioned observation of Mattson and Gardner (1991), of a link between weather conducive to ablation and slope failure activity. Ice cored moraines have been shown in other environments around the world (e.g. Östrem, 1959; Bennett *et al.*, 2000; Schomacker and Kjaer, 2008; Tonkin *et al.*, 2015) but there are few examples of work conducted in the European Alps beyond the early studies of Barsch, Fierz and Haeberli (1979) and Haeberli and Epifani (1986). It is highly unlikely that the moraines surveyed in this study were ice-cored and indeed, maximal densities of secondary slope failures were shown to occur around 2,250 m a.s.l. (fig. 5.27) , below the estimated equilibrium line altitude of Argentière (2860 m a.s.l.) (Six and Vincent, 2014).

In terms of the effect of ice retreat on the behaviour of secondary slope failures, section 5.3.1 analysed the proportion of failures against the height above the ice, across a section of slope where previous ice height has been well constrained by earlier work. Using ice height as a proxy for slope exposure time, figure 5.11 revealed the highest proportion of activity occurred across moraine heights that have been exposed the longest suggesting that there may be a lag time (approximately 30 years) between exposure of fresh sediments and failure. However, in contrast to large magnitude primary slope failures that have previously been shown to have lag times of several millennia, larger secondary failures may occur within a matter of decades after exposure whilst a high frequency of activity begins immediately upon ice retreat. However, the theory of a lag time is not supported by data from other sites with no clear patterns between height above the ice surface and proportional secondary failure activity. More likely, is that the steepest slopes and thus, those most vulnerable to slope failure activity are found across the highest sections of slope. Distributions of secondary failures are controlled by slope gradient and appear to be driven by patterns in meteorological conditions. If it is assumed that the principal mechanisms of failure are debris flows, then the presence of water (through precipitation or snow melt) is the most likely (Ballantyne, 2002b; Curry, Cleasby and Zukowskyj, 2006; Curry, Sands and Porter, 2009; Mercier *et al.*, 2009) control on the spatial distribution of secondary slope failures.

6.3.2 Structural Controls

The identification of controlling and driving mechanisms for primary slope failures is somewhat more difficult than secondary failures given the time scale of this observation, scale of rock slope surveyed and magnitude of potential mechanisms. The spatial distribution highlights that proportional (i.e. normalised against total failure and slope area) maximal densities occur on very steep (> 50˚) NE facing slopes, though only marginally maximal against SW aspect. This is most likely a pattern driven by the high failure concentration across the NE facing slope of the Bossons, where a higher resolution model, combined with greater level of rock slope weathering resulted in a high number of detected primary failures. One of the most effective methods of determining potential triggering mechanisms, and drivers of rock slope erosion is a structural assessment of the rock slope (Moore *et al.*, 2009). Paraglacial rock slopes failures are controlled by the distribution of discontinuities which are a preconditioning factor on stability (McColl, 2012). Assessments of rock mass strength are typically static and involve time consuming, often labour-intensive field measurements that are constrained to accessible areas. Utilising open source algorithms and 3D data generated using SfM-MVS, structural analysis of the rock slope in the pro glacial zone of the Bossons where a number of primary slope failures were detected in high concentration highlighted some key properties of the slope (section 5.4.3). The workflow presented in this thesis does not necessarily negate the requirement of an experienced assessor however, the use of 3D SfM-MVS data to identify and characterise the structural properties of rock slopes presents a unique opportunity to capture stability data in challenging environments rapidly across much wider scales than previously possible.

Figure 6.3: Field photograph to highlight the highly weathered nature of the rock slope in the pro glacial zone of the Glacier de Bossons.

A lag time of 7 ka between deglaciation and very large magnitude slope failure occurrence was observed by (Ballantyne, Stone and Fifield, 1998), which they attribute to progressive joint extension. Such lag times imply that it would be highly unlikely that any of the relatively recently deglaciated rock slopes surveyed in this project would be at a critical state however, McColl (2012) explains that this long response time may only be a characteristic of good quality rock. If the rock mass is already highly fractured, such as that in the pro glacial zone of the Glacier de Bossons (example in figure 6.4), stress release may happen much sooner after the removal of ice, or even during the transition from glaciated to non-glaciated conditions (McColl, 2012). This may go some way to explaining the extraordinarily high rate of rock wall retreat (52.39 mm a^{-1}) detected across the rock slope in the pro glacial zone of the Glacier de Bossons, though this slope can be considered very different to the other rock slopes considered in this study and has been scoured multiple times by serac collapses since the glacier receded.

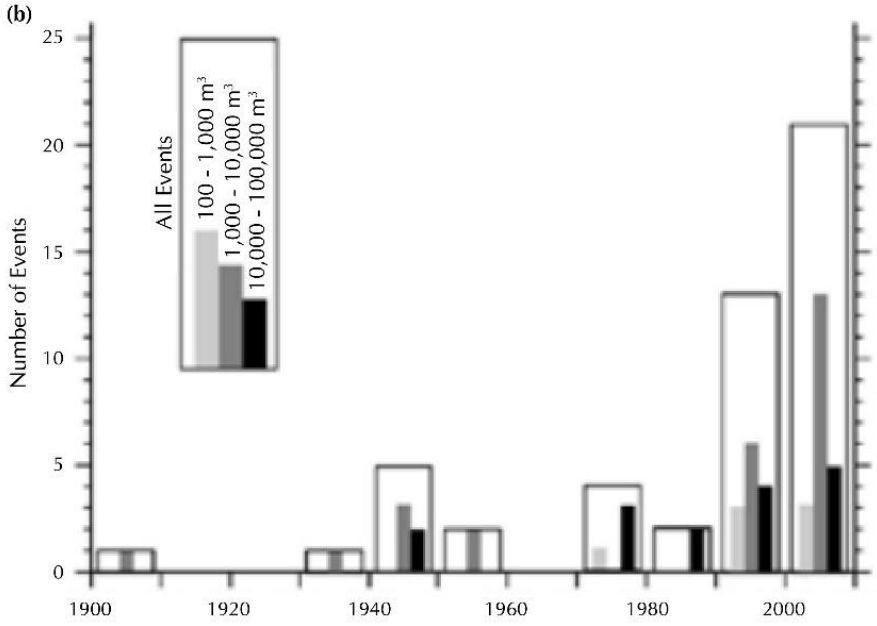

Figure 6.4: Frequency of rock slope failures between 1900 and 2010 across the Mont Blanc massif. (both from Huggel et al. (2012)).

In contrast to the Bossons site, very few primary failures were detected across the rock slopes above Argentière and Mer de Glace. No failures above the LOD threshold were detected across the HARW. It is assumed that a significantly greater number of small magnitude primary failures would have been detected across the more weathered slopes of the HARW that bordered the Glacier d'Argentière and Mer de Glace, had survey images been taken at a closer distance and thus, reducing the LOD threshold. However, the images were of enough resolution to detect large magnitude failures, of which there were none during the observation period which highlights their infrequency. Others have noted an increase of primary slope failures across HARW correlating with a rise in the mean annual air temperature (fig. 6.5), suggesting permafrost degradation and melting of surface and sub surface ice as key drivers (Huggel *et al.*, 2012). The absence of larger magnitudes in this data is most likely another consequence of temporal censoring, as outlined in section 6.4.2, whereby extrapolating the P-L fitted to primary failures detected in this study significantly underestimates the likelihood of larger magnitudes. There were contrasting forms of rock slope identified during field campaigns, qualitatively characterised as; (i) highly weathered rock slopes, such as those in the pro glacial zone of the Glacier de Bossons (fig. 6.4) and across the HARW. The Bossons rock slope has been uncovered following the rapid up slope retreat of the Glacier de Bossons over the last two decades and is characterised by highly fragmented joints perpendicular to the bedding. HARW are weathered and heavily fractured, with failures driven by permafrost degradation and freeze/thaw mechanisms (Deline *et al.*, 2014; Krautblatter and Moore, 2014). (ii) Glacially moulded comparatively un weathered rock slopes such as those observed above and in the immediate pro glacial zone of the Glacier d'Argentière and part of the Mer de Glace (e.g. figure

6.6). These slopes are continually exposed through surface lowering of the adjacent ice and appear smoothed with joints running sub parallel to the bedding plane, often marked by water passing across the upper surface but with no evidence of sub surface flow. Commonly referred to as sheeting joints, exfoliation joints or stress release/relief joints (fig. 6.6), they are discussed in great detail by McColl (2012). They're non-tectonic in origin and it is generally accepted that they are generated through gravitational stresses that are typically triggered by unloading. Very few failures were detected across the slopes characterised by sheeting joints, as a consequence of a higher LOD threshold and the infrequency of larger magnitude events.

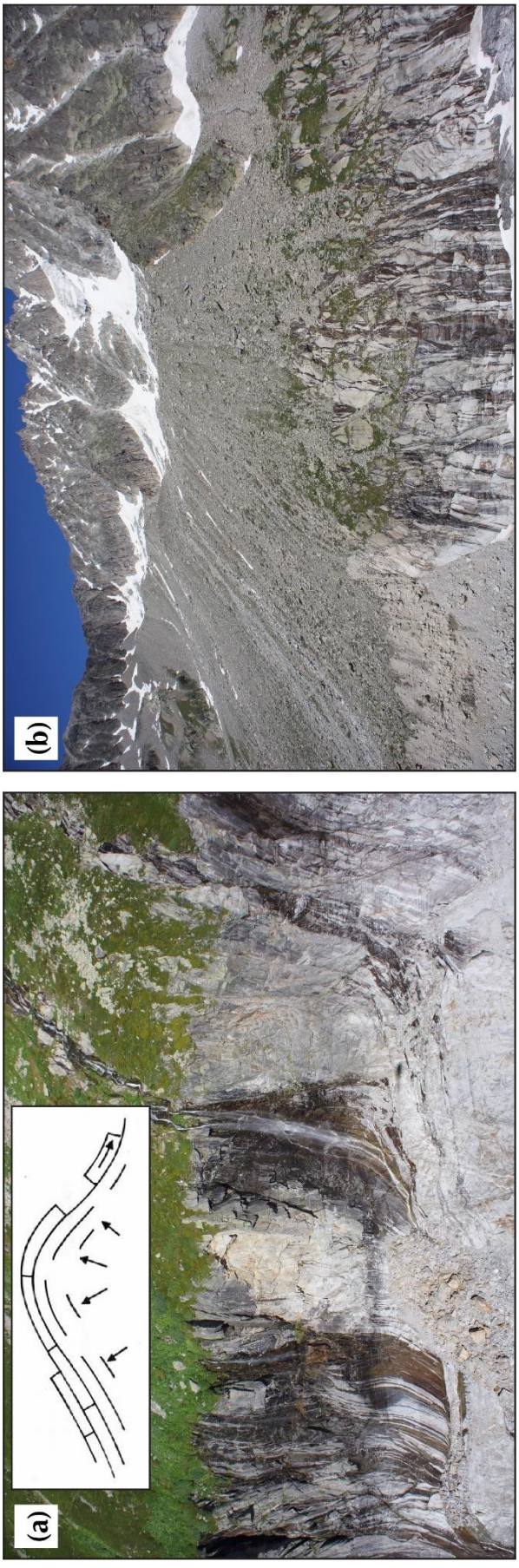

Figure 6.5: (a) & (b) Examples of rock slopes above the Glacier d'Argentière (SW facing). Inset on (a); schematic representation of unloading and formation of sheeting/ exfoliation joints (from sierracollege.edu).

The use of SMR to assess rock slope stability at the Bossons site indicated that much of the slope was rated from I to III, with two discontinuity sets rates as IV. A summary of the classification descriptions can be found in table 2.3. Much of the rock slope considered for the stability assessment was characterised by an SMR that suggests at best, completely stable conditions and at worst, partially stable however, it was clearly failing through frequent small magnitude events and thus, the face value of SMR (i.e. broad classification of good, very good etc.) may not be suitable for determining the likelihood of small magnitudes. Others have shown that the SMR rating correlates well with rock wall recession rate (Moore *et al.*, 2009), though their dataset appears to be characterised by SMR values of 21 and higher (fig. 2.9) which would be broadly categorised as 'normal',' good', or 'very good' with indicative stabilities of 'partially stable', 'stable' and 'completely stable', though much like this study, they also observe a number of small magnitude failures across their studies slopes (Moore *et al.*, 2009). No such correlation can be created in this study as only one rock slope was tested, though points to a useful area for future work. SMR could be a useful metric for determining whether large magnitude primary failures are part and course of a rock slopes trajectory towards stabilisation using pre and post-failure data. Nevertheless, the structural characterisation of a rock slope in this study does offer a unique and invaluable insight into the mechanisms of failure across slopes. For example, the largest failure at the Bossons site was correctly characterised as wedge type through calculation of auxiliary angles between sets, failing along the v shaped intersection of two discontinuities that dipped out of the slope (fig. 5.19). A wedge type failure can only occur when the dip angle of at least one of the intersecting discontinuities is greater than the friction angle, and can occur rapidly or over much longer periods of time (Hoek and Bray, 1981). Their formation and occurrence are dependent on the lithology and structure of the rock mass (Piteau, 1972). Failure was most likely driven by pressure from water infiltrating along the failure surfaces (Hoek and Bray, 1981) and successive freeze/thaw cycling, though again, without in-situ measurements this interpretation is speculative at best.

6.4 Size Distribution of Slope Failures

Section 5.7.2 presented the results of size distribution analysis for the combined inventories of detected primary and secondary slope failures. The actual frequency (i.e. the number of slope failures detected) and cumulative percentage (i.e. the contribution of slope failures to the total volumetric change detected) of logarithmically binned primary and secondary slope failure volumes are shown in figure 6.7. Both inventories are dominated by smaller magnitude failures though the cumulative volume lost is dominated by the largest detected events. It has often been suggested that the MF distribution of slope failure volumes are best described by an inverse power-law (e.g. Guzzetti *et al.*, 2002, 2002; Malamud *et al.*, 2004; Korup, 2005; Korup and Clague, 2009).

Whilst this is often true, such a distribution is commonly observed across only a truncated portion of the inventory data, often referred to as the heavy tail (Stumpf and Porter, 2012). Some have attributed the flattening and rolling of the frequency of small magnitude failures to data bias arising from under sampling (Stark and Hovius, 2001), whilst others have suggested a physical basis driven by failure mechanics and material properties (Barlow *et al.*, 2012).

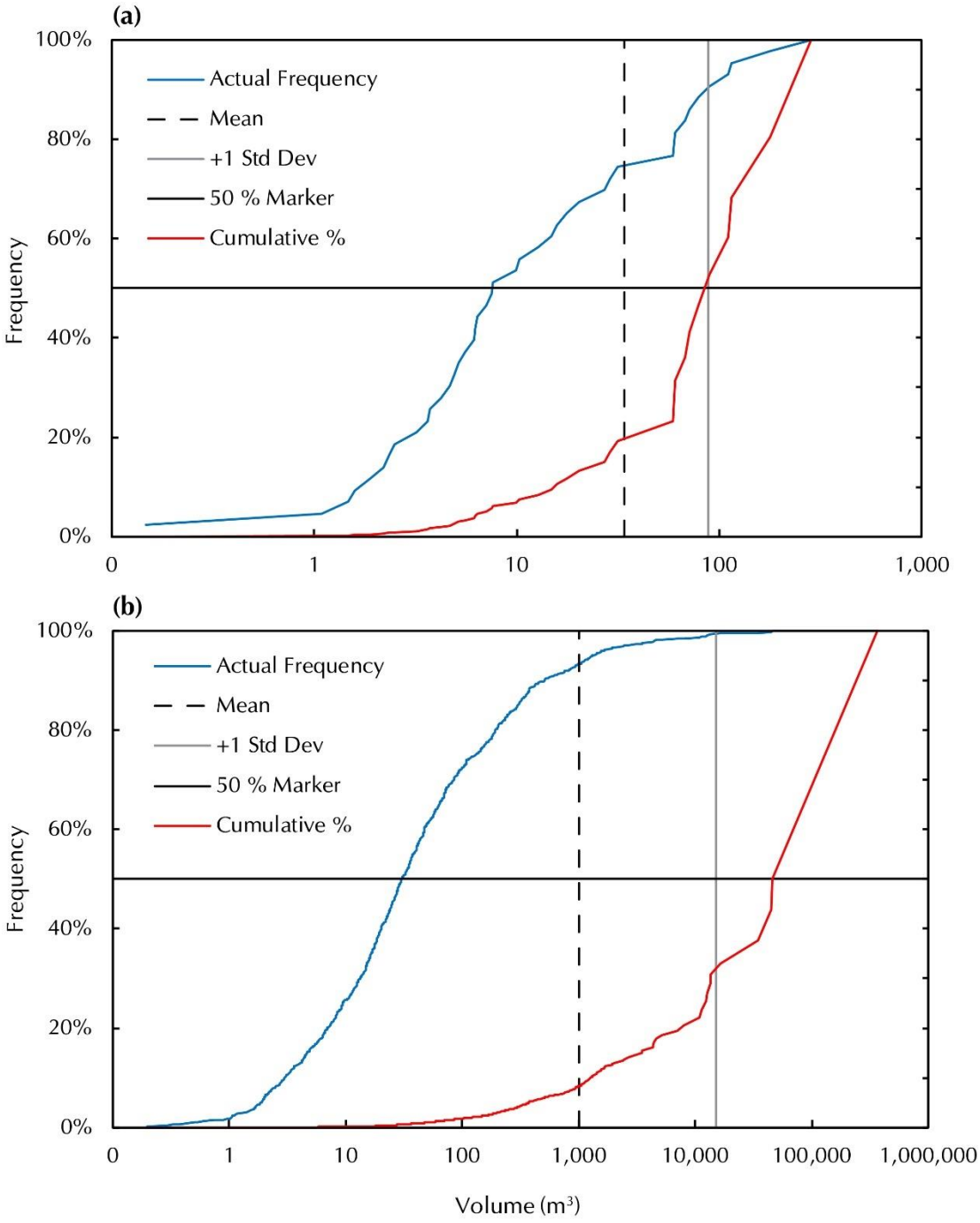

Figure 6.6: Graphs showing the actual frequency and cumulative percentage of volumes for (a) primary and (b) secondary slope failures detected in this study. Lines are overlain to denote the mean, +1 standard deviation and a marker for 50 % frequency.

It is crucially important to consider the MF distributions of primary and secondary failures separately as their controls are fundamentally different from one another. Variations in the characteristics of fitted models have been attributed to regional differences in structural geology, morphology, hydrology and climate (Barlow *et al.*, 2012). In general, previous work has shown that the rollover in MF distributions of primary slope failures is a product of censoring through survey resolution and an under representation of small magnitude failures (e.g. Marques, 2008; Barlow *et al.*, 2012). However, inventories of secondary slope failures often exhibit a rollover that some have attributed to changes in the physical driving mechanisms where root cohesion and anchoring act to limit the frequency of smaller magnitudes (Stark and Hovius, 2001; Brunetti, Guzzetti and Rossi, 2009). The majority of datasets presented in this thesis are shown by means of a bootstrapping procedure (Clauset, Shalizi and Newman, 2009), to be better described by a L-N distribution rather than an inverse P-L. That does not mean that a P-L is an unsuitable fit to a truncated portion of the data (i.e. above a minimum volume) (fig. 6.8), rather that the log-normal is a more appropriate fit across a wider range of magnitudes, hence providing an equated relationship that better describes the distribution of observations. To date, there are relatively few examples of non-power-law distributions reported for failure inventories. Dunning *et al.* (2007) find that failures mapped before and after the 2005 Kashmir Earthquake are best described by a log-normal distribution, as do Chaytor *et al.* (2009), who mapped submarine failures along the U.S. Atlantic margin. A log-normal distribution was also proposed by Kelsey *et al.* (1995) for failures mapped in Redwood Creek, northern California. Hurst *et al.* (2013) allude to the fact that their MF distributions are curved for failures in unconsolidated material and although they do not suggest an alternative, they do explain that a P-L may not be the most appropriate fit to their data.

To understand the implications of this, it is necessary to highlight the difference between P-L and L-N distributions as they often connect naturally through similar generative models and thus, it is not uncommon for datasets to apparently follow both. However, distinguishing between the two is no trivial matter and in this study, a statistical likelihood test initially proposed by Clauset, Shalizi and Newman (2009), was performed to generate a goodness of fit value for both power-law and log-normal distributions. A log log distribution over several orders of magnitude is strictly required for a power-law. Such a distribution also typically generates orders of magnitude more events of larger x than would be expected under a normal distribution (Virkar and Clauset, 2014). A dataset is said to be log-normal when the probability distribution of the logarithm of x is normally distributed (i.e. magnitude is log-normally distributed if $log(V_L)$ has a normal distribution). A log-normal distribution, much in the same way as a power-law distribution, is a skew distribution with many small values of magnitude and fewer large values and therefore the mean is usually found to be greater than the mode. The argument over whether a log-normal or power-law distribution is a better fit to empirically observed data is a matter that has been widely discussed and debated

across a large variety of disciplines from biology to astronomy, chemistry to computer sciences (Mitzenmacher, 2004). Mitzenmacher (2004) states that "given the close relationship between the two models [P-L and L-N], it is not clear that a definitive answer is possible [as to which is better]; it may be that in seemingly similar situations slightly different assumptions prevail."

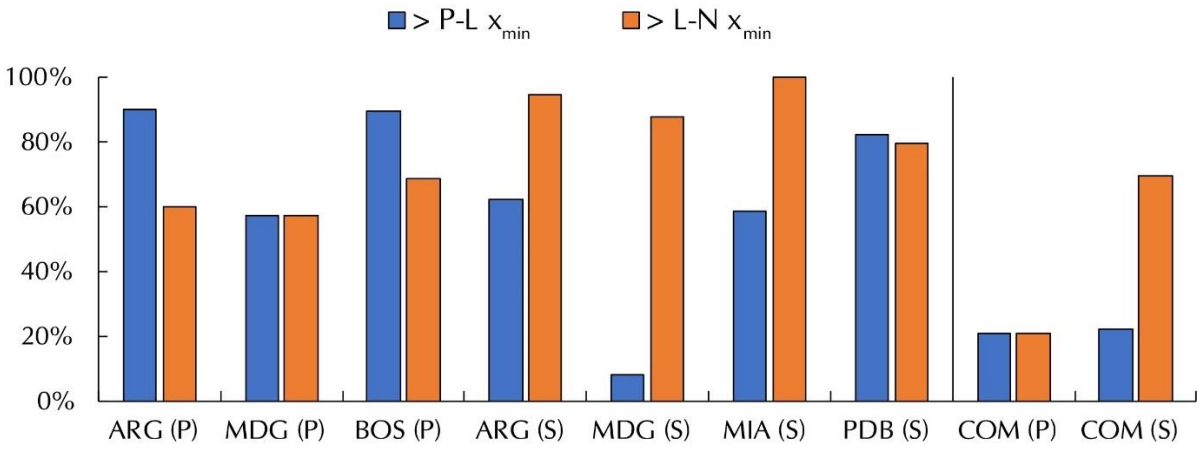

Figure 6.7: A column chart showing the proportion of failures above the lower bound of the fitted P-L and L-N at each of the study sites. P = Primary, S = Secondary, ARG = Glacier d'Argentière, MDG = Mer de Glace, BOS = Glacier de Bossons, MIA = Ghiacciaio del Miage, PDB = Pre de Bard, COM = Combined.

6.4.1 Overview

To summarise the size distribution of failures detected in this study; a P-L is a better fit to the inventories of primary failures at the Glacier d'Argentière and Mer de Glace individually. Meanwhile, a L-N is a better fit to the distribution of primary failures at Glacier de Bossons and the secondary failures detected at the Glacier d'Argentière, Mer de Glace, Ghiacciaio del Miage and Pre de Bard. Combined (fig. 5.31), both primary and secondary slopes failures are shown to be best described by log-normal distributions. To explore this further, a reminder of the minimum bounds (x_{min}) and scaling exponents (α) (eqn. 2.7) from the P-L and L-N models fitted to the MF distributions in this study are summarised in table 6.1 and some examples from previous work are presented below in table 6.2 (after Bennett *et al.*, 2012). Firstly, focussing on the P-L models fitted in this study allows a simpler comparison before considering the application of the L-N model. The highest α for a P-L fitted to primary slope failures in table 6.2 (0.76) is lower than any of the α in this study. Lower exponents suggests the data may be biased towards larger magnitude events, and indeed it seems reasonable to assume that detailed field studies are preferentially carried out for larger failure events. Guzzetti *et al.* (2009) described the low scaling exponent as characteristic of inventories which predominantly contain small magnitude failures which they attribute to either; (i) sample size; (ii) result of the volume calculation method or; (iii) a reflection of a change in the scaling of the self-similar dependency of volume on the geometry of the failures as the magnitude increases.

Larsen, Montgomery and Korup (2010) found significant variability in the scaling exponent dependent upon hill slope material. In general, lower values were calculated for secondary failures and higher for primary, which they attribute to the deeper failure depths for the latter (Larsen, Montgomery and Korup, 2010). This theory agrees with the P-L α for the combined inventories of primary and secondary failures presented in table 6.1. The robustness of the P-L and scaling parameter for primary failures was tested by (Strunden *et al.*, 2015b), and a general trend towards larger α as higher events were removed from the inventory was found (fig. 6.9) It is critically important to establish why different sites are characterised best by different models and to determine this, the size distributions of primary and secondary failures will now be discussed in the following sections before the implications of the findings are outlined.

Table 6.1: Summary of scaling exponents (α) and rollover values (x_{min}) for the inventories of slope failures from each site and the combined inventory.

		Power-law		Log-normal	
		α	x_{min} (m^3)	α	x_{min} (m^3)
Primary	Argentière	2.84	4.67	2.57, 0.24	6.19
	Mer de Glace	4.50	59.40	4.24, 0.33	59.40
	Bossons	1.91	1.48	1.49, 0.94	2.35
Secondary	Argentière	1.90	4.36	1.74, 1.30	1.01
	Mer de Glace	2.93	1,048.00	3.61, 1.95	10.30
	Mer de Glace (intra annual)	5.47	294.00	3.44, 1.38	10.90
	Miage	2.75	20.10	2.88, 0.91	4.43
	Pre de Bard	2.52	1.93	1.08, 0.69	1.99
Combined	Primary	3.02	59.40	4.02, 0.79	60.20
	Secondary	1.75	167.00	1.32, 2.99	13.80

Table 6.2: Comparison of values of the lower bound (x_{min}) and scaling exponents (α) of the power-law tails obtained for previous slope failure inventories. Adapted from Bennett et al. (2012). Type indicates whether distributions are obtained from inventories of primary (P) or secondary (S) failures. Attribute indicates whether distributions where fit to MF distributions considering A_L (A measured in m^2) or V_L (V measured in m^3).

Study	Period	Type	Attribute	xmin (m^2/m^3)	α
Bennett et al., 2012	19 yrs	P/S	V	10^2	0.65
Bennett et al., 2012	19 yrs	P/S	V	10^3	0.76
Guzzetti et al., 2003	145 yrs	P	V	10^1	0.10
Dussauge Peisser et al., 2002	60 yrs	P	V	10^1	0.41
Hungr et al., 1999	30 yrs	P	V	10^2	0.43
Dussauge Peisser et al., 2002	22 yrs	P	V	10^1	0.45
Hungr et al., 1999	22 yrs	P	V	10^1	0.65
Malamud et al., 2004	Mixed	S	V (from A)	10^6	0.93
Stark and Guzzetti, 2009	17/28 yrs	S	V (from A)	10^3	1.00
Stark and Hovius, 2001	2 yrs	S	A (eroded)	10^3	1.11
Stark and Guzzetti, 2009	17/28 yrs	S	A (disturbed)	10^3	1.19

Malamud et al., 2004	Few Hours	S	A (disturbed)	10^3	1.40
Malamud et al., 2004	Weeks	S	A (disturbed)	10^3	1.40
Malamud et al., 2004	2 Months	S	A (disturbed)	10^3	1.40
Stark and Hovius, 2001	8 yrs	S	A (eroded)	10^3	1.48

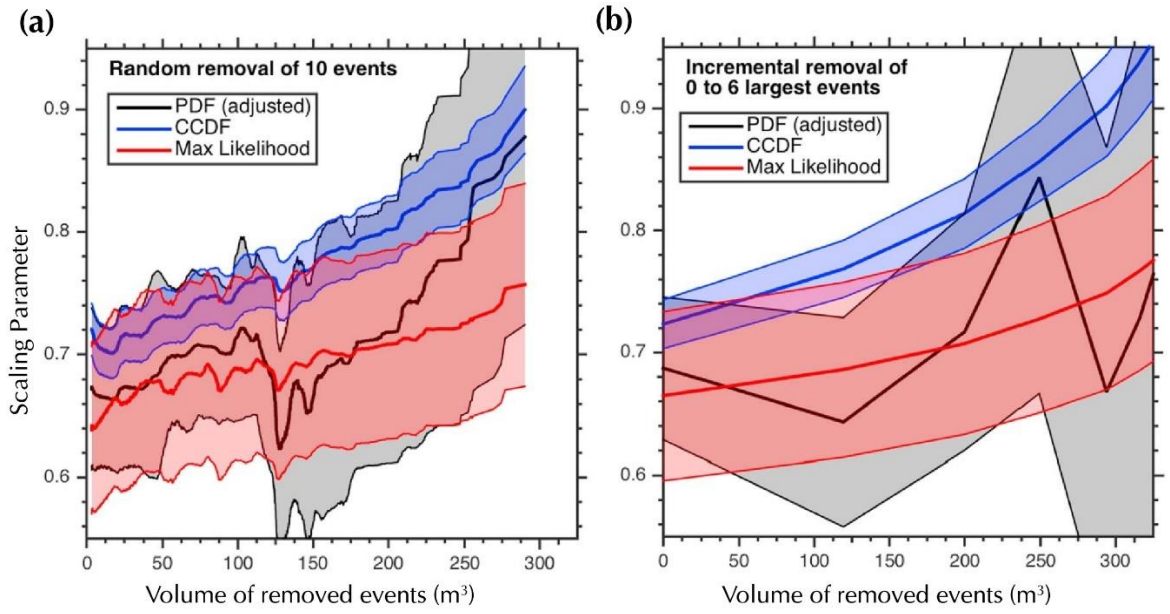

Figure 6.8: Monte Carlo sensitivity analysis for the range of P-L scaling parameter for observed rockfall events. The model randomly removed different events from the data set and calculated how the power-law exponent b would differ. (a) 10 events of any size were randomly removed in each of the 10,000 simulations. (b) The worst cast scenario is explored for the exponent b by incrementally removing the six largest events. From Strunden et al. (2015)

6.4.2 Primary Slope Failures

Figure 6.10 (a) is a reminder of the MF distribution of primary failures in the combined inventory with only the better fitting L-N model overlain (see sections 5.2.2, 5.3.2, 5.4.2 and 5.7.2 for both models overlain onto MF). The lower bound of the L-N also marks a clear break in the distribution (denoted with dashed box) and the events below the rollover are plotted separately and inset on figure 6.10 (a). This distribution is also best described with a L-N and can be fitted from the same lower bound as that of the inventory at the Glacier de Bossons (fig. 6.10 c) . As explained in the previous chapter, given the sparsity of data at the Glacier d'Argentière and Mer de Glace, the distributions of primary failures cannot be considered statistically valid assessments individually, though their slopes are geologically and structurally similar. When combined to create a more robust dataset, their distributions can be fit to both a P-L and L-N with the same p values and similar lower bounds (fig. 6.10 b), yet there remains a clear break similar to that in figure 6.10 (a) and a separate distribution of lower magnitudes. When extracted, (inset on fig. 6.10 b), the events below the rollover are also best described by a L-N. All of the primary failures at the Glacier d'Argentière fall into the lower distribution (i.e. below the rollover) whilst only 29 % of the Mer de Glace primary

failures do. However, as stated in the previous section, when plotted individually the inventory of primary failures at the Glacier d'Argentière are best described by a P-L and thus, the addition of the lower 29 % of the Mer de Glace events is enough to change this to a L-N.

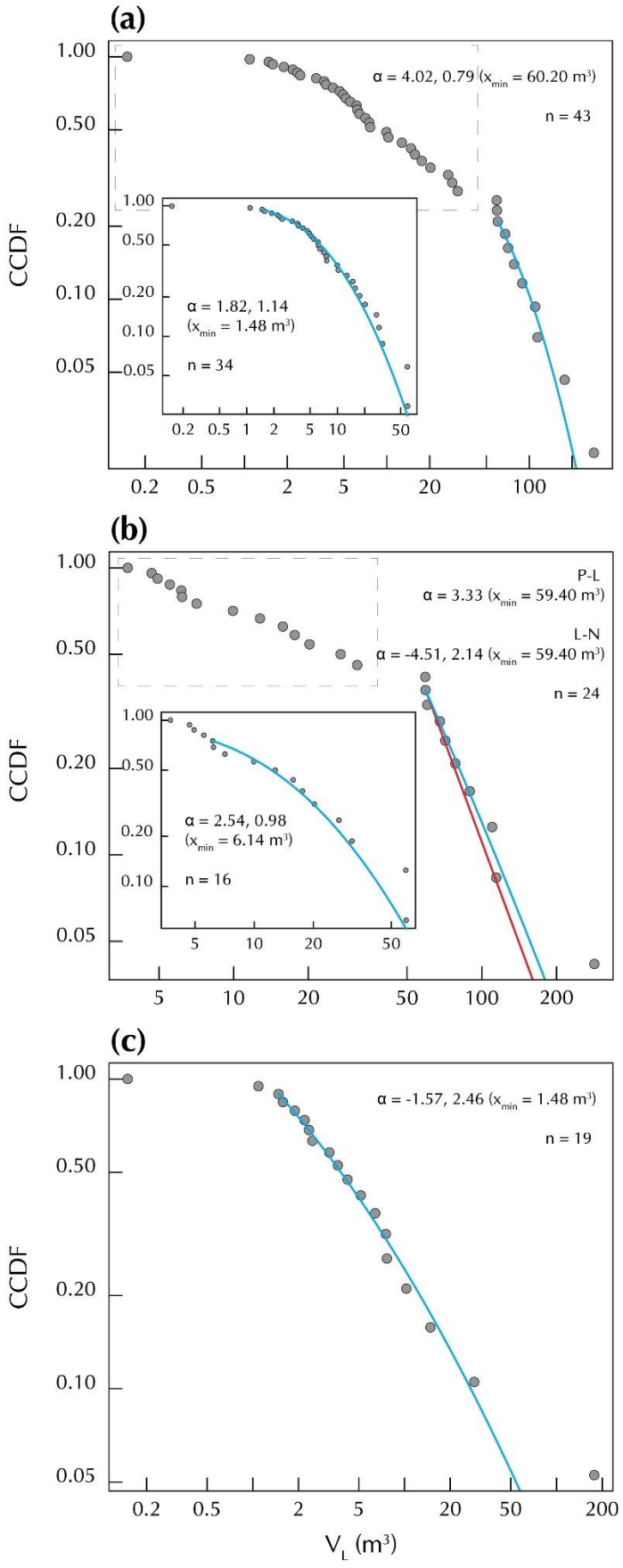

Figure 6.9: Cumulative Distribution Functions (CDF) for (a) combined inventory of primary slope failures, (b) inventory of primary slope failures from Glacier d'Argentière and Mer de Glace and (c) inventory of primary slope failures from the Glacier de Bossons. Volumes are plotted against their CDF with their maximum likelihood power-law (red) and log-normal (blue) fit (only the best fit model is shown). Scaling exponents (α) and rollover values (x_{min}) are given on each graph. Inset on (a) and (b) are the CDF for the lower region of the MF distribution of each with their own fitted distributions.

Here, the highest level of accuracy (and thus, the lowest LOD threshold) was achieved at the Bossons site, where a failure with a V_L of 0.15 m^3 represented the lowest magnitude primary slope failure detected. The x_{min} of the P-L fitted to the data from the Bossons site is also the lowest (1.48 m^3), and others have fit a P-L to their data from a similar magnitude (Hungr, Evans and Hazzard, 1999) (table 6.2). However, the rock slope at the Glacier de Bossons is clearly of a very different character to those at Argentière and Mer de Glace (see section 6.3.2). A fundamentally important question is whether the presence of a rollover in inventories of primary slope failures, including the one in this study, are a product of under sampling of smaller magnitudes (censoring) or a mechanical difference between driving processes of small and large events. Firstly, let's explore the former possibility of under sampling. There are a number of reasons why this could happen, including a high LOD threshold and censoring of small magnitude deposits in the landscape. The censoring of smaller magnitude deposits and scars within the landscape, and difficulty associated with identifying and quantifying small magnitude events post failure is an important consideration for studies that quantify volume based on deposited material and observational measurements of failure scars. However, this study measured failure volume as direct loss from the rock slope rather than deposited mass. As such, censoring is limited to events masked by the LOD threshold at each of the sites, which for SfM-MVS, is driven by the factors discussed earlier in section 6.2.

Temporal censoring is also an important consideration at both ends of the magnitude spectrum (Hungr, Evans and Hazzard, 1999), whereby the time interval may be too short to adequately represent low frequency events. The majority of inventories are compiled considering failures over decades, centuries or even millennia by mapping historic scars or deposit volumes. The preservation potential of small magnitude failures within the glacial or fluvial system over these time scales is extremely poor and the resolution of such mapping studies is often too coarse to consider small magnitude events. Others are compiled over shorter time scales, for example Ravanel *et al.* (2010), who create an inventory of rockfalls in the Mont Blanc massif based upon observations from mountain guides, hut keepers and rescue teams. However, such observational inventories are unlikely to account for high frequency small magnitude events. This is the reasoning behind some suggesting under sampling as a probable cause of underestimating small and overestimating large magnitude failures in probability distributions (Stark and Hovius, 2001). There appears to be a tenable link between the observation period of the studies in table 6.2 and the scaling parameters of the fitted P-L (fig. 6.11) whereby longer periods are characterised by lower parameters. It seems reasonable to say that the higher scaling parameters, and perhaps the derivation of a L-N distribution across some sites in this study are a consequence of temporal censoring and do not account for rarer high magnitude events. When comparing the x_{min} to those in table 6.2, it can be seen that the observation period of the lowest bound (10^2 m^3) is several decades whilst the highest is 19 years. Both are considerably longer time scales than that

considered here and could go some way to explaining the variability between the lower bounds and scaling exponents determined in this study and those from previous work. Bennett *et al.* (2012) calculate P-L (α = 1.76) for a dataset of primary failures in the Swiss Alps over an observation period of 19 years that suggests a 30 % probability (CDF = 10^{3}) for a failure of 10^{6} m^{3}. Extrapolating the much steeper P-L (α = 3.02) fitted to the primary failures in this study to the same magnitude gives a probability of less than 0.20 % of occurrence highlighting the effect of a short observation period and lack of large magnitude failures in the dataset.

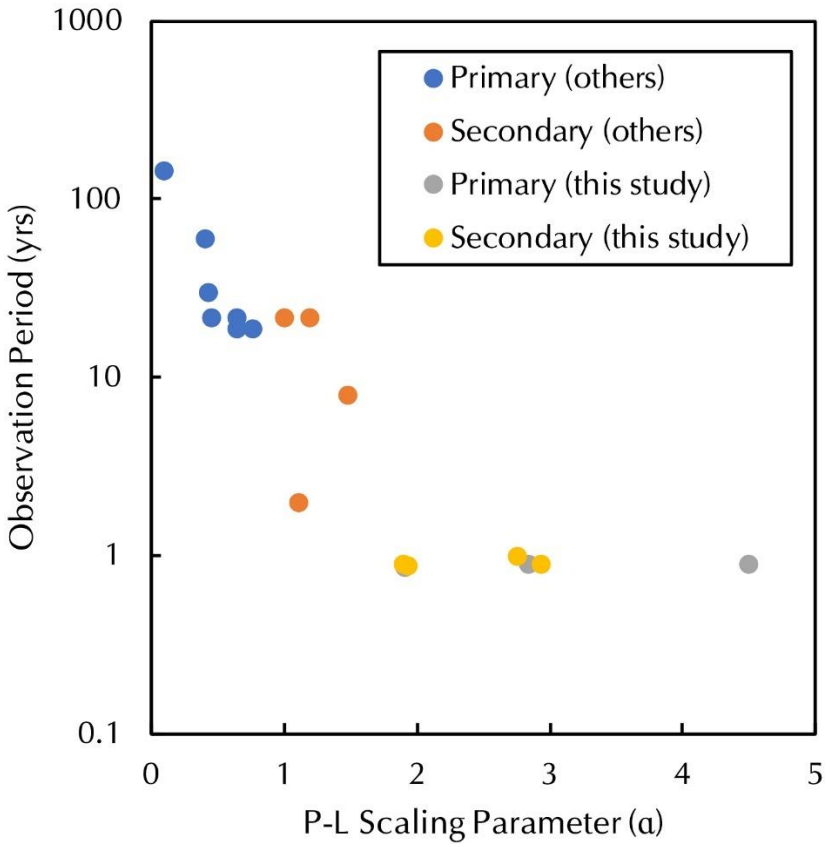

Figure 6.10: A graph showing the relationship between the observation period and scaling parameter of a P-L distribution for primary and secondary failures. Data from table 6.2 and table 5.11 (this study) shown.

Alternatively, the models fitted to the primary data could be subject to bias as a result of the small sample size. Clauset, Shalizi and Newman (2009) explain that the MLE used to calculate the lower bound can only be guaranteed as unbiased when used with large sample sizes, suggesting that $n > 50$ is a reasonable 'rule of thumb' for extracting reliable estimates. Li, Lan and Wu (2016) demonstrate the effect of sample size on the quality of derived distributions through numerical modelling, explaining that as sample size gets smaller, the reliability of the scaling exponent and the statistical significance of the distribution observed gets worse. The inventory of primary slope failures is relatively small (n = 43) and could account for the low scaling exponent. In contrast, the

inventory of secondary failures is more robust with a larger sample size than that of others (e.g. Guzzetti *et al.*, 2009) (*n* = 723) which would suggest sample size is not a factor in the case of the latter, which are discussed in more detail in the following section (6.4.3). Just two of the three sites where primary slope failures were detected are characterised by a P-L; Argentière and Mer de Glace, whilst Bossons was better described by a L-N. The LOD thresholds (section 4.9.1) across Argentière and Mer de Glace were higher than those at Bossons owing to factors discussed earlier in this chapter (section 6.2) which means that failures below these thresholds are censored. Only 24 events above the LOD threshold were detected across both sites combined, a small sample size whereby the MLE used to calculate the lower bound and scaling parameter cannot be guaranteed to be unbiased (Clauset, Shalizi and Newman, 2009). Alignment and GSD across the Bossons site was of greater quality, though a small survey area resulted in a small sample size which could also be subject to the same biases but is a more complete inventory of failures given the lower threshold. However, even if the LOD threshold across the slopes of Argentière and Mer de Glace were of a similar quality to the Bossons, they remain very different structurally (section 6.3.2).

6.4.3 Secondary Slope Failures

In all inventories of secondary slope failures, the MF distribution was better described by a L-N than a P-L, though for comparative reasons, an overview of key differences in P-L characteristics will be discussed first. When considering the P-L fitted to secondary slope failures, some interesting comparisons can be drawn between tables 6.1 and 6.2. Firstly, values of α are generally higher than those for the P-L fitted to primary events in both tables, which suggest a bias towards smaller magnitudes in secondary failures. Similarly, values of x_{min} are also higher, with a minimum of 167 m^3 for the combined inventory of secondary failures in this study and significantly higher in the comparative studies presented in table 6.2 (10^3 m^3). 78 % of the detected secondary events in this study fall below the minimum bound of the fitted P-L (fig. 6.8), suggesting that; (i) the poorly fit distribution is not an artefact of data bias due to censoring of smaller magnitudes, and; (ii) an alternative model would be better suited to fit the MF distribution of secondary failures. This supports the theory that the MF distribution of secondary failures is genuinely characterised by a rollover in probability, dictated by geomorphological processes, not methodologically constrained. As mentioned earlier, there are few examples in existing work that have attempted to resolve the MF distribution by considering alternative models. However, a model that can only be robustly applied over a fraction of the orders of magnitude within an inventory provides at best, a weak description of the entire data and at worst, a false one.

In this study, a L-N was also tested and found to be a better fit across a wider range of magnitudes in all cases of secondary slope failures with a minimum bound on the combined

inventory an order of magnitude smaller than that of the P-L and two orders smaller than the minimum reported by the comparative studies in table 6.2. As mentioned, the L-N and P-L connect naturally through similar generative models and thus, it is not uncommon for datasets to apparently follow both for a portion of the data. Following a L-N distribution means that secondary failures are not scale free, or at least are not scale free through their entire population. Qualitatively, the L-N for the combined inventory of secondary slope failures can be fitted to a portion of the data below the lower bound of the P-L where the probabilities of smaller magnitude failures begin to flatten. It follows the same course as the P-L through the mid magnitudes before separating towards a lower probability for the largest magnitudes. Importantly, the data do not appear to rollover completely in that the probabilities of the smallest magnitudes are no less than any other magnitudes which is in contrast to earlier work (e.g. Malamud *et al.*, 2004; Bennett *et al.*, 2012), where the rollover has been preceded by a distribution increasing in likelihood before the decay. Others have suggested that prior to the rollover, a positive power-law distribution can be good fit to the data (van den Eeckhaut *et al.*, 2007) indicating fundamentally different driving mechanisms behind the generative models of small magnitude and large magnitude distributions. Determining the cause of the rollover in the probability of small magnitude failures is no trivial matter, though the secondary failure inventory presented in this study is substantially more complete (in terms of small magnitude inclusion) than others. For example, Guzzetti *et al.* (2009) mapped failures down to 1.3 x 10^1 m^3, and Bennett *et al.* (2012) also examined the distribution of failures down to 1.0 x 10^1 m^3, whilst failures an order of magnitude lower (2.0 x 10^1 m^3) were accounted for in this study.

Some have proposed that the decrease in frequency for small failures is caused by a transition of the dominant resistance from friction to cohesion (Guzzetti *et al.*, 2002; Li, Lan and Wu, 2014) (see section 4.7 for more details). It may dictate the rollover through restricting failure dimensions, as when an object increases in size, it must reshape itself towards a small volume to surface area ratio (V/S) to avoid crushing. Using an inventory of 5466 Fujian secondary slope failures, Li, Lan and Wu (2014) found that the V/S is a useful metric for determining the resistance effect of cohesion. They found that a decrease in V/S magnifies the resistance effect and results in a decrease of failure frequency. The V/S to V_L relationship for secondary slope failures detected in this study was presented in figure 5.33. V/S is positively correlated with failure magnitude and thus, could explain why a rollover is observed in the MF distribution of secondary failures in this study. Small magnitude failures have small basal depths, and failure is mostly controlled by cohesive strength (Guzzetti *et al.*, 2002). The gravitational body force is proportional to the basal depth and thus cohesive forces prevent smaller magnitudes (Guzzetti *et al.*, 2002; Li, Lan and Wu, 2014). However, as mentioned in the previous paragraph, the rollover in the likelihood of small magnitude failures is not in the conventional manner whereby likelihood decreases, but rather remains at a steady state of probability for failures smaller than approximately 10 m^3. This could represent a

critical threshold where the likelihood of failures sub 10 m^3 are controlled by different mechanisms to those above.

This research has shown that an inverse P-L can be fitted to a portion of the secondary failure data that typically would have fallen below the lower bound of previous inventories (table 6.2) which raises questions regarding the completeness of such inventories and whether the scaling of their P-L is an artefact of censoring. Similarly, to the primary slope failures, there is most likely an element of temporal censoring for secondary events whereby rarer large magnitude events are unaccounted for, which may influence the scaling of fitted distributions. However, unlike slopes in other environments, the size of secondary failures above and around glaciers may be restricted by lateral moraine height and depth and the largest magnitude secondary failure observed here (4.6 x 10^4 m^3) may be in the range of the maximum possible failure. The work has also shown that a L-N is a much better fit to the data in this magnitude range and that small secondary failures are not scale free. The data contradicts earlier work where a positive correlation between smaller magnitudes and their likelihood was observed prior to a decay following a rollover.

6.4.4 Implications

In terms of paraglacial hill slope adjustment, the discovery of a MF distribution that is best described by a L-N model has interesting implications. The data in this study have highlighted what others have previously stated (e.g. Ballantyne, 2002), that very soon after the removal of ice through retreat or thinning, newly exposed over steepened sediment-mantled slopes are capable of delivering vast quantities of sediment to the ice surface and valley floor through high frequency low magnitude events. Previous work to quantify the rates of secondary failures from such slopes has been constrained to glacier forelands (e.g. Curry, 2000; Curry, Sands and Porter, 2009) though this PhD highlights the necessity to consider slopes above actively wasting glaciers as well as those in the pro glacial zone. The time scale of observation is less than commonly considered in inventories of historic failures that have been shown to follow inverse power-laws and with this being the case, it could be hypothesised that the dominant short-term failure activity is in fact best described with a L-N distribution whilst longer term slope response adheres more strongly to an inverse P-L. In other words, the immediate release and remobilisation of sediment from temporary storages such as lateral moraines are dominated by small to medium magnitude events with a MF that is best described by a L-N distribution. Over the longer term, large magnitude primary events have been shown to play a much more fundamental role in slope adjustment (Ballantyne, 2008), thus increasing the likelihood of larger magnitudes in MF distributions that are therefore better characterised with a P-L.

In terms of secondary failures specifically from sediment-mantled slopes above and around actively wasting glaciers, it is likely that a change in the driving mechanisms of smaller magnitudes will result in a decrease in their likelihood (Guzzetti *et al.*, 2002; Li, Lan and Wu, 2014) whilst larger magnitudes are restricted by the dimensions of the slope and sediment availability thus it is unlikely that an event of a similar magnitude to the rarer large primary events is possible. Thus, a L-N may be the better model by which to characterise the immediate paraglacial response of sediment-mantled slopes. This is discussed in greater detail in section 6.5. Therefore, it seems appropriate to consider the statistical distributions of slope failure MF as time variable (fig. 6.12), whereby there are two distributions, short and long term, that should be considered separately but are occurring simultaneously through the transition to non-glaciated state characterised by a L-N in the immediate and decadal period following removal of ice to a P-L over centennial and millennial time scales. The two models are characterised by different failure types, mechanisms and size distributions.

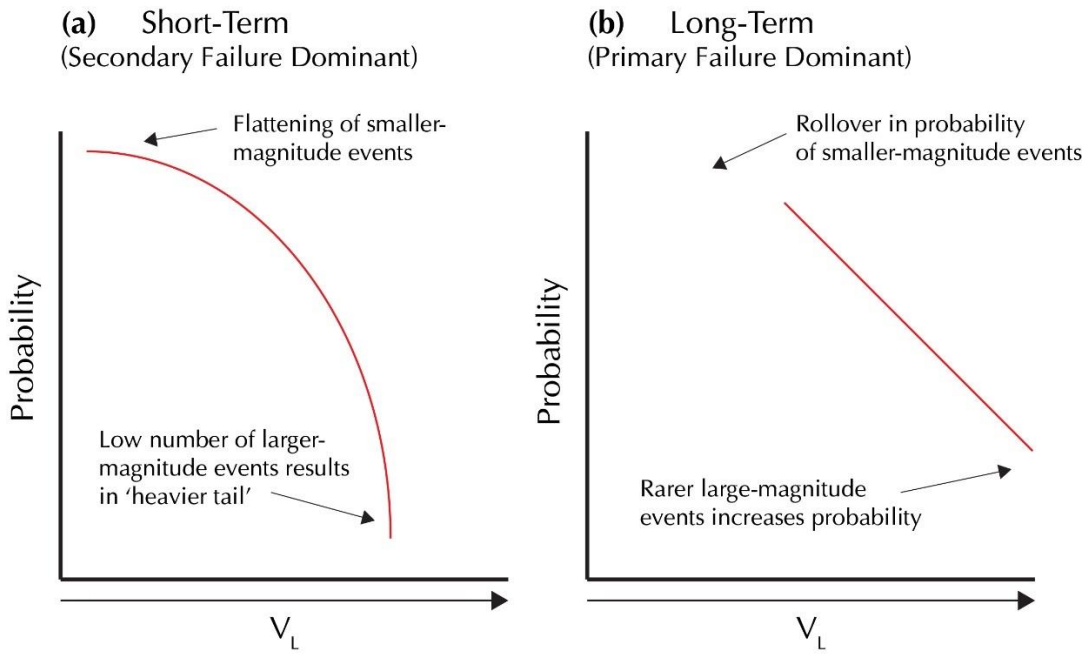

Figure 6.11: A conceptual diagram of the L-N and P-L models with key characteristics annotated. (a) Short term paraglacial adjustment dominated by secondary failures and characterised by a L-N distribution. (b) Long term adjustment where sediment stores are exhausted and sediment-mantled slopes are stabilised. Dominated by primary slope failures and larger magnitude rock slope failures that are characterised by a P-L through the medium to large magnitude events.

It is important to consider the implications of such an increase in material deposition following deglaciation for the overall sediment cascade. The total of secondary slope failure volumes over the period of one year across all sites was 3.6 x 10^5 m^3. 99.78 % of this was detected across the lateral moraines surrounding the Glacier d'Argentière and Mer de Glace where failures are deposited at the base of moraine slopes and onto the glacier surface. Retreat rates for

sediment-mantled slopes from which the greatest quantity of change was detected were calculated and given in table 5.12. The results reveal considerable variability but also highlight on the most active slopes; Mer de Glace and Miage, that extremely high rates of sediment working prevail on very recently deglaciated slopes. It may be no coincidence that these higher rates are observed at glaciers that are almost completely (Miage) or significantly (Mer de Glace) debris covered whilst the rates across the slopes of Argentière, which is principally debris free, are considerably lower and for the Pre de Bard, which has not been ice bound for several decades, are lower still. It is expected that the rates observed across lateral moraines which remain ice bound in their lower sections are characteristic of actively deglaciating slopes where continual wasting exposes fresh sediment supplies whilst those in the pro glacial zone are transient rates that are likely to decline through time in response to sediment exhaustion, increasing slope stability and dis connectivity. Despite the degrading speed of erosion across sediment-mantled slopes that have been completely free of ice for several decades, Curry (1999) points out that even the lowest rates often greatly exceed the background 'norm'.

The high rates of erosion observed across the Mer de Glace are far greater than those observed by Ballantyne and Benn (1994) and Curry (1999) across slopes in the Jotunheimen and Jostedalen, Norway. Here, rates varied from 2.5 to 169 mm a^{-1}, much in line with those observed across the slopes of Argentière, Miage and Pre de Bard, with the variability attributed to differences in precipitation and topographical characteristics by Curry (1999). However, Harrison and Winchester (1997) observed extraordinarily high rates of erosion in the region of 330 to 400 mm a^{-1} for the slopes in the recently deglaciated zone of the San Rafael glacier in the Chilean Patagonia, much more similar to the rates observed at the Mer de Glace, noting that fluvial action plays an important role in remobilisation of sediments. Deriving the lowest erosion rates at the site that has been deglaciated for the longest period of time agrees with the theory that after deglaciation, moraines can stabilise within 80 to 140 years, with gullies reaching their maximum width within approximately 50 years (Curry, 1998, 1999; Curry, Cleasby and Zukowskyj, 2006).

The aforementioned link between erosion rates and glacial debris cover whereby higher rates were found across slopes above glaciers with a greater level of coverage raises the question of whether the rate of geomorphic activity is responsible for variable rates of debris cover across different glaciers. Many glacier ablation zones are mantled in a near continuous blanket of debris (Benn *et al.*, 2012) and in some cases this can continue up most of the glacier length. The deposition of failure material on the ice surface has significant implications for the glacier's mass balance regime. Once the thickness of supra glacial debris reaches above 1-2 cm, mean ice ablation decreases logarithmically with thicker cover (Östrem, 1959; Deline, 2005a). Nowhere is this effect more clear than the glaciers of the Himalayas that have received considerable attention over recent years (Reid and Brock, 2010; Scherler, Bookhagen and Strecker, 2011; Benn *et al.*, 2012). Scherler,

Bookhagen and Strecker (2011) found retreat rates of 286 mountain glaciers to vary from high for debris free glaciers to zero for glaciers with debris cover greater than 20 %, explaining that supraglacial cover of just a few centimetres can lead to significant reduction in melt rates thus slowing a response time to climate change. In this project, the debris mantled slopes across the entire length of Glacier d'Argentière and Mer de Glace were surveyed as well as a section of moraine above the Miage, detecting a total loss of 5.5 x 10^3, 3.6 x 10^5 and 6.0 x 10^2 m^3 respectively representing a significant volume of debris delivered to the surfaces of each glacier. With significant simplification, such a volume of material is theoretically capable of creating a layer of 0.20 and 10.00 cm across the surface area of Argentière and Mer de Glace respectively (surface areas of 3.7 x 10^6 and 2.6 x 10^6 m^2).

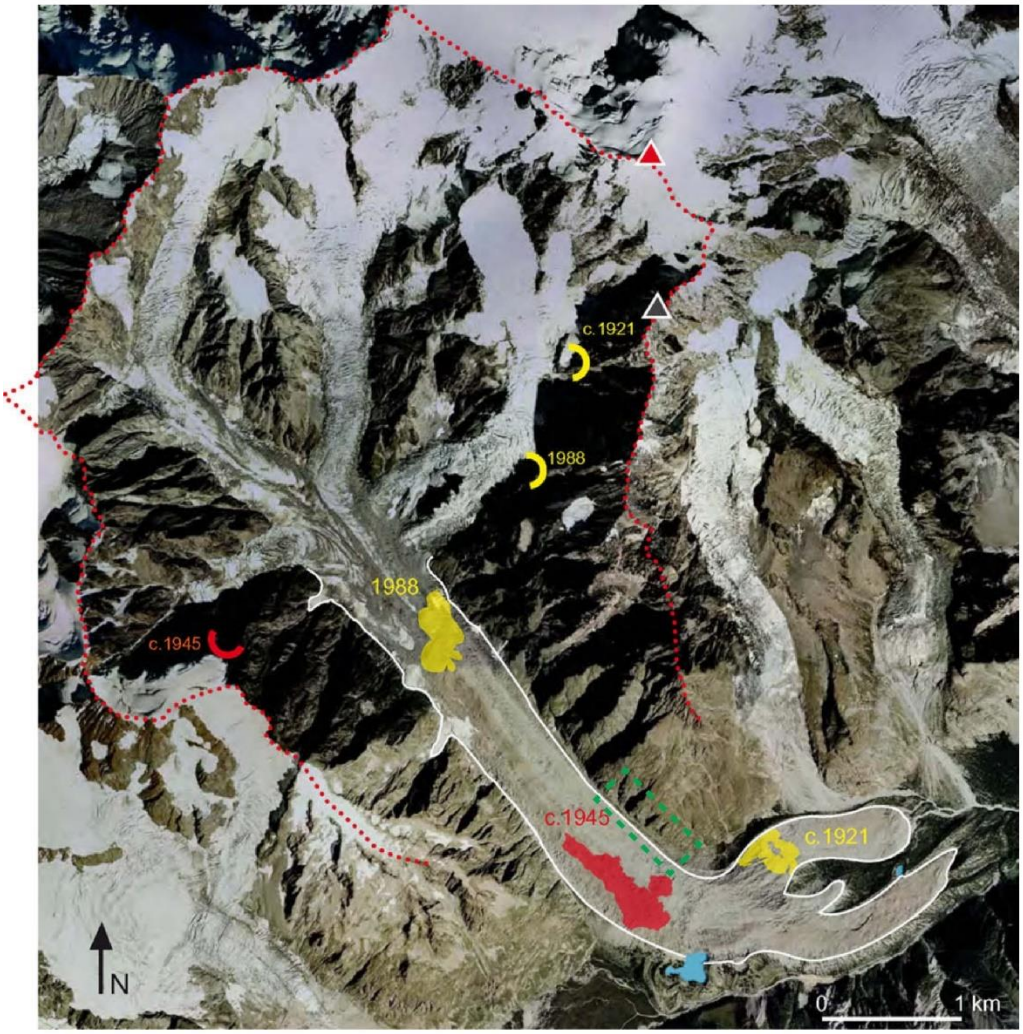

Figure 6.12: Locations of scars and deposits of low frequency 20th century rock avalanches on the debris covered Miage (from Deline, 2009). Green dashed box denotes area of slope covered in this study.

All glaciers studied here are in a state of negative mass balance and are retreating. Kirkbride's expansionary model of glacial debris cover (Kirkbride, 2000) states that "in periods of positive mass balance, faster ice flow and lower bare ice ablation ("transport dominant" conditions) cause the [debris] cover to contract towards the terminus; under negative balance, reduced flow and increased ablation ("ablation dominant" conditions) favour the upstream spread of the debris cover." Sources of debris vary dependent upon availability, though not all debris that is deposited supra glacially will remain there, with some being transported sub glacially and some re deposited further down glacier in lateral moraine formations. Debris covered glaciers are inefficient at evacuating their debris loads (Kirkbride, 2011) and therefore, the high erosion rates observed above such glaciers may not necessarily result in a higher sediment yield. Low frequency, high magnitude primary slope failure events further serve to rapidly increase glacial debris cover, such those that have occurred in the past at the Miage. At least ten rock falls and avalanches have occurred at this glacier through the 20th century and of the largest three, the most recent occurred in 1988 (fig. 6.14) (Deline, 2009). The deposit of the 1921 rock avalanche deposit can be seen on the Northern lobe of the glacier (fig. 6.14) surface almost 100 years after the event highlighting the buffer role (Fryirs *et al.*, 2007) played by the glacier in restricting sediment delivery to the fluvial system. Whilst the rarer larger magnitude events, such as those described by Deline (2009), are capable of covering large areas upon failure, such a low frequency may not be capable of covering the entire surface and the debris characteristics of glaciers such as the Miage and Mer de Glace are therefore most likely a result of a combination with highly frequent lower magnitude failures such as those shown in this study.

Slope failures dominate the sediment budgets of many mountain drainage basins around the world, with deposits locally affecting the morphology and linkages between hill slope and fluvial channels. Such erosional activity has significant implications for the dynamics of downstream channels by increasing sediment supply, storage and transport. Aggradation and subsequent incision have also been shown to be transient downstream effects of failure driven increases in sediment supply, as well as channel width adjustments, changes to grain size characteristics, transformation of single channels to braided beds and construction of terraces (Benda and Dunne, 1997). However, this sediment influx is inherently stochastic as it is driven by perturbations that are discrete in time and space across landscapes with considerable topographical, meteorological and lithological variability and thus, occurs as a complex series of pulses (Benda and Dunne, 1997). This work has gone some way towards demonstrating the frequency, magnitude and spatial distribution of sediment supply from recently deglaciated lateral moraines. The erosion rates presented in table 5.12 imply that maximum influxes of sediment to the glacier surface are achieved soon after the removal of ice prior to complete deglaciation, when slope stability is at its lowest and sediment availability is at its highest. However, there is a significant lag time between the deposition of

sediment onto the glacier surface and its delivery to the fluvial system following supra-, sub- or en-glacial transportation. This relationship is conceptually envisaged as a modified sediment yield in a following section (6.6).

A face-average retreat rate was also calculated for the rockslope at the Bossons survey site (section 5.8.1). A retreat rate of 52.39 mm a^{-1} is significantly higher than the range of values reported for similar environments (e.g. Krautblatter and Dikau, 2007), although their range stretches across three orders of magnitude from 0.0005 to 4.5 mm a^{-1} (Krautblatter and Dikau, 2007). The derivation of such a high annual retreat rate raises a number of questions. The smallest detected failure was 0.15 m^3, a minimum size that is smaller than most rockwall retreat studies are capable of capturing and enabling a more complete interpretation of the role of high-frequency, low-magnitude failures. These small scale failures are often unaccounted for in inventories and as such (owing to such factors as landscape censoring), are potentially miss-represented in current probabilistic models and sediment budgets. A high rockwall retreat rate could also be the result of site-specific geological characteristics that affect the structural stability of the rockface or leave it vulnerable to rapid change – this was discussed further in section 6.3.2. The retreat rate calculated here is also significantly greater (by an order of magnitude) than any reported in Ballantyne and Harris (1994) (table 12.2) for similar lithologies. The greatest retreat rates (3.29 mm a-1) were calculate by Ballantyne and Kirkbride (1987) for the Lock Lomond Stadial in upland Britain. Despite these rates remaining significantly lower than those calculated for the Bossons study site, the authors suggest that conditions favourable for freeze-thaw activity were most likely the driver of such high rates and noted that mid-latitude alpine mountains offer the closest modern analogue for this situation (Ballantyne and Kirkbride, 1987; Ballantyne and Harris, 1994). Surveys with a greater temporal resolution would be required over a larger spatial scale in order to clarify whether the large retreat rate calculate at the Bossons glacier is representative of early postglacial rockslope response or whether low-frequency mid-magnitude failures skewed the final calculation.

6.5 Modification of Slope Form

The dominance of secondary slope failures in the slope failure inventory compiled in this study presents a unique opportunity to consider the short-term (i.e. one year) modification of slope form. Paraglacial slope adjustment at the sites considered in this study operates primarily through the development of gully systems cut into sediment-mantled slopes (see figure 5.34). The slope failures detected and shown in figure 5.35 across the slopes of the Mer de Glace are most likely the product of many smaller discrete failures that have coalesced along a weakened section of drift slope. Without further surveys at a shorter temporal scale, this is a general assumption based upon process knowledge. They reflect a pattern observed across most of the studied sites where failures

across sediment-mantled slopes have been quantified; that is, the stripping of sediment from the upper parts of the slope and redeposition downslope. The result of such processes is an overall lowering of slope gradient, as shown by others (Curry, 1998, 1999; Curry, Cleasby and Zukowskyj, 2006; Curry, Sands and Porter, 2009; Mercier *et al.*, 2009) to lead to progressive atrophy of the slope and ultimate stabilisation. The larger of the two failures highlighted in figure 5.35 appears to show the collapse or failure of an inter-gully arête/sidewall and the widening of a gully which correlates well with the progression of gully formation reported in Norway by Curry (1999).

Slope modification through extensive development of gully networks is primarily controlled by debris flows. Decaulne and Sæmundsson (2007) outlined four meteorological controls to debris-flow initiation: 'pure' snowmelt, snowmelt associated with rainfall, long- lasting rainfall and intense rainfall, whilst Mercier *et al.* (2009) added the rapid melting of ice-core bodies as an additional control. In the case of the slope failure shown in figure 5.35, 'pure' snowmelt could be a controlling factor owing to a snow patch lying immediately above the LIA trimline at the head of the gully system. Whilst gully development has previously been shown to lower slope gradients, deplete sediment supplies and ultimately stabilise the slope (vegetation is sometimes used as an indicator of stability), in the case of slopes above actively retreating glaciers such as those surveyed in this study, continual exposure of previously ice-bound slope at the base of newly-formed gully systems means that maturation and stabilisation cannot be achieved whilst ice is still present. Once the glacier has been fully removed from the slope, only then can slopes stabilise with debris cone formation acting to decouple slopes from the fluvial system. A larger temporal scale would be required to understand the development of slopes over this timescale. Curry (1999) argues that whilst vegetation colonisation might be expected as a response to stabilisation, a more likely control on larger gully stabilisation is depletion of the upslope supply of sediment. For as long as the glacier is still present, fresh unworked supplies are continually becoming exposed through reduction in glacial mass. Thus, sediment yield from slopes above and around wasting glaciers may be proportional to the rate at which deglaciation is occurring with a decline and trajectory towards depletion only occurring following the complete removal of ice.

6.6 Conceptual Models

6.6.1 Sediment Yield

A conceptual model of the yield from sediment-mantled slopes during the early phase of the paraglacial period is presented in the form of a curve in figure 6.15. At each major point, the state of sediment availability (A) and slope stability (B) is hypothesised. It is a simple curve based on a similar model to the paraglacial reworking proposed by Church and Ryder (1972) (fig. 2.5) where maximum sediment yield is achieved very soon after the exposure of slopes under retreating

glacier ice. However, there are two fundamental differences; (i) the model accounts for the decadal to centennial period following deglaciation, rather than the entire paraglacial period therefore not covering a timescale required to account for low frequency rock slope adjustment and as such, a conceptual yield considering only remobilised sediments; (ii) the period of deglaciation is characterised by a flat top rather than a curved peak to reflect the ongoing exposure of fresh sediments thus availability is at a steady state. The curve builds on the work of Ballantyne (2002a), who produced multiple curves to envisage various processes though different curves though is focussed on the decadal period following deglaciation as oppose to the centennial and millennial time scales. The omitted values along the x axis denote the period of time taken from the commencement to the completion of deglaciation.

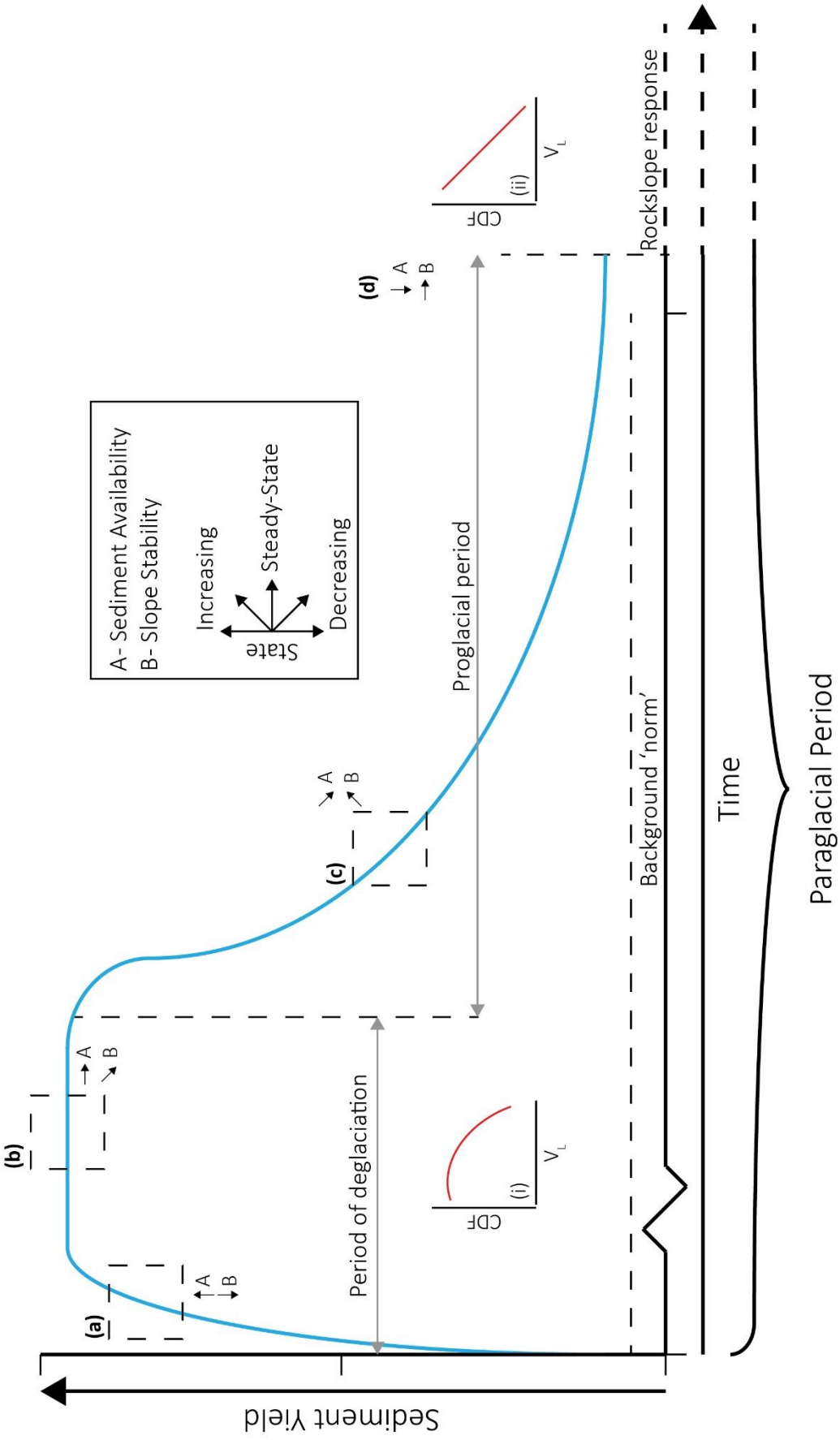

Figure 6.13: Theoretical model of sediment yield following the onset, and during the period of, deglaciation. Curve covers a period of sediment yield that is dominated by secondary failures. Points (a) to (d) summarise the theoretical state of the yield at each stage; (a) commencement of deglaciation; (b) continuous period of deglaciation; (c) period following the complete removal of ice and; (d) completion of stabilisation of sediment-mantled slopes in the short term. Time scale continues beyond the right of the axis as delayed rock slope response continues.

There are four major stages, denoted by (a) to (d), and the extension of the x axis represents the switch in dominant geomorphological activity from the remobilisation of sediment-mantled slopes through secondary failures to the delayed large-magnitude rock slope adjustment in response to the removal of ice. The proglacial period, as with that of Church and Ryder (1972) is defined as the duration of glacier shrinkage. The transition of the statistical model that best fits the size distribution of slope failure activity (as discussed in section 6.4) from L-N to P-L is also indicated in figure 6.15 (i & ii). The four phases of the early paraglacial period can be summarised as;

a) The onset of deglaciation (fig. 6.15 a);

The beginning of the paraglacial period is the same as the onset of deglaciation as at this stage, there is a rapid increase in the availability of sediment as previously ice bound stores are initially exposed. As the glacier retreats, the pro glacial zone grows. As discussed earlier in section 2.6.3, the impact of this growth upon sediment connectivity is dependent on a number of site-specific factors. Newly-exposed, previously-buttressed over-steepened slopes are unstable during this phase. (N.B. as outlined in section 2.3.2.1, glacier ice cannot support a failed slope but repeat loading/un loading cycles can lead to fracture propagation).

b) The period of deglaciation (fig. 6.15 b);

As the glacier continues to retreat and thin, sediment availability remains in a steady state through continual exposure of fresh, un worked sediments. Secondary failures continue to dominate geomorphological activity at rates that are proportional to the rate of glacier wastage. Further increases in the size of the proglacial zone serves to slow and disconnect downstream aggradation as a result of site-specific landforms (e.g. terminal moraines, proglacial lakes, debris cones etc.). Slopes remain critically unstable as over steepened slopes are continually revealed.

c) Complete removal of ice (fig. 6.15 c);

At this point, the curve of the sediment yield begins to decline steeply following the complete removal of ice, as secondary failures from sediment-mantled slopes rapidly exhaust sediment supplies along a trajectory towards stabilisation. Depositional landforms at the base of previously ice bound slopes serve to decrease the efficiency and connectivity of the system.

d) Stabilisation of sediment-mantled slopes (fig. 6.15 d);

Within a matter of decades following complete ice removal, sediment-mantled slopes have reached stabilisation through progressive secondary failures and thus the availability of fresh sediment for reworking is at its lowest. Mature depositional landforms disconnect the slope from the valley floor, effectively reducing and halting their fluvial sedimentation rates. Erosion rates are at the lowest, though still higher than the background 'norm' as the principal activity transitions to longer term rock slope adjustment through primary failures in response to deglaciation.

Over the short to long term response, the theoretical magnitude frequency distributions, as discussed in section 6.4, are also featured in the curve where;

i) Immediate release and remobilisation of sediment from previously ice bound storages such as lateral moraines through secondary failures following deglaciation is dominated by small to medium magnitude events with a MF distribution that is best fit with a log-normal distribution (fig. 6.15 i). Under this distribution, a process-driven flattening (or rollover) in the probability of small-magnitude failures is expected as discussed earlier. The log-normal curve also reduces the probability of large-magnitudes when compared to a power-law fitted to equivalent data. Large-magnitude failures of secondary sediments are controlled by site-specific factors and sediment availability and observations of such are likely to be comprised of many coalescent failures from a weakened slope rather than one single event, thus further reducing their probability.

ii) Over the longer term, large magnitude rockslope events (> 10^4 m^3) play a much more fundamental role in hill slope adjustment, thus increasing the likelihood of larger events with a primary failure MF distribution that is best described with a power-law (fig. 6.15 ii).

The exact nature, frequency and drivers of failure from sediment stores are not implied in the curve, though minor perturbations throughout the exponential decline could certainly result from extrinsic driving forces such as exceptional precipitation, insolation and tectonics. Glacial fluctuations are also not accounted for, where re-advances and surges may re-envelop sediment stores, thus reducing availability earlier than complete deglaciation. Re-advances and surges may also serve to reconnect previously-decouple landsystems. In these cases, secondary dips and rises in the sediment yield could be expected, similar to the longer term secondary peaks envisaged by Ballantyne (2002a) for the failures driven by extreme weather events. In contrast to the earlier

model of Church and Ryder (1972), where there is a peak in the yield soon or immediately after deglaciation, this curve is characterised by a flat peak throughout the duration of glaciation representing the continual exposure of fresh sediment stores followed by a period of rapid decline following the complete removal of ice. A significant proportion of the sediment yield is driven by slopes above actively thinning glaciers, such as those surveyed in this study and thus, the flat peak is dependent upon a steady state of sediment delivery from the glacier surface to the fluvial system through glacial transport. As previously discussed, this may not be as efficient at some glaciers as others and thus, the exact magnitude of yield may also vary considerably at the valley scale.

It is expected that the overall yield would increase again beyond the temporal boundary of figure 6.15 to a level similar, if not greater than achieved through sediment remobilisation in response to large magnitude rock slope failures such as rock avalanches. In fact, a single large magnitude rock slope failure in response to stress redistribution holds the potential to completely dominate sediment yield over a time scale of several millennia. For example, using beryllium 10 (^{10}Be), Ballantyne *et al.* (2014) dated the exposure age of a rock slope failure deposit with a minimum volume of 1.85 x 10^5 m^3 at Beinn Shiantaidth, Scotland. They calculate a weighted mean of 14.14 to 15.11 ka, which falls in the period of the Late Devensian (Lare Weichselian) Lateglacial, in the interval between ice sheet deglaciation and the beginning of the Loch Lomond (= Younger Dryas) Stade (LLS) (Ballantyne *et al.*, 2014). Thus, the rock slope failure was calculated to have occurred up to 2000 years after deglaciation (Ballantyne *et al.*, 2014), long after the maturation, exhaustion and stabilisation of loose sediments from newly exposed stores. This single event delivered almost 50 % of the total volume of the 785 events observed in this study (3.7 x 10^5 m^3). Peaks in the sediment yield from primary failures may also be driven by other (non-paraglacial) rock slope failures around the world, such as the Mt Haast rock avalanche, New Zealand (9.8 x 10^5 m^3) (Hancox and Thomson, 2013; Dunning *et al.*, 2015) and 16 rock avalanches in the Canadian Cordillera (> 10 x 10^5 m^3) (Evans and Clague, 1994) represent significant volumes of sediment release into the glacial and fluvial system. Similarly at the Mont Blanc massif, Deline and Kirkbride (2009) estimated a total volume of 7.3 9.8 x 10^6 m^3 for a rock avalanche deposited in Val Ferret in 1717, approximately 95 % larger than the combined volume of all detected failures across all sites in this study.

6.6.2 Paraglacial Landsystem

A conceptual schematic of a paraglacial land system is presented in figure 6.16 for the onset of deglaciation (fig. 6.16 a), 40 60 % deglaciation (fig. 6.16 b), and nearing complete deglaciation (fig. 6.16 c). The three stages can be summarised as;

a) the onset of deglaciation (fig. 6.16 a);

Whilst the glacier occupies the majority of the valley, most of the sediment stores remain ice-bound. Periglacial processes drive deposits of primary slope failures from HARW (Magnin et al., 2015) and cirque erosion (Sanders et al., 2012) that fall into the accumulation area where they have been shown to be rapidly sequestered (e.g. Dunning et al., 2015) into the glacier and transported en-/sub-glacially. Where exposure of sediments has begun, secondary failures commence immediately driven by meteorological conditioning and ice-core degradation.

b) the period of deglaciation (fig. 6.16 b);

The proglacial zone expands and where connected, is fed from freshly exposed sediment stores whilst the glacial outwash channel incises the area and carries glaciofluvial deposits further downstream in the basin. Site-specific landforms and topography decouple slopes from the channel and limit the delivery of secondary failures in the proglacial zone to the fluvial system. Those that fail above the glacier are delivered to the ice surface which buffers the time taken to reach the fluvial system, if at all. Drift slopes above recently exposed glacially moulded rock slopes are mostly stabilised and partly vegetated, serving as a disconnection between the primary failures from HARW and the glacier surface/ valley bottom. Historic deposits of large magnitude primary failures are carried with the glacier and where conditions are suitable, may serve to create a continuous blanket of debris across the surface and thus, reduce surface ablation rates.

c) nearing complete deglaciation (fig. 6.16 c);

Sediment-mantled slopes that were amongst the first to become fully exposed are reaching maturation. Gullies have widened, and inter-gully arêtes have collapsed. Deepening coalescent gullies have shallowed the slope gradient towards stabilisation and deposited sediments have formed debris cones at the base of the slopes, disconnecting the slope from the fluvial system and reducing yield from these sources. The size distribution of slope failures that previously followed a L-N model, such as that shown in this study, is superseded by the distribution of lower frequency but larger magnitude failures which are better characterised by a P-L.

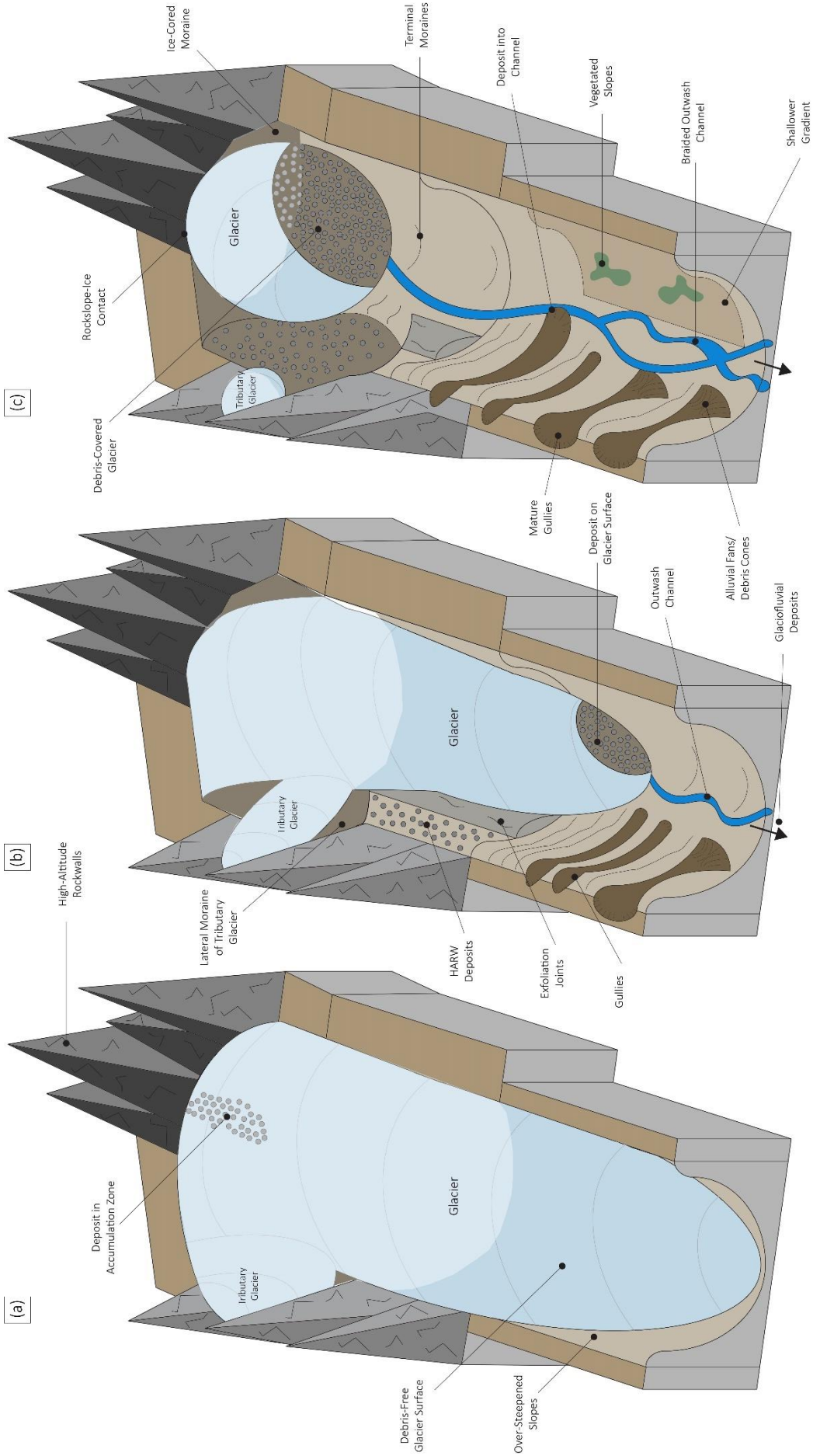

Figure 6.14: Schematic of a paraglacial land system during (a) the onset of deglaciation, (b) mid deglaciation, (c) nearing complete deglaciation.

6.7 Summary

Glacial cycles directly condition slope stability in a number of ways; (i) they scour and erode valley slopes resulting in undercutting and over steepening. This increases the shear stress acting within the slope, thereby reducing stability once the ice is completely removed; (ii) wasting de-buttresses slopes though the removal of lateral support, which, depending on the geological characteristics of the slope, may lead to the formation and expansion of discontinuities, and; (iii) recession often exposes valley side slopes that are mantled by unconsolidated glaciogenic sediments that often rest against adjacent, over steepened bedrock slopes (Hugenholtz *et al.*, 2008). This study has demonstrated that across these sediment-mantled slopes, short term failure distributions are dominated by high frequency, low magnitude events that are driven by over-steepening and meteorological conditioning. With the projection of continued warming across the European Alps (Gobiet *et al.*, 2014) and subsequent glacier down wastage, it can be expected that such a hill slope response will continue at rates relative to the rate of ice removal and exposure of previously ice bound sediment stores.

To summarise, this study set out to detect and quantify the distribution of failures on slopes above and around glaciers in the Mont Blanc massif. SfM-MVS photogrammetry was shown to be a particularly robust tool, capable of creating high resolution, accurate topographic datasets providing due care and consideration were given during the survey planning, execution and post capture processing phases. A fully three dimensional workflow utilising open source algorithms ensured the complex topography of mountain slopes was not obscured through 2/2.5D surface interpolation. The results in this study have demonstrated that the dominant erosional process in the immediate period following ice removal across the slopes above and around glaciers are secondary failures from sediment-mantled slopes. Given the observation of slopes adjusting long before complete deglaciation, this agrees with the temporal pattern of paraglacial sediment reworking proposed by Church and Ryder (1972), in that the paraglacial period coincides with the onset of deglaciation as there appears to be no lag time between ice removal and sediment remobilisation. Such rapidity has been reported on by others (e.g. Ballantyne and Benn, 1994; Ballantyne, 1995; Curry, Cleasby and Zukowskyj, 2006) but this study presents the first quantification of the size and spatial distribution of failures at such a high resolution, across such a wide scale and provides a unique insight into the short term dynamics of paraglacial land systems. The spatial distributions presented here suggest precipitation and insolation are key drivers. The following and final Chapter (7) will summarise the main conclusions from this work from the perspective of each objective, highlight key limitations and point to possible future research directions.

7 Conclusions

7.1 Introduction

The aim of this research was:

Understand the spatial and size distributions of slope failures above and around wasting glaciers.

To address this aim, the project has;

1) Explored the potential drivers and controls of short-term slope failures using their spatial distributions and through structural analysis of a recently deglaciated rockslope.
2) Analysed the effect of observed failure activity on the modification of slope form and mobilisation of sediment within the landsystem. Developed a conceptual model of a sediment yield and a deglaciating landsystem that considers the implications of these findings alongside existing knowledge.

This was achieved by:

a) Using an emergent photogrammetric technique to reconstruct the complex topography of mountain slopes. Building upon an existing body of recent literature and developing an optimal and appropriate workflow for minimising and dealing with known sources of error consistently;
b) Detecting and quantifying failures at a number of glacial sites in the Mont Blanc massif using high-resolution topographic data created using the workflow developed in the previous step. Resolving their probabilistic nature by means of magnitude-frequency distributions and analysing their spatial distribution using GIS, and;
c) Utilising a statistical goodness-of-fit test to determine the best model fitted to the magnitude-frequency distributions of detected slope failures and resolve whether the rollover in small-magnitude failures observed in other inventories are likely to be caused by geomorphological processes or a manifestation of data bias.

This chapter will summarise the key findings and implications of this study in regard to each of the research objectives outlined in Chapter 1, identify limitations of the research and suggest directions for future work.

7.2 SfM-MVS Photogrammetry

- Using an emergent photogrammetric technique to reconstruct the complex topography of mountain slopes. Build upon an existing body of recent literature and develop an optimal and appropriate workflow for minimising and dealing with known sources of error consistently.
- Detecting and quantifying failures at a number of glacial sites in the Mont Blanc massif using high-resolution topographic data created using the workflow developed in the previous step. Resolving their probabilistic nature by means of magnitude-frequency distributions and analysing their spatial distribution using GIS.

Building upon an ever-growing body of research that utilises SfM-MVS photogrammetry for geoscientific analysis, this study has established a robust workflow that can produce models across multiple scales that are then usable within a 3D workflow for multi-temporal change analysis. The key points are:

- SfM-MVS is capable of producing accurate, repeatable models at high resolutions and densities providing due care and consideration is given to the collection of image data and ground control. Most importantly, to; (i) combine nadir with oblique offset images to minimise the effect of inherent lens distortion and; (ii) collect an even spread of ground control across surfaces that face a combination of directions relative to the image.
- Capturing outdoors imagery in challenging environments does not necessarily present optimal capturing conditions. To ensure that erroneous data points caused by harsh shadowing under sub-optimal lighting conditions do not permeate through to the final results, an effective thresholding method utilising a composite of RGB was presented and shown to reduce average RMSE values.
- An innovative multi-scale model-to-model comparison technique was shown to correctly identify areas of significant change, considering the local surface topography and alignment parameters.
- An approach to volume calculation based on the projection cylinders of the M3C2 algorithm constrained to a single orientation was presented and shown to produce accurate estimations of slope failure volume.
- Open-source algorithms were shown to work well with models produced using SfM-MVS for the semi-automatic extraction and characterisation of rock mass discontinuities and their spacings; essential parameters for the assessment of rock mass strength by means of SMR.

SfM-MVS has brought with it a revolution in the accessibility of high-resolution topographical data, reducing the capital and logistical investments required by more traditional approaches whilst producing models of comparable accuracy. There are a number of caveats, and a significant processing time requirement but these are acceptable compromises for the ability to create models across scales such as those presented in this study. Utilising the processed data, M3C2 was shown to be a robust tool which removes the need to interpolate 2/2.5D surfaces from 3D data and as such, the entire slopes geometry is considered during the change detection phase. The result is a robust and repeatable workflow that is capable of detecting and characterising slope failures above a detection threshold determined by the model resolution, alignment quality and data noise.

Using a combination of terrestrial and airborne SfM-MVS photogrammetry and the workflow established in step 1, over 31 km of slope was surveyed around wasting glaciers in the Mont Blanc massif in the summers of 2014 and 2015. The first-such attempt to quantify short-term slope failure activity across this scale. The main conclusions from this can be summarised as:

- 3D topographical change detection has been used to document 785 slope failures across five sites over a one year observation period, including 43 primary and 742 secondary slope failures representing a total volumetric loss of $3.7 \times 10^5\ m^3$.
- Secondary slope failures (i.e. the remobilisation and reworking of previously ice-bound sediment stores) were clearly shown to dominate short-term sediment flux, representing 99.61 % of the total volume.
- The dominance of secondary slope failures is attributed to the lag-time required for rock-slope adjustment following de-glaciation versus the short-term observation in this project and higher detection threshold across high-altitude rock-walls limiting detection to topographic change in excess of 1.5 to 4 m. Analysis of the rock mass strength by means of an SMR also suggests that the majority of rock-slopes are currently stable, though the SMR may not be appropriate for predicting the rates of smaller-magnitude failures.
- Erosion rates of lateral moraines were shown to be highly variable across the sites and range from 4 to 320 mm a^{-1} with maximal rates observed across slopes above glaciers that are partly debris covered whilst the lowest rates were observed across slopes at debris-free glaciers and those which have been free of ice for several decades.
- Maximal densities of slope failures were observed across SW-facing slopes which are most susceptible to prevailing weather systems and solar insolation implying meteorological conditioning through precipitation and sub-surface ice thawing are principal triggering mechanisms.

The findings from this objective highlight the unique, and rapid response of sediment-mantled slopes to de-glaciation, with the majority of detected slope failure activity shown to occur across these areas. Spatial distributions suggest principle triggering mechanisms of slope failure are moisture and insolation, and maximal erosion rates were observed across slopes at debris-covered glaciers. Such a relationship could indicate that debris-cover is a result of a combination of high moraine erosion rates comprised of high-frequency low-magnitude events and rarer large-magnitude primary slope failures such as rock avalanches.

7.3 Size Distribution of Slope Failures

- Utilising a statistical goodness-of-fit test to determine the best model fitted to the magnitude-frequency distributions of detected slope failures and resolve whether the rollover in small-magnitude failures observed in other inventories are likely to be caused by geomorphological processes or a manifestation of data bias.

The general consensus is that the size distribution of slope failures is best described by means of an inverse power-law across a truncated portion of inventory datasets, with the rollover in probability of smaller magnitudes attributed to systematic under-sampling at high-enough resolutions, or fundamentally different generative models. In a lot of cases, these distributions are inferred from a qualitative analysis of data plotted on a log-log scale and lack thorough statistical analysis. The size distribution of slope failures detected in this project were analysed by means of magnitude-frequency analysis using the complimentary cumulative distribution function, and the suitability of the hypothetical distributions were tested using a statistical bootstrapping approach. The results and implications of this can be summarised as:

- The majority of datasets presented are shown to better described by a log-normal distribution at both site- and range-scale. The scaling exponents of the log-normal distributions for the cumulative primary and secondary slope failure datasets are 4.02, 0.79 and 1.32, 2.99 respectively.
- The discovery of a log-normal distribution is based upon a dataset captured within a short temporal scale in contrast to the majority of existing inventories that consider much greater time-scales, highlighting the importance of rarer large-magnitude slope failures in driving the generative models of the distribution. P-L models fitted to the data in this study were shown to significantly underestimate the likelihood of large-magnitude events and were characterised by large scaling parameters which suggests a bias towards small-magnitude failures.
- It is hypothesised that short-term immediate release and remobilisation of sediment from temporary storages such as lateral moraines are dominated by high-frequency, low-magnitude events that are best described by a log-normal distribution, whilst longer-term rock-slope adjustment is closer to that of an inverse power-law with low-frequency large-magnitude events playing an important role in landscape evolution.

This is the first study to suggest a log-normal distribution as a better fit for slope failure distributions across a short observation period in Alpine catchments. As mentioned in the summary above, this has significant implications for understanding the probability of slope failures in the

early stages of the paraglacial period and is most likely driven by the abundance of low-magnitude high-frequency events. It is proposed that other studies do not find a similar distribution as a result of; (i) not considering the distribution in their analysis; (ii) having larger temporal scales included in their inventories that are more likely to include rarer large-magnitude events or; (iii) not considering slopes undergoing paraglacial slope adjustment which has been shown to produce erosion rates far higher than slopes which have not previously been glaciated.

7.4 Spatial Distribution of Slope Failures

- Exploring the potential drivers and controls of short-term slope failures using their spatial distributions and through structural analysis of a recently de-glaciated rock-slope.
- Analysing the effect of observed failure activity on the modification of slope form and mobilisation of sediment within the land-system. Developing a conceptual model of a sediment yield and a de-glaciating land system that considers the implications of these findings alongside existing knowledge.

The analysis of slope failures across such a large scale presents a number of unique insights into their spatial distribution and potential drivers and controls that would not be gained from single slope-scale surveys. The key findings are:

- Maximal densities of secondary failures were found to occur on SW-facing slopes which could suggest that slope failures, dominated by debris flows, are driven by precipitation. As well as this, the largest area of slope with the highest level of insolation is found on the SW-facing slope suggesting that secondary failures are driven by meteorological conditioning. Without in-situ measurements, any interpretation of driving mechanisms is speculative.
- The use of SMR to assess rock-slope stability at the Bossons site indicated that much of the slope was rated by an SMR that suggests at best, completely stable conditions and at worst, partially stable however, it was clearly failing through frequent small-magnitude events and thus, the face value of SMR (i.e. broad classification of good, very good etc.) may not be suitable for determining the likelihood of small-magnitudes. Nevertheless, the structural characterisation of a rock-slope in this study does offer a unique and invaluable insight into the mechanisms of failure across slopes.

The discovery of such a significant amount of slope failure activity from lateral moraines undergoing continual exposure at the margins of wasting glaciers led to the development of a conceptual model of sediment yield during the early phase of the paraglacial period and can be summarised as:

- Sediment yield reaches a peak very soon after the onset of de-glaciation as over-steepened sediment stores become readily available for reworking and remobilisation.
- Continual wasting ensures sediment availability remains in a steady-state during the period of de-glaciation whilst an increasing pro-glacial zone serves to increase connectivity.
- Following the complete removal of ice, sediment availability declines exponentially as previously ice-bound lateral moraines reach maturity and stabilisation within a matter of

decades, with sediment stores exhausted. Meanwhile, the formation of debris cones and alluvial fans reduce the state of connectivity.

- Over the longer-term, the maximum yield shown in this model will most likely be significantly dominated by large-magnitude rock-slope failure in response to de-glaciation.

The model presented is driven by the three primary agents of sediment yield in the early phase of the paraglacial period; availability, connectivity and slope stability. Unlike previous models, this proposes an elongated phase of steady-state availability and increasing connectivity during the period of de-glaciation after which, the yield begins to exponentially decline as slopes begin to stabilise within a matter of decades. This model is a logical development upon existing work that considers the entire paraglacial period as this study has shown different generative models of slope failure distribution are at work across different temporal scales. In the earlier phase, the availability of sediments from previously ice-bound lateral moraines are rapidly exhausted, long in-advance of major rock-slope adjustment and thus a separate model to reflect this is deemed appropriate.

7.5 Limitations of this Research

Although a good understanding of the short-term slope failure distributions above and around wasting glaciers was achieved using 3D topographic data at five sites in the Mont Blanc massif, there are some limitations. Whilst some of these are inherent within the use of SfM-MVS photogrammetry and the interpretation of 3D data, others could be improved upon with the benefit of hindsight:

1) Image data of the high-altitude rock-walls above most of Glacier d'Argentière and some of the Mer de Glace were not at a resolution high-enough to accurately reconstruct the complex geometry of such surfaces and as a result, the detection threshold was considerably higher across these slopes which potentially resulted in a significant quantity of primary slope failure activity undetected. Whilst the thresholds were not poor enough to mask medium- to large-magnitude slope failures and a higher-resolution of a rock-slope was conducted at the Glace de Bossons, this study has highlighted the short-term importance of small-magnitude events and an ideal remedy would be to re-survey these slopes using a higher-resolution sensor or within a closer proximity to the surface through repeat flight lines along each valley.
2) Whilst a considerable number of published slope failure inventory studies examine the size distribution of slope failures across longer time-scales, there are none that specifically deal with the short-term response of recently de-glaciated slopes and as such, direct comparisons between the characteristics of published distributions and those in this study are difficult.
3) Much of the slope failure deposits were observed to fall below the limit of the survey and therefore could not be quantified. A crucial assumption was made that these deposits were subsequently transported away from the depositional zone whilst in reality, they could potentially be held in secondary storage landforms and therefore, the full volume of sediment calculated may not represent the total volume delivered to the glacial or fluvial system.
4) The conceptual sediment yield, although theoretical, does not account for likely extrinsic perturbations across the course of the exponential decline following complete de-glaciation. Extreme weather events, tectonics and glacier re-advances would all significantly alter the slope three factors driving yield.

7.6 Suggestions for Future Work

This PhD has offered some unique insights into the short-term slope failure distributions on slopes recently exposed by wasting glaciers, significantly furthering the knowledge base of size distributions across sediment-mantled slopes and presenting a conceptual model of sediment yield that reflects this. With this in mind, there are a number of key research areas that would benefit from further work, including:

1) The continual development of SfM-MVS photogrammetry, most importantly the development of direct-georeferencing approaches to scaling models. Whilst a considerable number of benchmarking tests and optimal work-flows have recently been published, the collection and registration of GCPs, along with the post-collection processing are by-far the biggest time commitments required for using the technique. Whilst the latter is reducible through upgrading computer processing components, direct-georeferencing offers a very promising alternative for the other. Especially in areas where GCPs are constrained to accessible parts of the terrain, an approach that can accurately scale models based on the GPS location of the sensor and its orientation parameters will come into its own.
2) Although a number of inferences have been made into potential triggering mechanisms based on the spatial distribution of slope failures with respect to slope aspect, further work would benefit from knowledge of precise event timing to correlate with extrinsic factors such as meteorological conditions. Such work could be conducted using fixed-position time-lapse photography or in-situ seismic detection devices.
3) Detecting such a large volume of sediment being deposited onto the surface of glaciers has significant implications on glacial dynamics. Whilst beyond the scope of this work, additional research into the distribution and characteristics of deposits on the ice surface would offer useful insights into the potential glacial response which in turn is important for understanding rates of wasting and flow.
4) Whilst a number of small-magnitude slope failures where observed at slopes in this study, the detection threshold across higher-altitude rock-walls potentially masked a number of events occurring at these sites. Higher-resolution data across these slopes will be beneficial to our understanding of rock-wall response to thawing sub-surface ice, another important factor of climatic change in Alpine environments.
5) Erosion rates of lateral moraines in themselves are useful for describing the variability across slopes at different stages of the paraglacial period however, would greatly benefit from field measurements of debris thickness and gully depth across the lateral moraines as these finite sources of sediment would be useful for estimating the timing of slope stabilisation.

7.7 Concluding Remarks

To finish the thesis, it is useful to highlight the novelties, findings and contributions of the data presented to advancing the current state of knowledge;

1) There are no previous examples of targeted topographical surveys at valley-scale with an alignment quality capable of detecting volumes to 0.28 m^3, which provides a first-of-its-kind analysis of valley-scale spatial distribution and process information that when combined with detailed sites surveys, present a unique insight into slope response at the range scale.
2) The dominance of secondary failures is clear. When compared to existing inventories that consider these, 99 % of failures detected in this study are below the lower bound of their P-L model and therefore, data bias through under-representing small magnitudes is unlikely. Very few have even considered a L-N, rather maintain the status-quo, though statistically it's very clear that this is the better fit to secondary failures. It seems appropriate to consider that there are two distributions that act separately but are occurring simultaneously through the transition to non-glaciated state.
3) Such range-scale data highlights a number of spatial distribution patterns that suggest short-term rates of secondary failure activity are predominantly driven by meteorological conditioning. As well as this, observing the highest rates of moraine erosion at glaciers that partly debris-covered suggests that such failure distributions may be partly responsible for such a state.

Appendix 1

Inventory of Primary Slope Failures

Table 0.1: Inventory of detected primary slope failures at each of the field sites; Glacier d'Argentière (ARG), Mer de Glace (MDG) and Glacier de Bossons (BOS). Failure locations (Northing, Easting and Altitude) and descriptive characteristics (Volume, Width, Height, (mean) Depth) are given as well as characteristics of the failed slope (Aspect, Gradient). Digitised versions of this inventory are available upon request to the author.

ID	Glacier	Easting (m)	Northing (m)	Altitude (m.a.s.l.)	Volume (m^3)	Width (m)	Height (m)	Depth (m)	Slope Aspect	Slope Gradient (°)
1	ARG	346359.98	5089557.31	3,032.98	6.19	0.86	1.73	3.34	SSW	71-80
2	ARG	344588.05	5090180.73	2,685.03	4.67	3.32	1.40	0.93	WSW	51-60
3	ARG	344532.22	5091256.02	2,740.51	27.00	6.27	6.34	1.56	W	41-50
4	ARG	344539.89	5091275.26	2,744.77	31.47	7.38	6.28	1.93	WNW	51-60
5	ARG	344540.38	5091238.76	2,747.11	17.60	6.13	4.62	1.59	W	41-50
6	ARG	344609.12	5091285.40	2,798.18	12.77	10.54	6.17	1.22	W	41-50
7	ARG	344563.64	5091286.89	2,761.79	9.93	6.47	5.74	1.59	NW	41-50
8	ARG	344616.14	5091348.35	2,823.86	6.14	3.07	3.05	1.24	S	11-20
9	ARG	344600.26	5091352.43	2,824.58	5.53	2.41	3.46	1.14	SSW	31-40
10	ARG	344609.10	5091381.29	2,847.71	3.74	3.66	1.87	1.12	SW	21-30
11	MDG	339577.44	5086517.62	2,068.61	15.77	5.77	5.07	3.89	NE	21-30
12	MDG	339827.24	5086197.52	2,049.19	7.08	5.01	7.40	3.09	E	81-90
13	MDG	339829.82	5086101.05	2,082.13	4.93	5.45	2.43	2.71	ENE	61-70
14	MDG	339926.47	5087329.22	2,085.73	89.51	4.65	6.19	2.45	SSW	61-70
15	MDG	339981.37	5087337.84	2,128.11	20.22	4.80	4.09	1.74	SSW	71-80
16	MDG	341071.99	5085856.24	2,297.80	284.45	12.26	6.51	7.10	W	31-40
17	MDG	341108.47	5085684.07	2,315.37	110.22	5.93	5.06	6.93	WSW	31-40
18	MDG	340911.94	5085843.51	2,177.58	114.44	5.83	8.48	8.37	SW	11-20
19	MDG	340861.11	5086470.47	2,266.93	78.23	7.39	6.64	7.28	WNW	11-20
20	MDG	341107.87	5085895.79	2,340.12	67.85	6.54	3.63	6.79	WNW	61-70
21	MDG	340905.90	5086013.36	2,193.45	71.19	6.81	5.20	7.36	W	41-50
22	MDG	341333.41	5085710.80	2,526.76	60.22	6.50	6.85	6.70	WNW	51-60
23	MDG	341057.67	5085840.20	2,282.99	59.16	3.56	5.56	6.92	W	41-50
24	MDG	341098.69	5085881.27	2,330.40	59.39	4.29	4.57	7.91	W	51-60
25	BOS	333292.33	5084349.96	1,485.49	177.38	8.18	10.86	2.33	ENE	71-80
26	BOS	333290.78	5084353.18	1,471.89	14.79	3.26	4.17	1.50	E	81-90
27	BOS	333286.33	5084354.64	1,492.76	6.41	1.97	1.94	0.81	E	51-60
28	BOS	333292.94	5084334.65	1,496.19	7.53	2.21	1.95	1.07	ENE	61-70
29	BOS	333292.46	5084348.19	1,480.75	7.64	4.38	3.00	1.71	ENE	81-90
30	BOS	333292.00	5084345.62	1,489.20	3.19	1.45	1.16	1.14	ENE	71-80
31	BOS	333289.93	5084356.94	1,474.56	2.19	0.84	1.19	0.79	E	81-90
32	BOS	333299.53	5084330.01	1,490.28	3.63	3.02	2.47	1.41	NE	61-70
33	BOS	333296.99	5084332.65	1,485.85	2.47	1.36	2.45	1.13	NE	71-80
34	BOS	333293.37	5084341.30	1,489.66	1.48	0.51	0.52	0.75	E	51-60
35	BOS	333301.17	5084326.56	1,491.96	1.89	1.86	1.70	1.13	SW	51-60
36	BOS	333281.28	5084390.30	1,458.39	10.25	2.85	2.92	1.42	SE	41-50
37	BOS	333284.53	5084381.62	1,458.16	1.58	3.06	2.98	1.62	SSE	71-80
38	BOS	333280.57	5084391.97	1,452.84	5.15	4.00	2.27	0.91	NE	71-80
39	BOS	333280.36	5084396.61	1,448.38	1.09	2.49	0.94	1.02	E	81-90
40	BOS	333280.24	5084397.90	1,445.07	0.15	0.62	1.07	0.43	ENE	81-90

41	BOS	333252.02	5084429.10	1,450.35	4.20	0.71	1.22	0.97	NNE	61-70
42	BOS	333250.74	5084429.83	1,451.35	2.35	0.60	1.17	0.57	NE	61-70
43	BOS	333226.89	5084497.96	1,429.13	28.78	3.51	5.58	1.52	NE	71-80

Inventory of Secondary Slope Failures

Table 0.2: Inventory of detected secondary slope failures at each of the field sites; Glacier d'Argentière (ARG), Mer de Glace (MDG and MDG_I [intra-annual survey]), Ghiacciaio del Miage (MIA) and Pre de Bard (PDB). Failure locations (Northing, Easting and Altitude) and descriptive characteristics (Volume, Width, Height, (mean) Depth) are given as well as characteristics of the failed slope (Aspect, Gradient). Digitised versions of this inventory are available upon request to the author.

ID	Glacier	Easting (m)	Northing (m)	Altitude (m.a.s.l.)	Volume (m^3)	Width (m)	Height (m)	Depth (m)	Slope Aspect	Slope Gradient (°)
1	ARG	343132.95	5091512.99	2,466.77	71.05	18.49	9.28	1.07	SW	31-40
2	ARG	343071.74	5091512.24	2,454.45	63.34	18.96	7.72	1.02	NNE	21-30
3	ARG	343171.75	5091476.96	2,489.03	56.77	8.22	4.05	1.57	WNW	21-30
4	ARG	343148.52	5091522.55	2,458.69	39.41	8.85	4.41	1.31	WSW	11-20
5	ARG	343168.09	5091490.89	2,477.14	37.44	17.92	10.36	1.25	NNW	21-30
6	ARG	343125.00	5091474.63	2,490.17	49.10	9.91	8.87	1.90	NW	51-60
7	ARG	343208.16	5091494.68	2,480.60	36.01	6.79	2.46	1.43	W	11-20
8	ARG	343190.40	5091506.23	2,476.57	35.71	8.34	2.43	1.44	NW	21-30
9	ARG	343178.80	5091502.16	2,475.07	26.48	9.96	2.43	1.20	W	21-30
10	ARG	343073.89	5091523.87	2,450.42	15.50	10.04	6.10	0.99	NNW	21-30
11	ARG	343116.29	5091511.90	2,463.65	19.48	4.79	2.01	1.28	NNE	21-30
12	ARG	343084.14	5091457.19	2,498.83	20.05	6.37	5.81	1.36	NNW	51-60
13	ARG	343065.86	5091490.43	2,472.97	20.62	6.24	5.39	1.46	WNW	61-70
14	ARG	343072.80	5091537.34	2,443.88	12.84	6.42	3.70	0.98	S	21-30
15	ARG	343056.44	5091524.85	2,452.97	14.85	3.21	1.32	1.27	WNW	11-20
16	ARG	343028.69	5091550.91	2,441.11	16.88	4.89	3.06	1.49	ENE	31-40
17	ARG	343068.78	5091482.10	2,481.86	19.99	8.64	9.57	1.84	WNW	41-50
18	ARG	342902.95	5091575.51	2,410.98	10.76	4.58	1.40	1.12	NE	11-20
19	ARG	343014.13	5091528.47	2,445.95	8.80	5.22	3.48	0.94	N	31-40
20	ARG	343124.44	5091530.08	2,453.54	9.32	4.05	2.38	1.06	NW	21-30
21	ARG	343127.69	5091483.34	2,482.22	16.62	2.96	3.40	2.01	WNW	51-60
22	ARG	343143.66	5091516.43	2,461.02	9.25	1.52	0.89	1.19	NW	21-30
23	ARG	343003.07	5091543.93	2,433.21	8.85	4.70	1.41	1.23	NNW	21-30
24	ARG	343132.70	5091449.96	2,512.24	9.19	5.48	4.75	1.39	WNW	31-40
25	ARG	343159.21	5091498.03	2,474.67	6.34	2.31	0.63	1.18	NNW	31-40
26	ARG	343021.88	5091543.94	2,437.46	4.95	9.45	3.81	1.16	WNW	11-20
27	ARG	343100.81	5091516.66	2,458.99	4.22	1.31	0.59	1.08	NW	21-30
28	ARG	343008.50	5091519.43	2,451.56	5.20	2.31	1.98	1.33	NNW	41-50
29	ARG	343084.86	5091533.45	2,447.58	3.63	2.76	1.62	0.96	W	21-30
30	ARG	343207.65	5091488.31	2,482.87	3.15	4.86	2.17	0.88	NNE	21-30
31	ARG	343013.27	5091548.36	2,434.77	3.57	1.52	0.46	1.01	NNW	21-30
32	ARG	343040.90	5091554.71	2,439.32	3.63	1.76	1.06	1.06	SW	11-20
33	ARG	343118.58	5091507.14	2,465.63	3.04	1.46	0.75	0.90	NNW	21-30
34	ARG	343191.45	5091496.42	2,479.54	3.45	1.85	0.37	1.06	NW	21-30

35	ARG	342991.30	5091542.23	2,432.62	3.36	3.12	1.66	1.04	NNW	31-40
36	ARG	343088.08	5091473.64	2,493.35	4.02	3.80	3.05	1.29	WNW	61-70
37	ARG	343034.99	5091548.09	2,442.00	2.79	4.78	2.57	1.13	SSW	31-40
38	ARG	343150.62	5091515.95	2,462.15	2.02	1.12	0.40	0.96	NNW	21-30
39	ARG	343178.63	5091508.97	2,472.97	2.14	0.94	0.63	1.10	WNW	31-40
40	ARG	343011.45	5091543.90	2,436.37	1.72	0.82	0.29	0.94	N	21-30
41	ARG	343043.75	5091524.63	2,454.45	1.65	1.64	0.32	0.96	W	21-30
42	ARG	342998.45	5091551.21	2,429.84	1.54	0.88	0.37	0.93	NW	21-30
43	ARG	342407.40	5091884.08	2,323.28	159.01	22.56	5.94	1.38	E	0-10
44	ARG	342397.74	5091893.65	2,319.03	36.68	9.47	4.33	1.57	W	11-20
45	ARG	342485.36	5091803.42	2,351.95	8.19	2.58	1.05	1.22	ENE	0-10
46	ARG	342285.43	5091910.82	2,317.77	7.90	5.21	3.87	1.30	NNW	41-50
47	ARG	342590.96	5091765.38	2,360.96	4.70	2.99	2.13	1.03	SW	21-30
48	ARG	342275.91	5091909.15	2,319.09	4.39	3.72	1.60	1.02	SW	21-30
49	ARG	342551.01	5091814.76	2,345.59	5.38	1.88	0.65	1.34	SSW	11-20
50	ARG	342554.59	5091811.04	2,346.74	4.43	3.17	0.67	1.25	WNW	11-20
51	ARG	342577.13	5091798.23	2,350.24	4.60	3.10	0.74	1.29	NNW	11-20
52	ARG	342519.50	5091827.80	2,342.28	4.63	2.66	0.90	1.33	NW	11-20
53	ARG	342494.62	5091838.42	2,338.30	3.32	1.68	0.46	1.16	W	21-30
54	ARG	342415.07	5091800.42	2,363.49	2.60	4.27	3.55	0.96	N	31-40
55	ARG	342597.82	5091780.70	2,355.31	2.34	1.94	0.53	0.88	NW	21-30
56	ARG	342442.02	5091865.28	2,330.96	4.17	2.75	0.54	1.64	WSW	21-30
57	ARG	342610.84	5091775.96	2,357.21	2.36	1.32	0.23	0.96	WSW	11-20
58	ARG	342261.69	5091960.65	2,300.40	2.46	1.34	0.76	1.00	NW	31-40
59	ARG	342607.76	5091774.37	2,357.34	1.96	1.04	0.12	0.88	WNW	11-20
60	ARG	342595.02	5091766.45	2,360.23	2.27	2.36	1.46	1.02	NNE	31-40
61	ARG	342521.44	5091818.44	2,345.02	2.32	1.64	0.57	1.05	ENE	21-30
62	ARG	342435.38	5091869.07	2,329.45	2.67	1.60	0.31	1.23	W	21-30
63	ARG	342300.85	5091956.55	2,299.45	2.18	2.74	1.12	1.03	NE	11-20
64	ARG	342417.22	5091872.33	2,326.72	1.91	1.97	0.68	0.92	NW	31-40
65	ARG	342505.97	5091832.44	2,340.88	1.91	1.03	0.34	0.94	WNW	11-20
66	ARG	342268.00	5091981.51	2,291.12	2.11	2.23	1.67	1.06	WSW	31-40
67	ARG	342252.38	5091986.57	2,289.37	2.25	2.62	0.95	1.15	E	21-30
68	ARG	342424.63	5091874.75	2,327.74	1.40	1.51	0.37	0.86	NW	11-20
69	ARG	342587.32	5091791.17	2,352.16	1.46	0.43	0.11	0.97	E	11-20
70	ARG	342541.51	5091819.64	2,344.39	1.45	0.74	0.28	0.96	NW	11-20
71	ARG	342273.82	5091955.04	2,303.58	1.53	1.23	1.00	1.22	WSW	41-50
72	ARG	342574.09	5091799.75	2,349.89	1.03	0.71	0.13	0.86	SSE	11-20
73	ARG	342536.72	5091762.99	2,369.48	1.01	4.50	2.95	0.84	WNW	41-50
74	ARG	342281.79	5091913.62	2,315.63	1.14	2.08	1.31	0.98	W	31-40
75	ARG	342466.19	5091848.05	2,335.15	1.06	0.96	0.20	0.96	S	11-20
76	ARG	342589.74	5091788.27	2,352.69	0.88	1.80	0.38	0.83	SE	11-20
77	ARG	342437.29	5091862.71	2,330.99	0.95	1.70	0.27	0.92	NW	31-40
78	ARG	342573.79	5091802.02	2,349.16	1.06	0.60	0.39	1.05	W	11-20
79	ARG	342294.04	5091906.04	2,319.08	1.17	2.03	1.92	1.24	E	31-40
80	ARG	342272.55	5091972.49	2,293.96	1.21	1.40	0.80	1.32	ENE	31-40
81	ARG	342407.56	5091851.00	2,333.25	1.80	1.96	1.13	2.05	NW	11-20
82	ARG	342267.43	5091936.47	2,309.50	0.73	0.44	0.66	0.94	ENE	41-50
83	ARG	342588.03	5091764.79	2,362.43	0.60	0.65	0.35	0.87	NNE	21-30
84	ARG	342275.72	5091940.72	2,309.63	1.05	3.27	1.02	1.59	WNW	31-40
85	ARG	342270.74	5091912.97	2,317.99	0.54	0.92	0.57	0.91	W	21-30

86	ARG	342279.50	5091946.40	2,307.73	0.50	0.54	0.40	1.00	NNW	31-40
87	ARG	342273.26	5091901.78	2,322.31	0.43	0.32	0.34	0.98	NNW	21-30
88	ARG	342385.49	5091892.77	2,318.45	1.09	1.88	1.02	2.90	NE	21-30
89	ARG	342314.97	5091903.42	2,317.37	0.37	1.04	1.16	1.08	NNE	31-40
90	ARG	342597.37	5091770.56	2,358.06	0.29	0.79	0.32	0.84	ENE	21-30
91	ARG	342266.04	5091983.25	2,289.33	0.32	0.42	0.50	1.02	WNW	21-30
92	ARG	342585.91	5091794.13	2,351.38	0.28	0.42	0.09	0.88	NW	11-20
93	ARG	344980.55	5089933.75	2,774.62	239.79	19.97	21.28	1.46	SSW	41-50
94	ARG	345011.96	5089903.88	2,759.16	180.49	11.90	9.26	1.47	SW	41-50
95	ARG	345360.01	5089655.20	2,771.74	142.70	10.67	8.11	1.28	SW	41-50
96	ARG	345290.78	5089720.47	2,774.00	69.12	9.46	7.46	1.13	SW	31-40
97	ARG	345279.96	5089726.07	2,770.98	35.23	7.19	4.21	1.10	SW	31-40
98	ARG	345349.91	5089707.86	2,792.15	35.65	3.27	3.50	1.48	SW	41-50
99	ARG	344942.71	5089946.63	2,756.42	27.42	5.02	2.70	1.28	SSW	31-40
100	ARG	345152.67	5089797.97	2,756.83	22.12	7.33	5.77	1.09	SW	51-60
101	ARG	344921.53	5089905.07	2,724.97	22.13	6.78	2.38	1.26	WSW	11-20
102	ARG	345099.88	5090073.85	2,845.43	31.19	26.15	14.69	1.99	W	21-30
103	ARG	345474.33	5089665.27	2,827.46	28.23	10.03	5.86	2.21	WSW	41-50
104	ARG	345451.69	5089687.24	2,834.88	16.93	1.18	2.68	1.61	SW	41-50
105	ARG	345301.22	5089705.73	2,767.31	12.40	2.03	1.47	1.23	SW	31-40
106	ARG	345401.88	5089694.16	2,815.17	12.53	3.64	2.74	1.26	WSW	41-50
107	ARG	344933.31	5089918.44	2,735.71	11.78	2.80	2.15	1.23	WSW	41-50
108	ARG	344939.54	5089891.26	2,726.12	16.16	5.32	2.23	1.92	WNW	11-20
109	ARG	345011.36	5090000.97	2,803.55	13.34	12.61	10.75	1.63	W	41-50
110	ARG	345534.20	5089664.67	2,858.44	9.41	3.29	3.16	1.18	SSW	41-50
111	ARG	345376.25	5089705.46	2,808.64	8.47	1.07	1.32	1.24	SW	31-40
112	ARG	344927.42	5089916.59	2,732.03	7.32	3.35	1.47	1.10	S	21-30
113	ARG	345176.45	5089799.04	2,778.11	8.06	1.59	1.40	1.30	SW	41-50
114	ARG	345306.88	5089699.04	2,764.66	6.54	2.65	2.98	1.06	SW	41-50
115	ARG	344957.93	5089939.71	2,763.44	6.97	1.61	3.46	1.16	SW	51-60
116	ARG	344945.35	5089943.61	2,756.73	6.80	1.10	1.42	1.16	SW	41-50
117	ARG	345034.51	5089997.87	2,814.58	11.42	14.08	8.58	2.02	S	31-40
118	ARG	345521.32	5089672.27	2,856.42	6.43	1.68	2.25	1.20	WSW	41-50
119	ARG	345063.76	5090033.04	2,831.88	20.18	12.08	7.86	3.76	W	31-40
120	ARG	345281.56	5089741.45	2,786.59	7.64	1.56	1.15	1.47	SW	41-50
121	ARG	345157.37	5090211.94	2,888.48	7.07	7.71	5.80	1.37	W	31-40
122	ARG	345367.57	5089703.87	2,802.07	5.86	2.54	2.05	1.17	WSW	41-50
123	ARG	344933.63	5089903.36	2,728.85	5.85	1.44	0.61	1.21	WSW	21-30
124	ARG	345461.24	5089675.79	2,828.55	5.70	1.03	1.14	1.22	SW	51-60
125	ARG	345405.73	5089692.35	2,814.86	5.61	1.48	3.06	1.20	SSW	41-50
126	ARG	345148.01	5090145.60	2,882.35	12.74	14.07	6.82	2.78	SE	41-50
127	ARG	345105.21	5089838.90	2,767.99	4.91	2.30	2.33	1.08	SSW	41-50
128	ARG	345142.52	5090133.00	2,877.34	8.35	11.28	6.65	1.85	SE	41-50
129	ARG	345310.11	5089699.97	2,767.86	5.26	1.12	0.88	1.20	SW	31-40
130	ARG	345338.40	5089712.19	2,790.97	4.56	0.76	0.94	1.13	SW	41-50
131	ARG	345116.59	5090094.98	2,861.54	8.01	8.85	7.81	2.30	E	51-60
132	ARG	344920.42	5089921.68	2,733.78	4.45	4.29	1.33	1.29	SSW	21-30
133	ARG	345126.63	5090124.24	2,867.06	5.17	6.28	3.29	1.58	WNW	41-50
134	ARG	345483.96	5089700.76	2,859.91	3.33	0.64	1.37	1.06	SW	31-40
135	ARG	345003.61	5089973.04	2,802.69	14.52	11.18	7.65	4.62	WNW	61-70
136	ARG	345448.16	5089685.48	2,830.61	3.61	0.97	0.87	1.25	SW	41-50

137	ARG	345333.16	5089711.80	2,786.38	3.21	0.65	0.85	1.11	SSW	51-60
138	ARG	345485.08	5089687.03	2,848.00	2.94	0.78	1.53	1.05	SW	41-50
139	ARG	345129.84	5090115.71	2,871.18	5.09	11.27	6.35	1.86	WNW	21-30
140	ARG	344986.18	5089924.87	2,763.98	2.70	1.69	1.48	1.07	SW	41-50
141	ARG	345134.78	5090084.34	2,848.61	6.29	5.73	4.89	2.50	S	31-40
142	ARG	345028.54	5089883.81	2,755.24	2.94	0.84	0.63	1.19	SW	51-60
143	ARG	345129.44	5089811.54	2,757.26	2.84	0.90	0.66	1.19	SW	51-60
144	ARG	345153.32	5090131.75	2,870.87	6.66	6.90	6.22	2.87	SE	31-40
145	ARG	345112.24	5089831.68	2,766.70	2.47	0.71	0.60	1.08	SW	41-50
146	ARG	345147.91	5089805.67	2,765.33	2.78	0.61	0.77	1.21	SSW	51-60
147	ARG	345074.10	5090041.95	2,838.11	4.25	8.02	5.19	1.88	WSW	21-30
148	ARG	345048.71	5090021.43	2,821.83	3.09	7.17	6.28	1.56	WNW	31-40
149	ARG	344928.02	5089911.31	2,729.89	2.23	0.79	0.45	1.13	S	31-40
150	ARG	345403.62	5089637.36	2,777.63	2.04	0.95	0.71	1.05	SW	31-40
151	ARG	345398.00	5089636.97	2,774.93	2.05	0.68	0.46	1.07	SSW	41-50
152	ARG	345343.12	5089710.46	2,792.00	1.85	0.63	1.60	1.03	SW	51-60
153	ARG	344996.59	5089960.49	2,797.79	2.71	6.98	2.78	1.63	WNW	51-60
154	ARG	345479.26	5089687.69	2,845.35	1.73	0.34	0.56	1.10	SSW	41-50
155	ARG	344065.42	5091216.48	2,583.20	1,432.48	63.52	24.55	2.17	WNW	21-30
156	ARG	344467.98	5091599.55	2,879.52	504.17	47.74	38.06	2.48	S	31-40
157	ARG	344071.10	5091336.30	2,621.43	426.20	8.73	19.44	2.44	WSW	41-50
158	ARG	344131.19	5091188.71	2,593.86	135.70	20.24	9.42	2.17	WSW	31-40
159	ARG	344116.40	5091190.74	2,592.10	92.55	16.44	7.88	1.85	WSW	21-30
160	ARG	344287.13	5091398.76	2,739.80	81.46	30.39	28.29	2.86	SSE	31-40
161	ARG	344134.08	5091288.65	2,652.81	47.52	3.78	6.76	1.68	SW	41-50
162	ARG	344048.31	5091240.99	2,574.73	59.56	21.22	8.80	2.17	W	31-40
163	ARG	344126.26	5091190.90	2,597.35	46.68	7.68	4.46	1.93	W	31-40
164	ARG	344192.48	5091321.59	2,710.13	57.39	47.68	29.86	2.83	WNW	31-40
165	ARG	344035.36	5091380.29	2,622.14	46.82	15.59	8.66	2.66	WSW	41-50
166	ARG	344118.47	5091280.95	2,637.91	32.24	7.89	5.94	2.04	WSW	31-40
167	ARG	344150.92	5091173.29	2,595.27	34.47	2.25	1.47	2.18	SW	11-20
168	ARG	344207.88	5091324.14	2,699.61	24.21	3.10	2.90	1.94	S	31-40
169	ARG	344126.32	5091276.19	2,640.48	20.93	2.55	1.96	1.74	WSW	41-50
170	ARG	344138.78	5091274.37	2,647.21	18.81	1.74	3.70	1.91	SSW	31-40
171	ARG	344004.16	5091368.20	2,588.34	49.73	25.27	9.54	5.40	WSW	31-40
172	ARG	344112.79	5091303.35	2,649.48	14.94	1.60	2.07	1.74	WSW	41-50
173	ARG	344167.87	5091474.13	2,721.34	18.37	7.42	6.39	2.33	SSE	41-50
174	ARG	344227.37	5091191.03	2,611.64	17.69	9.32	6.32	2.35	S	41-50
175	ARG	344121.03	5091274.06	2,635.19	9.34	2.47	2.15	1.71	SW	41-50
176	ARG	344142.53	5091169.17	2,592.41	9.68	2.97	2.22	1.83	SW	21-30
177	ARG	344008.66	5091346.08	2,582.42	21.00	10.21	8.01	4.15	WSW	51-60
178	ARG	344153.09	5091274.32	2,652.37	7.80	1.52	1.86	1.70	SSW	41-50
179	ARG	344157.73	5091168.99	2,595.41	7.55	1.53	0.87	1.74	WSW	21-30
180	ARG	344123.71	5091201.61	2,599.96	7.47	3.80	1.34	1.74	WSW	31-40
181	ARG	344181.38	5091313.52	2,693.77	9.45	9.93	5.33	2.21	WNW	31-40
182	ARG	344141.47	5091181.46	2,595.91	7.32	6.72	2.96	1.77	SW	31-40
183	ARG	344095.85	5091280.40	2,623.03	8.77	7.36	7.78	2.15	WSW	51-60
184	ARG	344042.98	5091376.17	2,625.09	12.50	3.85	3.26	3.43	SSE	31-40
185	ARG	344080.66	5091337.63	2,635.66	10.49	7.08	3.65	3.18	SW	41-50
186	ARG	344131.76	5091278.26	2,645.47	5.48	0.84	0.64	1.78	WSW	41-50
187	ARG	344502.23	5091596.92	2,890.39	5.56	4.31	4.54	1.81	SSW	31-40

188	ARG	344129.89	5091200.17	2,601.70	4.84	2.32	2.36	1.69	WSW	41-50
189	ARG	344167.86	5091163.93	2,595.69	5.75	1.58	1.35	2.08	W	21-30
190	ARG	344282.21	5091397.70	2,742.31	8.24	13.47	7.97	3.05	W	31-40
191	ARG	343978.43	5091356.87	2,565.99	19.10	6.53	5.70	7.24	SW	31-40
192	ARG	344001.73	5091308.25	2,565.75	10.92	8.62	4.59	4.40	SW	41-50
193	ARG	344164.08	5091306.84	2,683.49	6.32	5.76	3.49	2.72	WNW	31-40
194	ARG	344450.13	5091561.37	2,858.40	4.36	3.96	3.20	1.88	S	41-50
195	ARG	344116.76	5091262.09	2,624.95	4.41	2.40	0.76	2.03	SW	31-40
196	ARG	344150.84	5091305.94	2,673.02	3.37	2.58	3.54	1.95	NNW	41-50
197	MDG	339158.53	5083579.42	2,343.28	8,037.17	63.71	81.50	4.02	NNE	61-70
198	MDG	339249.49	5083889.87	2,270.87	13,591.78	58.94	89.90	6.90	ENE	41-50
199	MDG	339141.76	5083615.86	2,375.16	1,199.46	29.06	29.18	4.69	SSE	51-60
200	MDG	339119.84	5083594.37	2,400.40	857.07	21.44	28.03	3.81	N	71-80
201	MDG	339230.92	5083784.98	2,301.57	447.91	15.00	18.98	3.02	NE	41-50
202	MDG	339199.00	5083519.49	2,356.02	367.15	14.62	23.04	3.04	NNE	41-50
203	MDG	339263.48	5083723.12	2,291.34	592.57	23.25	42.05	5.78	ESE	41-50
204	MDG	339214.21	5083830.10	2,311.32	281.94	11.68	11.13	3.13	ENE	41-50
205	MDG	339291.20	5083836.61	2,243.28	233.61	10.80	11.46	3.15	NE	61-70
206	MDG	339266.06	5083641.07	2,284.21	253.86	10.07	9.82	3.84	NNE	41-50
207	MDG	339246.72	5083629.41	2,312.48	177.72	10.43	7.26	3.49	ENE	41-50
208	MDG	339189.23	5083731.72	2,345.38	188.26	12.42	8.73	3.84	NNE	41-50
209	MDG	339286.56	5083795.28	2,249.98	154.68	7.55	7.59	3.18	NNE	51-60
210	MDG	339144.77	5083628.30	2,390.24	204.81	10.43	12.05	4.23	SE	51-60
211	MDG	339302.88	5083808.71	2,228.13	131.92	6.06	5.99	2.78	ENE	21-30
212	MDG	339227.38	5083523.77	2,334.70	183.55	7.76	18.84	3.91	NW	51-60
213	MDG	339226.79	5083747.35	2,323.24	157.91	8.00	11.52	4.07	S	61-70
214	MDG	339278.42	5083716.43	2,266.91	108.58	11.00	6.31	3.14	NE	51-60
215	MDG	339259.85	5083656.11	2,288.26	107.78	11.36	8.41	3.12	NNE	41-50
216	MDG	339239.86	5083613.14	2,301.93	66.36	5.63	11.71	2.77	SE	51-60
217	MDG	339147.44	5083603.27	2,364.56	70.00	5.55	8.53	3.20	NE	41-50
218	MDG	339226.73	5083690.99	2,329.26	66.49	4.54	8.50	3.21	NE	41-50
219	MDG	339266.95	5083603.52	2,279.11	58.95	6.85	4.07	3.25	N	41-50
220	MDG	339243.20	5083589.97	2,300.19	73.41	10.12	20.09	4.30	NNW	61-70
221	MDG	339167.61	5083601.53	2,350.34	54.38	7.33	4.71	3.59	NE	51-60
222	MDG	339186.23	5083612.84	2,339.73	43.17	2.47	2.81	3.01	SSE	41-50
223	MDG	339272.28	5083621.15	2,277.96	42.30	5.36	4.13	2.97	NE	51-60
224	MDG	339279.33	5083789.50	2,257.97	56.39	6.55	6.82	4.12	NE	31-40
225	MDG	339226.36	5083769.53	2,318.85	34.86	3.82	5.68	2.61	NE	51-60
226	MDG	339239.68	5083564.29	2,301.13	41.47	6.78	2.95	3.21	SSE	31-40
227	MDG	338924.59	5083628.46	2,581.98	57.70	10.26	13.53	4.48	ESE	61-70
228	MDG	339295.12	5083798.16	2,238.41	34.14	2.76	4.23	2.72	NE	61-70
229	MDG	339283.71	5083744.28	2,263.76	30.07	4.87	2.49	2.77	E	41-50
230	MDG	339254.05	5083579.40	2,297.31	29.81	6.59	5.12	2.79	E	41-50
231	MDG	339274.60	5083931.87	2,227.07	34.49	6.67	5.65	3.25	E	51-60
232	MDG	339232.25	5083664.50	2,323.60	23.28	2.17	2.21	2.61	ENE	51-60
233	MDG	339226.74	5083595.45	2,308.96	28.19	5.74	6.09	3.19	NNE	41-50
234	MDG	339279.92	5083691.64	2,268.47	24.85	8.91	1.63	3.18	ENE	51-60
235	MDG	339231.19	5083569.79	2,310.46	22.46	5.07	2.83	3.06	ESE	31-40
236	MDG	339259.37	5083628.84	2,293.04	17.89	4.00	2.20	2.73	E	51-60
237	MDG	339277.41	5083771.24	2,272.91	15.66	1.66	2.82	2.54	E	51-60
238	MDG	339257.29	5083540.93	2,302.65	18.82	2.69	4.39	3.22	NNW	61-70

239	MDG	339236.63	5083743.95	2,314.39	17.53	3.70	4.26	3.05	S	61-70
240	MDG	339256.61	5083771.80	2,299.40	15.67	1.98	4.39	2.92	NNE	51-60
241	MDG	339210.13	5083781.88	2,326.62	14.17	4.22	2.31	2.78	NE	41-50
242	MDG	338924.55	5083608.48	2,557.78	16.28	4.54	7.10	3.41	ESE	71-80
243	MDG	339270.56	5083989.59	2,207.62	13.32	3.30	3.71	2.92	ENE	31-40
244	MDG	339260.08	5083283.11	2,374.71	14.96	6.25	4.93	3.38	ESE	51-60
245	MDG	339212.30	5083601.09	2,315.75	10.17	4.20	1.56	2.79	E	21-30
246	MDG	339307.20	5083702.36	2,238.54	10.63	4.70	1.05	3.22	SSW	11-20
247	MDG	339280.74	5083695.35	2,264.43	9.23	2.85	1.55	2.83	E	41-50
248	MDG	339245.15	5083578.86	2,309.82	9.11	4.53	5.29	2.81	SE	41-50
249	MDG	339257.76	5083777.82	2,285.33	9.46	1.28	2.68	3.04	NNW	61-70
250	MDG	339251.90	5083555.22	2,291.94	7.93	4.27	1.34	2.72	ENE	31-40
251	MDG	338917.76	5083617.59	2,587.21	16.18	5.05	5.44	8.05	ENE	71-80
252	MDG	339302.44	5084146.86	2,204.97	1,071.38	26.70	39.62	2.71	E	31-40
253	MDG	339254.49	5084717.36	2,293.70	378.70	9.79	13.89	2.85	ESE	41-50
254	MDG	339293.11	5084167.75	2,202.18	239.98	13.99	14.45	2.19	ESE	51-60
255	MDG	339274.15	5084134.56	2,218.38	243.62	5.87	15.32	2.39	E	41-50
256	MDG	339246.23	5084191.75	2,266.15	174.43	12.14	11.65	2.12	E	61-70
257	MDG	339264.59	5084177.91	2,244.38	231.61	20.29	20.44	3.02	ESE	51-60
258	MDG	339261.73	5084694.24	2,273.29	250.32	14.09	19.69	4.29	S	51-60
259	MDG	339283.43	5084179.03	2,224.85	109.01	10.48	17.22	2.16	ENE	51-60
260	MDG	339299.79	5084754.62	2,264.02	84.50	5.40	6.62	2.16	E	41-50
261	MDG	339282.81	5084155.35	2,214.60	74.27	9.24	5.92	2.40	SE	51-60
262	MDG	339292.64	5084731.54	2,265.07	25.02	2.69	2.50	1.96	ESE	31-40
263	MDG	339270.13	5084156.47	2,231.48	42.63	7.62	9.05	4.10	SSE	51-60
264	MDG	339247.31	5084162.76	2,257.63	19.16	10.67	14.84	5.04	SE	71-80
265	MDG	339295.90	5084257.31	2,214.72	14.70	7.74	5.95	4.33	ENE	61-70
266	MDG	339282.45	5084172.21	2,218.86	6.34	0.95	1.51	1.98	NE	51-60
267	MDG	339258.60	5084193.96	2,244.99	5.94	1.59	2.24	2.10	ESE	41-50
268	MDG	339275.80	5084164.34	2,227.62	3.98	1.16	2.00	1.86	ENE	41-50
269	MDG	339310.40	5084142.38	2,190.91	3.42	1.02	0.74	2.02	E	11-20
270	MDG	339220.67	5084631.32	2,265.80	5,124.54	72.76	84.65	5.92	E	51-60
271	MDG	339394.45	5084786.25	2,205.12	1,560.07	29.16	18.33	4.15	ESE	31-40
272	MDG	339402.88	5084797.52	2,205.73	1,363.67	22.98	18.37	4.14	E	31-40
273	MDG	339280.84	5084610.81	2,241.63	970.58	21.02	17.87	3.72	E	71-80
274	MDG	339321.45	5084676.57	2,223.30	738.88	16.05	14.69	3.62	E	31-40
275	MDG	339254.15	5084503.69	2,243.34	940.03	11.97	16.66	5.59	NE	51-60
276	MDG	339423.73	5084845.21	2,212.28	508.94	11.90	15.64	3.78	ENE	31-40
277	MDG	339457.85	5084966.07	2,244.09	313.27	9.88	19.39	3.65	ENE	51-60
278	MDG	339359.12	5084693.44	2,196.42	340.24	11.29	7.22	4.05	E	11-20
279	MDG	339439.23	5084861.15	2,210.18	315.43	7.74	12.19	3.78	SE	41-50
280	MDG	339606.28	5085171.43	2,229.53	336.65	16.40	16.19	4.42	ESE	41-50
281	MDG	339257.02	5084623.92	2,278.65	310.53	10.92	15.17	4.22	E	61-70
282	MDG	339192.63	5084617.07	2,313.66	465.96	7.43	22.33	7.03	SE	31-40
283	MDG	339433.64	5084828.51	2,202.07	198.44	3.77	12.43	3.28	ESE	41-50
284	MDG	339713.86	5085330.78	2,192.25	191.14	18.16	9.87	3.33	SE	41-50
285	MDG	339378.99	5084911.08	2,265.78	203.26	4.60	6.31	3.68	SE	31-40
286	MDG	339338.04	5084700.61	2,209.44	171.75	5.71	12.20	3.34	E	31-40
287	MDG	339522.70	5085063.43	2,252.98	188.19	12.71	11.55	4.08	ESE	41-50
288	MDG	339525.91	5085056.27	2,241.88	189.68	6.97	5.71	4.67	SSE	31-40
289	MDG	339474.22	5084920.22	2,208.24	146.27	13.31	7.23	4.30	ENE	31-40

290	MDG	339189.85	5084637.97	2,326.17	218.17	6.02	10.88	7.60	ENE	31-40
291	MDG	339364.96	5084730.95	2,209.07	90.30	4.17	4.73	3.22	SE	41-50
292	MDG	339279.09	5084579.25	2,229.04	92.71	4.78	7.55	3.50	ENE	51-60
293	MDG	339283.95	5084656.04	2,237.25	87.12	2.83	7.08	3.35	ENE	41-50
294	MDG	339581.91	5084979.55	2,172.28	103.42	13.65	5.93	4.25	ESE	21-30
295	MDG	339409.18	5084726.49	2,175.07	93.52	14.39	7.64	4.11	E	41-50
296	MDG	339371.66	5084727.61	2,201.85	70.49	3.25	3.50	3.20	SE	41-50
297	MDG	339587.04	5085172.76	2,249.16	76.68	6.90	5.80	3.61	ESE	31-40
298	MDG	339457.20	5084974.00	2,255.25	70.39	4.08	7.20	3.49	SE	41-50
299	MDG	339565.23	5084961.26	2,171.64	59.17	7.03	2.23	3.57	ENE	21-30
300	MDG	339333.24	5084673.93	2,209.13	45.29	3.20	4.07	3.12	E	31-40
301	MDG	339269.19	5084622.54	2,254.61	47.74	5.88	4.37	3.33	E	51-60
302	MDG	339272.97	5084656.95	2,247.00	40.91	2.69	4.73	3.13	NE	41-50
303	MDG	339337.91	5084681.70	2,207.60	40.27	2.04	2.66	3.30	SE	41-50
304	MDG	339840.39	5085452.98	2,120.23	40.28	7.49	4.50	3.49	ENE	21-30
305	MDG	339589.29	5085143.80	2,238.27	34.74	3.12	2.73	3.22	SE	41-50
306	MDG	339344.74	5084672.28	2,201.06	29.89	2.06	4.05	3.09	ESE	31-40
307	MDG	339275.50	5084662.14	2,243.10	23.35	1.29	2.19	3.06	NE	31-40
308	MDG	339416.78	5084746.32	2,168.84	29.63	9.44	5.37	3.96	ESE	31-40
309	MDG	339552.76	5084940.96	2,166.53	29.52	7.42	3.07	4.10	E	21-30
310	MDG	339264.98	5084409.47	2,228.18	25.04	3.37	3.19	3.54	E	61-70
311	MDG	339783.46	5085467.25	2,161.91	24.51	7.09	3.20	3.50	E	31-40
312	MDG	339372.29	5084710.57	2,194.12	23.46	5.65	3.09	3.41	ESE	31-40
313	MDG	339578.81	5085185.97	2,263.61	23.33	4.62	4.95	3.64	SSW	41-50
314	MDG	339397.86	5084736.55	2,185.04	25.07	6.55	3.65	4.41	S	31-40
315	MDG	339404.47	5084698.66	2,165.95	22.79	5.92	6.28	4.22	SE	31-40
316	MDG	339624.94	5085166.29	2,213.22	18.27	1.57	2.91	3.38	ESE	31-40
317	MDG	339563.05	5085006.68	2,188.95	15.15	2.92	0.81	3.11	NE	11-20
318	MDG	339403.89	5084738.31	2,181.38	14.87	3.42	1.87	3.14	ESE	61-70
319	MDG	339392.93	5084770.49	2,195.92	6.63	0.75	0.85	3.10	E	51-60
320	MDG	339337.88	5086568.79	2,111.70	45,779.46	99.12	82.92	7.39	NE	31-40
321	MDG	339540.11	5086514.34	2,074.32	16,419.72	44.97	47.39	12.82	NE	31-40
322	MDG	339334.78	5086632.60	2,049.56	3,051.30	60.36	40.52	5.37	N	31-40
323	MDG	339554.46	5086669.33	1,947.26	1,563.83	31.69	14.37	3.93	NE	21-30
324	MDG	339098.44	5086813.19	2,032.86	1,268.87	14.35	23.20	4.42	NNE	61-70
325	MDG	339563.69	5086563.48	2,033.12	1,315.35	22.43	29.99	4.99	NE	51-60
326	MDG	339191.07	5086653.81	2,106.76	830.38	16.91	17.02	4.61	ENE	41-50
327	MDG	339310.09	5086660.21	2,060.39	833.99	18.58	24.48	7.10	E	41-50
328	MDG	339407.84	5086619.94	2,060.20	544.12	17.09	13.33	4.67	NE	61-70
329	MDG	339356.85	5086618.80	2,072.70	422.30	14.01	15.10	4.25	NW	51-60
330	MDG	339254.03	5086684.27	2,043.67	393.36	12.93	11.07	4.59	NE	31-40
331	MDG	339517.51	5086701.48	1,950.88	293.30	12.03	7.85	3.70	NE	21-30
332	MDG	339068.33	5086850.72	2,021.02	297.99	10.56	12.77	4.03	SE	41-50
333	MDG	339080.92	5086831.14	2,020.69	366.53	10.64	11.00	5.28	NNE	51-60
334	MDG	338815.50	5087332.25	1,891.70	194.78	12.89	6.13	3.63	NE	31-40
335	MDG	339245.65	5086623.39	2,104.08	190.22	8.02	11.91	3.97	N	41-50
336	MDG	339501.72	5086680.93	1,971.16	295.56	13.09	7.05	6.49	E	21-30
337	MDG	339482.83	5086692.51	1,975.23	232.52	9.20	5.21	5.14	NNE	51-60
338	MDG	339501.23	5086589.40	2,041.97	184.33	7.04	5.93	4.21	N	41-50
339	MDG	339149.62	5086564.90	2,169.36	166.71	6.33	8.10	3.90	ENE	41-50
340	MDG	339081.43	5086855.15	2,004.04	144.96	7.30	8.76	4.03	NNE	51-60

341	MDG	339213.32	5086576.19	2,137.83	151.76	6.05	5.48	4.27	NNE	41-50
342	MDG	338773.18	5087986.75	1,795.62	159.08	10.12	3.88	4.78	SE	0-10
343	MDG	339132.42	5086807.27	2,019.14	121.52	7.23	7.88	4.18	NE	71-80
344	MDG	339283.13	5086769.17	1,977.13	91.27	9.66	6.69	3.29	NNE	31-40
345	MDG	338687.48	5087356.92	1,990.25	91.30	6.98	2.95	3.73	E	21-30
346	MDG	339253.86	5086631.00	2,101.81	84.69	5.53	4.81	3.62	NW	51-60
347	MDG	339168.53	5086784.18	2,022.54	100.67	9.40	6.56	4.44	SW	51-60
348	MDG	339249.27	5086674.42	2,054.89	69.64	5.39	3.91	3.42	NNE	31-40
349	MDG	339569.99	5086650.87	1,946.50	81.62	7.41	5.01	4.14	E	21-30
350	MDG	339527.01	5086698.09	1,950.44	63.95	7.59	4.09	3.67	NNE	41-50
351	MDG	339511.23	5086587.78	2,040.09	64.74	2.85	4.05	4.03	NW	41-50
352	MDG	339555.43	5086652.31	1,951.70	62.53	6.39	4.34	4.18	ESE	41-50
353	MDG	339127.70	5086805.70	2,025.38	38.24	3.94	5.00	3.89	SSE	41-50
354	MDG	339512.26	5086686.49	1,963.18	28.11	4.59	2.28	3.86	NE	41-50
355	MDG	339548.30	5086664.35	1,945.44	30.28	2.76	2.74	4.57	NE	21-30
356	MDG	339507.84	5086685.70	1,965.12	15.91	1.79	1.47	3.21	NE	31-40
357	MDG	339403.84	5086630.02	2,052.15	8.17	1.56	1.08	3.25	NE	51-60
358	MDG	339558.98	5086664.69	1,942.02	6.40	1.08	0.29	3.34	ENE	21-30
359	MDG	338954.76	5086970.94	1,993.81	109.10	8.71	9.46	1.94	ENE	51-60
360	MDG	338954.05	5086952.21	2,015.11	42.89	4.86	6.23	2.07	NNW	51-60
361	MDG	338954.51	5086996.80	1,978.86	26.95	2.88	5.31	1.70	NNE	61-70
362	MDG	338955.05	5087001.65	1,970.86	18.69	2.13	2.61	1.75	NNE	41-50
363	MDG	338968.98	5086970.25	1,982.54	14.09	1.73	3.74	1.85	N	51-60
364	MDG	338966.59	5086967.03	1,990.97	4.82	0.67	1.40	1.69	W	61-70
365	MDG	339406.26	5088082.88	1,899.68	44,383.64	83.78	71.56	10.99	SW	51-60
366	MDG	339410.26	5088389.61	1,893.97	34,471.59	50.44	88.06	13.52	SSW	51-60
367	MDG	339342.68	5088297.32	1,791.25	12,588.30	83.41	26.76	6.04	WSW	21-30
368	MDG	339345.14	5088208.73	1,780.23	2,474.11	35.88	15.60	6.38	WSW	31-40
369	MDG	339429.41	5087899.56	1,925.51	1,470.65	19.02	25.07	7.04	NW	41-50
370	MDG	339347.20	5088227.95	1,798.20	947.43	19.60	16.34	5.87	W	31-40
371	MDG	339389.60	5088296.62	1,856.12	1,041.52	31.72	15.61	8.20	NW	51-60
372	MDG	339383.81	5088204.72	1,845.19	895.65	37.54	31.55	7.05	WNW	51-60
373	MDG	339408.30	5088221.01	1,866.34	1,047.74	17.31	23.79	9.78	NW	51-60
374	MDG	339383.93	5088355.95	1,832.18	1,086.02	10.53	20.64	10.21	W	41-50
375	MDG	339443.83	5088376.37	1,879.58	2,670.67	43.08	25.35	28.97	WSW	31-40
376	MDG	339325.87	5088156.88	1,780.62	503.69	11.97	7.26	6.30	WNW	31-40
377	MDG	339460.36	5088348.35	1,906.52	824.33	12.07	11.03	11.12	NNW	51-60
378	MDG	339317.79	5088143.04	1,781.07	370.91	12.23	6.42	6.13	WNW	41-50
379	MDG	339415.08	5088368.91	1,848.22	1,200.09	19.94	23.96	27.54	NW	31-40
380	MDG	339392.16	5088362.06	1,851.61	375.97	12.92	13.71	10.00	W	51-60
381	MDG	339407.41	5087955.30	1,898.17	274.64	19.80	6.10	7.95	WSW	51-60
382	MDG	339412.97	5088354.40	1,870.53	202.40	9.65	9.45	7.96	NW	61-70
383	MDG	339381.59	5087862.15	1,871.78	188.97	7.74	8.78	7.69	NNW	51-60
384	MDG	339419.83	5088337.13	1,882.02	350.18	15.51	18.68	14.33	WSW	51-60
385	MDG	339331.46	5088157.37	1,798.90	106.69	12.63	4.98	6.20	NW	31-40
386	MDG	339373.72	5088215.02	1,826.31	84.49	8.37	6.75	6.72	W	61-70
387	MDG	339327.10	5088122.82	1,791.60	71.74	3.93	3.55	5.77	WNW	31-40
388	MDG	339372.46	5088374.99	1,832.13	90.41	8.25	10.90	7.38	W	51-60
389	MDG	339397.96	5087920.88	1,878.81	95.05	8.17	11.48	7.82	N	61-70
390	MDG	339425.11	5088514.20	1,889.69	86.29	13.73	13.50	7.42	NNW	21-30
391	MDG	339387.00	5088340.44	1,843.22	217.10	8.41	13.37	21.46	SW	41-50

392	MDG	339417.41	5087877.27	1,911.47	75.58	6.12	7.80	7.89	SSW	61-70
393	MDG	339333.94	5088171.45	1,793.53	57.11	11.91	5.90	6.27	WNW	31-40
394	MDG	339391.70	5088205.85	1,866.93	55.54	10.26	5.84	6.41	WNW	61-70
395	MDG	339366.17	5088150.03	1,843.50	56.72	7.47	5.62	6.57	WSW	51-60
396	MDG	339370.39	5088204.58	1,826.69	64.32	8.60	6.25	7.53	WNW	51-60
397	MDG	339366.63	5088183.27	1,818.23	46.43	4.33	3.19	6.03	N	41-50
398	MDG	339364.91	5088156.17	1,840.41	51.28	8.73	4.82	6.77	W	51-60
399	MDG	339395.80	5088267.31	1,859.46	47.03	4.18	9.02	6.45	SSW	71-80
400	MDG	339411.97	5087930.20	1,899.98	38.82	6.16	4.36	5.86	WSW	41-50
401	MDG	339317.39	5087786.87	1,841.18	48.76	5.96	6.33	7.76	W	31-40
402	MDG	339386.43	5088350.73	1,852.31	54.23	1.56	6.62	9.54	S	71-80
403	MDG	339359.70	5088132.49	1,836.67	30.25	6.05	4.88	6.02	NW	51-60
404	MDG	339282.35	5087712.30	1,819.28	33.54	11.52	3.18	7.17	E	0-10
405	MDG	339282.44	5088431.05	1,759.81	38.36	8.34	3.03	8.42	W	21-30
406	MDG	339405.09	5088300.20	1,874.69	26.31	2.73	5.11	6.25	WNW	51-60
407	MDG	339355.08	5088373.75	1,819.86	25.67	3.66	3.21	6.43	NNW	51-60
408	MDG	339375.34	5088459.41	1,833.36	34.44	6.99	4.59	9.14	NW	51-60
409	MDG	339404.21	5087899.97	1,906.18	22.64	2.79	2.93	6.38	WNW	41-50
410	MDG	339401.64	5088342.33	1,852.65	19.48	4.21	4.61	6.53	W	31-40
411	MDG	339372.24	5088291.06	1,829.22	18.23	3.30	5.13	6.17	WSW	41-50
412	MDG	339396.55	5088232.28	1,864.56	22.86	2.39	4.64	8.08	WNW	51-60
413	MDG	339391.09	5088208.73	1,861.86	18.55	4.52	3.85	6.95	WNW	61-70
414	MDG	339350.14	5088483.68	1,812.80	24.69	3.31	3.52	10.76	W	51-60
415	MDG	339367.44	5088477.69	1,840.64	10.32	3.49	5.06	5.87	W	51-60
416	MDG	339388.73	5088348.75	1,845.47	27.08	2.07	6.62	16.26	SSW	61-70
417	MDG	339336.55	5088366.03	1,809.30	9.86	3.97	2.73	5.92	WNW	51-60
418	MDG	339372.41	5088194.11	1,826.03	11.16	3.06	4.16	6.96	WNW	41-50
419	MDG	339398.08	5088368.20	1,844.30	37.13	2.84	3.90	23.64	NW	41-50
420	MDG	340081.56	5087148.86	1,998.05	12,429.09	56.37	29.58	7.62	W	21-30
421	MDG	340272.35	5087057.88	2,052.48	13,453.81	84.04	85.21	9.26	WSW	11-20
422	MDG	339953.11	5087240.48	1,991.98	6,953.30	32.14	33.56	7.88	WSW	51-60
423	MDG	340415.59	5086931.08	2,125.33	4,317.90	32.71	27.71	6.23	S	41-50
424	MDG	340026.81	5087168.12	1,964.71	3,454.44	48.34	36.80	5.14	SSW	31-40
425	MDG	340339.46	5086847.27	2,039.70	3,495.94	17.59	39.65	7.03	W	51-60
426	MDG	339988.15	5087178.24	1,980.67	1,918.19	29.38	34.27	4.90	SSE	41-50
427	MDG	340355.15	5086761.64	2,024.94	1,697.17	20.74	26.86	5.04	WSW	41-50
428	MDG	340575.88	5086575.19	2,100.11	2,376.92	33.77	30.95	7.21	SSW	31-40
429	MDG	340032.56	5087180.83	2,000.09	1,650.75	13.18	22.08	5.28	SSE	51-60
430	MDG	340499.50	5086595.29	2,054.52	1,310.10	16.61	20.76	4.49	WSW	31-40
431	MDG	339921.34	5087252.12	1,984.38	969.75	15.20	13.81	5.92	SSE	51-60
432	MDG	340067.59	5087107.27	1,969.90	418.06	11.95	10.55	4.77	WSW	21-30
433	MDG	340432.38	5087071.76	2,143.57	2,062.60	24.12	16.29	23.68	SSW	31-40
434	MDG	339833.17	5087282.61	1,978.73	403.73	12.85	12.22	4.95	SW	11-20
435	MDG	340411.01	5087063.51	2,123.64	334.09	12.93	13.21	4.90	SW	41-50
436	MDG	339901.78	5087256.79	1,979.92	299.51	14.05	15.34	5.02	SSW	41-50
437	MDG	340485.75	5086655.63	2,078.27	378.09	18.45	11.39	6.78	S	51-60
438	MDG	339987.32	5087228.36	2,005.87	255.02	6.33	6.12	4.86	WSW	51-60
439	MDG	340365.33	5086896.21	2,077.55	236.61	2.90	13.87	5.29	SSW	51-60
440	MDG	340311.30	5086964.01	2,057.64	169.85	22.27	4.78	5.09	WSW	61-70
441	MDG	340342.82	5086947.11	2,085.70	130.38	10.92	12.49	4.51	NW	51-60
442	MDG	340037.25	5087192.51	2,008.37	113.78	4.47	7.92	4.45	SW	41-50

443	MDG	340218.58	5087008.34	2,015.66	122.18	8.57	8.80	4.88	SSE	41-50
444	MDG	340193.65	5087020.47	2,006.89	83.21	3.37	2.96	4.29	WSW	51-60
445	MDG	340190.47	5086953.90	1,973.16	75.56	7.28	4.00	4.71	SSW	21-30
446	MDG	339715.65	5087292.19	1,945.61	94.02	8.81	2.41	5.88	SSE	0-10
447	MDG	340353.20	5086879.90	2,042.21	65.85	4.02	4.05	5.20	SW	31-40
448	MDG	340448.16	5086612.48	2,032.88	44.81	3.06	2.10	4.18	WSW	31-40
449	MDG	340377.28	5086834.07	2,079.42	44.55	6.09	5.11	4.28	W	41-50
450	MDG	340040.32	5087125.01	1,972.48	52.43	8.12	6.92	5.23	SW	41-50
451	MDG	340329.69	5086829.05	2,018.66	39.79	3.68	4.63	4.21	W	51-60
452	MDG	339995.72	5087283.97	2,074.75	38.25	5.43	6.49	4.74	SW	41-50
453	MDG	339962.06	5087199.31	1,971.65	32.96	3.30	3.47	4.21	W	41-50
454	MDG	340366.60	5086868.31	2,048.78	37.38	7.60	7.29	4.88	NW	51-60
455	MDG	339665.36	5087325.13	1,940.92	42.06	8.18	2.80	5.49	SSE	21-30
456	MDG	340388.67	5086876.34	2,080.66	50.22	8.30	6.42	6.80	NNW	71-80
457	MDG	340340.05	5086875.41	2,035.75	199.71	6.85	7.23	31.79	SSE	61-70
458	MDG	340354.62	5086868.17	2,040.29	27.21	4.05	3.97	4.46	NW	51-60
459	MDG	340329.44	5086819.67	2,015.20	27.29	7.26	4.69	4.75	W	41-50
460	MDG	339957.32	5087207.56	1,970.74	22.51	5.26	2.56	4.14	WSW	51-60
461	MDG	340550.27	5086582.77	2,093.71	21.95	4.79	6.96	4.29	W	61-70
462	MDG	339961.96	5087212.72	1,975.87	24.32	5.52	3.36	5.34	W	31-40
463	MDG	340410.51	5087014.51	2,152.96	28.02	2.48	7.33	6.33	S	61-70
464	MDG	340534.78	5086553.22	2,070.92	30.39	4.79	5.24	7.11	SW	41-50
465	MDG	340561.85	5086515.91	2,071.63	21.76	7.46	3.53	9.62	WSW	41-50
466	MDG	339708.11	5087294.83	1,945.56	17.63	3.05	2.78	9.20	WNW	21-30
467	MDG	340638.18	5086540.90	2,160.01	10,731.61	67.73	33.20	8.10	SSW	41-50
468	MDG	340716.80	5086334.11	2,119.96	11,338.54	35.37	48.64	8.61	S	51-60
469	MDG	340672.36	5086420.63	2,148.97	4,585.55	34.71	52.54	7.39	WNW	61-70
470	MDG	340599.53	5086491.97	2,100.95	4,389.78	34.00	45.86	8.15	WSW	11-20
471	MDG	340669.16	5086430.17	2,107.64	1,909.77	29.10	39.28	7.16	WNW	51-60
472	MDG	340848.96	5085945.97	2,122.77	912.58	19.48	6.98	5.03	W	41-50
473	MDG	341168.47	5085358.99	2,215.03	751.04	19.11	11.73	4.39	W	41-50
474	MDG	340767.46	5086466.57	2,187.51	1,138.02	36.92	27.21	7.03	S	51-60
475	MDG	340725.97	5086406.43	2,170.62	1,235.66	26.20	13.76	7.95	SSW	11-20
476	MDG	341040.41	5085617.86	2,222.43	654.56	22.84	18.46	4.42	WSW	51-60
477	MDG	341042.70	5085637.18	2,230.06	738.45	20.67	13.63	5.18	WNW	41-50
478	MDG	340857.56	5085899.74	2,118.42	602.99	13.46	4.42	4.75	W	41-50
479	MDG	341120.32	5085508.65	2,244.62	650.53	34.71	26.01	5.22	SW	41-50
480	MDG	340827.13	5086126.80	2,152.47	498.62	13.01	20.53	4.71	WSW	51-60
481	MDG	340857.06	5085923.27	2,121.24	374.54	17.45	4.34	4.71	SW	51-60
482	MDG	340979.57	5085654.35	2,177.03	353.42	15.21	20.15	4.76	W	51-60
483	MDG	340974.85	5085711.79	2,193.32	326.91	10.72	12.11	4.68	WNW	41-50
484	MDG	341193.13	5085356.51	2,234.89	321.80	15.28	6.92	4.68	W	31-40
485	MDG	341071.44	5085487.52	2,178.76	357.96	10.59	11.85	5.42	W	41-50
486	MDG	341210.98	5085336.44	2,239.88	289.74	12.22	15.53	4.98	WSW	41-50
487	MDG	340785.34	5086227.74	2,131.07	265.55	7.76	5.88	4.73	SSW	51-60
488	MDG	341093.05	5085539.27	2,226.98	306.16	7.16	10.57	5.69	SW	71-80
489	MDG	340807.56	5086186.24	2,145.62	258.04	13.04	14.42	5.22	WNW	41-50
490	MDG	340732.58	5086307.22	2,123.84	231.96	13.62	9.60	4.82	SW	41-50
491	MDG	340615.21	5086475.30	2,096.34	446.47	14.07	16.01	9.95	WSW	61-70
492	MDG	340750.48	5086373.37	2,170.99	308.16	16.92	10.82	7.55	SW	31-40
493	MDG	340939.61	5085769.76	2,165.63	177.13	9.94	13.42	4.65	NNW	51-60

494	MDG	340951.70	5085750.47	2,175.67	147.02	10.80	11.69	4.57	WSW	41-50
495	MDG	341284.94	5085236.15	2,227.52	167.81	10.48	9.20	5.32	WNW	21-30
496	MDG	341396.40	5085129.31	2,216.70	144.58	11.42	11.71	4.77	WSW	51-60
497	MDG	340695.87	5086322.24	2,098.03	197.24	13.62	8.72	7.05	W	41-50
498	MDG	341076.53	5085554.96	2,219.96	113.04	4.43	6.25	4.39	W	41-50
499	MDG	340999.67	5085636.73	2,175.80	96.06	6.02	7.37	4.52	WNW	51-60
500	MDG	340678.98	5086443.40	2,121.78	100.11	8.71	3.98	4.75	SW	21-30
501	MDG	341313.95	5085246.87	2,251.01	81.97	11.50	15.13	4.89	WSW	51-60
502	MDG	340650.88	5086378.76	2,083.37	72.30	5.05	4.63	4.33	SW	41-50
503	MDG	340833.29	5086034.93	2,126.78	68.23	7.75	4.80	4.40	WNW	41-50
504	MDG	340960.68	5085684.19	2,161.87	72.35	10.84	4.70	4.69	WSW	61-70
505	MDG	340997.00	5085624.70	2,171.17	71.67	8.20	5.69	4.81	W	41-50
506	MDG	340845.85	5086104.45	2,155.24	106.98	7.41	12.14	7.29	W	31-40
507	MDG	340912.99	5085828.14	2,152.72	54.54	2.92	3.33	4.27	W	51-60
508	MDG	341082.01	5085476.43	2,181.11	64.18	10.77	11.64	5.66	WNW	51-60
509	MDG	340966.71	5085684.24	2,170.53	45.91	3.83	2.37	4.18	WSW	41-50
510	MDG	341385.67	5085154.60	2,228.28	43.22	8.90	4.33	4.31	SW	51-60
511	MDG	341021.59	5085607.32	2,185.04	49.80	7.36	4.36	5.23	WSW	41-50
512	MDG	340995.23	5085632.69	2,168.26	35.14	3.75	3.45	4.27	W	61-70
513	MDG	340953.27	5085698.90	2,159.59	34.23	6.53	5.42	4.34	W	41-50
514	MDG	341002.95	5085633.98	2,183.56	36.33	8.73	5.16	4.86	W	41-50
515	MDG	341108.06	5085521.74	2,239.12	29.51	6.35	7.82	4.27	WSW	31-40
516	MDG	340842.19	5085862.37	2,101.85	28.91	3.86	1.64	4.26	W	31-40
517	MDG	340975.55	5085667.50	2,171.50	36.15	7.23	4.19	5.81	W	51-60
518	MDG	341028.41	5085533.61	2,158.04	28.55	8.14	5.37	4.73	W	51-60
519	MDG	340834.60	5086105.93	2,147.47	32.19	5.15	5.47	5.51	W	41-50
520	MDG	341204.05	5085341.03	2,234.37	23.94	4.90	3.64	4.21	SW	61-70
521	MDG	340958.09	5085681.05	2,156.33	22.96	3.53	2.60	4.18	W	51-60
522	MDG	341026.38	5085570.94	2,169.44	20.53	5.40	5.48	4.36	W	61-70
523	MDG	340742.78	5086034.55	2,070.37	18.29	5.00	1.98	4.70	SSE	21-30
524	MDG	341023.77	5085633.06	2,204.25	22.41	5.08	5.40	5.85	S	41-50
525	MDG	340919.41	5085749.79	2,141.92	17.01	5.03	3.70	4.44	WSW	41-50
526	MDG	340950.13	5085776.26	2,168.24	17.65	4.88	6.69	4.68	WSW	51-60
527	MDG	340799.21	5086188.67	2,141.28	24.68	6.38	4.85	6.83	W	41-50
528	MDG	340596.61	5086473.18	2,077.35	20.00	4.10	6.22	5.54	WSW	51-60
529	MDG	341001.80	5085614.15	2,163.37	14.72	2.14	1.76	4.08	WSW	51-60
530	MDG	340599.58	5086447.15	2,069.17	16.14	5.80	2.99	4.63	W	31-40
531	MDG	340613.76	5086479.92	2,096.81	58.80	5.55	5.15	17.17	SW	51-60
532	MDG	341304.46	5085263.38	2,258.42	26.83	7.30	4.23	7.91	SSE	41-50
533	MDG	341061.20	5085495.83	2,173.56	15.45	5.92	3.06	4.60	SW	51-60
534	MDG	341370.99	5085179.25	2,237.66	14.16	3.15	1.78	4.25	WSW	31-40
535	MDG	341172.91	5085429.86	2,256.24	24.17	8.35	5.55	7.33	WNW	31-40
536	MDG	341086.38	5085555.99	2,240.26	14.43	4.84	2.68	4.78	SW	31-40
537	MDG	340963.77	5085730.22	2,180.98	12.13	2.53	3.37	4.11	WNW	41-50
538	MDG	341015.86	5085617.82	2,185.74	11.92	4.25	2.20	4.21	W	31-40
539	MDG	341093.18	5085484.30	2,200.11	15.18	6.20	5.53	6.53	NW	61-70
540	MDG	340969.71	5085719.10	2,187.77	11.87	3.61	2.22	5.18	SW	41-50
541	MDG	340511.11	5083720.05	2,366.42	4,288.05	39.99	33.31	4.30	NW	31-40
542	MDG	340488.61	5083764.61	2,330.32	1,657.53	30.68	24.91	3.86	W	41-50
543	MDG	340546.81	5083726.55	2,389.17	1,228.77	20.00	13.51	4.10	NW	31-40
544	MDG	340710.15	5084278.72	2,226.62	1,405.84	18.38	9.79	5.54	WSW	41-50

545	MDG	340520.29	5083842.27	2,317.64	618.74	13.72	19.47	3.88	NW	51-60
546	MDG	340417.32	5083706.55	2,310.21	376.16	8.52	11.45	3.94	WNW	41-50
547	MDG	340390.41	5083738.04	2,274.59	318.65	8.28	10.87	3.95	WNW	41-50
548	MDG	340320.81	5083705.86	2,239.97	260.58	8.71	8.76	3.39	WNW	31-40
549	MDG	340485.67	5083825.39	2,300.55	417.91	23.31	11.12	5.56	WSW	51-60
550	MDG	340843.43	5084490.44	2,204.84	298.16	21.58	20.35	4.15	N	61-70
551	MDG	340614.57	5084092.31	2,249.86	320.69	57.31	19.15	4.55	NW	61-70
552	MDG	340504.02	5084048.46	2,219.81	354.02	25.24	16.31	5.08	NNW	31-40
553	MDG	340576.75	5083970.33	2,284.93	216.00	12.46	18.80	3.40	NW	41-50
554	MDG	340613.17	5084012.52	2,280.94	177.80	8.91	9.86	3.36	WNW	41-50
555	MDG	340646.41	5084148.20	2,242.79	209.93	46.36	22.42	5.20	NW	31-40
556	MDG	340528.97	5084168.49	2,187.18	160.02	23.26	14.57	4.03	NW	21-30
557	MDG	340548.89	5083904.55	2,288.18	153.70	8.00	4.12	4.11	NNW	31-40
558	MDG	340611.03	5084038.89	2,270.97	128.56	4.68	6.67	3.69	W	41-50
559	MDG	340327.06	5083680.55	2,270.52	98.25	5.78	9.07	3.61	NW	61-70
560	MDG	340325.86	5083693.67	2,255.26	77.51	8.39	7.67	3.44	NW	51-60
561	MDG	340825.44	5084548.45	2,159.78	85.83	8.20	3.25	4.01	ENE	51-60
562	MDG	340601.26	5083971.36	2,297.84	71.01	6.06	5.46	3.62	W	21-30
563	MDG	340525.18	5084138.24	2,188.51	69.76	12.05	7.45	3.70	W	31-40
564	MDG	340310.29	5083671.49	2,259.41	82.30	5.42	10.62	4.40	NNW	61-70
565	MDG	340616.74	5084002.56	2,291.49	61.24	7.49	10.43	3.29	NW	41-50
566	MDG	340541.63	5084148.12	2,194.97	66.69	14.52	5.87	3.72	S	21-30
567	MDG	340643.65	5084325.21	2,183.87	102.55	9.17	2.43	6.05	NNW	0-10
568	MDG	340524.73	5084098.79	2,207.06	61.85	6.48	3.21	3.67	NW	31-40
569	MDG	340718.62	5084434.38	2,182.30	62.38	8.99	8.85	3.74	NW	41-50
570	MDG	340515.17	5084040.81	2,228.31	71.53	22.01	10.86	4.36	NNW	31-40
571	MDG	340510.28	5084075.65	2,210.25	56.08	6.75	6.32	3.89	NW	41-50
572	MDG	340591.71	5084243.55	2,190.38	61.46	17.46	1.93	4.59	S	0-10
573	MDG	340294.77	5083668.64	2,244.72	47.05	6.37	7.21	3.64	NW	61-70
574	MDG	340433.38	5083759.00	2,306.05	47.60	11.94	6.44	3.70	WNW	41-50
575	MDG	340511.44	5084083.62	2,204.66	42.09	3.29	2.67	3.43	NW	41-50
576	MDG	340637.99	5084235.60	2,200.16	52.47	15.44	6.30	4.36	WSW	31-40
577	MDG	340516.86	5084110.26	2,197.78	47.59	6.81	3.83	4.09	NW	51-60
578	MDG	340604.36	5084006.14	2,278.03	37.00	1.94	3.94	3.35	WNW	41-50
579	MDG	340511.28	5084120.15	2,190.44	43.75	11.10	4.98	3.96	WNW	31-40
580	MDG	340598.14	5083849.28	2,338.24	36.45	4.69	5.08	3.44	W	51-60
581	MDG	340557.00	5084156.21	2,201.39	40.88	9.90	5.72	3.94	S	11-20
582	MDG	340317.77	5083685.18	2,247.75	34.46	2.09	5.09	3.32	NW	61-70
583	MDG	340465.97	5083770.21	2,310.35	51.68	8.36	14.14	5.36	NNW	41-50
584	MDG	340568.28	5084158.07	2,204.85	32.80	9.34	6.04	3.82	ENE	31-40
585	MDG	340339.24	5083752.61	2,234.77	33.44	9.57	4.67	4.03	WSW	31-40
586	MDG	340522.66	5083895.27	2,281.84	34.23	7.23	3.83	4.14	NE	41-50
587	MDG	340499.10	5084073.13	2,202.02	28.37	6.91	3.17	3.70	WNW	31-40
588	MDG	340553.43	5084189.22	2,188.29	32.45	17.04	5.76	4.34	W	31-40
589	MDG	340522.50	5084076.28	2,214.41	27.97	6.01	2.74	3.92	NNW	21-30
590	MDG	340494.26	5084053.99	2,208.07	25.77	6.05	5.32	3.93	NW	41-50
591	MDG	340596.85	5084257.53	2,190.99	27.02	9.58	2.66	4.14	SSE	21-30
592	MDG	340518.63	5084094.23	2,204.89	19.65	5.17	2.04	3.33	NW	41-50
593	MDG	340738.41	5084381.40	2,220.25	28.55	7.66	3.20	5.02	NNW	41-50
594	MDG	340527.47	5084105.95	2,204.61	19.89	5.91	3.61	3.73	NW	31-40
595	MDG	340416.90	5083734.15	2,305.04	20.27	8.51	5.92	3.96	WNW	41-50

596	MDG	340302.91	5083678.84	2,240.09	25.88	7.29	5.59	5.28	WSW	11-20
597	MDG	340545.23	5084063.64	2,231.25	17.08	3.88	4.44	3.65	NNW	51-60
598	MDG	340551.90	5084170.89	2,190.77	17.13	5.95	2.48	3.73	SW	21-30
599	MDG	340613.94	5084033.77	2,276.16	14.77	0.81	1.86	3.24	NW	51-60
600	MDG	340442.02	5083830.99	2,268.20	15.71	4.66	3.16	3.60	NE	31-40
601	MDG	340465.81	5083645.75	2,374.16	20.16	7.37	6.45	4.68	NNW	41-50
602	MDG	340588.67	5083930.39	2,304.31	19.45	10.27	3.07	4.55	NNW	21-30
603	MDG	340440.84	5083835.08	2,263.52	18.56	4.99	5.29	4.34	W	31-40
604	MDG	340665.25	5084393.19	2,173.34	19.65	8.94	2.25	4.89	NNW	21-30
605	MDG	340526.26	5083804.92	2,340.16	17.75	6.36	3.58	4.59	NNW	21-30
606	MDG	340489.35	5083828.98	2,301.75	16.83	4.16	3.27	4.39	N	51-60
607	MDG	340535.78	5084105.42	2,211.18	13.46	3.48	2.49	3.51	NW	41-50
608	MDG	340610.47	5084281.00	2,190.48	13.82	7.20	1.53	3.93	W	11-20
609	MDG	340583.22	5084179.73	2,198.13	21.96	7.27	5.26	6.24	NW	21-30
610	MDG	340598.10	5083997.67	2,276.01	12.32	4.17	2.46	3.60	NW	31-40
611	MDG	340443.74	5083836.16	2,257.40	26.26	7.99	7.96	7.67	NNE	51-60
612	MDG	340618.28	5083992.13	2,299.34	11.14	1.73	1.90	3.35	NW	31-40
613	MDG	340735.21	5084426.40	2,201.25	13.16	6.35	4.92	4.23	NNW	51-60
614	MDG	340908.63	5084502.63	2,221.93	13.53	3.63	7.12	4.58	N	61-70
615	MDG	340629.67	5084135.58	2,240.27	18.46	12.01	4.28	6.25	WNW	41-50
616	MDG	340655.56	5084204.97	2,227.28	15.01	6.13	5.30	5.08	WNW	41-50
617	MDG	340530.57	5083861.10	2,308.11	15.06	5.15	3.64	5.27	NNW	41-50
618	MDG	340624.72	5084308.49	2,188.03	12.56	6.51	2.19	4.39	NW	31-40
619	MDG	340508.84	5084106.93	2,193.50	11.39	4.30	1.90	4.03	NW	41-50
620	MDG	340545.23	5083888.09	2,297.14	12.63	5.09	4.95	4.47	NW	41-50
621	MDG	340462.32	5083817.45	2,282.27	9.06	3.90	2.51	3.47	NNW	51-60
622	MDG	340600.65	5083933.32	2,306.21	8.19	5.70	1.67	3.83	NNW	21-30
623	MDG	340541.66	5083905.36	2,283.14	13.79	7.51	3.52	6.55	WNW	41-50
624	MDG	340833.71	5084495.88	2,198.12	7.20	3.90	2.51	3.53	NW	51-60
625	MDG	340544.80	5084120.41	2,209.23	6.97	4.33	0.96	3.63	WNW	21-30
626	MDG	341106.34	5084061.60	2,524.48	759.25	25.80	15.60	5.34	WSW	41-50
627	MDG	340798.20	5083857.00	2,418.45	228.41	10.98	15.42	1.69	NW	21-30
628	MDG	340797.83	5083843.05	2,430.89	223.40	14.57	17.66	1.76	NW	31-40
629	MDG	340614.51	5083731.66	2,410.82	77.07	6.12	4.29	2.26	NNW	41-50
630	MDG	340832.99	5083868.22	2,428.81	46.18	5.78	3.42	1.65	WNW	31-40
631	MDG	340635.69	5083823.05	2,364.98	62.72	4.29	2.45	2.39	NW	41-50
632	MDG	340854.47	5083854.95	2,446.31	41.11	4.62	6.20	1.64	WNW	31-40
633	MDG	341038.84	5084175.99	2,422.14	136.48	9.52	6.20	5.82	W	51-60
634	MDG	341109.61	5083868.08	2,575.66	40.30	5.91	7.59	2.08	NNW	41-50
635	MDG	340771.82	5084070.08	2,315.99	45.95	3.94	2.56	2.99	SW	31-40
636	MDG	340829.17	5083857.46	2,432.30	24.90	3.14	3.62	1.65	NW	31-40
637	MDG	340616.38	5083828.38	2,358.86	25.89	4.81	2.99	1.73	N	21-30
638	MDG	340799.76	5083871.38	2,413.52	24.57	3.70	2.48	1.67	WNW	31-40
639	MDG	340692.81	5083846.84	2,374.38	27.25	2.40	2.49	1.95	NNW	21-30
640	MDG	340800.53	5083829.28	2,429.87	17.09	2.65	3.26	1.64	NW	31-40
641	MDG	340675.55	5083850.96	2,368.77	17.53	2.65	1.70	1.70	NW	31-40
642	MDG	340805.09	5083880.83	2,412.97	16.32	2.41	3.65	1.59	NW	31-40
643	MDG	341044.49	5083843.77	2,559.25	30.95	5.85	7.54	3.27	NNW	31-40
644	MDG	340608.50	5083754.76	2,396.58	13.03	2.59	1.81	1.84	NNW	31-40
645	MDG	340996.13	5084123.74	2,405.50	11.74	2.41	2.37	1.81	NNW	41-50
646	MDG	340640.90	5083782.86	2,383.95	11.06	3.13	1.88	1.73	N	31-40

647	MDG	340623.19	5083863.43	2,347.60	12.40	2.87	1.19	1.95	N	31-40
648	MDG	341035.97	5084173.93	2,415.48	40.43	4.23	4.53	6.85	WSW	31-40
649	MDG	341033.54	5083853.06	2,543.74	11.60	2.91	3.42	2.32	NW	31-40
650	MDG	340628.42	5083862.59	2,349.09	8.37	1.44	1.30	1.69	NW	31-40
651	MDG	341099.29	5083879.81	2,561.76	8.32	1.70	2.30	1.98	NW	51-60
652	MDG	340792.72	5083848.24	2,418.13	4.24	1.48	0.96	1.61	NW	21-30
653	MDG	341039.58	5083849.69	2,549.46	6.22	2.15	2.47	2.42	NNW	51-60
654	MDG	341067.87	5083816.23	2,595.50	6.06	1.73	3.27	2.97	NW	41-50
655	MDG	341029.71	5084172.21	2,408.59	12.78	2.26	2.38	6.46	SW	61-70
656	MDG	341076.25	5083870.11	2,552.95	3.09	1.20	0.85	1.97	NW	31-40
657	MDG	340261.30	5083587.45	2,243.71	1,128.89	42.95	21.12	6.17	SE	0-10
658	MDG	340259.18	5082870.15	2,358.99	517.82	16.33	4.12	4.09	NW	21-30
659	MDG	340238.98	5083400.98	2,279.23	551.48	19.77	9.62	5.60	SSE	0-10
660	MDG	340247.74	5083446.64	2,281.47	290.24	8.46	8.49	3.97	WNW	31-40
661	MDG	340245.76	5083568.07	2,258.19	184.20	16.52	12.15	4.39	NW	41-50
662	MDG	340270.50	5083591.78	2,257.88	145.17	10.81	5.22	3.90	W	41-50
663	MDG	340255.87	5083414.55	2,285.71	143.80	17.06	4.40	4.24	SW	21-30
664	MDG	340278.06	5083229.01	2,328.30	114.46	3.72	8.19	3.71	WNW	41-50
665	MDG	340270.18	5083575.67	2,264.77	118.25	6.61	2.11	3.91	NW	11-20
666	MDG	340235.68	5083555.61	2,259.90	107.41	9.09	6.08	4.36	SW	11-20
667	MDG	340251.92	5083561.36	2,265.88	69.36	7.93	4.00	4.17	NW	21-30
668	MDG	340259.19	5083466.54	2,282.54	53.98	6.43	2.82	3.87	NE	11-20
669	MDG	340265.70	5083581.92	2,260.59	47.46	5.16	9.11	3.99	NNW	61-70
670	MDG	340261.30	5083392.47	2,287.14	48.43	9.47	2.40	4.11	NNE	11-20
671	MDG	340236.67	5083456.83	2,271.35	45.90	6.61	4.50	3.97	W	21-30
672	MDG	340351.85	5083437.61	2,387.73	41.07	5.41	3.78	4.42	WNW	41-50
673	MDG	340241.67	5083349.46	2,284.03	23.15	8.85	3.08	3.76	NW	11-20
674	MDG	340311.97	5083270.29	2,355.34	16.31	7.18	4.44	5.35	SW	51-60
675	MDG	340251.66	5083580.46	2,248.65	17.96	1.97	7.28	6.57	NW	31-40
676	MDG	340273.02	5083284.13	2,312.94	11.00	3.69	2.72	4.02	W	51-60
677	MDG	340425.12	5083315.11	2,460.05	9.58	6.10	3.80	5.26	W	31-40
678	MDG_I	339354.43	5088007.30	1,808.96	12,846.61	116.24	36.78	2.36		
679	MDG_I	339322.11	5087903.65	1,807.53	3,246.19	53.75	16.33	2.89		
680	MDG_I	339324.51	5088056.00	1,802.14	2,453.96	35.88	23.90	2.33		
681	MDG_I	339410.39	5088099.08	1,895.49	1,063.39	18.23	19.90	2.65		
682	MDG_I	339394.92	5088071.41	1,868.37	1,057.70	13.73	35.13	2.97		
683	MDG_I	339387.86	5088094.45	1,863.89	773.26	23.72	18.39	2.54		
684	MDG_I	339388.72	5088022.39	1,863.92	417.14	5.93	18.29	2.55		
685	MDG_I	339326.18	5087924.69	1,812.07	324.20	8.55	11.23	2.30		
686	MDG_I	339397.74	5088117.08	1,887.21	305.53	11.50	17.52	2.18		
687	MDG_I	339316.51	5087920.29	1,810.51	339.03	9.06	13.03	2.42		
688	MDG_I	339398.59	5088001.96	1,878.87	381.10	9.47	13.56	2.83		
689	MDG_I	339359.04	5088048.46	1,820.81	300.49	13.88	10.63	2.29		
690	MDG_I	339393.36	5088082.54	1,872.24	341.15	8.41	13.52	2.90		
691	MDG_I	339427.93	5088090.52	1,915.30	294.48	14.68	9.51	2.74		
692	MDG_I	339354.43	5087982.07	1,824.31	139.90	5.48	6.51	2.08		
693	MDG_I	339407.06	5088042.71	1,886.64	159.15	8.24	8.43	2.70		
694	MDG_I	339308.18	5087973.40	1,795.13	124.39	8.83	5.53	2.11		
695	MDG_I	339417.85	5088061.03	1,896.63	152.45	8.47	4.73	2.61		
696	MDG_I	339303.88	5087855.71	1,811.07	162.59	6.80	5.57	2.97		
697	MDG_I	339359.92	5088065.52	1,819.48	105.14	9.88	3.58	2.23		

698	MDG_I	339386.84	5088104.55	1,864.98	114.02	4.36	7.87	2.46
699	MDG_I	339417.35	5087952.79	1,910.90	104.00	2.56	6.74	2.30
700	MDG_I	339379.03	5088080.06	1,848.94	111.55	7.48	5.39	2.50
701	MDG_I	339394.82	5087964.47	1,879.27	132.01	7.77	4.58	2.98
702	MDG_I	339393.60	5088096.93	1,874.23	111.68	5.39	4.76	2.66
703	MDG_I	339395.96	5088089.24	1,881.57	110.47	5.02	5.81	2.75
704	MDG_I	339313.19	5087956.43	1,797.77	69.19	4.40	4.24	2.06
705	MDG_I	339354.16	5087975.71	1,821.77	67.79	6.99	4.01	2.04
706	MDG_I	339342.28	5087954.79	1,819.08	67.61	5.75	3.82	2.03
707	MDG_I	339386.42	5087982.47	1,862.01	87.96	5.24	4.19	2.65
708	MDG_I	339305.74	5087955.04	1,794.62	66.41	6.86	3.34	2.15
709	MDG_I	339387.98	5088105.22	1,873.65	65.68	2.86	6.99	2.32
710	MDG_I	339402.68	5088032.59	1,882.84	74.65	4.95	5.61	2.67
711	MDG_I	339369.11	5088034.19	1,834.27	76.99	2.85	7.23	2.76
712	MDG_I	339380.42	5088078.94	1,854.15	63.84	4.94	3.42	2.30
713	MDG_I	339398.09	5088096.68	1,881.61	65.05	3.53	3.72	2.35
714	MDG_I	339313.71	5088006.90	1,792.84	86.93	5.84	5.09	3.22
715	MDG_I	339393.27	5088053.56	1,863.93	60.21	8.33	4.85	2.29
716	MDG_I	339384.63	5088075.53	1,858.04	61.12	3.42	4.20	2.36
717	MDG_I	339402.77	5087963.61	1,896.07	73.87	2.84	5.61	3.21
718	MDG_I	339314.07	5087986.29	1,796.51	47.81	2.23	4.03	2.10
719	MDG_I	339379.02	5088062.96	1,842.50	49.75	6.08	4.16	2.22
720	MDG_I	339371.29	5088071.30	1,834.31	48.13	5.05	3.93	2.18
721	MDG_I	339395.91	5088053.34	1,872.47	57.57	4.61	4.10	2.63
722	MDG_I	339407.27	5087979.44	1,889.77	47.08	2.93	4.81	2.19
723	MDG_I	339399.95	5088028.00	1,879.25	47.57	2.98	3.27	2.60
724	MDG_I	339423.04	5087966.87	1,913.63	42.00	2.84	2.29	2.38
725	MDG_I	339336.05	5088038.68	1,805.37	37.22	4.29	1.76	2.21
726	MDG_I	339388.72	5088086.04	1,874.94	40.02	5.64	6.57	2.59
727	MDG_I	339347.19	5088042.65	1,813.07	31.30	2.59	3.68	2.04
728	MDG_I	339389.90	5088029.66	1,856.18	35.48	1.80	5.11	2.35
729	MDG_I	339389.29	5087875.62	1,884.16	29.34	1.98	2.55	2.02
730	MDG_I	339382.35	5087947.94	1,867.58	31.99	2.42	2.51	2.27
731	MDG_I	339323.30	5087898.88	1,814.49	26.91	3.90	2.54	1.97
732	MDG_I	339390.55	5088112.34	1,870.97	31.57	2.40	3.01	2.38
733	MDG_I	339323.45	5087892.64	1,817.29	25.45	2.95	3.24	1.98
734	MDG_I	339392.48	5088112.66	1,874.49	31.43	2.29	2.75	2.55
735	MDG_I	339375.15	5087939.54	1,849.71	23.73	2.57	5.39	1.98
736	MDG_I	339387.87	5088232.72	1,857.75	28.83	3.07	2.74	2.54
737	MDG_I	339362.93	5088059.49	1,823.63	22.82	2.43	3.59	2.06
738	MDG_I	339310.08	5087983.27	1,794.42	22.20	2.34	2.71	2.07
739	MDG_I	339390.08	5088027.44	1,861.00	21.48	1.78	1.78	2.18
740	MDG_I	339319.52	5087882.46	1,816.35	19.45	2.50	1.61	2.04
741	MDG_I	339394.98	5088023.13	1,879.25	23.07	1.87	2.29	2.42
742	MDG_I	339392.20	5088028.23	1,864.73	21.51	1.85	2.71	2.28
743	MDG_I	339391.47	5088056.83	1,861.79	20.02	2.09	2.67	2.23
744	MDG_I	339405.63	5087958.52	1,897.82	20.48	1.22	2.36	2.31
745	MDG_I	339418.92	5087946.67	1,913.40	19.45	1.90	2.44	2.42
746	MDG_I	339414.49	5088083.53	1,897.09	15.88	2.20	2.37	2.16
747	MDG_I	339388.92	5088060.63	1,859.92	17.69	2.04	1.90	2.43
748	MDG_I	339383.60	5088090.77	1,857.75	14.98	1.97	2.36	2.12

749	MDG_I	339379.04	5087916.40	1,864.95	13.54	1.21	2.28	1.94
750	MDG_I	339351.98	5087958.99	1,823.65	14.18	1.72	1.14	2.07
751	MDG_I	339417.43	5087941.77	1,913.58	13.97	1.91	2.17	2.10
752	MDG_I	339326.25	5088032.01	1,799.65	12.52	1.56	0.92	2.04
753	MDG_I	339391.97	5088013.60	1,872.67	13.10	1.53	2.38	2.16
754	MDG_I	339332.33	5088036.84	1,803.01	11.13	2.40	1.09	1.95
755	MDG_I	339331.55	5087899.96	1,820.00	10.91	2.19	2.14	1.93
756	MDG_I	339420.85	5088079.36	1,904.37	12.38	1.72	1.70	2.23
757	MDG_I	339374.32	5087997.62	1,842.70	10.63	1.36	1.82	2.04
758	MDG_I	339315.86	5088025.91	1,793.05	11.86	2.45	1.11	2.29
759	MDG_I	339412.64	5088065.81	1,897.37	10.89	0.95	1.73	2.34
760	MDG_I	339357.93	5087971.92	1,824.25	11.04	2.70	0.98	2.46
761	MDG_I	339385.61	5088056.51	1,853.14	10.04	1.82	2.07	2.28
762	MDG_I	339338.11	5087925.66	1,817.98	8.78	1.37	1.33	2.03
763	MDG_I	339386.73	5088098.01	1,858.79	9.19	1.76	1.79	2.15
764	MDG_I	339370.36	5088007.04	1,837.97	9.50	1.70	1.22	2.24
765	MDG_I	339418.34	5087959.79	1,908.45	9.22	1.35	1.58	2.22
766	MDG_I	339342.21	5087956.60	1,818.71	7.83	2.03	1.38	1.90
767	MDG_I	339311.94	5087963.73	1,797.06	7.58	1.50	1.29	1.96
768	MDG_I	339353.77	5087962.22	1,823.37	7.17	1.15	0.70	1.85
769	MDG_I	339383.36	5088044.54	1,850.65	7.33	1.57	1.22	2.05
770	MDG_I	339335.25	5087926.97	1,815.85	6.96	1.10	1.17	1.96
771	MDG_I	339395.07	5088111.31	1,878.96	7.07	1.47	1.05	2.03
772	MDG_I	339421.77	5087981.37	1,907.57	8.42	1.73	2.30	2.44
773	MDG_I	339410.22	5088107.44	1,898.81	8.07	1.03	1.16	2.36
774	MDG_I	339330.54	5087981.07	1,807.82	6.80	1.12	0.99	1.99
775	MDG_I	339396.26	5088027.25	1,873.49	6.62	1.41	1.60	2.03
776	MDG_I	339396.46	5088112.62	1,880.76	7.17	1.31	1.12	2.22
777	MDG_I	339324.01	5087895.69	1,816.25	5.91	1.62	0.95	1.86
778	MDG_I	339396.64	5087963.33	1,885.08	7.08	2.10	1.23	2.35
779	MDG_I	339333.24	5087954.74	1,813.35	5.51	0.93	1.10	1.89
780	MDG_I	339378.85	5087946.51	1,860.63	6.45	1.50	0.90	2.23
781	MDG_I	339400.99	5087919.97	1,884.05	6.73	1.24	1.29	2.44
782	MDG_I	339393.42	5088025.37	1,873.63	5.45	0.93	1.42	1.99
783	MDG_I	339303.09	5087860.54	1,808.55	6.61	1.68	0.82	2.45
784	MDG_I	339306.87	5087859.20	1,811.73	5.55	1.10	0.43	2.16
785	MDG_I	339342.26	5088022.09	1,809.48	5.34	1.50	1.25	2.13
786	MDG_I	339386.44	5088072.45	1,860.03	5.36	0.95	1.93	2.28
787	MDG_I	339418.00	5088077.60	1,900.16	4.79	1.34	1.28	2.03
788	MDG_I	339351.22	5088056.83	1,813.28	5.09	1.34	0.79	2.25
789	MDG_I	339353.13	5088042.94	1,815.56	5.10	1.94	0.76	2.25
790	MDG_I	339322.46	5087984.48	1,802.50	4.28	1.55	1.16	1.89
791	MDG_I	339410.31	5087917.60	1,900.66	5.28	0.83	1.03	2.40
792	MDG_I	339332.69	5088028.91	1,803.89	4.10	0.78	0.44	1.89
793	MDG_I	339320.54	5088004.10	1,797.97	4.06	0.98	0.73	1.93
794	MDG_I	339328.85	5088063.43	1,799.20	4.13	1.24	0.65	1.99
795	MDG_I	339312.61	5087980.59	1,796.13	4.18	0.86	0.72	2.04
796	MDG_I	339386.13	5087992.85	1,863.89	4.57	0.90	1.11	2.24
797	MDG_I	339314.81	5087982.66	1,797.67	3.99	0.91	0.75	1.99
798	MDG_I	339341.09	5087960.75	1,816.98	3.69	0.78	0.63	1.87
799	MDG_I	339304.69	5087903.28	1,801.84	3.73	1.05	0.50	1.91

800	MDG_I	339345.25	5087955.80	1,820.63	3.68	0.97	0.51	2.02		
801	MDG_I	339333.54	5087933.02	1,814.58	3.64	0.93	0.71	2.03		
802	MDG_I	339349.80	5087986.93	1,819.72	3.34	0.88	0.54	1.90		
803	MDG_I	339356.93	5087964.27	1,823.60	3.49	0.99	0.88	2.06		
804	MDG_I	339318.96	5088007.09	1,796.26	3.36	0.80	0.83	2.06		
805	MDG_I	339358.69	5087976.87	1,825.06	3.08	0.73	1.89	1.96		
806	MDG_I	339419.56	5088062.21	1,901.91	3.16	0.98	0.92	2.05		
807	MDG_I	339324.69	5087983.18	1,803.62	2.96	0.81	0.40	1.96		
808	MDG_I	339323.80	5087903.57	1,812.92	3.36	0.88	0.36	2.43		
809	MDG_I	339337.77	5087953.86	1,815.97	2.62	0.78	0.45	1.94		
810	MDG_I	339316.53	5087975.66	1,798.57	2.38	0.64	0.53	1.90		
811	MDG_I	339380.25	5088041.13	1,844.71	3.21	0.80	0.74	2.55		
812	MIA	333885.62	5072958.15	2,257.47	7.42	1.04	1.08	1.37	SSW	41-50
813	MIA	333847.68	5072952.96	2,237.36	4.43	1.44	1.10	1.44	S	61-70
814	MIA	333960.40	5072810.93	2,184.70	136.51	6.62	7.18	4.73	SSW	21-30
815	MIA	333969.64	5072807.15	2,186.12	20.12	2.82	3.81	4.51	SW	0-10
816	MIA	333800.21	5072959.58	2,211.65	202.22	17.11	6.12	1.75	SSW	31-40
817	MIA	333874.71	5072884.80	2,196.80	105.25	5.55	6.09	1.83	SW	41-50
818	MIA	333849.63	5072904.40	2,198.51	40.32	2.57	3.30	1.59	SW	51-60
819	MIA	333856.76	5072882.77	2,181.98	27.94	3.74	1.92	1.70	SW	31-40
820	MIA	333846.39	5072912.29	2,202.73	24.22	5.58	1.95	1.55	SW	41-50
821	MIA	333849.61	5072896.63	2,188.31	15.13	1.42	1.30	1.57	SW	41-50
822	MIA	333889.85	5072870.66	2,196.91	11.39	0.96	0.82	1.71	SW	41-50
823	MIA	333856.56	5072898.51	2,196.66	7.19	0.98	0.70	1.53	SW	51-60
824	PDB	349239.01	5083863.92	2,194.59	28.14	6.73	4.05	0.77	NNE	61-70
825	PDB	349303.89	5083764.98	2,192.79	29.12	5.47	5.12	0.84	NE	41-50
826	PDB	349314.42	5083671.93	2,228.11	32.21	3.72	6.34	1.10	NE	51-60
827	PDB	349334.27	5083643.12	2,226.48	16.61	3.21	3.39	0.78	NE	41-50
828	PDB	349237.22	5083799.78	2,221.47	9.11	2.49	4.53	0.67	NE	41-50
829	PDB	349324.52	5083665.00	2,220.09	10.64	4.44	2.49	0.85	ENE	41-50
830	PDB	349318.99	5083678.75	2,216.87	8.29	2.46	2.65	0.83	NNE	41-50
831	PDB	349299.74	5083840.73	2,165.57	6.54	1.58	1.44	0.84	ENE	31-40
832	PDB	349343.71	5083647.77	2,216.85	6.56	1.37	2.04	0.85	NNE	41-50
833	PDB	349274.70	5083778.98	2,201.24	6.93	1.31	2.02	0.90	NE	31-40
834	PDB	349330.55	5083661.95	2,217.27	4.85	2.08	2.58	0.72	NNE	41-50
835	PDB	349260.93	5083865.30	2,180.40	3.87	4.28	3.04	0.64	ENE	31-40
836	PDB	349229.89	5083744.92	2,254.23	4.12	1.67	2.24	0.71	NE	51-60
837	PDB	349263.61	5083851.18	2,182.81	3.61	2.19	1.33	0.65	ENE	31-40
838	PDB	349216.81	5083775.87	2,247.12	4.69	0.94	1.17	0.84	NNE	51-60
839	PDB	349417.77	5083768.31	2,139.90	4.18	1.59	2.63	0.89	ESE	21-30
840	PDB	349251.88	5083720.11	2,248.37	2.76	2.18	2.60	0.64	NNE	41-50
841	PDB	349336.51	5083660.14	2,216.11	3.25	1.37	2.47	0.75	NE	41-50
842	PDB	349343.65	5083674.53	2,202.18	3.02	1.37	1.10	0.80	NE	21-30
843	PDB	349267.65	5083850.87	2,179.48	2.50	1.05	1.34	0.68	E	31-40
844	PDB	349228.69	5083787.55	2,231.12	2.95	0.85	1.20	0.83	NE	51-60
845	PDB	349205.86	5083771.18	2,260.18	2.18	0.93	1.75	0.68	NE	51-60
846	PDB	349248.95	5083862.98	2,188.18	1.99	1.57	0.69	0.63	NNE	41-50
847	PDB	349228.23	5083813.57	2,220.39	1.99	1.21	1.57	0.63	NNE	31-40
848	PDB	349261.20	5083881.12	2,174.35	2.01	3.24	0.69	0.67	ENE	21-30
849	PDB	349258.89	5083868.46	2,181.22	1.94	0.95	0.89	0.65	NE	41-50
850	PDB	349256.21	5083865.63	2,183.84	1.71	1.51	2.06	0.61	NE	31-40

851	PDB	349265.63	5083788.69	2,203.56	1.83	0.61	0.95	0.69	NE	41-50
852	PDB	349302.74	5083687.10	2,224.23	1.93	0.70	0.97	0.74	NNE	51-60
853	PDB	349240.38	5083866.49	2,189.64	1.64	2.45	0.94	0.63	NE	21-30
854	PDB	349243.46	5083810.13	2,210.47	1.67	0.71	0.87	0.68	NE	41-50
855	PDB	349353.12	5083825.81	2,146.03	1.62	3.16	0.73	0.82	NNE	21-30
856	PDB	349154.62	5083924.46	2,225.57	2.88	3.45	1.80	1.56	ENE	31-40
857	PDB	349248.31	5083859.71	2,189.95	0.20	0.17	0.20	0.63	NE	31-40

Appendix 2

Introduction

Throughout the course of the PhD, I have had several unique opportunities to present and work outside of academia because of an artistic collaboration, a prestigious bursary and other opportunities that have arisen. Such work beyond the realm of academia has allowed me to develop new contacts, learn about the transferability of a skill-set and present work for outreach and science communication to non-academic audiences. This appendix summarises those activities.

Art Collaboration - Dan Holdsworth

This PhD has been part of a unique collaboration between Northumbria University and UK artist, Dan Holdsworth. His work explores the relationship between landscape photography, science and technology. As a result of this collaboration, Holdsworth has produced two series of work;

1) Spatial Objects (2015) (fig. 9.1), and
2) Continuous Topography (2016) (fig. 9.2).

The series look at the data collected for this PhD in an entirely new perspective. Alistair Robinson, programme director for the Northern Gallery for Contemporary Art, has written texts around each of the series from which, the following extracts are taken:

Spatial Objects, 2015

"To start at the beginning: the title Spatial Objects, is wilfully misleading - at least in one sense. The title derives from a term in computer programming to designate objects that exist, as Holdsworth notes, “in simultaneous symmetry within the virtual and the real”. The starting point for Spatial Objects, despite their appearance as works marking a departure from Holdsworth’s work to date, were the digitally recorded GPS points harvested in the production of an earlier series."

"In Spatial Objects, the medium of artistic investigation is made the object of that investigation, and its objects are made opaque and knowable to us rather than being taken for granted and seen as transparent in their effects and operations. This investigation has its own, peculiar poetry, of course: looking at the Spatial Objects have been described as “like zooming in on the individual scales of a butterfly’s wing” with good reason. The glistening expanses of saturated, vivid colour remind us that the links between the ‘luminous’ and the ‘numinous’ is not merely phonetic." (Robinson, 2015)

Figure 0.1: Installation View, Spatial Objects by Dan Holdsworth, 2015.

Continuous Topography, 2016

"Continuous Topography creates an image of what Holdsworth calls a “future archaeology”, in which our own temporal horizons are thrown into relief. The works invite us to imaginatively inhabit what initially appears to be an almost entirely abstract and immaterial, or virtual space."

"We might imagine Continuous Topography as a twenty-first century rethinking of the ambitions of Von Humboldt’s epic, five-volume treatise about science and planetary development, Kosmos. Holdsworth’s method certainly alerts us to the subtitle of Kosmos, namely A Sketch of a Physical Description of the Universe. Continuous Topography does indeed offers kinds of ‘sketches’ – but only in the sense that they are artistic interpretations made from scientific observations." (Robinson, 2016)

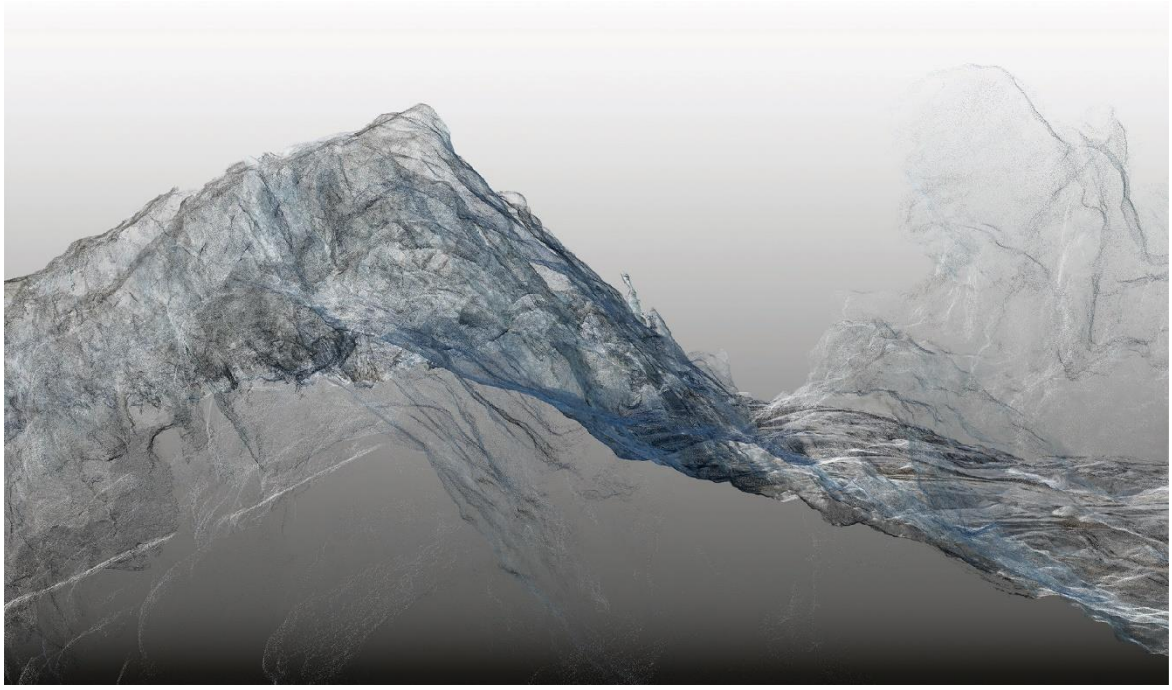

Figure 0.2: Argentière Glacier no. 01, Continuous Topography by Dan Holdsworth, 2016

These works have been displayed at a number of exhibitions, including:

1) Southampton City Art Gallery, Southampton, UK, 09/05/2015 - 31/08/2015.
2) Scheublin + Bak, Zurich, Switzerland, 01/06/2016 - 02/09/2016.
3) Art Basel (Audemars Piguet Commission), Basel, Switzerland, 16/06/2016 - 19/06/2016.
4) Musée des Beaux-Arts Le Locle, Le Locle, Switzerland, 06/11/2016 - 29/01/2017.
5) Graves Gallery, Sheffield, United Kingdom, 16/12/2017 – 16/03/2018.
6) Sidney Cooper Gallery, Canterbury, United Kingdom, 01/03/2018 – 29/03/2018.
7) Denver Art Museum, Denver, USA, 24/06/2018 – 16/09/2018.

Royal Geographical Society (with IBG) Land Rover Bursary

In 2013, the project was awarded additional funding from the Land Rover bursary to support a field campaign in the Alps. The Land Rover Bursary, run by the Royal Geographical Society (with IBG) on behalf of Jaguar Land Rover, offered funding of £30,000 and the use of a Land Rover Defender 110. The bursary is awarded with the expectation to inspire and engage others, both from the field and on return. The bursary came with a number of commitments outside of academia such as presenting a Monday evening lecture at the society, and at the annual fieldwork and exploration conference, EXPLORE. The project also resulted in a number of non-academic outreach articles about the project in publications such as (amongst others);

1) Geographical, Magazine of the RGS (with IBG), July 2015.

2) Land Rover Owner International, World's best-selling Land Rover and Range Rover Magazine, October 2014.
3) Land Rover, ONELIFE, Issue 30.
4) Stuff Magazine, 2014.

As well as magazine publications, teaching resources for Key Stage 4 pupils were developed, based on this project are available online with the following key topics and themes;

1) The indicators of glacial retreat in Alpine regions.
2) How the processes that create landslides inform wider understanding of Alpine environments.
3) The challenge of living and working in Alpine environments.
4) The factors that continue to draw people to the Alps, as researchers and as tourists.
5) How different groups, both from and visiting the region, perceive the Alpine environment and culture.
6) Comparing how the Alps has been portrayed through history in a visual form.

References

Abellán, A. *et al.* (2014) 'Terrestrial laser scanning of rock slope instabilities', *Earth Surface Processes and Landforms*, 39(1), pp. 80–97. doi: 10.1002/esp.3493.

Abellan, A., Derron, M.-H. and Jaboyedoff, M. (2016) '"Use of 3D Point Clouds in Geohazards" Special Issue: Current Challenges and Future Trends', *Remote Sensing*, 8(2), p. 130. doi: 10.3390/rs8020130.

Abellán, A., Vilaplana, J. and Martínez, J. (2006) 'Application of a long-range Terrestrial Laser Scanner to a detailed rockfall study at Vall de Núria (Eastern Pyrenees, Spain)', *Engineering Geology*, 88(3–4), pp. 136–148. doi: 10.1016/j.enggeo.2006.09.012.

Agarwal, S. *et al.* (2011) 'Building Rome in a Day', *Communications of the ACM*, 55(10), pp. 105–112. doi: 10.1145/2001269.

Agassiz, L. (1840) *Etudes sur les Glaciers*. Neuchâtel, Jent et Gassmann.

AgiSoft LLC (2016) 'Agisoft PhotoScan User Manual', in *Professional Edition, Version 0.9.1*.

Al-Rawabdeh, A. *et al.* (2016) 'Using an Unmanned Aerial Vehicle-Based Digital Imaging System to Derive a 3D Point Cloud for Landslide Scarp Recognition', *Remote Sensing*, 8(2), p. 95. doi: 10.3390/rs8020095.

Allen, J. (2006) *Rhone Glacier, Switzerland*, *NASA Earth Observatory*. Available at: http://earthobservatory.nasa.gov/IOTD/view.php?id=7066 (Accessed: 16 February 2015).

Arya, S. *et al.* (1998) 'An optimal algorithm for approximate nearest neighbor searching in fixed dimensions', *Journal of the Association for Computing Machinery*, 45, pp. 891–923. doi: 10.1145/293347.293348.

Assali, P. *et al.* (2016) 'Solid images for geostructural mapping and key block modeling of rock discontinuities', *Computers and Geosciences*. Elsevier. doi: 10.1016/j.cageo.2016.01.002.

Astre, H. (2015) *SFMToolkit*, *Structure from motion toolkit (BundlerFocalExtractor, BundlerMatcher, Bundler, CMVS, PMVS2)*. Available at: https://github.com/dddExperiments/SFMToolkit.

Augustinus, P. (1995) 'Glacial valley cross-profile development: the influence of in situ rock stress and rock mass strength, with examples from the Southern Alps, New Zealand', *Geomorphology*, 14(95), pp. 87–97.

Autodesk (2015) *123D Catch*, *123D Catch*. Available at: http://www.123dapp.com/catch.

Bak, P., Tang, C. and Wiesenfeld, K. (1987a) 'Self-Organized Criticality: An Explanation of 1/f Noise', *Physical Review Letters*, 59(4), pp. 381–384. doi: 10.1103/PhysRevLett.59.381.

Bak, P., Tang, C. and Wiesenfeld, K. (1987b) 'Self-organized criticality: An explanation of the 1/f noise', *Physical Review Letters*, 59(4), pp. 381–384. doi: 10.1103/PhysRevLett.59.381.

Ballantyne, C. (1995) 'Paraglacial debris-cone formation on recently deglaciated terrain, western Norway', *The Holocene*, 5(1), pp. 25–33. doi: 10.1177/095968369500500104.

Ballantyne, C. (2002a) 'A general model of paraglacial landscape response', *The Holocene*, 12(3), pp. 371–376. doi: 10.1191/0959683602hl553fa.

Ballantyne, C. (2002b) 'Paraglacial geomorphology', *Quaternary Science Reviews*, 21(February 2001), pp. 1935–2017.

Ballantyne, C. (2008) 'After the Ice: Holocene Geomorphic Activity in the Scottish Highlands', *Scottish Geographical Journal*, 124(1), pp. 8–52. doi: 10.1080/14702540802300167.

Ballantyne, C. *et al.* (2014) 'Enhanced rock-slope failure following ice-sheet deglaciation: timing and causes', *Earth Surface Processes and Landforms*, 39(7), pp. 900–913. doi: 10.1002/esp.3495.

Ballantyne, C. and Benn, D. (1994) 'Resedimentation Recent Glacier Slope Following Paraglacial Adjustment Retreat, Fabergstolsdalen, Norway', *Arctic and Alpine Research*, 26(3), pp. 255–269.

Ballantyne, C. and Harris, C. (1994) *The periglaciation of Great Britain*. Cambridge: Cambridge University Press.

Ballantyne, C. and Kirkbride, M. (1987) 'Rockfall activity in upland Britain during the Loch Lomond Stadial', *Geographical Journal*, 153(1), pp. 86–92. doi: 10.2307/634474.

Ballantyne, C., Stone, J. and Fifield, L. (1998) 'Cosmogenic Cl-36 dating of postglacial landsliding at The Storr, Isle of Skye, Scotland', *The Holocene*, 8, pp. 347–351. doi: 10.1191/095968398666797200.

Bangen, S. *et al.* (2014) 'A methodological intercomparison of topographic survey techniques for characterizing wadeable streams and rivers', *Geomorphology*. Elsevier B.V., 206(February), pp. 343–361. doi: 10.1016/j.geomorph.2013.10.010.

Barker, R., Dixon, L. and Hooke, J. (1997) 'Use of terrestrial photogrammetry for monitoring and measuring bank erosion', *Earth Surface Processes and Landforms*, 22(13), pp. 1217–1227. doi: 10.1002/(SICI)1096-9837(199724)22:13<1217::AID-ESP819>3.0.CO;2-U.

Barlow, J. *et al.* (2012) 'Modeling cliff erosion using negative power law scaling of rockfalls', *Geomorphology*. Elsevier B.V., 139–140, pp. 416–424. doi: 10.1016/j.geomorph.2011.11.006.

Barnhart, T. and Crosby, B. (2013) 'Comparing two methods of surface change detection on an evolving thermokarst using high-temporal-frequency terrestrial laser scanning, Selawik River, Alaska', *Remote Sensing*, 5(6), pp. 2813–2837. doi: 10.3390/rs5062813.

Barr, I. and Spagnolo, M. (2014) 'Testing the efficacy of the glacial buzzsaw: Insights from the Sredinny Mountains, Kamchatka', *Geomorphology*. Elsevier B.V., 206, pp. 230–238. doi: 10.1016/j.geomorph.2013.09.026.

Barsch, D., Fierz, H. and Haeberli, W. (1979) 'Shallow Core Drilling and Bore-Hole Measurements in the Permafrost of an Active Rock Glacier near the Grubengletscher, Wallis, Swiss Alps', *Arctic and Alpine Research*, 11(2), pp. 215–228.

Barton, N. (1978) 'Suggested methods for the quantitative description of discontinuities in rock masses', *International Journal of Rock Mechanics and Mining Sciences*, pp. 319–368. doi: 10.1016/0148-9062(79)91476-1.

Bemis, S. *et al.* (2014) 'Ground-based and UAV-Based photogrammetry: A multi-scale, high-resolution mapping tool for structural geology and paleoseismology', *Journal of Structural Geology*. Elsevier Ltd, 69, pp. 163–178. doi: 10.1016/j.jsg.2014.10.007.

Benda, L. and Dunne, T. (1997) 'Stochastic forcing of sediment supply to channel networks from landsliding and debris flow', *Water Resources Research*, 33(12), pp. 2849–2863.

Benjamin, J., Rosser, N. and Brain, M. (2016) 'Rockfall detection and volumetric characterisation using LiDAR', *Landslides and Engineered Slopes. Experience, Theory and Practice*, pp. 389–395.

Benn, D. *et al.* (2012) 'Response of debris-covered glaciers in the Mount Everest region to recent warming, and implications for outburst flood hazards', *Earth-Science Reviews*, 114(1–2), pp. 156–174. doi: 10.1016/j.earscirev.2012.03.008.

Bennett, G. *et al.* (2012) 'Erosional power in the Swiss Alps: Characterization of slope failure in the Illgraben', *Earth Surface Processes and Landforms*, 37(15), pp. 1627–1640. doi: 10.1002/esp.3263.

Bennett, G. *et al.* (2014) 'A probabilistic sediment cascade model of sediment transfer in the Illgraben', *Water Resources Research*, 50(2), pp. 5375–5377. doi: 10.1002/2013WR014979.Reply.

Bennett, M. *et al.* (2000) 'Resedimentation of debris on an ice-cored lateral moraine in the high-Arctic (Kongsvegen, Svalbard)', *Geomorphology*, 35(1–2), pp. 21–40. doi: 10.1016/S0169-555X(00)00017-9.

Berthier, E. (2004) 'Recent rapid thinning of the "Mer de Glace" glacier derived from satellite optical images', *Geophysical Research Letters*, 31(17), p. L17401. doi: 10.1029/2004GL020706.

Berthier, E. and Vincent, C. (2012) 'Relative contribution of surface mass-balance and ice-flux

changes to the accelerated thinning of Mer de Glace, French Alps, over 1979–2008', *Journal of Glaciology*, 58(209), pp. 501–512. doi: 10.3189/2012JoG11J083.

Besl, P. and McKay, N. (1992) 'A Method for Registration of 3-D Shapes', *IEEE Transactions on Pattern Analysis and Machine Intelligence*, 14(2), pp. 239–256. doi: 10.1109/34.121791.

Beylich, A. and Lamoureux, S. (2016) *SEDIBUD Working Group*, *International Association of Geomorphologists*. Available at: http://www.geomorph.org/sedibud-working-group/.

Bieniawski, Z. (1976) 'Rock mass classification in rock engineering', in *Proceedings of the Symposium on Exploration for Rock Engineering*, pp. 97–106.

Blair, R. (1994) 'Moraine and Valley Wall Collapse due to Rapid Deglaciation in Mount Cook National Park, New Zealand', *Mountain Research and Development*, 14(4), pp. 347–358.

Bodin, X. *et al.* (2015) 'Mountain permafrost and associated geomorphological processes: recent changes in the French Alps', *Journal of Alpine Research | Revue de géographie alpine*, 103(2), pp. 2–16.

Borgatti, L. and Soldati, M. (2010) 'Landslides as a geomorphological proxy for climate change: A record from the Dolomites (northern Italy)', *Geomorphology*. Elsevier B.V., 120(1–2), pp. 56–64. doi: 10.1016/j.geomorph.2009.09.015.

Bornaz, L. and Dequal, S. (2004) 'The solid image: an easy and complete way to describe 3D objects', *XXth ISPRS Congress*, pp. 432–437.

Bovis, M. (1982) 'Uphill-facing (antislope) scarps in the Coast Mountains, southwest British Columbia.', *Geological Society of America Bulletin*, 93(8), pp. 804–812. doi: 10.1130/0016-7606(1982)93<804:UASITC>2.0.CO;2.

Bracken, L. *et al.* (2015) 'Sediment connectivity: A framework for understanding sediment transfer at multiple scales', *Earth Surface Processes and Landforms*, 40(2), pp. 177–188. doi: 10.1002/esp.3635.

Brardinoni, F. and Church, M. (2004) 'Representing the landslide magnitude-frequency relation: Capilano River basin, British Columbia', *Earth Surface Processes and Landforms*, 29(1), pp. 115–124. doi: 10.1002/esp.1029.

Brodu, N. and Lague, D. (2012) '3D terrestrial lidar data classification of complex natural scenes using a multi-scale dimensionality criterion: Applications in geomorphology', *ISPRS Journal of Photogrammetry and Remote Sensing*. International Society for Photogrammetry and Remote Sensing, Inc. (ISPRS), 68, pp. 121–134. doi: 10.1016/j.isprsjprs.2012.01.006.

Brown, D. (1965) 'Decentering distortion and the definitive calibration of metric cameras', *The*

American Society of Photogrammetry Convention.

Brun, F. *et al.* (2016) 'Quantifying volume loss from ice cliffs on debris-covered glaciers using high resolution terrestrial and aerial photogrammetry', *Journal of Glaciology*, l(May), p. accepted. doi: 10.1017/jog.2016.54.

Brunetti, M., Guzzetti, F. and Rossi, M. (2009) 'Probability distributions of landslide volumes', *Nonlinear Processes in Geophysics*, 16(2), pp. 179–188. doi: 10.5194/npg-16-179-2009.

Brunier, G. *et al.* (2016) 'Close-range airborne photogrammetry : an effective tool for high-resolution sandy beach morphometric surveys . Examples from embayed beaches in French Guyana', *Geomorphology*. Elsevier B.V., 17, p. 6019. doi: 10.1016/j.geomorph.2016.02.025.

Bühler, Y. *et al.* (2016) 'Mapping snow depth in alpine terrain with unmanned aerial systems (UAS): potential and limitations', *The Cryosphere*, 10, pp. 1075–1088. doi: doi:10.5194/tc-2015-220.

Carbonneau, P. and Dietrich, J. (2016) 'Cost-Effective Non-Metric Photogrammetry from Consumer-Grade sUAS: Implications for Direct Georeferencing of Structure from Motion Photogrammetry', *Earth Surface Processes and Landforms*. doi: 10.1002/esp.4012.

Cardinali, M. *et al.* (2001) 'Photo geological and landslide inventory map for the Upper Tiber River basin', *Pubblication CNR GNDCI*, 2116.

Carrivick, J. *et al.* (2013) 'Contemporary geomorphological activity throughout the proglacial area of an alpine catchment', *Geomorphology*. Elsevier B.V., 188, pp. 83–95. doi: 10.1016/j.geomorph.2012.03.029.

Carrivick, J. and Heckmann, T. (2017) 'Short-term geomorphological evolution of proglacial systems', *Geomorphology*. Elsevier B.V. doi: 10.1016/j.geomorph.2017.01.037.

Casas, D. *et al.* (2016) 'Magnitude-frequency distribution of submarine landslides in the Gioia Basin (southern Tyrrhenian Sea)', *Geo-Marine Letters*. Geo-Marine Letters. doi: 10.1007/s00367-016-0458-2.

Chau, K. *et al.* (2004) 'Landslide hazard analysis for Hong Kong using landslide inventory and GIS', *Computers and Geosciences*, 30(4), pp. 429–443. doi: 10.1016/j.cageo.2003.08.013.

Chaytor, J. *et al.* (2009) 'Size distribution of submarine landslides along the U.S. Atlantic margin', *Marine Geology*. Elsevier B.V., 264(1–2), pp. 16–27. doi: 10.1016/j.margeo.2008.08.007.

Chesley, J. *et al.* (2017) 'Using unmanned aerial vehicles and structure-from-motion photogrammetry to characterize sedimentary outcrops: An example from the Morrison Formation, Utah, USA', *Sedimentary Geology*. doi: 10.1016/j.sedgeo.2017.03.013.

Church, M. and Ryder, J. (1972) 'Paraglacial sedimentation: a consideration of fluvial processes conditioned by glaciation', *Geological Society of America Bulletin*, 10(10), pp. 3059–3072. doi: 10.1130/0016-7606(1972)83.

Clague, J. (2013) *Encyclopedia of Earth Sciences Series: Encyclopedia of Natural Hazards*. Edited by P. Bobrowsky. Dordrecht: Springer.

Clauset, A., Shalizi, C. and Newman, M. (2009) 'Power-Law Distributions in Empirical Data', *SIAM Review*, 51(4), p. 661. doi: 10.1137/070710111.

Cleveland, W. (1994) *The Elements of Graphing Data*. Summit, NJ, USA: Hobart Press.

CloudCompare (2017) *M3C2 projection cylinders - overlapping?*, *CloudCompare Forum*. Available at: http://www.danielgm.net/cc/forum/viewtopic.php?t=755 (Accessed: 24 June 2017).

Collins, B. and Stock, G. (2016) 'Rockfall triggering by cyclic thermal stressing of exfoliation fractures', *Nature Geoscience*, (March). doi: 10.1038/ngeo2686.

Colomina, I. and Molina, P. (2014) 'Unmanned aerial systems for photogrammetry and remote sensing: A review', *ISPRS Journal of Photogrammetry and Remote Sensing*. International Society for Photogrammetry and Remote Sensing, Inc. (ISPRS), 92, pp. 79–97. doi: 10.1016/j.isprsjprs.2014.02.013.

Conforti, D. and Deline, P. (2005) 'Terrestrial scanning lidar technology applied to study the evolution of the ice-contact Miage lake (Mont Blanc, Italy)', *Proceedings of the 9th Alpine Glaciological Meeting*.

Conrady, A. (1919) 'Decentred Lens-Systems', *Monthly Notices of the Royal Astronomical Soceity*, 79, pp. 384–390. Available at: http://scholar.google.com/scholar?hl=en&btnG=Search&q=intitle:Decentred+Lens-Systems#0.

Cook, K. (2016) 'An evaluation of the effectiveness of low-cost UAVs and structure from motion for geomorphic change detection', *Geomorphology (in revisions)*. Elsevier B.V. doi: 10.1016/j.geomorph.2016.11.009.

Cossart, E. *et al.* (2008) 'Slope instability in relation to glacial debuttressing in alpine areas (Upper Durance catchment, southeastern France): Evidence from field data and 10Be cosmic ray exposure ages', *Geomorphology*, 95(1–2), pp. 3–26. doi: 10.1016/j.geomorph.2006.12.022.

Cossart, E. and Fort, M. (2008) 'Sediment release and storage in early deglaciated areas: Towards an application of the exhaustion model from the case of Massif des Écrins (French Alps) since the Little Ice Age', *Norsk Geografisk Tidsskrift - Norwegian Journal of Geography*, 62(October 2014), pp. 115–131. doi: 10.1080/00291950802095145.

Crepaldi, S. *et al.* (2015) 'Landslide analysis by multi-temporal terrestrial laser scanning (TLS) data: the Mont de la Saxe landslide', *Rendiconti online della Società Geologica Italiana*, 35, pp. 92–95. doi: 10.3301/ROL.2015.72.

Crozier, M. (2010) 'Deciphering the effect of climate change on landslide activity: A review', *Geomorphology*. Elsevier B.V., 124(3–4), pp. 260–267. doi: 10.1016/j.geomorph.2010.04.009.

Cruden, D. and Hu, X. (1993) 'Exhaustion and steady state models for predicting landslide hazards in the Canadian Rocky Mountains', *Geomorphology*, 8(4), pp. 279–285. doi: 10.1016/0169-555X(93)90024-V.

Cruden, D. and Varnes, D. (1993) 'Landslide Types and Processes, Special Report', in *Landslides: Investigation and Mitigation*. Washington DC: National Academy Press. Available at: https://www.researchgate.net/publication/269710355_CrudenDM_Varnes_DJ_1996_Landslide_Types_and_Processes_Special_Report_Transportation_Research_Board_National_Academy_of_Sciences_24736-75.

Curry, A. (1998) 'Paraglacial modification of drift-mantled hillslopes', *PhD Thesis*. Available at: https://research-repository.st-andrews.ac.uk/handle/10023/7115.

Curry, A. (1999) 'Paraglacial modification of slope form', *Earth Surface Processes and Landforms*, 24(13), pp. 1213–1228. doi: 10.1002/(SICI)1096-9837(199912)24:13<1213::AID-ESP32>3.0.CO;2-B.

Curry, A. (2000) 'Observations on the distribution of paraglacial reworking of glacigenic drift in western Norway', *Norsk Geografisk Tidsskrift*, 54(4), pp. 139–147. doi: 10.1080/002919500448512.

Curry, A., Cleasby, V. and Zukowskyj, P. (2006) 'Paraglacial response of steep, sediment-mantled slopes to post-'Little Ice Age' glacier recession in the central Swiss Alps', *Journal of Quaternary Science*, 21(3), pp. 211–225. doi: 10.1002/jqs.954.

Curry, A., Sands, T. and Porter, P. (2009) 'Geotechnical controls on a steep lateral moraine undergoing paraglacial slope adjustment', *Geological Society, London, Special Publications*, 320(1), pp. 181–197. doi: 10.1144/SP320.12.

Danielgm.net (2016) 'CloudCompare: 3D point cloud and mesh processing software, Open Source Project', *http://www.danielgm.net/cc/*, v2.6.1.

Davies, M., Hamza, O. and Harris, C. (2001) 'The effect of rise in mean annual temperature on the stability of rock slopes containing ice-filled discontinuities', *Permafrost and Periglacial Processes*, 144, pp. 137–144. doi: 10.1002/ppp.

Davies, T. and Korup, O. (2010) 'Sediment Cascades in Active Landscapes', in Burt, T. and Allison,

R. (eds) *Sediment Cascades: An Intergrated Approach*. John Wiley & Sons Ltd., pp. 89–115.

Davies, T. and Shroder, J. (eds) (2014) *Landslide Hazards, Risks, and Disasters*. Amsterdam: Elsevier. doi: 10.1016/B978-0-12-394846-5.01001-8.

Decaulne, A. and Sæmundsson, Þ. (2007) 'Spatial and temporal diversity for debris-flow meteorological control in subarctic oceanic periglacial environments in Iceland', *Earth Surface Processes and Landforms*, 32, pp. 1971–1983.

Deline, P. (2005a) 'Change in surface debris cover on Mont Blanc massif glaciers after the "Little Ice Age" termination', *The Holocene*, 15, pp. 302–309. doi: 10.1191/0959683605hl809rr.

Deline, P. (2005b) 'Large rock avalanches on glacier since 2500 BP on the Italian flank of the Mont Blanc massif.', *Geophysical Research Abstracts*, 7(i), p. 7962.

Deline, P. *et al.* (2008) 'Ground-Based LiDAR data on permafrost-related rock fall activity in the Mont-Blanc massif', *Ninth international conference on Permafrost*, (i).

Deline, P. (2009) 'Interactions between rock avalanches and glaciers in the Mont Blanc massif during the late Holocene', *Quaternary Science Reviews*. Elsevier Ltd, 28(11–12), pp. 1070–1083. doi: 10.1016/j.quascirev.2008.09.025.

Deline, P. *et al.* (2012) 'The Morphodynamics of the Mont Blanc Massif in a Changing Cryosphere: a Comprehensive Review', *Geografiska Annaler: Series A, Physical Geography*, 94(2), pp. 265–283. doi: 10.1111/j.1468-0459.2012.00467.x.

Deline, P. *et al.* (2014) *Ice Loss and Slope Stability in High-Mountain Regions*, *Snow and Ice-Related Hazards, Risks, and Disasters*. doi: 10.1016/B978-0-12-394849-6.00015-9.

Deline, P. and Kirkbride, M. (2009) 'Rock avalanches on a glacier and morainic complex in Haut Val Ferret (Mont Blanc Massif, Italy)', *Geomorphology*. Elsevier B.V., 103, pp. 80–92. doi: 10.1016/j.geomorph.2007.10.020.

Dent, B. (1999) *Cartography: Thematic Map Design*. 5th edn. Boston, MA, USA: WCB McGraw-Hill.

Dewez, T., Leroux, J. and Morelli, S. (2016) 'Cliff collapse hazard from repeated multicopter UAV acquisitions: return on experience', *The International Archives of the Photogrammetry, Remote Sensing and Spatial Information Sciences: XXIII ISPRS Congress, 12–19 July 2016, Prague, Czech Republic*, XLI(B5), pp. 805–811. doi: 10.5194/isprsarchives-XLI-B5-805-2016.

Dikau, R. and Schrott, L. (1999) 'The temporal stability and activity of landslides in Europe with respect to climatic change (TESLEC): Main objectives and results', *Geomorphology*, 30(1–2), pp. 1–12. doi: 10.1016/S0169-555X(99)00040-9.

Dortch, J. *et al.* (2009) 'Nature and timing of large landslides in the Himalaya and Transhimalaya of northern India', *Quaternary Science Reviews*. Elsevier Ltd, 28(11–12), pp. 1037–1054. doi: 10.1016/j.quascirev.2008.05.002.

Dunning, S. *et al.* (2007) 'Landslides predating and triggered by the 2005 Kashmir Earthquake: rockfall to rock avalanches', *Geophysical Research Abstracts*, 9(06376).

Dunning, S. *et al.* (2015) 'Rapid sequestration of rock avalanche deposits within glaciers', *Nature Communications*. Nature Publishing Group, 6, p. 7964. doi: 10.1038/ncomms8964.

Dunning, S., Massey, C. and Rosser, N. (2009) 'Structural and geomorphological features of landslides in the Bhutan Himalaya derived from Terrestrial Laser Scanning', *Geomorphology*. Elsevier B.V., 103(1), pp. 17–29. doi: 10.1016/j.geomorph.2008.04.013.

van den Eeckhaut, M. *et al.* (2007) 'Characteristics of the size distribution of recent and historical landslides in a populated hilly region', *Earth and Planetary Science Letters*, 256(3–4), pp. 588–603. doi: 10.1016/j.epsl.2007.01.040.

Egli, D. and Mancktelow, N. (2013) 'The structural history of the Mont Blanc massif with regard to models for its recent exhumation', *Swiss Journal of Geosciences*, 106(3), pp. 469–489. doi: 10.1007/s00015-013-0153-5.

Eltner, A. *et al.* (2016) 'Image-based surface reconstruction in geomorphometry – merits, limits and developments of a promising tool for geoscientists', *Earth Surface Dynamics*, (May), pp. 1445–1508. doi: 10.5194/esurfd-3-1445-2015.

Ester, M. *et al.* (1996) 'A Density-Based Algorithm for Discovering Clusters', *KDD*, pp. 226–231.

Etzelmüller, B. and Frauenfelder, R. (2009) 'Factors Controlling The Distribution of Mountain Permafrost in The Northern Hemisphere and Their Influence on Sediment Transfer', *Arctic, Antarctic, and Alpine Research*, 41(1), pp. 48–58. doi: 10.1657/1938-4246(08-026)[ETZELMUELLER]2.0.CO;2.

Evans, S. and Clague, J. (1994) 'Recent climatic change and catastrophic geomorphic processes in mountain environments', *Geomorphology*, 10(1–4), pp. 107–128. doi: 10.1016/0169-555X(94)90011-6.

Fischer, L. *et al.* (2010) 'Assessment of periglacial slope stability for the 1988 Tschierva rock avalanche (Piz Morteratsch, Switzerland)', *Engineering Geology*. Elsevier B.V., 116(1–2), pp. 32–43. doi: 10.1016/j.enggeo.2010.07.005.

Fischer, L. *et al.* (2012) 'On the influence of topographic, geological and cryospheric factors on rock avalanches and rockfalls in high-mountain areas', *Natural Hazards and Earth System Science*,

12(1), pp. 241–254. doi: 10.5194/nhess-12-241-2012.

Fischer, L. *et al.* (2013) 'Slope failures and erosion rates on a glacierized high-mountain face under climatic changes', *Earth Surface Processes and Landforms*, 38(8), pp. 836–846. doi: 10.1002/esp.3355.

Fonstad, M. *et al.* (2013) 'Topographic structure from motion: a new development in photogrammetric measurement', *Earth Surface Processes and Landforms*, 38(4), pp. 421–430. doi: 10.1002/esp.3366.

Frankl, A. *et al.* (2015) 'Detailed recording of gully morphology in 3D through image-based modelling', *Catena*. Elsevier B.V., 127, pp. 92–101. doi: 10.1016/j.catena.2014.12.016.

Frauenfelder, R. *et al.* (2016) 'Ground thermal and geomechanical conditions in a permafrost-affected high-latitude rockslide site (Polvartinden, Northern Norway)', *The Cryosphere Discussions*, (November), pp. 1–31. doi: 10.5194/tc-2016-223.

Frigg, R. (2003) 'Self-organised criticality - What it is and what it isn't', *Studies in History and Philosophy of Science*, 34(3), pp. 613–632. doi: 10.1016/S0039-3681(03)00046-3.

Fryirs, K. *et al.* (2007) 'Buffers, barriers and blankets: The (dis)connectivity of catchment-scale sediment cascades', *Catena*, 70, pp. 49–67. doi: 10.1016/j.catena.2006.07.007.

Furukawa, Y. *et al.* (2010) 'Towards Internet-scale multi-view stereo', *IEEE Conference on Computer Vision and Pattern Recognition (CVPR)*, pp. 1434–1441. doi: 10.1109/CVPR.2010.5539802.

Furukawa, Y. and Ponce, J. (2007) 'Accurate, Dense, and Robust Multi-View Stereopsis', *IEEE Conference on Computer Vision and Pattern Recognition (CVPR)*, Minneapoli, pp. 1–8.

Geilhausen, M. *et al.* (2013) 'Sediment discharge from the proglacial zone of a retreating Alpine glacier', *Zeitschrift für Geomorphologie, Supplementary Issues*, 57(2), pp. 29–53. doi: 10.1127/0372-8854/2012/S-00122.

Gienko, G. and Terry, J. (2014) 'Three-dimensional modeling of coastal boulders using multi-view image measurements', *Earth Surface Processes and Landforms*, 39(7), pp. 853–864. doi: 10.1002/esp.3485.

Gillespie, C. (2015) 'Fitting heavy tailed distributions: the poweRlaw package', *Journal of Statistical Software*, 64(2), pp. 1–16. Available at: http://arxiv.org/abs/1407.3492.

Girod, L. *et al.* (2017) 'Terrain changes from images acquired on opportunistic flights by SfM photogrammetry', *Cryosphere*, 11(2), pp. 827–840. doi: 10.5194/tc-11-827-2017.

Glade, T. (1998) 'Establishing the frequency and magnitude of landslide-triggering rainstorm events in New Zealand', *Environmental Geology*, 35(August), pp. 2–3.

Glotzbach, C. *et al.* (2008) 'Neogene exhumation history of the Mont Blanc massif, western Alps', *Tectonics*, 27(4), p. n/a-n/a. doi: 10.1029/2008TC002257.

Gobiet, A. *et al.* (2014) 'Science of the Total Environment 21st century climate change in the European Alps — A review', *Science of the Total Environment*. The Authors, 493, pp. 1138–1151. doi: 10.1016/j.scitotenv.2013.07.050.

Godon, C. *et al.* (2013) 'The Bossons glacier protects Europe's summit from erosion', *Earth and Planetary Science Letters*. Elsevier, 375(1996), pp. 135–147. doi: 10.1016/j.epsl.2013.05.018.

Goehring, B. *et al.* (2012) 'Holocene dynamics of the Rhone Glacier, Switzerland, deduced from ice flow models and cosmogenic nuclides', *Earth and Planetary Science Letters*. Elsevier, 351–352, pp. 27–35. doi: 10.1016/j.epsl.2012.07.027.

Gonçalves, J. and Henriques, R. (2015) 'UAV photogrammetry for topographic monitoring of coastal areas', *ISPRS Journal of Photogrammetry and Remote Sensing*, 104, pp. 101–111. doi: 10.1016/j.isprsjprs.2015.02.009.

Gruber, S. (2012) 'Derivation and analysis of a high-resolution estimate of global permafrost zonation', *Cryosphere*, 6(1), pp. 221–233. doi: 10.5194/tc-6-221-2012.

Gruber, S. and Hoelzle, M. (2001) 'Statistical Modelling of Mountain Permafrost Distribution: Local Calibration and Incorporation of Remotely Sensed Data', *Permafrost and Periglacial Processes*, 12, pp. 69–77. doi: 10.1002/ppp.

Gruber, S., Hoelzle, M. and Haeberli, W. (2004) 'Permafrost thaw and destabilization of Alpine rock walls in the hot summer of 2003', *Geophysical Research Letters*, 31, pp. 1–4. doi: 10.1029/2004GL020051.

Guthrie, R. *et al.* (2007) 'Exploring the magnitude-frequency distribution: A cellular automata model for landslides', *Landslides*, 5(1), pp. 151–159. doi: 10.1007/s10346-007-0104-1.

Guthrie, R. and Evans, S. (2004) 'Magnitude and frequency of landslides triggered by a storm event, Loughborough Inlet, British Columbia', *Natural Hazards and Earth System Science*, 4(3), pp. 475–483. doi: 10.5194/nhess-4-475-2004.

Guzzetti, F. *et al.* (1999) 'Landslide hazard evaluation: A review of current techniques and their application in a multi-scale study, Central Italy', *Geomorphology*, 31(1–4), pp. 181–216. doi: 10.1016/S0169-555X(99)00078-1.

Guzzetti, F. *et al.* (2002) 'Power-law correlations of landslide areas in central Italy', *Earth and*

Planetary Science Letters, 195(3–4), pp. 169–183. doi: 10.1016/S0012-821X(01)00589-1.

Guzzetti, F. *et al.* (2008) 'Distribution of landslides in the Upper Tiber River basin, central Italy', *Geomorphology*, 96(1–2), pp. 105–122. doi: 10.1016/j.geomorph.2007.07.015.

Guzzetti, F. *et al.* (2009) 'Landslide volumes and landslide mobilization rates in Umbria, central Italy', *Earth and Planetary Science Letters*. Elsevier B.V., 279(3–4), pp. 222–229. doi: 10.1016/j.epsl.2009.01.005.

Haas, F. *et al.* (2016) 'Quantification and analysis of geomorphic processes on a recultivated iron ore mine on the Italian island Elba using long-time ground-based LIDAR and photogrammetric data by an UAV', *Natural Hazards and Earth System Sciences*, 16, pp. 1269–1288. doi: 10.5194/nhessd-3-6271-2015.

Haeberli, W. *et al.* (2007) 'Integrated monitoring of mountain glaciers as key indicators of global climate change: the European Alps', *Annals of Glaciology*, pp. 150–160.

Haeberli, W. and Beniston, M. (1998) 'Climate Change and its Impacts on Glaciers and Permafrost in the Alps', *Ambio*, 27(4), pp. 258–265.

Haeberli, W. and Epifani, F. (1986) 'Mapping the distribution of buried glacier ice - an example from Lago Delle Locce, Monte Rosa, Italian Alpes', *Annals of Glaciology*, 8, pp. 78–81. Available at: http://www.igsoc.org:8080/annals/8/igs_annals_vol08_year1985_pg78-81.pdf.

Hambrey, M. and Ehrmann, W. (2004) 'Modification of sediment characteristics during glacial transport in high-alpine catchments: Mount Cook area, New Zealand', *Boreas*, 33(4), pp. 300–318. doi: 10.1080/03009480410001965.

Hancox, G. and Thomson, R. (2013) *The January 2013 Mt Haast Rock Avalanche The January 2013 Mt Haast Rock Avalanche and Ball Ridge Rock Fall in Aoraki / Mt Cook National Park , New Zealand*, *GNS Science Report*.

Haneberg, W. (2008) 'Using close range terrestrial digital photogrammetry for 3-D rock slope modeling and discontinuity mapping in the United States', *Bulletin of Engineering Geology and the Environment*, 67(4), pp. 457–469. doi: 10.1007/s10064-008-0157-y.

Harland, W. (1957) 'Exfoliation joints and ice action', *Journal of Glaciology*, 3, p. 8\,--\,10.

Harrison, S. and Winchester, V. (1997) 'Age and nature of paraglacial debris cones along the margins of the San Rafael Glacier, Chilean Patagonia', *The Holocene*, 7(4), p. 481–487. 10.1177/095968369700700410. doi: 10.1177/095968369700700410.

Hasler, A., Gruber, S. and Beutel, J. (2012) 'Kinematics of steep bedrock permafrost', *Journal of Geophysical Research: Earth Surface*, 117(1), pp. 1–17. doi: 10.1029/2011JF001981.

Heckmann, T. *et al.* (2016) 'Integrating field measurements, a geomorphological map and stochastic modelling to estimate the spatially distributed rockfall sediment budget of the Upper Kaunertal, Austrian Central Alps', *Geomorphology*. Elsevier B.V., 260, pp. 16–31. doi: 10.1016/j.geomorph.2015.07.003.

Helmstetter, A. *et al.* (2015) 'Basal icequakes recorded beneath an Alpine glacier (Glacier d'Argentiere, Mont Blanc, France): Evidence for stick-slip motion?', *Journal of Geophysical Research: Earth Surface*, Accepted A. doi: 10.1002/2014JF003288.

Hencher, S. *et al.* (2011) 'Sheeting joints: Characterisation, shear strength and engineering', *Rock Mechanics and Rock Engineering*, 44(1), pp. 1–22. doi: 10.1007/s00603-010-0100-y.

Hobbs, B., Means, W. and Williams, P. (1976) *An outline of Structural Geology*. 1st edn. New York: John Wiley & Sons Ltd.

Hoek, E. (2000) *Practical rock engineering*. doi: 10.1016/S0022-3913(12)00047-9.

Hoek, E. and Bray, J. (1981) *Rock Slope Engineering*. 3rd edn. London: Taylor & Francis Routledge.

Hoskins, E., Jaeger, J. and Rosengren, K. (1968) 'A Medium-Scale Direct Friction Experiment', *International Journal of Rock Mechanics and Mining Sciences*, pp. 143–154.

Hovius, N. and Stark, C. (2006) 'Landslide-driven erosion and topographic evolution of active mountain belts', *Landslides from massive rock slope failure*, pp. 573–590.

Hovius, N., Stark, C. and Allen, P. (1997) 'Sediment flux from a mountain belt derived by landslide mapping', *Geology*. doi: 10.1130/0091-7613(1997)025<0231.

Hugemann, W. (2010) 'Correcting lens distortions in digital photographs', *Ingenieurbüro Morawski+ Hugemann: Leverkusen, …*, pp. 1–12. Available at: ftp://mirrors.linsrv.net/pub/imagemagick_html/Usage/lens/correcting_lens_distortions.pdf.

Hugenholtz, C. *et al.* (2008) 'Large-scale moraine deformation at the Athabasca Glacier, Jasper National Park, Alberta, Canada', *Landslides*, 5, pp. 251–260. doi: 10.1007/s10346-008-0116-5.

Huggel, C. *et al.* (2012) 'Ice thawing, mountains falling-are alpine rock slope failures increasing', *Geology Today*, 28(3), pp. 98–104. doi: 10.1111/j.1365-2451.2012.00836.x.

Huggel, C., Clague, J. and Korup, O. (2012) 'Is climate change responsible for changing landslide activity in high mountains?', *Earth Surface Processes and Landforms*, 37(1), pp. 77–91. doi: 10.1002/esp.2223.

Hungr, O. *et al.* (2001) 'A review of the classification of landslides of the flow type', *Environmental & Engineering Geoscience*, VII(3), pp. 221–238.

Hungr, O. *et al.* (2008) 'Magnitude–frequency relationships of debris flows and debris avalanches in relation to slope relief', *Geomorphology*, 96(3–4), pp. 355–365. doi: 10.1016/j.geomorph.2007.03.020.

Hungr, O., Evans, S. and Hazzard, J. (1999) 'Magnitude and frequency of rock falls and rock slides along the main transportation corridors of southwestern British Columbia', *Canadian Geotechnical Journal*, 36(Mackay 1997), pp. 224–238. doi: 10.1139/t98-106.

Hungr, O., Leroueil, S. and Picarelli, L. (2013) 'The Varnes classification of landslide types, an update', *Landslides*, 11(2), pp. 167–194. doi: 10.1007/s10346-013-0436-y.

Hürlimann, M., Abancó, C. and Moya, J. (2012) 'Rockfalls detached from a lateral moraine during spring season. 2010 and 2011 events observed at the Rebaixader debris-flow monitoring site (Central Pyrenees, Spain)', *Landslides*, 9(3), pp. 385–393. doi: 10.1007/s10346-011-0314-4.

Hurst, M. *et al.* (2013) 'Controls on the magnitude-frequency scaling of an inventory of secular landslides', *Earth Surface Dynamics*, 1, pp. 67–78. doi: 10.5194/esurf-1-67-2013.

Hutchinson, J. (1988) 'General report: morphological and geotechnical parameters of landslides in relation to geology and hydrogeology', *Proc 5th International Symposium on Landslides, Lausanne, 10–15 July*, 26(2), pp. 3–35.

Imhof, P. (2010) 'Glacier fluctuations in the Italian Mont Blanc massif from the Little Ice Age until the present', *Master's Thesis*, University.

Immerzeel, W. *et al.* (2014) 'High-resolution monitoring of Himalayan glacier dynamics using unmanned aerial vehicles', *Remote Sensing of Environment*. Elsevier Inc., 150, pp. 93–103. doi: 10.1016/j.rse.2014.04.025.

James, M. and Robson, S. (2012) 'Straightforward reconstruction of 3D surfaces and topography with a camera: Accuracy and geoscience application', *Journal of Geophysical Research*, 117(F3), p. F03017. doi: 10.1029/2011JF002289.

Javernick, L., Brasington, J. and Caruso, B. (2014) 'Modelling the topography of shallow braided rivers using Structure-from-Motion photogrammetry', *Geomorphology*. Elsevier B.V., 213, pp. 166–182. doi: 10.1016/j.geomorph.2014.01.006.

Kaiser, A. *et al.* (2014) 'Small-Scale Surface Reconstruction and Volume Calculation of Soil Erosion in Complex Moroccan Gully Morphology Using Structure from Motion', *Remote Sensing*, 6(8), pp. 7050–7080. doi: 10.3390/rs6087050.

Kalvoda, J. and Rosenfeld, C. (eds) (1998) *Geomorphological Hazards in High Mountain Areas*. Springer Netherlands. doi: 10.1659/0276-4741(2000)020[0203:GHIHMA]2.0.CO;2.

Keiler, M., Knight, J. and Harrison, S. (2010) 'Climate change and geomorphological hazards in the eastern European Alps.', *Philosophical transactions. Series A, Mathematical, physical, and engineering sciences*, 368(1919), pp. 2461–79. doi: 10.1098/rsta.2010.0047.

Kellerer-Pirklbauer, A., Proske, H. and Strasser, V. (2010) 'Paraglacial slope adjustment since the end of the Last Glacial Maximum and its long-lasting effects on secondary mass wasting processes: Hauser Kaibling, Austria', *Geomorphology*. Elsevier B.V., 120(1–2), pp. 65–76. doi: 10.1016/j.geomorph.2009.09.016.

Kelsey, K. *et al.* (1995) 'Geomorphic analysis of streamside landslides in the Redwood Creek basin, northwestern California', in *Geomorphic processes and aquatic habitat in the Redwood Creek basin, Northwestern California*. Profession. US Geological Survey, p. 292A–292A. Available at: http://www.ingentaconnect.com/content/els/01489062/1996/00000033/00000007/art83335%5Cnhttp://dx.doi.org/10.1016/0148-9062(96)83335-3%5Cnhttp://www.ingentaconnect.com/content/els/01489062/1996/00000033/00000007/art83335%5Cnhttp://dx.doi.org/10.1016/0148-90.

Kenner, R. *et al.* (2011) 'Investigation of rock and ice loss in a recently deglaciated mountain rock wall using terrestrial laser scanning: Gemsstock, Swiss Alps', *Cold Regions Science and Technology*. Elsevier B.V., 67(3), pp. 157–164. doi: 10.1016/j.coldregions.2011.04.006.

Kilburn, C. and Petley, D. (2003) 'Forecasting giant, catastrophic slope collapse: Lessons from Vajont, Northern Italy', *Geomorphology*, 54(1–2), pp. 21–32. doi: 10.1016/S0169-555X(03)00052-7.

Kirkbride, M. (2000) 'Ice-marginal geomorphology and Holocene expansion of debris-covered Tasman Glacier, New Zealand', *Debris-Covered Glaciers (Proceedings of a workshop held at Seattle, Washington, USA, September 2000)*. IAHS Publ, 264.

Kirkbride, M. (2011) 'Debris-Covered Glaciers', in Singh, V., Singh, P., and Haritashyma, U. (eds) *Encyclopedia of Earth Sciences Series: Encyclopedia of Snow, Ice and Glaciers*. Dordrecht: Springer, pp. 190–192.

Kirkbride, M. and Deline, P. (2018) 'Spatial heterogeneity in the paraglacial response to post-Little Ice Age deglaciation of four headwater cirques in the Western Alps', *Land Degradation & Development*, (March), pp. 1–14. doi: 10.1002/ldr.2975.

Kociuba, W. (2015) 'Assessment of sediment sources throughout the proglacial area of a small Arctic catchment based on high-resolution digital elevation models', *Geomorphology*. Elsevier B.V. doi: 10.1016/j.geomorph.2016.09.011.

Korup, O. (2005a) 'Distribution of landslides in southwest New Zealand', *Landslides*, 2(1), pp. 43–

51. doi: 10.1007/s10346-004-0042-0.

Korup, O. (2005b) 'Large landslides and their effect on sediment flux in South Westland, New Zealand', *Earth Surface Processes and Landforms*, 30, pp. 305–323. doi: 10.1002/esp.1143.

Korup, O. *et al.* (2007a) 'Giant landslides, topography, and erosion', *Earth and Planetary Science Letters*, 261(3–4), pp. 578–589. doi: 10.1016/j.epsl.2007.07.025.

Korup, O. *et al.* (2007b) 'Giant landslides, topography, and erosion', *Earth and Planetary Science Letters*, 261(3–4), pp. 578–589. doi: 10.1016/j.epsl.2007.07.025.

Korup, O. and Clague, J. (2009) 'Natural hazards, extreme events, and mountain topography', *Quaternary Science Reviews*. Elsevier Ltd, 28(11–12), pp. 977–990. doi: 10.1016/j.quascirev.2009.02.021.

Korup, O., Densmore, A. and Schlunegger, F. (2010) 'The role of landslides in mountain range evolution', *Geomorphology*. Elsevier B.V., 120(1–2), pp. 77–90. doi: 10.1016/j.geomorph.2009.09.017.

Korup, O., Strom, A. and Weidinger, J. (2006) 'Fluvial response to large rock-slope failures: Examples from the Himalayas, the Tien Shan, and the Southern Alps in New Zealand', *Geomorphology*, 78(1–2), pp. 3–21. doi: 10.1016/j.geomorph.2006.01.020.

Kovanen, D. and Slaymaker, O. (2015) 'Geomorphology The paraglacial geomorphology of the Fraser Lowland , southwest British Columbia and northwest Washington', *Geomorphology*. Elsevier B.V., 232, pp. 78–93. doi: 10.1016/j.geomorph.2014.12.021.

Krautblatter, M. and Dikau, R. (2007) 'Towards a uniform concept for the comparison and extrapolation of rockwall retreat and rockfall supply', *Swedish Society for Anthropology and Geography*, 89(1), pp. 21–40. doi: 10.1111/j.1468-0459.2007.00305.x.

Krautblatter, M., Funk, D. and Günzel, F. (2013) 'Why permafrost rocks become unstable: a rock-ice-mechanical model in time and space', *Earth Surface Processes and Landforms*, 38(8), pp. 876–887. doi: 10.1002/esp.3374.

Krautblatter, M. and Moore, J. (2014) 'Rock slope instability and erosion: toward improved process understanding', *Earth Surface Processes and Landforms*, 39(9), pp. 1273–1278. doi: 10.1002/esp.3578.

Krautblatter, M. and Moser, M. (2009) 'A nonlinear model coupling rockfall and rainfall intensity based on a four year measurement in a high Alpine rock wall (Reintal, German Alps)', *Natural Hazards and Earth System Science*, 9, pp. 1425–1432.

Lague, D. (2014) 'What's the Point of a Raster? Advantages of 3D Point Cloud Processing over

Raster Based Methods for Accurate Geomorphic Analysis of High Resolution Topography', in *AGU Fall Meeting 2014, San Francisco, US*, p. EP43E–05. Available at: https://hal-insu.archives-ouvertes.fr/insu-01088527/.

Lague, D., Brodu, N. and Leroux, J. (2013) 'Accurate 3D comparison of complex topography with terrestrial laser scanner: Application to the Rangitikei canyon (NZ)', *ISPRS Journal of Photogrammetry and Remote Sensing*. International Society for Photogrammetry and Remote Sensing, Inc. (ISPRS), 82, pp. 10–26. doi: 10.1016/j.isprsjprs.2013.04.009.

Lane, S. *et al.* (2016) 'Sediment export, transient landscape response and catchment-scale connectivity following rapid climate warming and Alpine glacier recession', *Geomorphology*. Elsevier B.V. doi: 10.1016/j.geomorph.2016.02.015.

Larsen, I., Montgomery, D. and Korup, O. (2010) 'Landslide erosion controlled by hillslope material', *Nature Geoscience*. Nature Publishing Group, 3(4), pp. 247–251. doi: 10.1038/ngeo776.

Lato, M. and Vöge, M. (2012) 'Automated mapping of rock discontinuities in 3D lidar and photogrammetry models', *International Journal of Rock Mechanics and Mining Sciences*, 54, pp. 150–158. doi: 10.1016/j.ijrmms.2012.06.003.

Laute, K. and Beylich, A. (2013) 'Holocene hillslope development in glacially formed valley systems in Nordfjord, western Norway', *Geomorphology*. Elsevier B.V., 188, pp. 12–30. doi: 10.1016/j.geomorph.2012.11.021.

Laute, K. and Beylich, A. (2014) 'Environmental controls, rates and mass transfers of contemporary hillslope processes in the headwaters of two glacier-connected drainage basins in western Norway', *Geomorphology*. Elsevier B.V., 216, pp. 93–113. doi: 10.1016/j.geomorph.2014.03.021.

Leon, J. *et al.* (2015) 'Measuring coral reef terrain roughness using "Structure-from-Motion" close-range photogrammetry', *Geomorphology*. Elsevier B.V., pp. 1–8. doi: 10.1016/j.geomorph.2015.01.030.

Leonelli, G. and Pelfini, M. (2013) 'Past surface instability of Miage debris-covered glacier tongue (Mont Blanc Massif, Italy): a decadal-scale tree-ring-based reconstruction', *Boreas*, 42, pp. 613–622. doi: 10.1111/j.1502-3885.2012.00291.x.

Li, L., Lan, H. and Wu, Y. (2014) 'The volume-to-surface-area ratio constrains the rollover of the power law distribution for landslide size', *The European Physical Journal Plus*, 129(5), p. 89. doi: 10.1140/epjp/i2014-14089-y.

Li, L., Lan, H. and Wu, Y. (2016) 'How sample size can effect landslide size distribution',

Geoenvironmental Disasters. Geoenvironmental Disasters, 3(1), p. 18. doi: 10.1186/s40677-016-0052-y.

Lim, M. *et al.* (2005) 'Combined digital photogrammetry and time-of-flight laser scanning for monitoring cliff evolution', *Photogrammetric Record*, 17, pp. 0–26.

Lin, G. *et al.* (2008) 'Effects of earthquake and cyclone sequencing on landsliding and fluvial sediment transfer in a mountain catchment', *Earth Surface Processes and Landforms*. doi: 10.1002/esp.1716.

Lowe, D. (1999) 'Object recognition from local scale-invariant features', *Proceedings of the Seventh IEEE International Conference on Computer Vision*. Ieee, 2, pp. 1150–1157. doi: 10.1109/ICCV.1999.790410.

Lowe, D. (2004) 'Distinctive Image Features from Scale-Invariant Keypoints', *International Journal of Computer Vision*, 60(2), pp. 91–110. doi: 10.1023/B:VISI.0000029664.99615.94.

Lucieer, A., Jong, S. and Turner, D. (2013) 'Mapping landslide displacements using Structure from Motion (SfM) and image correlation of multi-temporal UAV photography', *Progress in Physical Geography*, 38(1), pp. 97–116. doi: 10.1177/0309133313515293.

MacEachren, A. (2004) *How Maps Work*. New York, NY, USA: The Guildford Press.

Magnin, F. *et al.* (2015) 'Determination of warm, sensitive permafrost areas in near-vertical rockwalls and evaluation of distributed models by Electrical Resistivity Tomography', *Journal of Geophysical Research: Earth Surface*, Accepted A, p. n/a-n/a. doi: 10.1002/2014JF003351.

Magnin, F. *et al.* (2016) 'Modelling rock wall permafrost degradation in the Mont Blanc massif from the LIA to the end of the 21st century', *The Cryosphere Discussions*, 6(July), pp. 1–37. doi: 10.5194/tc-2016-132.

Maizels, J. (1979) 'Proglacial Aggradation and Changes in Braided Channel Patterns During a Period of Glacier Advance: An Alpine Example', *Geografiska Annaler, Series A: Physical Geography*, 61(1–2), pp. 87–101.

Maizels, J. (1983) 'Proglacial channel systems: change and thresholds for change over long, intermediate and short time-scales', in Collinson, J. and Lewin, J. (eds) *Modern and Ancient Fluvial Systems*. John Wiley & Sons Ltd., pp. 251–266.

Malamud, B. *et al.* (2004a) 'Landslide inventories and their statistical properties', *Earth Surface Processes and Landforms*, 29, pp. 687–711. doi: 10.1002/esp.1064.

Malamud, B. *et al.* (2004b) 'Landslides, earthquakes, and erosion', *Earth and Planetary Science Letters*, 229(1–2), pp. 45–59. doi: 10.1016/j.epsl.2004.10.018.

Mancini, F. *et al.* (2013) 'Using Unmanned Aerial Vehicles (UAV) for High-Resolution Reconstruction of Topography: The Structure from Motion Approach on Coastal Environments', *Remote Sensing*, 5(12), pp. 6880–6898. doi: 10.3390/rs5126880.

Marinos, P., Marinos, V. and Hoek, E. (2007) 'The Geological Strength Index (GSI): a Characterization Tool for Assessing Engineering Properties for Rock Masses', *Proceedings International Workshop on Rock Mass Classification for Underground Mining*, 9498, pp. 87–94.

Marques, F. (2008) 'Magnitude-frequency of sea cliff instabilities', *Natural Hazards and Earth System Sciences* , 8, pp. 1161–1171. Available at: www.nat-hazards-earth-syst-sci.net/8/1161/2008/.

Martel, S. (2006) 'Effect of topographic curvature on near-surface stresses and application to sheeting joints', *Geophysical Research Letters*, 33(1), pp. 1–5. doi: 10.1029/2005GL024710.

Matasci, B. *et al.* (2014) 'Rockfalls detection and characterization in the west face of the Drus (Mont Blanc), based on Gigapixel images and Terrestrial Laser Scanning', *Vertical Geology Conference*, (February), p. 7.

Mattson, E. and Gardner, J. (1991) 'Mass Wasting on Valley-Side Ice-Cored Moraines, Boundary Glacier, Alberta, Canada', *Geografiska Annaler, Series A: Physical Geography*, 73(3), pp. 123–128.

McColl, S. (2010) 'Glacier retreat and rock-slope stability: debunking debuttressing', *Geologically active: delegate papers 11th Congress of the International Association for Engineering Geology and the Environment*, pp. 467–474.

McColl, S. (2012) 'Paraglacial rock-slope stability', *Geomorphology*. Elsevier B.V., 153–154, pp. 1–16. doi: 10.1016/j.geomorph.2012.02.015.

McColl, S. and Davies, T. (2013) 'Large ice-contact slope movements: glacial buttressing, deformation and erosion', *Earth Surface Processes and Landforms*, 38(10), pp. 1102–1115. doi: 10.1002/esp.3346.

Mercier, D. (2008) 'Paraglacial and paraperiglacial landsystems: concepts, temporal scales and spatial distribution', *Géomorphologie: relief, processus, environnement*, 4(December 2008), pp. 223–234. doi: 10.4000/geomorphologie.7396.

Mercier, D. *et al.* (2009) 'Paraglacial gullying of sediment-mantled slopes: A case study of Colletthogda, Kongsfjorden area, West Spitsbergen (Svalbard)', *Earth Surface Processes and Landforms*, 34(13), pp. 1772–1789. doi: 10.1002/esp.1862.

Messenzehl, K., Hoffmann, T. and Dikau, R. (2014) 'Sediment connectivity in the high-alpine valley of Val Müschauns, Swiss National Park - linking geomorphic field mapping with geomorphometric

modelling', *Geomorphology*. Elsevier B.V., 221, pp. 215–229. doi: 10.1016/j.geomorph.2014.05.033.

Mihalcea, C. *et al.* (2008) 'Using ASTER satellite and ground-based surface temperature measurements to derive supraglacial debris cover and thickness patterns on Miage Glacier (Mont Blanc Massif, Italy)', *Cold Regions Science and Technology*, 52(3), pp. 341–354. doi: 10.1016/j.coldregions.2007.03.004.

Miles, E. *et al.* (2016) 'Refined energy-balance modelling of a supraglacial pond, Langtang Khola, Nepal', *Annals of Glaciology*, 57(71), pp. 29–40. doi: 10.3189/2016AoG71A421.

Mitchell, S. and Montgomery, D. (2006) 'Influence of a glacial buzzsaw on the height and morphology of the Cascade Range in central Washington State, USA', *Quaternary Research*, 65(1), pp. 96–107. doi: 10.1016/j.yqres.2005.08.018.

Mitzenmacher, M. (2004) 'A Brief History of Generative Models for Power Law and Lognormal Distributions', *Internet Mathematics*, 1(2), pp. 226–251.

Moore, J. *et al.* (2009) 'Influence of rock mass strength on the erosion rate of alpine cliffs', *Earth Surface Processes and Landforms*, 34(10), p. 1339. doi: 10.1002/esp.

Muller, S. (1947) 'Permafrost or Permanently Frozen Ground and Related Engineering Problems', *Ann Arbor: J.W. Edwards.*

Muniruzzaman, A. (1957) 'On measures of location and dispersion and test of hypothesis on a Pareto distribution', *Calcutta Statistical Association Bulletin*, 7, pp. 115–123.

Newman, M. (2005) 'Power laws, Pareto distributions and Zipf's law', *Contemporary Physics*, 46(5), pp. 323–351. doi: 10.1016/j.cities.2012.03.001.

Nichols, T. (1980) 'Rebound, its nature and effect on engineering works', *Quarterly Journal of Engineering Geology*, 13, pp. 133–152.

Nile, W. (1872) 'Peculiar Phenomena Observed in Quarrying', *Pacific Rural Press*, p. 195.

Noetzli, J., Hoelzle, M. and Haeberli, W. (2003) 'Mountain permafrost and recent Alpine rock-fall events: a GIS-based approach to determine critical factors', *Permafrost*, pp. 827–832.

Nöthiger, C. and Elsasser, H. (2004) 'Natural Hazards and Tourism: New Findings on the European Alps', *Mountain Research and Development*, 24(1), pp. 24–27. doi: 10.1659/0276-4741(2004)024[0024:NHATNF]2.0.CO;2.

Nouwakpo, S., Weltz, M. and McGwire, K. (2015) 'Assessing the performance of Structure-from-Motion photogrammetry and terrestrial lidar for reconstructing soil surface microtopography of

naturally vegetated plots', *Earth Surface Processes and Landforms*, p. n/a-n/a. doi: 10.1002/esp.3787.

Nussbaumer, S. and Zumbühl, H. (2012) 'The Little Ice Age history of the Glacier des Bossons (Mont Blanc massif, France): a new high-resolution glacier length curve based on historical documents', *Climatic Change*, 111, pp. 301–334. doi: 10.1007/s10584-011-0130-9.

Nussbaumer, S., Zumbühl, H. and Steiner, D. (2007) 'Fluctuations of the" Mer de Glace"(Mont Blanc area, France) AD 1500-2050: an interdisciplinary approach using new historical data and neural network', *Zeitschrift für Gletscherkunde und Glazialgeologie*, 40.

Östrem, G. (1959) 'Ice Melting under a Thin Layer of Moraine, and the Existence of Ice Cores in Moraine Ridges', *Geografiska Annaler*, 4(4), pp. 228–230.

Otto, J. *et al.* (2009) 'Quantifying sediment storage in a high alpine valley (Turtmanntal, Switzerland)', *Earth Surface Processes and Landforms*, 34, pp. 1726–1742. doi: 10.1002/esp.

Ouédraogo, M. *et al.* (2014a) 'The evaluation of unmanned aerial system-based photogrammetry and terrestrial laser scanning to generate DEMs of agricultural watersheds', *Geomorphology*. Elsevier B.V., 214, pp. 339–355. doi: 10.1016/j.geomorph.2014.02.016.

Ouédraogo, M. *et al.* (2014b) 'The evaluation of unmanned aerial systems-based photogrammetry and terrestrial laser scanning to generate DEMs of agricultural watersheds', *Geomorphology*. Elsevier B.V. doi: 10.1016/j.geomorph.2014.02.016.

Passalacqua, P. *et al.* (2015) 'Analyzing high resolution topography for advancing the understanding of mass and energy transfer through landscapes: A review', *Earth-Science Reviews*. Elsevier B.V., 148, pp. 174–193. doi: 10.1016/j.earscirev.2015.05.012.

Pelfini, M. *et al.* (2007) 'Investigating surface movements of debris-covered Miage glacier, Western Italian Alps, using dendroglaciological analysis', *Journal of Glaciology*, 53(180), pp. 141–152. doi: 10.3189/172756507781833839.

Pellicciotti, F. *et al.* (2015) 'Mass-balance changes of the debris-covered glaciers in the Langtang Himal, Nepal, from 1974 to 1999', *Journal of Glaciology*, 61(226), pp. 373–386. doi: 10.3189/2015JoG13J237.

Peppa, M. *et al.* (2016) 'Accuracy assessment of a UAV-based landslide monitoring system', *The International Archives of the Photogrammetry, Remote Sensing and Spatial Information Sciences: XXIII ISPRS Congress, 12–19 July 2016, Prague, Czech Republic*, XLI(B5), pp. 12–19. doi: 10.5194/isprsarchives-XLI-B5-895-2016.

Perline, R. (2005) 'Strong, Weak and False Inverse Power Laws', *Statistical Science*, 20(1), pp. 68–

88. doi: 10.1214/088342304000000215.

Petley, D. (2012) 'Global patterns of loss of life from landslides', *Geology*, 40(10), pp. 927–930. doi: 10.1130/G33217.1.

Petzl (2014) *Mont Blanc: how can we reduce accidents in the Goûter couloir?*, *The Petzl Foundation*. Available at: http://www.petzl.com/fondation/projets/accidents-couloir-gouter?language=en#.Viigf36rRhE.

Piermattei, L. *et al.* (2015) 'Monitoring of a debris-covered and avalanche-fed glacier in the Eastern Italian Alps using ground-based SfM-MVS', *Geophysical Research Abstracts*, 17, p. 5236.

Piermattei, L., Carturan, L. and Guarnieri, A. (2015) 'Use of terrestrial photogrammetry based on structure from motion for mass balance estimation of a small glacier in the Italian Alps', *Earth Surface Processes and Landforms*. doi: 10.1002/esp.3756.

Piteau, D. (1972) 'Engineering Geology Aspects Relating to Preliminary Damsite Investigations on the Nelson River, Manitoba', *Canadian Geotechnical Journal*, 9(3), pp. 304–313.

Pix4D, S. (2015) *Pix4D*, *Pix4Dmapper Pro*. Available at: https://pix4d.com/products/.

Porter, S. and Orombelli, G. (1980) 'Catastrophic rockfall of September 12, 1717 on the Italian flank of the Mont Blanc massif', *Zeitschrift für Geomorphologie*, 24, pp. 200–218.

Pröbstl-Haider, U., Dabrowska, K. and Haider, W. (2016) 'Risk perception and preferences of mountain tourists in light of glacial retreat and permafrost degradation in the Austrian Alps', *Journal of Outdoor Recreation and Tourism*. Elsevier, pp. 1–13. doi: 10.1016/j.jort.2016.02.002.

Purdie, H., Gomez, C. and Espiner, S. (2015) 'Glacier recession and the changing rockfall hazard: Implications for glacier tourism', *New Zealand Geographer*, Article in. doi: 10.1111/nzg.12091.

von Raumer, J. and Bussy, F. (2004) 'Mont Blanc and Aiguilles Rouges: Geology of their polymetamorphic Basement', *Memoires de Geologie*, (42).

Ravanel, L. *et al.* (2010) 'Rock falls in the Mont Blanc Massif in 2007 and 2008', *Landslides*, 7, pp. 493–501. doi: 10.1007/s10346-010-0206-z.

Ravanel, L. and Deline, P. (2011) 'Climate influence on rockfalls in high-Alpine steep rockwalls: The north side of the Aiguilles de Chamonix (Mont Blanc massif) since the end of the "Little Ice Age"', *The Holocene*, 21(2), pp. 357–365. doi: 10.1177/0959683610374887.

Ray, R. and De Smedt, F. (2009) 'Slope stability analysis on a regional scale using GIS: A case study from Dhading, Nepal', *Environmental Geology*, 57(7), pp. 1603–1611. doi: 10.1007/s00254-008-1435-5.

Reid, T. and Brock, B. (2010) 'An energy-balance model for debris-covered glaciers including heat conduction through the debris layer', *Journal of Glaciology*, 56(199), pp. 903–916. doi: 10.3189/002214310794457218.

Remondino, F. *et al.* (2014) 'State of the art in high density image matching', *The Photogrammetric Record*, 29(June), pp. 144–166. doi: 10.1111/phor.12063.

Reznichenko, N. *et al.* (2010) 'Effects of debris on ice-surface melting rates: an experimental study', *Journal of Glaciology*, 56(197), pp. 384–394. doi: 10.3189/002214310792447725.

Reznichenko, N. *et al.* (2012) 'A new technique for identifying rock avalanche-sourced sediment in moraines and some paleoclimatic implications', *Geology*, 40(4), pp. 319–322. doi: 10.1130/G32684.1.

Reznichenko, N. (2012) 'Rock Avalanches on Glaciers: Processes and Implications', *PhD Thesis*.

Rich, P. *et al.* (1994) 'Using Viewshed Models to Calculate Intercepted Solar Radiation: Applications in Ecology', *American Society for Photogrammetry and Remote Sensing Technical Papers*, pp. 524–529.

Rippin, D., Pomfret, A. and King, N. (2015) 'High resolution mapping of supraglacial drainage pathways reveals link between micro-channel drainage density, surface roughness and surface reflectance', *Earth Surface Processes and Landforms*, 1290(March), pp. 1279–1290. doi: 10.1002/esp.3719.

Riquelme, A. *et al.* (2014) 'A new approach for semi-automatic rock mass joints recognition from 3D point clouds', *Computers & Geosciences*. Elsevier, 68, pp. 38–52. doi: 10.1016/j.cageo.2014.03.014.

Riquelme, A. *et al.* (2015) 'Semi-automatic characterization of fractured rock masses using 3D point clouds: discontinuity orientation, spacing and SMR geomechanical classification', *Geophysical Research Abstracts*, 17, p. 15459.

Riquelme, A. *et al.* (2016) 'Using open-source software for extracting geomechanical parameters of a rock mass from 3D point clouds: Discontinuity Set Extractor and SMRTool', *Rock Mechanics and Rock Engineering*, pp. 1091–1096.

Riquelme, A., Abellán, A. and Tomás, R. (2015) 'Discontinuity spacing analysis in rock masses using 3D point clouds', *Engineering Geology*. Elsevier B.V., 195, pp. 185–195. doi: 10.1016/j.enggeo.2015.06.009.

Riquelme, A., Tomás, R. and Abellán, A. (2014) 'SMRTool beta: A calculator for determining Slope Mass Rating (SMR)'. Universidad de Alicante. Available at:

http://personal.ua.es/es/ariquelme/smrtool.html.

Rizaldy, A. and Firdaus, W. (2012) 'Direct Georeferencing: a New Standard in Photogrammetry for High Accuracy Mapping', *ISPRS - International Archives of the Photogrammetry, Remote Sensing and Spatial Information Sciences*, 39(September), pp. 5–9. doi: 10.5194/isprsarchives-XXXIX-B1-5-2012.

Robinson, A. (2015) *Spatial Objects: Temporal Subjects*, *Dan Holdsworth Studio*. Available at: http://www.danholdsworth.com/texts/spatialobjectstemporalsubjects/ (Accessed: 21 November 2016).

Robinson, A. (2016) *Continuous Topography*, *Dan Holdsworth Studio*. Available at: http://www.danholdsworth.com/texts/continuoustopography/ (Accessed: 21 November 2016).

RocScience (2014) 'RocProp 2.0'. RocScience. Available at: http://www.rocscience.com/.

Rolland, Y. *et al.* (2003) 'Rare earth and trace element mobility in mid-crustal shear zones: Insights from the Mont Blanc Massif (Western Alps)', *Earth and Planetary Science Letters*, 214(1–2), pp. 203–219. doi: 10.1016/S0012-821X(03)00372-8.

Romana, M. (1993) *A Geomechanical Classification for Slopes: Slope Mass Rating*, *Comprehensive Rock Engineering*.

Rose, D. (2003) 'Record heatwave closes Mont Blanc to tourists', *The Guardian*, August. Available at: https://www.theguardian.com/environment/2003/aug/17/france.climatechange1.

Rosser, N. *et al.* (2005) 'Terrestrial laser scanning for monitoring the process of hard rock coastal cliff erosion', *Quarterly Journal of Engineering Geology and Hydrogeology*, 38, pp. 363–375.

Rosser, N. *et al.* (2007) 'Patterns of precursory rockfall prior to slope failure', *Journal of Geophysical Research*, 112, p. F04014. doi: 10.1029/2006JF000642.

Roussel, E. *et al.* (2008) 'Processes and rates of post-Little Ice Age proximal sandar incision (southern Iceland)', *Géomorphologie : relief, processus, environnement*, 4, pp. 235–248. doi: 10.4000/geomorphologie.8765.

Le Roy, M. *et al.* (2015) 'Calendar-dated glacier variations in the western European Alps during the Neoglacial: the Mer de Glace record, Mont Blanc massif', *Quaternary Science Reviews*, 108, pp. 1–22. doi: 10.1016/j.quascirev.2014.10.033.

Ryan, J. *et al.* (2015) 'UAV photogrammetry and structure from motion to assess calving dynamics at Store Glacier, a large outlet draining the Greenland ice sheet', *The Cryosphere*, 9(1), pp. 1–11. doi: 10.5194/tc-9-1-2015.

Sanders, J. *et al.* (2012) 'Periglacial weathering and headwall erosion in cirque glacier bergschrunds', *Geology*, 40(9), pp. 779–782. doi: 10.1130/G33330.1.

Scherler, D., Bookhagen, B. and Strecker, M. (2011) 'Spatially variable response of Himalayan glaciers to climate change affected by debris cover', *Nature Geoscience*. Nature Publishing Group, 4(3), pp. 156–159. doi: 10.1038/ngeo1068.

Schmidt, J. and Dikau, R. (2004) 'Modeling historical climate variability and slope stability', *Geomorphology*, 60(3–4), pp. 433–447. doi: 10.1016/j.geomorph.2003.11.001.

Schomacker, A. and Kjaer, K. (2008) 'Quantification of dead-ice melting in ice-cored moraines at the high-Arctic glacier Holmstrombreen, Svalbard', *Boreas*, 37(2), pp. 211–225. doi: 10.1111/j.1502-3885.2007.00014.x.

Schürch, P. *et al.* (2011) 'Detection of surface change in complex topography using terrestrial laser scanning: application to the Illgraben debris-flow channel', *Earth Surface Processes and Landforms*, 36(14), pp. 1847–1859. doi: 10.1002/esp.2206.

Selby, M. (1980) 'A rock mass strength classification for geomorphic purposes: with tests from Antarctica and New Zealand', *Zeitschrift für Geomorphologie*, 24(1), pp. 31–51.

Selby, M. (1982) 'Controls on the Stability and Inclinations of Hillslopes formed on Hard Rock', *Earth Surface Processes and Landforms*, 7, pp. 449–467.

Selby, M. (1993) *Hillslope Materials and Processes*. 2nd edn. Oxford: Oxford University Press.

Semyonov, D. (2014) *Algorithms used in Photoscan*, *Agisoft Photoscan User Forum*.

Shulmeister, J. *et al.* (2009) 'Catastrophic landslides, glacier behaviour and moraine formation – A view from an active plate margin', *Quaternary Science Reviews*. Elsevier Ltd, 28, pp. 1085–1096. doi: 10.1016/j.quascirev.2008.11.015.

Six, D. and Vincent, C. (2014) 'Sensitivity of mass balance and equilibrium-line altitude to climate change in the French Alps', *Journal of Glaciology*, 60(223), pp. 867–878. doi: 10.3189/2014JoG14J014.

Slaymaker, O. (2009) 'Proglacial, periglacial of paraglacial?', *The Geological Society, London, Special Publications*, 320, pp. 71–84.

Slob, S. *et al.* (2005) 'Method for Automated Discontinuity Analysis of Rock Slopes with Three-Dimensional Laser Scanning', *Transportation Research Record*, 1913(1), pp. 187–194. doi: 10.3141/1913-18.

Smith, M. *et al.* (2014) 'Reconstructing flash flood magnitudes using "Structure-from-Motion": A

rapid assessment tool', *Journal of Hydrology*. Elsevier B.V., 519(PB), pp. 1914–1927. doi: 10.1016/j.jhydrol.2014.09.078.

Smith, M., Carrivick, J. and Quincey, D. (2015) 'Structure from motion photogrammetry in physical geography', *Progress in Physical Geography*, pp. 1–29. doi: 10.1177/0309133315615805.

Snavely, N. (2008) 'Scene reconstruction and visualization from internet photo collections', *Unpublished PhD Thesis*, Unpublishe.

Snavely, N., Seitz, S. and Szeliski, R. (2008) 'Modeling the World from Internet Photo Collections', *International Journal of Computer Vision*, 80(2), pp. 189–210. doi: 10.1007/s11263-007-0107-3.

Stark, C. and Hovius, N. (2001) 'The characterization of landslide size distributions', *Geophysical Research Letters*, 28(6), pp. 1091–1094. doi: 10.1029/2000GL008527.

Stöcker, C., Eltner, A. and Karrasch, P. (2015) 'Measuring gullies by synergetic application of UAV and close range photogrammetry - A case study from Andalusia, Spain', *Catena*. Elsevier B.V., 132, pp. 1–11. doi: 10.1016/j.catena.2015.04.004.

Stocker, T. *et al.* (2013) *IPCC, 2013: Climate Change 2013: The Physical Science Basis. Contribution of Working Group I to the Fifth Assessment Report of the Intergovernmental Panel on Climate Change*. Cambridge, UK & New York, USA. doi: 10.1017/CBO9781107415324.

Strunden, J. *et al.* (2015a) 'Spatial and temporal variations in rockfall determined from TLS measurements in a deglaciated valley, Switzerland', *Journal of Geophysical Research: Earth Surface*. doi: 10.1002/2014JF003274.

Strunden, J. *et al.* (2015b) 'Spatial and temporal variations in rockfall determined from TLS measurements in a deglaciated valley, Switzerland', *Journal of Geophysical Research: Earth Surface*, 120, pp. 1251–1273. doi: 10.1002/2014JF003275.Received.

Stumpf, A. *et al.* (2014) 'Ground-based multi-view photogrammetry for the monitoring of landslide deformation and erosion', *Geomorphology*. Elsevier B.V. doi: 10.1016/j.geomorph.2014.10.039.

Stumpf, M. and Porter, M. (2012) 'Critical Truths About Power Laws', *Science*, 335(6069), pp. 665–666. doi: 10.1126/science.1216142.

Tamminga, A., Eaton, B. and Hugenholtz, C. (2015) 'UAS-based remote sensing of fluvial change following an extreme flood event', *Earth Surface Processes and Landforms*, 40(11), pp. 1464–1476. doi: 10.1002/esp.3728.

Terzaghi, K. (1962) 'Stability of Steep Slopes on Hard Unweathered Rock', *Géotechnique*, 12(4), pp. 251–270.

Tinti, S., Maramai, A. and Cerutti, A. (1999) 'The Miage Glacier in the Valley of Aosta (Western Alps, Italy) and the extraordinary detachment which occurred on August 9, 1996', *Physics and Chemistry of the Earth, Part A*, 24(2), pp. 157–161.

Tomás, R., Delgado, J. and Serón, J. (2007) 'Modification of slope mass rating (SMR) by continuous functions', *International Journal of Rock Mechanics and Mining Sciences*, 44(7), pp. 1062–1069. doi: 10.1016/j.ijrmms.2007.02.004.

Tonkin, T. *et al.* (2014) 'The potential of small unmanned aircraft systems and structure-from-motion for topographic surveys: A test of emerging integrated approaches at Cwm Idwal, North Wales', *Geomorphology*. Elsevier B.V., 226, pp. 35–43. doi: 10.1016/j.geomorph.2014.07.021.

Tonkin, T. *et al.* (2015) 'Ice-cored moraine degradation mapped and quantified using an unmanned aerial vehicle: a case study from a polythermal glacier in Svalbard', *Geomorphology*. Elsevier B.V. doi: 10.1016/j.geomorph.2015.12.019.

Turner, D., Lucieer, A. and Wallace, L. (2014) 'Direct georeferencing of ultrahigh-resolution UAV imagery', *IEEE Transactions on Geoscience and Remote Sensing*, 52(5), pp. 2738–2745. doi: 10.1109/TGRS.2013.2265295.

Varnes, D. (1978) 'Slope Movement Types and Processes', *Transportation Research Board Special Report*, pp. 11–33.

Vasuki, Y. *et al.* (2014) 'Semi-automatic mapping of geological Structures using UAV-based photogrammetric data: An image analysis approach', *Computers and Geosciences*. Elsevier, 69, pp. 22–32. doi: 10.1016/j.cageo.2014.04.012.

Vincent, C. *et al.* (2009) 'Glacier thickening and decay analysis from 50 years of ` re , glaciological observations performed on Glacier d ' Argentie Mont Blanc area , France', *Annals of Glaciology*, 50, pp. 73–79.

Virkar, Y. and Clauset, A. (2014) 'Power-law distributions in binned empirical data', *Annals of Applied Statistics*, 8(1), pp. 89–119. doi: 10.1214/13-AOAS710.

Ward, S. and Day, S. (2003) 'Ritter Island Volcano - Lateral collapse and the tsunami of 1888', *Geophysical Journal International*, 154(3), pp. 891–902. doi: 10.1046/j.1365-246X.2003.02016.x.

Westoby, M. *et al.* (2012) '"Structure-from-Motion" photogrammetry: A low-cost, effective tool for geoscience applications', *Geomorphology*. Elsevier B.V., 179, pp. 300–314. doi: 10.1016/j.geomorph.2012.08.021.

Westoby, M. *et al.* (2015a) 'Instruments and Methods: Sedimentological characterization of Antarctic moraines using UAVs and Structure-from-Motion photogrammetry', *Journal of*

Glaciology, 61(230), pp. 1088–1102. doi: 10.3189/2015JoG15J086.

Westoby, M. *et al.* (2015b) 'Inter-annual surface evolution of an Antarctic blue-ice moraine using multi-temporal DEMs', *Earth Surface Dynamics Discussions*, 3(4), pp. 1317–1344. doi: 10.5194/esurfd-3-1317-2015.

Whuber (2010) *How to use CDF and PDF statistics for analysis*, *StackExchange*. Available at: https://stats.stackexchange.com/questions/4810/how-to-use-cdf-and-pdf-statistics-for-analysis (Accessed: 30 July 2017).

Wilkie, K. and Clague, J. (2009) 'Fluvial response to Holocene glacier fluctuations in the Nostetuko River valley, southern Coast Mountains, British Columbia', *Geological Society, London, Special Publications*, 320, pp. 199–218.

Wilkinson, M. *et al.* (2016) 'A comparison of terrestrial laser scanning and structure-from-motion photogrammetry as methods for digital outcrop acquisition', *Geosphere*, 12(6), p. GES01342.1. doi: 10.1130/GES01342.1.

de Winter, I., Storms, J. and Overeem, I. (2012) 'Numerical modeling of glacial sediment production and transport during deglaciation', *Geomorphology*. Elsevier B.V., 167–168, pp. 102–114. doi: 10.1016/j.geomorph.2012.05.023.

Wolman, M. and Miller, J. (1960) 'Magnitude and Frequency of Forces in Geomorphic Processes', *The Journal of Geology*, 68(1).

Wood, J., Harrison, S. and Reinhardt, L. (2015) 'Landslide inventories for climate impacts research in the European Alps', *Geomorphology*. Elsevier B.V., 228, pp. 398–408. doi: 10.1016/j.geomorph.2014.09.005.

Woodget, A. *et al.* (2014) 'Quantifying submerged fluvial topography using hyperspatial resolution UAS imagery and structure from motion photogrammetry', *Earth Surface Processes and Landforms*, 64(August 2014), pp. 47–64. doi: 10.1002/esp.3613.

Wu, C. (2015) *VisualSFM*, *VisualSFM : A Visual Structure from Motion System*. Available at: http://ccwu.me/vsfm/.

Zumbühl, H., Steiner, D. and Nussbaumer, S. (2008) '19th century glacier representations and fluctuations in the central and western European Alps: An interdisciplinary approach', *Global and Planetary Change*, 60(1–2), pp. 42–57. doi: 10.1016/j.gloplacha.2006.08.005.